# RHEOLOGICAL BEHAVIOR AND STRUCTURAL INTERPRETATION OF MODEL WAXY OILS UNDER GELLING CONDITIONS

Thiago Oliveira Marinho

Tese de Doutorado apresentada ao Programa de Pós-graduação em Engenharia Química, COPPE, da Universidade Federal do Rio de Janeiro, como parte dos requisitos necessários à obtenção do título de Doutor em Engenharia Química.

Orientador: Márcio Nele de Souza

Rio de Janeiro

Setembro de 2019

RHEOLOGICAL BEHAVIOR AND STRUCTURAL INTERPRETATION OF MODEL WAXY OILS UNDER GELLING CONDITIONS

Thiago Oliveira Marinho

TESE SUBMETIDA AO CORPO DOCENTE DO INSTITUTO ALBERTO LUIZ COIMBRA DE PÓS-GRADUAÇÃO E PESQUISA DE ENGENHARIA (COPPE) DA UNIVERSIDADE FEDERAL DO RIO DE JANEIRO COMO PARTE DOS REQUISITOS NECESSÁRIOS PARA A OBTENÇÃO DO GRAU DE DOUTOR EM CIÊNCIAS EM ENGENHARIA QUÍMICA.

Examinada por:

_____

Prof. Márcio Nele de Souza, D.Sc.

_____

Prof. Frederico Wanderley Tavares, D.Sc.

_____

Prof.(a) Helen Conceição Ferraz, D.Sc.

_____

Prof. Roney Leon Thompson, D.Sc.

_____

Prof. Cézar Otaviano Ribeiro Negrão, Ph.D.

RIO DE JANEIRO, RJ - BRASIL
SETEMBRO DE 2019

Marinho, Thiago Oliveira

Rheological Behavior and Structural Interpretation of Model Waxy Oils under Gelling Conditions/Thiago Oliveira Marinho. – Rio de Janeiro: UFRJ/COPPE, 2019.

XVIII, 167 p.: il.; 29,7 cm.

Orientador: Márcio Nele de Souza

Tese (doutorado) – UFRJ/ COPPE/ Programa de Engenharia Química, 2019.

Referências Bibliográficas: p. 153-167.

1. Reologia. 2. Óleo Parafínico. 3. Estrutura Química. 4. Tensão de Escoamento. 5 Garantia de Escoamento I. Souza, Márcio Nele de. II. Universidade Federal do Rio de Janeiro, COPPE, Programa de Engenharia Química. III. Título.

*To my mom, who correctly believed that education would be of utmost importance to me, and dedicated her life to give me this opportunity.*

**AGRADECIMENTOS**

Doutorado é uma longa jornada de constante aprendizado. Erros, acertos, contratempos, surpresas... exatamente como a vida deve ser. Muitas pessoas me apoiaram direta ou indiretamente na conclusão desta etapa de importância sem precedentes e portanto merecem meu reconhecimento.

Minha família é detentora da minha maior gratidão. Encontrei em vocês todo amor e carinho e os melhores exemplos que poderia esperar. Obrigado por tudo, muito além das minhas simples palavras.

Obrigado aos meus grandes amigos, companheiros de luta e aprendizado. A vida só é boa quando podemos compartilhar. Sou muito grato a vocês, nos mais diferentes níveis.

Ao meu orientador, muito obrigado pela oportunidade e pelas lições compartilhadas. Obrigado também aos demais professores e colegas da engenharia, com quem pude conviver e aprender muito além dos livros.

Larry Page e Sergey Brin, os “caras do google”, detém meu sincero agredecimento por viabilizarem a mais poderosa ferramente de aprendizado já criada. O mundo inteiro ganhou com a genialidade de vocês!

Por fim, agradeço aos milhões de trabalhadores brasileiros, honestos e anônimos, cujo fruto de seu suor é convertido em incontáveis tributos e financiam boa parte da pesquisa no Brasil. *Laborum aedificat.*

Resumo da Tese apresentada à COPPE/UFRJ como parte dos requisitos necessários para a obtenção do grau de Doutor em Ciências (D.Sc.)

# COMPORTAMENTO REOLÓGICO E INTERPRETAÇÃO ESTRUTURAL DE ÓLEOS PARAFÍNICOS MODELO SOB CONDIÇÕES DE GELIFICAÇÃO

Thiago Oliveira Marinho

Setembro/2019

Orientador: Márcio Nele de Souza

Programa: Engenharia Química

A gelificação de óleos parafínicos representa um grande desafio para a produção segura e econômica de petróleo. Caso temperaturas inferiores à Temperatura de Precipitação de Parafinas seja atingida, uma fração dessas moléculas precipita-se como sólidos cristalinos. Sob condições quiescentes, a precipitação e deposição de parafina é potencializada e o óleo aprisionado nas tubulações pode tornar-se um gel. Este gel não pode ser quebrado com a pressão original do bombeamento, aplicada antes da gelificação para transporte do óleo. Assim, o comportamento reológico de óleos parafínicos sob condições de gelificação é de crucial importância no projeto de tubulações, armazenamento e para fins de remediação de tubulações obstruídas. Neste sentido, esta tese apresenta uma melhor compreensão da transição de fases gel-fluido, baseada no comportamento reológico de óleos parafínicos modelo. A investigação abrangeu quatro diferentes parafinas comerciais solubilizadas em uma matriz de óleo mineral, caracterizadas por meio de análises térmicas, técnicas de espalhamento de raios-X, microscopia de luz polarizada, entre outras. O deslizamento aparente na parede, um dos principais desafios relatados na caracterização reológica de materiais estruturados, é abordado de antemão. A influência de variáveis experimentais sobre a tensão de escoamento de óleos gelificados e o nível de reestruturação da rede cristalina após a quebra do gel é avaliada. A relação entre diferentes estruturas químicas das parafinas e a tensão de escoamento também é investigada. Finalmente, modelos de escala foram obtidos para uma melhor compreensão da microestrutura do material gelificado e para descrever quantitativamente suas propriedades viscoelásticas. Os resultados apresentados e discutidos nesta Tese são de interesse científico e industrial, pois podem ser úteis para os métodos de garantia de escoamento.

Abstract of Thesis presented COPPE/UFRJ as a partial fulfillment of the requirements for the degree of Doctor of Science (D.Sc.)

RHEOLOGICAL BEHAVIOR AND STRUCTURAL INTERPRETATION OF MODEL WAXY OILS UNDER GELLING CONDITIONS

Thiago Oliveira Marinho

September/2019

Advisor: Márcio Nele de Souza

Department: Chemical Engineering

The gelation of waxy crude oils represents a major challenge to safe and economic petroleum production. At temperatures below the Wax Precipitation Temperature (WPT) a fraction of wax molecules precipitates as solid crystals. Under quiescent conditions, the precipitation and wax deposition are enhanced. The crude oil trapped in the pipelines below the WPT may become a waxy-oil gel because of the interlocking of solid wax crystals. This gel cannot be broken with the original steady-state flow operating pressure applied before gelation. Thus, the flow behavior of waxy crude oils under gelling conditions is of crucial importance in the design of pipelines, storage aspects, and for remediation purposes of clogged pipes. In this regard, this Thesis presents a better understanding of the gel-fluid phase transition, based on the rheological behavior of gelled model waxy oils. The investigation encompassed four different commercial waxes solubilized in a mineral oil matrix, molecularly characterized by means of thermal analysis, X-ray scattering techniques, polarized light microscopy, among other procedures. Apparent wall slip, one of the main challenges reported in the rheological characterization of structured materials, is addressed beforehand. The influence of experimental variables on the yield stress of gelled oils and the wax network restructuring level after gel breakage is then evaluated. The relationship among different wax chemical structures and the consecutive yield stress response is also investigated. Scaling models were derived to better understand the microstructure and the wax crystals organization of gelled oils, and also to quantitatively describe their viscoelastic properties. The results presented and discussed in this Thesis incorporate scientific and industrial interest, since they may be useful for flow assurance techniques.

# Contents

**List of Figures** ..... **xi**

**List of Tables** ..... **xviii**

**1 Introduction** ..... **1**

1.1 Contextualization ..... 1
1.2 Research Objectives ..... 6
1.3 Originality Statement ..... 7
1.4 Thesis Structure ..... 7
1.5 Published work ..... 8

**2 Literature Review** ..... **11**

2.1 Flow Assurance ..... 11
2.2 Waxy Gels ..... 16
2.3 Yield Stress ..... 24
2.4 Apparent Wall Slip ..... 33
2.5 Scaling Models ..... 39
2.6 Literature Critical Review ..... 48

**3 Materials and Methods** ..... **52**

3.1 Materials ..... 52
3.2 Methods ..... 52
3.2.1 $^{13}$C Nuclear Magnetic Resonance ($^{13}$C-NMR) ..... 52
3.2.2 X-Ray Diffraction (X-RD) ..... 53
3.2.3 Fourier Transform Infrared Spectroscopy (FT-IR) ..... 53
3.2.4 Differential Scanning Calorimetry (DSC) ..... 53
3.2.5 Gas Chromatography Flame Ionization (GC-FID) ..... 54
3.2.6 Small Angle X-Ray Scattering (SAXS) ..... 54
3.2.7 Model Oils Preparation ..... 54
3.3 Rheological Experiments ..... 55
3.3.1 Investigation on the Effect of Apparent Wall Slip ..... 55
3.3.2 Investigation on the Effect of Experimental Variables ..... 57
3.3.3 Investigation on the Effect of Chemical Structure ..... 61
3.3.4 Rheological Experiments to Derive Scaling Models ..... 62
3.4 Optical Microscopy ..... 62

**4 Results and Discussion..... 64**
4.1 Materials Physicochemical Characterization..... 65
4.1.1 Differential Scanning Calorimetry..... 65
4.1.2 $^{13}C$ Nuclear Magnetic Resonance..... 67
4.1.3 Gas Chromatography Flame Ionization..... 68
4.1.4 X-ray Diffraction..... 69
4.1.5 Small Angle X-Ray Scattering..... 71
4.1.6 Fourier Transform Infrared Spectroscopy..... 73
4.1.7 Rheology of Spindle Oil..... 74
4.1.8 Waxes Morphology..... 76
4.1.9 Conclusions..... 78
4.2 Apparent Wall Slip Phenomenon..... 80
4.2.1 Aging Time..... 80
4.2.2 Yield Stress Frequency Dependency..... 82
4.2.3 Viscoelastic Properties and Apparent Wall Slip..... 83
4.2.4 Creep tests..... 92
4.2.5 Flow curves..... 94
4.2.6 Conclusions..... 97
4.3 Influence of Experimental Variables at Yield Stress..... 99
4.3.1 Viscosity Increase during Cooling..... 100
4.3.2 Cooling Rate Effect..... 102
4.3.3 Wax Content Effect..... 104
4.3.4 Shear Rate During Cooling..... 106
4.3.5 Final Cooling Temperature..... 107
4.3.6 Aging Time Effect..... 109
4.3.7 Storage Modulus and Yield Stress Correlation..... 112
4.3.8 Structure Recovery..... 114
4.3.9 Conclusions..... 117
4.4 Influence of Wax Chemical Structures at Yield Stress..... 119
4.4.1 Measurements of WPT, Yield Stress, $G'_{LVR}$ and $\gamma_{CR}$..... 119
4.4.2 Single Wax Model Oils..... 123
4.4.3 Blended Wax Model Oils..... 126
4.4.4 Conclusions..... 129
4.5 Scaling Models for Gelled Waxy Oils..... 131
4.5.1 Scaling Models for $L_{29}$ 7.5 wt% Model Oil..... 134
4.5.2 Scaling Models for $B_{53}$ 7.5 wt% Model Oil..... 140
4.5.3 Conclusions..... 146

**5 Final Remarks ..... 148**

**6 Further Developments ..... 151**

**7 Cited References ..... 153**

# List of Figures

**Figure 1** - The consequences of continuous wax deposition on (A) well tubing string, (B, C, and D) cross-section of flow lines, and (E) a pipe from a Norwegian production platform (extracted from Tukenov [9], with permission)**. ..... 2**

**Figure 2** - Polarized light microscopies of precipitated wax crystals of model oil 5.0 wt% freshly prepared and cooled at 1.0°C/min (images at 200x magnification)**. ..... 3**

**Figure 3** - Pipeline Inspection Gauges or PIGs are launched and retrieved at pump stations and travel through the pipeline with the moving oil. (A) retired PIG equipment of 1,160 kg, (B and C) a lighter and softer polyurethane PIG and (D) the resulting of pigging operation. Images extracted from "Trans Alaska Oil Pipeline Tour" video, available at https://www.youtube.com/watch?v=_OrAmGOFOEk **..... 5**

**Figure 4** - Schematic representation of wax deposition along a pipe portion in contact with a low-temperature surrounding. As the temperature drops below the WPT, the precipitation and deposition start (adapted from Mendes [51])**. ..... 13**

**Figure 5** - Different profiles of wax thickness distribution for various horizontal flow patterns of the two-phase gas-oil stream (adapted from Matzain et al. [52])**. ..... 14**

**Figure 6** - An artistic concept of a loose network of waxy crystals (A) and a highly connected waxy crystal network (B) (adapted from Paso et al. [2]). The microscopic images were generated throughout this investigation**..... 17**

**Figure 7** - Storage and loss modulus measurements for model oils containing wax at 5.0 wt% (triangles) and 15 wt% (squares) at 25 ºC. The macroscopic aspect of each sample is shown on the right**. ..... 18**

**Figure 8** - Cryo-SEM technique employed to obtain images of 10 wt% of a straight-chain wax (A) and polyethylene wax (B) prepared in isotridecyl isononanoate matrix. In addition, images of a 20 wt% of a straight-chain wax before (C) and after (D) yielding (extracted from Miyazaki and Marangoni [28], with permission)**. ..... 19**

**Figure 9** - The schematic of n-alkanes co-crystallization highlighting the "end-gauche" defect (adapted from Han et al. [73])**..... 20**

**Figure 10** - Storage modulus for model oil 3.0 wt% measured at two subsequent steps: oscillatory cooling from 50°C to 4°C (cooling rate of 1.0°C/min) followed by a time sweep (stress 0.1 Pa and frequency 0.2 Hz) of 100 minutes at 4°C**. ..... 23**

**Figure 11** - Typical yielding behavior for waxy gel sample analyzed in this investigation when submitted to logarithmic stress ramp with frequency 0.1 Hz and temperature of 4°C**. ..... 28**

**Figure 12** - Different yield stress determination method: (A) viscosity plot of 10 wt% bentonite suspension, shear stress-shear rate behavior of (B) Bingham fluid (C) Herschel-Bulkley fluid and (D) a blue ink sample (adapted from Barnes [100])**. ..... 29**

**Figure 13** - Creep experiment for yield stress determination of a waxy gelled oil. The test temperature was 4°C with 2 minutes duration and repeated with new samples for increasing stress values. The structure breakage occurs at levels of 190 to 195 Pa**... 30**

**Figure 14** - Three different situations of sample loading of using a parallel plate geometry 40 mm. A schematic representation of solvent trap, used to mitigate solvent evaporation, is also shown**. ..... 33**

**Figure 15** - The velocity profile for yield stress materials: (A) non-slip conditions, (B) shear banding phenomenon (material inhomogeneity is one possible cause), (C) true slip, and (D) apparent wall slip (adapted from Cloitre and Bonnecaze [108])**. ..... 34**

**Figure 16** - Schematic representation of apparent wall slip phenomenon in (A) parallel plates (adapted from Russel and Grant [118]) and (B) Couette flow, where the outer cylinder is rotated at angular velocity ω relative to the bob (adapted from Yoshimura et al., [119])**..... 36**

**Figure 17** – Geometry elements that can be used for adjustable roughness in the controlled-stress rheometer. Different assemblies can be employed by combining these elements**. ..... 38**

**Figure 18** - Schematic structure of a colloidal gel: the circles indicate fractal floc size and the arrows indicate regions of interfloc links (adapted from Shih et al. [69]). The fractal flocs pack closely and fill the sample volume as repeating units of the colloidal gel network**. ..... 40**

**Figure 19** - Examples of fractal images, including clusters of waxy crystals in a gelled model oil (image generated in this investigation). On microscopic examination, their morphology and structures geometrically exhibit self-similarity to a certain degree**..... 43**

**Figure 20** - $G'_{LVR}$ and $\gamma_E$ as a function of $\phi_w$. The mass of precipitated wax crystals was calculated on the basis of DSC experiments (extracted from Yang et al. [124], with permission)**. ..... 44**

**Figure 21** - Scaling behavior for the yield stress of soft material as a function of the volume fraction. The sample is a mixture of milk fat with canola oil crystallized for 24 h at 5.0 °C (extracted from Marangoni and Rogers [129], with permission)**..... 46**

**Figure 22** - Comparison between fractal dimension values obtained by the direct image-based approach and by rheological measurements for two crude oil samples at different temperatures. The division point is indicated by the arrow (extracted from Gao et al. [78], with permission)**..... 47**

**Figure 23** - Procedure adopted for the rheological experiments. Independent variables are assigned to $x_1$ to $x_6$ (see Table 3)**..... 60**

**Figure 24** - Thermal characterization by DSC for spindle oil and **$L_{29}$** and **$B_{53}$** waxes**…66**

**Figure 25** - Thermal characterization by means of DSC for **$L_{24}$** and **$B_{37}$** waxes**. ..... 66**

**Figure 26** - Detailed $^{13}$C-NMR spectra of **$L_{24}$** and **$L_{29}$** waxes**. ..... 67**

**Figure 27** - Detailed $^{13}$C-NMR spectra of **$B_{37}$** and **$B_{53}$** waxes**. ..... 68**

**Figure 28** - Carbon number distributions for spindle oil and **$L_{29}$** and **$B_{53}$** waxes**. ..... 68**

**Figure 29** - The range of boiling points for spindle oil**. ..... 69**

**Figure 30** - X-ray diffraction patterns for **$L_x$** and **$B_x$** waxes. From top to bottom: **$L_{24}$**, **$B_{37}$**, **$B_{53}$**, and **$L_{29}$**. **..... 70**

**Figure 31** - 2D SAXS images of waxy gels model oils model recorded with a Dectris Eiger R detector. The sample-to-detector distance is about 2.7 m**. ..... 72**

**Figure 32** - Distributions of intensities of scattered X-rays for 7.5 wt% model oils at a temperature of 4°C: at small scattering vector amplitude the profiles obtained are virtually superimposed**. ..... 72**

**Figure 33** - FTIR spectra for spindle oil, $\mathbf{L_x}$, and $\mathbf{B_x}$ waxes**. ..... 74**

**Figure 34** - Flow curve and viscosity curve for spindle oil at 50°C and 4°C (sweep from 0.1 to 1,000 $s^{-1}$ with 80 seconds of equilibration and 40 seconds averaging)**. ..... 75**

**Figure 35** - The viscosity of spindle oil: due to cooling process the viscosity increased 5.6x from an initial temperature of 50°C to 4°C (cooling rate of 1.0°C/min, shear rate 1.6 $s^{-1}$)**. ..... 75**

**Figure 36** - Microscopy images of precipitated wax crystals from freshly prepared model oils cooled from 50°C to 4°C at 1.0°C/min (200x magnification). Single systems are highlighted**. ..... 77**

**Figure 37** - Oscillatory cooling step from 50°C to 4°C of 3.0 wt% $\mathbf{L_{29}}$ wax (dT/dt = 1.0°C/min) followed by a time sweep step of 100 minutes. Inside the detail, the same rheological procedure is depicted, although with a time sweep of 30 minutes**. ..... 82**

**Figure 38** - Frequency sweep tests for $\mathbf{L_{29}}$ 3.0 wt% waxy gels at 4.0°C in the range of 0.1 to 10 Hz and different strain values (0.1% and 1%)**..... 83**

**Figure 39** - Yield stress results for model oil composed of 3.0 wt% $\mathbf{L_{29}}$ wax with seven different geometry assemblies**. ..... 86**

**Figure 40** - Yield stress results for model oils with 3.0 wt% $\mathbf{L_{29}}$ wax (red circles) and 7.5 wt% (green squares) measured with four representative geometries**. ..... 87**

**Figure 41** - Storage modulus in the linear viscoelastic region ($G'_{LVR}$) for 3.0 wt% model oils (red circles) and 7.5 wt% (green squares) measured with four representative geometries**. ..... 88**

**Figure 42** - Logarithmic stress sweep (4°C and 1 Hz, from 1 Pa to 500 Pa) for $\mathbf{L_{29}}$ 3.0 wt% model oil performed with seven different geometries assemblies. It is possible to observe that after G' and G'' crossing point the storage modulus still is captured for all geometries, except for the all-grooved GC+GC and V+GC. Also, there is a kink in the %strain curve for all geometries except for GC+GC and V+GC**. ..... 90**

**Figure 43** - Storage modulus for $\mathbf{L_{29}}$ 3.0 wt% systems measured during logarithmic stress sweep (4°C and 1 Hz, from 1 Pa to 1,000 Pa) for different geometry assemblies. The triplicates for SC+SC and GC+GC tests are shown in details**. ..... 92**

**Figure 44** - Creep tests for model oils **$L_{29}$** 3.0 wt% at (A) all smooth SC+SC geometry and (B) all-grooved GC+GC geometry. The procedure comprises holding the sample for 2 minutes at 4 °C under a constant stress value**. ..... 93**

**Figure 45** - Flow curves of model oil **$L_{29}$** 7.5 wt% at 4°C with GC+GC geometry employing two different equilibration times: (■) 15 seconds and (●) 150 seconds**. ..... 95**

**Figure 46** - Model oil **$L_{29}$** 3.0 wt%: (A) viscosity curve and (B) flow curve at 4°C (from $10^{-3}$ to $10^{3}$ $s^{-1}$) for (■) all smooth and (●) all-grooved geometries**..... 96**

**Figure 47** - Model oil **$L_{29}$** 7.5 wt%: (A) viscosity curve and (B) flow curve at 4°C (from $10^{-3}$ to $10^{3}$ $s^{-1}$) for (■) all smooth and (●) all-grooved geometries**. ..... 96**

**Figure 48** – Viscosity profile along the cooling step for experiment 12 (◧), experiment 10 (●) and spindle oil (▲). Cooling rate was 1.2°C/min and shear rate of 1.6 $s^{-1}$**..... 101**

**Figure 49** - Yield stress distribution for 0.5°C/min and 1.2°C/min cooling rates at two conditions: (A) quiescent and (B) disturbed cooling. Avg stands for the average value of yield stress and σ represents the standard deviation**. ..... 104**

**Figure 50** - Microscopy images for (A) **$L_{29}$** 5 wt%, (B) **$B_{53}$** 5 wt% and (C) **$L_{29}$** + **$B_{53}$** 2.5 + 2.5 wt% systems, taken after an isothermal cooling of 60 minutes at 4°C. The samples were previously cooled from 50°C to 4°C at 1.0°C/min**. ..... 105**

**Figure 51** - Yield stress distribution for final cooling temperatures of 4°C and 12°C. Avg stands for the average yield stress and σ represents the standard deviation**. ..... 107**

**Figure 52**- Microscopy images for a system of **$L_{29}$** + **$B_{53}$** 2.5 + 2.5 wt% cooled until 4.0°C at three different isothermal holding times: (A) 0 min, (B) 30 min, and (C) 60 min. The same composition was used to prepare and cool a model oil until 12°C at three different isothermal holding times: (D) 0 min, (E) 30 min, and (F) 60 min. The samples were cooled from the starting temperature of 50°C at 1.0°C/min**..... 109**

**Figure 53** - Storage modulus evolution in the isothermal holding time step (strain $5x10^{-4}$ and frequency 0.5 Hz) for five experiments. The first 10 minutes establish the major structural changes. The relative increase is represented by the double arrows**..... 110**

**Figure 54** - Yield stress distribution for the aging time variable of 0 min and 60 min. Avg stands for the average yield stress and σ represents the standard deviation**. ..... 112**

**Figure 55** - Typical result from the logarithmic stress ramp (experiment 5, Table 3). $G'_{LVR}$ and yield stress are obtained in this step. The frequency was set to 1 Hz**..... 113**

**Figure 56** - Model oil yield stress and the respective storage modulus in the linear viscoelastic region. Blue triangles represent experiments with shear rate during cooling equals to 1.6 $s^{-1}$, whereas in green squares quiescent cooling was applied**..... 114**

**Figure 57** - Storage and loss modulus at 4°C for different imposed strain (0.5 % and 25 %) for gelled model oil **$L_{29}$** + **$B_{53}$** 3.75 wt% + 3.75 wt%. The sample was freshly prepared and quiescently cooled from 50 to 4°C at 1.0°C/min and frequency of 0.5 Hz**..... 115**

**Figure 58** - Long term experiment to compare the storage modulus for a previous gelled model oil **$L_{29}$** 7.5 wt% at different imposed strains (0.5 % and 25 %). The duration of each step varied from 0.5 to 1.5 hours and it is presented in the red boxes. The sample was freshly prepared and quiescently cooled from 50 to 4°C at 1.0°C/min and frequency of 0.5 Hz**..... 116**

**Figure 59** - Viscosity behavior during the cooling process of **$L_{24}$**, **$B_{53}$** and **$L_{24}$** + **$B_{53}$** model oils with 1.0°C/min rate and shear rate of 0.8 $s^{-1}$**..... 120**

**Figure 60** - A profile of the logarithmic stress sweep used to obtain $\tau_0$, $G'_{LVR}$ and $\gamma_{CR}$ values (oscillatory stress ranging from 0.1 to 1,000 Pa at 0.1 Hz frequency)**..... 121**

**Figure 61** – Graphical representation of Matlab® code used for $G'_{LVR}$ calculations**... 122**

**Figure 62** - Model oils yield stress for singles waxes (left side) and blended waxes (right side)**..... 124**

**Figure 63** - $G'_{LVR}$ and yield stress correlation for single wax and blended waxes model oils**..... 125**

**Figure 64** - Cohesive energy density as a function of yield stress for single waxes and blended waxes systems**..... 129**

**Figure 65** - Strain and storage modulus as a function of oscillatory stress for a gelled model oil **$L_{29}$** 7.5 wt% at 4°C. Oscillatory stress ranged from 0.1 Pa to 500 Pa at a frequency of 1 Hz**..... 132**

**Figure 66** - Hypothetic DSC curves for a pure wax and a model oil prepared by wax solubilization in an oil matrix**..... 134**

**Figure 67** - Oscillatory test for the gelation point determination of **$L_{29}$** 7.5 wt% model oil. The cooling rate was set to 1.0°C/min, frequency of 1 Hz, and %strain of 0.5. Optical microscopy images are shown in details at 50°C and 25°C**. ..... 135**

**Figure 68** - Thermal behavior of **$L_{29}$** pure wax and model oil **$L_{29}$** 7.5 and 15 wt%. The cooling rate was set to 10°C/min**..... 136**

**Figure 69** - Mass fraction of precipitated wax crystals for model oils **$L_{29}$** 7.5 and 15 wt% (detail) under different temperatures calculated from DSC data**. ..... 137**

**Figure 70** - Elastic properties as a function of mass fraction of precipitated wax crystals for a model oil **$L_{29}$** 7.5 wt%**. ..... 138**

**Figure 71** - Precipitated wax crystals from freshly prepared **$L_{29}$** 7.5 wt% model oils cooled quiescently from 80°C to 4°C at 1.0°C/min (200x magnification)**. ..... 140**

**Figure 72** - Oscillatory test for the gelation point determination of **$B_{53}$** 7.5 wt% model oil. The cooling rate was set to 1.0°C/min, frequency of 1Hz, and %strain of 0.5. Optical microscopy images are shown in details at 70°C and 45°C**. ..... 141**

**Figure 73** - Thermal behavior of **$B_{53}$** pure wax and **$B_{53}$** 7.5 and 15 wt% model oils. The cooling rate was set to 10°C/min**..... 142**

**Figure 74** - Mass fraction of precipitated wax crystals of model oils **$B_{53}$** 7.5 and 15 wt% under different temperatures calculated from DSC data**..... 143**

**Figure 75** - Elastic properties as a function of mass fraction of precipitated wax crystals for model oil **$B_{53}$** 7.5 wt%**..... 144**

**Figure 76** - Precipitated wax crystals from freshly prepared **$B_{53}$** 7.5 wt% model oils cooled quiescently from 80°C to 4°C at 1.0°C/min (200x magnification)**. ..... 146**

# List of Tables

**Table 1** - Rheological tests according to the composition and geometry employed .... **57**

**Table 2** - Compositions used in the investigation of the experimental variables..... **57**

**Table 3** - Factorial experimental design $2^{6-1}$: independent variables and levels ..... **58**

**Table 4** - Experimental conditions for the rheological tests performed ..... **59**

**Table 5** - Waxes structural and physical features ..... **65**

**Table 6** - Morphological features for wax crystals of $\mathbf{L_x}$ and $\mathbf{B_x}$ model oils ..... **78**

**Table 7** - Geometries used in the apparent wall slip investigation..... **84**

**Table 8** - Yield stress, $\tau_0$ RPE and $G'_{LVR}$ for two different model oils composition..... **84**

**Table 9** - Experimental conditions, yield stress, storage modulus and final viscosity .. **99**

**Table 10** - Significant parameters calculated for Equation 14 ..... **102**

**Table 11** - WPT for the tests with shear rate during cooling set to 1.6 $s^{-1}$..... **108**

**Table 12** - Rheological properties and cohesive energy density ($E_c$) of waxy gels. ... **123**

**Table 13** - Parameter values for the scaling model of $\mathbf{L_{29}}$ 7.5 wt% system..... **139**

**Table 14** - Parameter values for the scaling model of $\mathbf{B_{53}}$ 7.5 wt% system ..... **145**

# 1 Introduction

In this introductory chapter of the Thesis entitled *"Rheological Behavior and Structural Interpretation of Model Waxy Oils under Gelling Conditions",* it is described the theme contextualization as well as the goals and contributions of this study in section 1.1 and 1.2, respectively. In addition, the document structure is presented in section 1.3 and the disclosed results related to this Thesis, presented at different conferences, and also the published papers are listed in section 1.4.

## 1.1 Contextualization

Waxy crude oils contain significant amounts of paraffin-wax compounds, referred as wax henceforward. These molecules are a mixture of hydrocarbons molecules known to produce a gel-like structure under specific circumstances when cooled below a critical temperature, referred to Wax Precipitation Temperature, WPT. The wax content may vary in great extent according to the crude oil origin, however, there is evidence that with as little as 2.0 wt% precipitated wax, gelling may occur [1]. The wax precipitation and deposition precede the fluid gelation and cause detrimental effects in several aspects of crude oil processing. This is a flow assurance problem faced in cold-environment, as in arctic climates or subsea producing fields [2]. The waxy gel deposits formed in the pipeline internal walls increase in thickness and hardness with time and they limit the throughput of oil by increasing the head losses required to produce it [3]. The cooling favors the fluid gelation, especially at quiescent conditions. This scenario leads to a strong waxy crystal interlocking network, which is accompanied by a drastic change in rheological properties [4], [5]. The consequences of continuous wax deposition during oil production and transportation are shown in Figure 1.

At a microscopic level, wax crystallization and gelation proceeds in several phases, the first of which is believed to be the formation of lamellar sub-crystals comprised of a solid solution of the paraffinic components. Mismatches between the length of the crystal molecules and the thickness of the packing layer cause conformational disorder in the interlamellar regions of the crystals [6]. Evidence indicates lamellar thicknesses of 1.5 to 3 nm, corresponding roughly to the length of linear $C_{20}$ wax, and interlamellar distances from 30 to 100 nm [7], [8]. The disorder in the interlamellar region favors the growth of these sub-crystals in two dimensions as sheet-like crystals. The next stage in the process suggests that these sub-crystals further associate into a second sort of elementary

structure of micrometer size incorporating a large volume of solvent. These finally aggregate to form the large space-filling network seen in microscopy images [6].

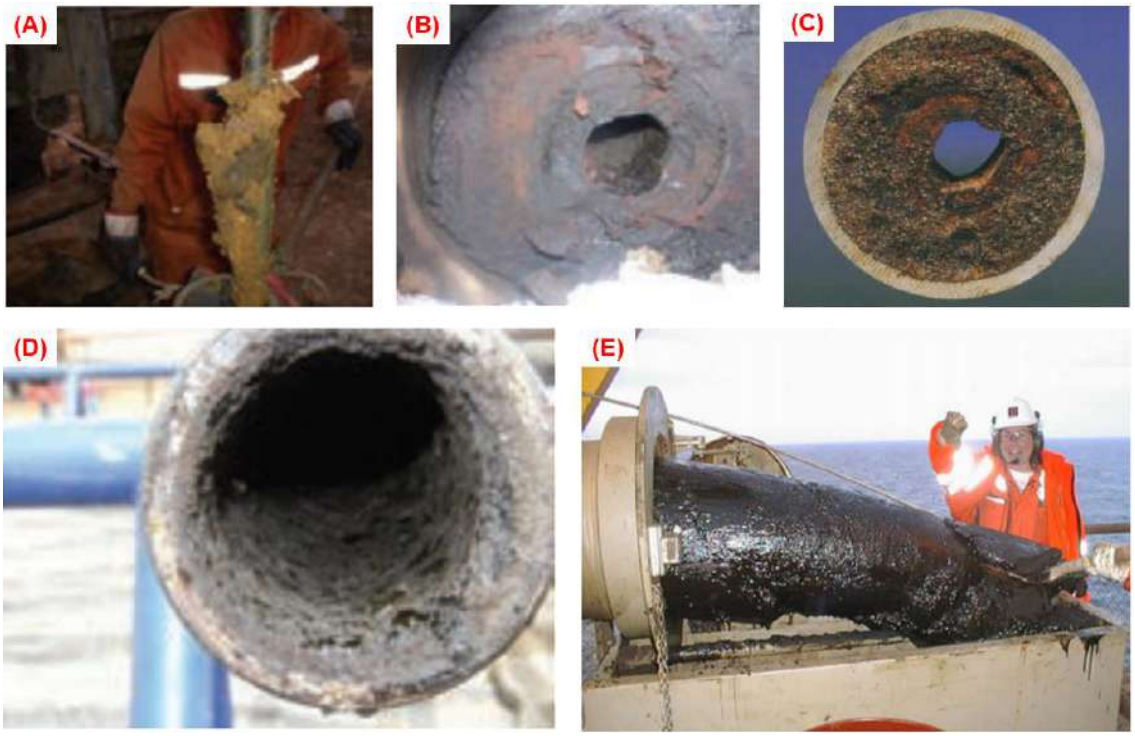


Figure 1 - The consequences of continuous wax deposition on (A) well tubing string, (B, C, and D) cross-section of flow lines, and (E) a pipe from a Norwegian production platform (extracted from Tukenov [9], with permission).

Most fluids exhibiting yield stress can be thought of as having a structural skeleton extending throughout the entire volume of the system. The strength of this skeleton is maintained by the structure of the dispersed phase and its interactions. High volume fractions of a dispersed phase and/or strong interactions between components can increase the viscosity by many orders of magnitude and induce solid-like behavior. In addition, the solidification of waxy compounds leads to the formation of a gel which is not composed of a pure crystalline phase, but it entraps a significant amount of liquid [10], [11].

Images of wax crystals generated in polarized light technique and precipitated from a model oil 5.0 wt% wax are exhibited in Figure 2. It is possible to observe a clear increase in the precipitated wax content due to the temperature drop. Ultimately, the interactions among these crystals are the main responsible for the changes in the rheological behavior of waxy crudes.

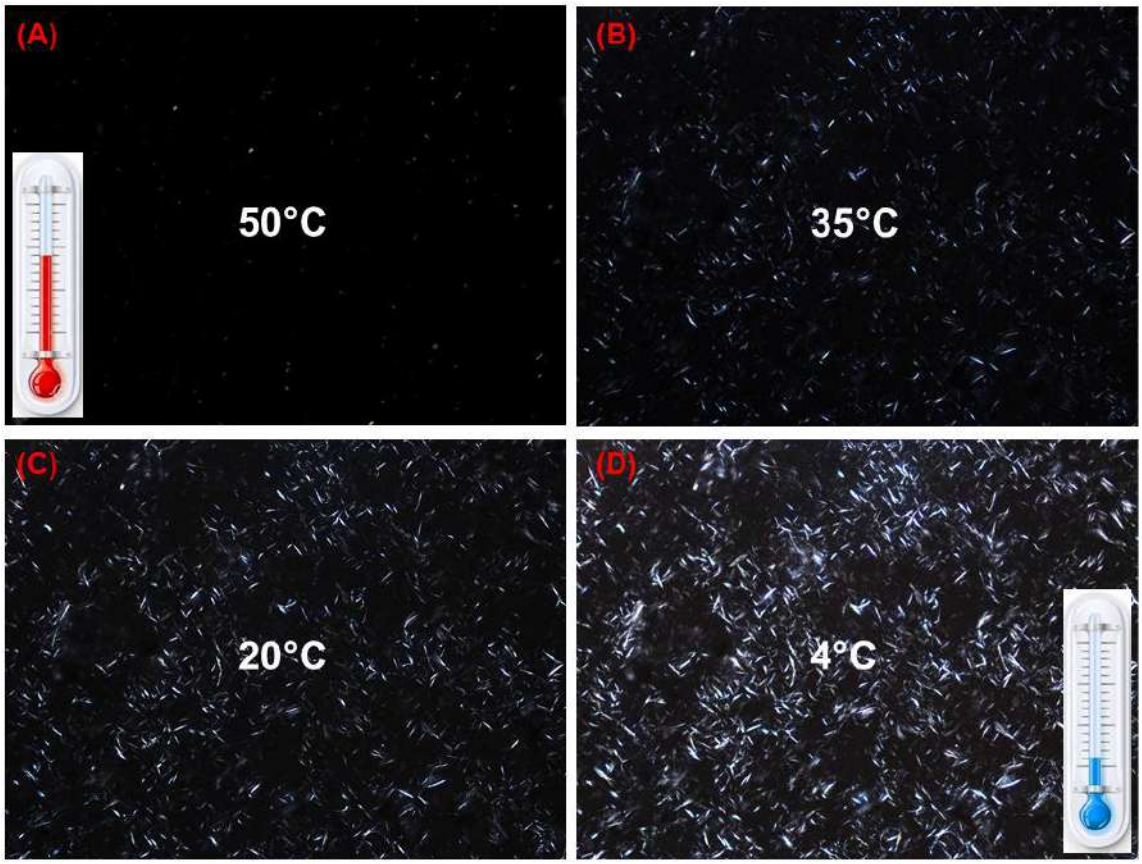


Figure 2 - Polarized light microscopies of precipitated wax crystals of model oil 5.0 wt% freshly prepared and cooled at 1.0°C/min (images at 200x magnification).

The interlocking lattice of wax crystals imparts yield stress to the oil and this additional rheological property must be considered in the design of crude oil transport pipelines. In other words, pumps maximum head pressure must be able to fracture the gel in order to resume the flow [12]. Upon application of sufficient force, the lattice will break down and the yield stress and viscosity of the oil will diminish considerably. When the pump pressure is nearby the material critical stress, the elastic elements of this material are sufficiently stretched. By the time that such elastic elements approach their critical strain, the structure begins to disrupt causing shear thinning and subsequent flow [13]. Thus, for the successful operation of a pipeline, the designer must understand the yielding behavior of gelled oils to determine the pump design and power required to achieve flow and also the time required to fully clear the line.

In rheological terms, the pumping of a waxy gelled material is connected to the yield stress. The yield stress is “the side effect” resulting from the gelation process of waxy crudes and, roughly speaking, it can be considered as the minimum stress required to impose a continuous deformation on the material, i.e., continuous flow [14]. For engineering purposes, it is also an essential parameter to estimate the restart pressure

of pipelines because it is related to fracture of gelled material [15], [16]. Equation 1 provides a straightforward relation to this respect [17]:

$$\Delta P = \frac{4\tau_0 L}{D} \quad \text{Eq. (1)}$$

In Eq. (1) $L$ and $D$ represent the characteristic length and diameter of a pipeline portion, and $\tau_0$ represents the static yield stress of the fluid. Whenever $4\tau_0 L/D$ is close to or higher than the maximum $\Delta P$ available, restart procedures can be problematic. Successful restart depends on the ability to pressurize the pipeline sufficiently to fracture the gel in order to resume the flow. Upon application of sufficient force, the lattice will break down and the yield stress and viscosity of the oil will diminish considerably [18]. If the mechanical strength of a gel in a pipeline becomes exceedingly high the pipeline must usually be replaced [11], [19].

It can be found several models for the yield stress prediction in the literature [20]–[22]. The cooling rate, wax content, shear effects, and physical aging of a wax crystal network greatly affect the rheology of a gelled oil [8], [23]. Also, the initial cooling temperature has an impact on the yield stress of waxy crude oils [24]–[26]. Another key aspect to be considered in order to predict and control the wax-oil gel properties is the relationship between the structure and mechanical response of this system [27], [28]. At a fundamental level, it is important to relate the bulk rheology of waxy oils under gelling conditions to the wax chemical structures present in the system. This task is especially relevant because, due to its complex composition, conventional rheological models such as Bingham or Herschel-Bulkley are not able to fully describe the rheological behavior of gelled waxy oils [14].

One of the adopted strategies for wax deposits removal consists of using a PIG (Pipeline Inspection Gauge), which promotes a mechanical scraping in order to remove encrusted material. Figure 3 exhibits PIG equipment used in a pipeline delivering oil from Prudhoe Bay to Valdez (Alaska, USA) and the resulting of a pigging operation. However, when the gel structure is strong enough, the PIG itself may be entrapped inside the pipe [29]. Another approach is to use chemical additives to prevent wax deposition. A wax crystal modifier can be added to the oil to prevent the deposition even below the WPT. Thermal methods include heating and insulating the pipeline or introducing hot fluids above the WPT to melt or prevent wax deposition. However, these solutions may not be feasible technically and/or economically for all situations [30]. Aiyejina et al. [31] reviewed a number of studies about chemical inhibitors of wax deposit and demonstrated that the

efficacy of commercially available inhibitors tends to be limited and it has to be evaluated on a case-by-case basis. In this regard, successful risk abatement strategies typically incorporate a comprehensive planning and implementation program, utilizing mechanical, thermal, and chemical remediation methods. Thus, a fundamental understanding of the wax gelation and deposition process is necessary in order to appropriately scale laboratory measurements to field conditions and obtain useful forecasts.


Figure 3 - Pipeline Inspection Gauges or PIGs are launched and retrieved at pump stations and travel through the pipeline with the moving oil. (A) retired PIG equipment of 1,160 kg, (B and C) a lighter and softer polyurethane PIG and (D) the resulting of pigging operation. Images extracted from “Trans Alaska Oil Pipeline Tour” video, available at https://www.youtube.com/watch?v=_OrAmGOFOEk

In recent years, scholars mostly adopted the flow loop as the experimental device for wax deposition research. With this system, it is possible to estimate the deposition rate by comparing the pressure drop difference between the test section and the reference section [32]. Despite the nearest design to actual field condition, it does have some shortcomings that should not be ignored, such as consuming overmuch oil sample, covering a large area, and requiring high investment and maintenance costs [33]. Therefore, laboratory tests employing a controlled-stress rheometer configures a

suitable option in flow assurance studies. Other accessory techniques such as differential scanning calorimeter and optical microscopy enhance the interpretation of the rheological results. Another important aspect of flow assurance regards the extreme compositional complexity and the differences between crude oils, which lead to some degree of variation in aggregate structures and physical behavior. An attempt to overcome this situation is to use model oils with a fixed and well-known composition. This strategy provides more straightforward relations between the rheological results obtained and the effect of experimental variables. Nonetheless, care should be taken in extrapolating results obtained for highly simplified systems to crude oils.

Finally, in order to obtain relevant, robust and reliable rheological data, some aspects of the practical measurement set-up must be considered. Experimental artifacts, such as the so-called apparent wall slip can exert great influence on the rheological property being measured and it must be avoided [34]. Due to its importance, this effect is judiciously analyzed in this Thesis. Despite the effort, there still many open questions regarding the gelation process and yield stress appearance in crude oils. Thus, the present investigation is inserted in an open and active field of flow assurance studies.

## 1.2 Research Objectives

The present Thesis aims to investigate the rheology of model oils under gelling conditions in controlled experiments, predict their flow behavior, and relate it to wax structural and morphological aspects. The main objectives are the following:

1. To perform physicochemical characterization of the materials composing the model oils to gain insight into the material structure and waxy crystals organization;
2. To establish suitable protocols for the yield stress measurement of gelled model oils;
3. To measure and analyze viscosity and other relevant viscoelastic properties in a wide range of conditions;
4. To analyze the experimental variables relevant in the gelling process quantitatively;
5. To obtain relationships among wax structural features and the consecutive yield stress response of the gelled oils;
6. To propose a quantitative description for the elastic properties of gelled waxy oils in the framework of the scaling theory;

## 1.3 Originality Statement

The rheology of waxy oils is currently well established and it is a core subject in the flow assurance context. Although, despite the myriad of papers already published in this regard, a more fundamental knowledge of the relationship between the gelled microstructure of the material and its rheology still necessary. It is precisely in this area that the original contribution of this Thesis lies. For example, it contains original and interesting results showing that mixture of branched and predominantly linear wax fractions can have various behaviors, including the unexpected increase of yield stress by adding a branched wax to a waxy oil of a linear wax, explaining some odd behavior sometimes found in crude oils. Besides, it brings to the literature the analysis of the storage modulus that has a sounder theoretical basis than the yield stress for relating the observed value to material properties. The derived scaling models were also a bridge between wax microstructure and the mechanical response of the gel. As the waxes and oil matrix were well characterized their influence could be better understood and the results are a meaningful addition to the literature.

## 1.4 Thesis Structure

The structure of this document is composed of seven chapters. The first (Introduction) established the scope, context, and objectives of this research, guided by the criterion of innovative relevance, time and experimental apparatus availability. Also, a list of published material related to the Thesis is available.

Literature Review is presented in Chapter 2, which encompass relevant aspects found in the literature in an organized way. The selected topics are related to the development and interpretation of the results contained in this Thesis. In addition, the last section, Literature Critical Review, provides a point of view of the author regarding the already published knowledge.

In Chapter 3, Materials and Methods, the relevant procedures and experimental details are described, and each equipment employed is cited. The main technique used was the rheometry, however many other accessory techniques are listed in this investigation.

Chapter 4, Results and Discussion, deals with the exposition, analysis, and interpretation of the significant data gathered in this study. It encloses the four important subjects of this Thesis: the quantification of apparent wall slip phenomenon, the influence of the

main experimental variables at yield stress of gelled oils, the relation of the wax chemical structure and yield stress and the modeling effort contained in the scaling models.

The concluding remarks are presented in Chapter 5 together with some suggestions for further developments, in Chapter 6. All cited references are available at the end of this document, in Chapter 7.

### 1.5 Published work

This section lists the work related to this Thesis presented in conferences, published as papers and also those ones in submitting process.

1. Published papers:

   T. O. Marinho, C. N. Barbato, G. B. Freitas, A. C. Duncke, M. C. K. de Oliveira, M. Nele, “Interaction Effects of Predominantly Linear and Branched Waxes on Yield Stress and Elastic Modulus of Waxy Oils”, *Energy and Fuels*, vol. 32, no. 8, pp. 8057–8068, 2018.

   T. O. Marinho, M. Nele, C. N. Barbato, M. C. K. de Oliveira, “Rheological and Thermal Behavior of Water-Waxy Crude Oil Emulsions and Model Oil Systems”, *Offshore Technology Conference*, 2015 (DOI: 10.4043/26242-MS).

   T. O. Marinho, M. C. K. De Oliveira, M. Nele, “An Experimental Investigation of Rheology and Crystal Morphology of Model Waxy Oils under Gelling Conditions”, *Energy and Fuels*, (just accepted, available on-line in October, 3, 2019).

2. Papers to be published:

   T. O. Marinho, F. H. Marchesini, M. C. K. de Oliveira, M. Nele, “Apparent wall slip effects on the viscoelastic properties and flow behavior of waxy gels”, *Journal of Rheology*, (submitted in October, 4, 2019).

3. Works presented in conferences:

T. O. Marinho, C. N. Barbato, G. B. Freitas, A. C. Duncke, M. C. K. de Oliveira, "Evaluation of yield stress in model oil systems under gelling conditions", *VII Brazilian Conference on Rheology*, 2015.

T. O. Marinho, C. N. Barbato, G. B. Freitas, A. C. Duncke, M. C. K. de Oliveira, M. Nele, "The Influence of Wax Chemical Structure at Model Oils Yield Stress", *XXI Brazilian Congress of Chemical Engineering*, 2016.

T. O. Marinho, C. N. Barbato, G. B. Freitas, A. C. Duncke, M. C. K. de Oliveira, M. Nele, "Evaluation of Wax Chemical Structure on Model Oils Yield Stress", *17th International Conference on Petroleum Phase Behavior and Fouling*, 2016.

T. O. Marinho, G. B. Freitas, A. C. Duncke, M. Nele, "Relationship between Model Oils Viscoelastic Properties and Wax Crystal Microstructure", *9th Brazilian Congress R&D in Petroleum and Gas*, 2017.

T. O. Marinho, G. B. Freitas, L. S. Barbosa, A. V. B. Silva, "Alternative Yield Stress Estimative Applied to Waxy Crude Oils", *IV Brazilian Congress of Rheology*, 2017.

T. O. Marinho, C. N. Barbato, G. B. Freitas, A. C. Duncke, M. C. K. de Oliveira, M. Nele, "Yield Stress Measurements Applied to Model Oils: A Discussion on Wall Slip and Geometry Effects", *IV Brazilian Congress of Rheology*, 2017.

T. O. Marinho, M. C. K. de Oliveira, M. Nele, "Influence of Wax Chemical Structure on Waxy Oils Yield Stress and Elastic Modulus", *19th International Conference on Petroleum Phase Behavior and Fouling*, 2018.

T. O. Marinho, A. R. de Andrade, H. C. M. Guilherme, A. L. da Nova, M. Nele, "Strategy to Evaluate Chemicals Flow Behavior for Oil Field Injection: A Flow Assurance Approach", *19th International Conference on Petroleum Phase Behavior and Fouling*, 2018.

T. O. Marinho, F. H. Marchesini, M. C. K. de Oliveira, M. Nele, "Investigation of Apparent Wall Slip Effects on Viscoelastic Properties of Waxy Gels", *VIII Brazilian Conference on Rheology*, 2018.

T. O. Marinho, M. Andreotti, A. Leocadio, H.C.M. Guilherme, G.E. Oliveira, “Rheological Behavior of Upstream Chemicals under HPLT conditions”, *20th International Conference on Petroleum Phase Behavior and Fouling*, 2019.

T. O. Marinho, M. Andreotti, H.C.M. Guilherme, G.E. Oliveira, “Aging Impact on the Rheological Behavior of Upstream Chemicals under HPLT conditions”, *20th International Conference on Petroleum Phase Behavior and Fouling*, 2019.

# 2 Literature Review

The gelling of waxy oils is not a recent subject. In fact, it has been the object of studies for more than 80 years [10]. Seminal papers regarding the waxy crude rheology and the yielding of gelled material have already been published, e.g., Wardhaugh and Boger [35], Rønningsen [36], Chang and Boger [18] and Barnes [37]. Despite that, the rheology of waxy oils still an active field either by its industrial importance or by academic interest. In this review, the works published in the last 20 years are prioritized since it is assumed that previous knowledge was already incorporated by the new authors.

Section 2.1 presents the general challenges of flow assurance by the waxy oil perspective, the consequences of continuous wax deposition and the mitigation mechanisms employed in real production scenarios. Section 2.2 gathers the information of waxy gelled systems. The objective here is to introduce this complex fluid, based on existing works. Section 2.3 presents the most important rheological property in the context of gelled waxy oil, the yield stress. Its origin, measurements methods, experimental artifacts such as apparent wall slip are discussed.

Next, in Section 2.4, mathematical models are discussed under the light of the scaling theory, derived to relate material structure to mechanical properties of the material. The concept of fractal dimension is also approached in this section. Finally, Section 2.5 presents the conclusions of this literature review and some author's own perspective on the researched field.

## 2.1 Flow Assurance

Flow assurance is a major concern to the petroleum industry when dealing with waxy crude oils, especially in offshore platforms and arctic environments. Wax precipitation and deposition is one of the pervasive nuisances in oil industry operations worldwide, with wax deposits creating problems from the wellhead to the refinery. Even when the oil is not in a completely gelled state, operations are adversely affected by paraffin wax precipitating out and solidifying at the wellbore, in the tubing, perforations, pump strings, and rods, in addition to transfer system and pipelines, as can be seen in Figure 1 [9]. The consequences are equipment failures, bottlenecks upstream and downstream, and loss

of production, transport capacity, and storage, all resulting in risk operations and loss of revenue [4], [31].

In this regard researchers generally address the efforts towards rheology, DSC, and microscopy analysis in order to unveil relevant data of waxy crude flow under cooling regimes [4], [31], [38], [39]. Likewise, a significant effort is devoted to model the oil intricate rheological behavior under gelation conditions and yield stress prediction. Due to petroleum multi-component nature and variable composition, the gel formation mechanism is quite complex. Cooling rate, shear rate, shear stress, solid fraction, initial cooling temperature and aging time are the experimental variables usually assessed [12], [24]–[26], [40]–[43]. It is also important to consider the influence of wax chemical structure on the yield stress since it is promoted by interlocking networks maintained by London-Van der Waals forces among wax crystals [36], [44].

At reservoir conditions, with temperatures ranging from 70 to 150°C and pressures of 8,000 up to 15,000 psi, waxes are completely solubilized, which favors oil transport through pipelines [45]. At regular production operation, the oil is pumped from the reservoir at temperatures above the Wax Precipitation Temperature, defined as the temperature below which solid crystals of paraffinic components start forming [2]. Although, due to heat transfer from oil bulk to cold neighborhoods, which results in temperatures lower than the WPT, wax crystal precipitation may occur during production, transportation, and storage [46], [47].

The Wax Precipitation Temperature is highly dependent on oil composition. Thus, it is not unusual to find waxy crudes with WPT of 40°C or higher [36], [48]. On the other hand, subsea pipelines at deep-water production sites might exhibit temperatures as low as 4°C [4], whereas the polar weather can easily produce temperatures below -10°C. Therefore, wax precipitation and deposition is such a ubiquitous problem in these scenarios. In fact, after hydrate precipitates, wax precipitates are the second most common cause of blocked flowlines in oil production scenarios [49].

Figure 4 contains a schematic representation of the deposition phenomenon along a pipe portion placed in contact with a cold neighborhood. The hot fluid coming from the reservoir experiences a temperature drop due to the heat loss to the surroundings. The decrease in oil temperature induces a partial crystallization of waxes by a supersaturation mechanism, involving in the first place the longest alkane molecules [8]. As the distance from the well is increased a radial temperature gradient is established and the wax deposits grow from the internal walls. Depending on the deposition severity,

a potential gelation region may develop. The issue is enhanced when a flow shutdown occurs, due to emergencies or maintenance situations, as, in this case, a gelled fluid appears for very low amounts of precipitated crystals (~ 1.0 to 2.0 %wt) [1], [50]. This scenario leads to a strong waxy crystal interlocking network which is accompanied by a drastic change in rheological properties, such as yield stress appearance. Under such conditions, the tendency of waxy crude oils to form a percolated gel phase may result in the blocking of a flow-line that can cause a halt in production. The strong gelled material can also cause partial or complete blockage of pipelines, damage to process equipment and complications at pumping restart operations [16], [31].

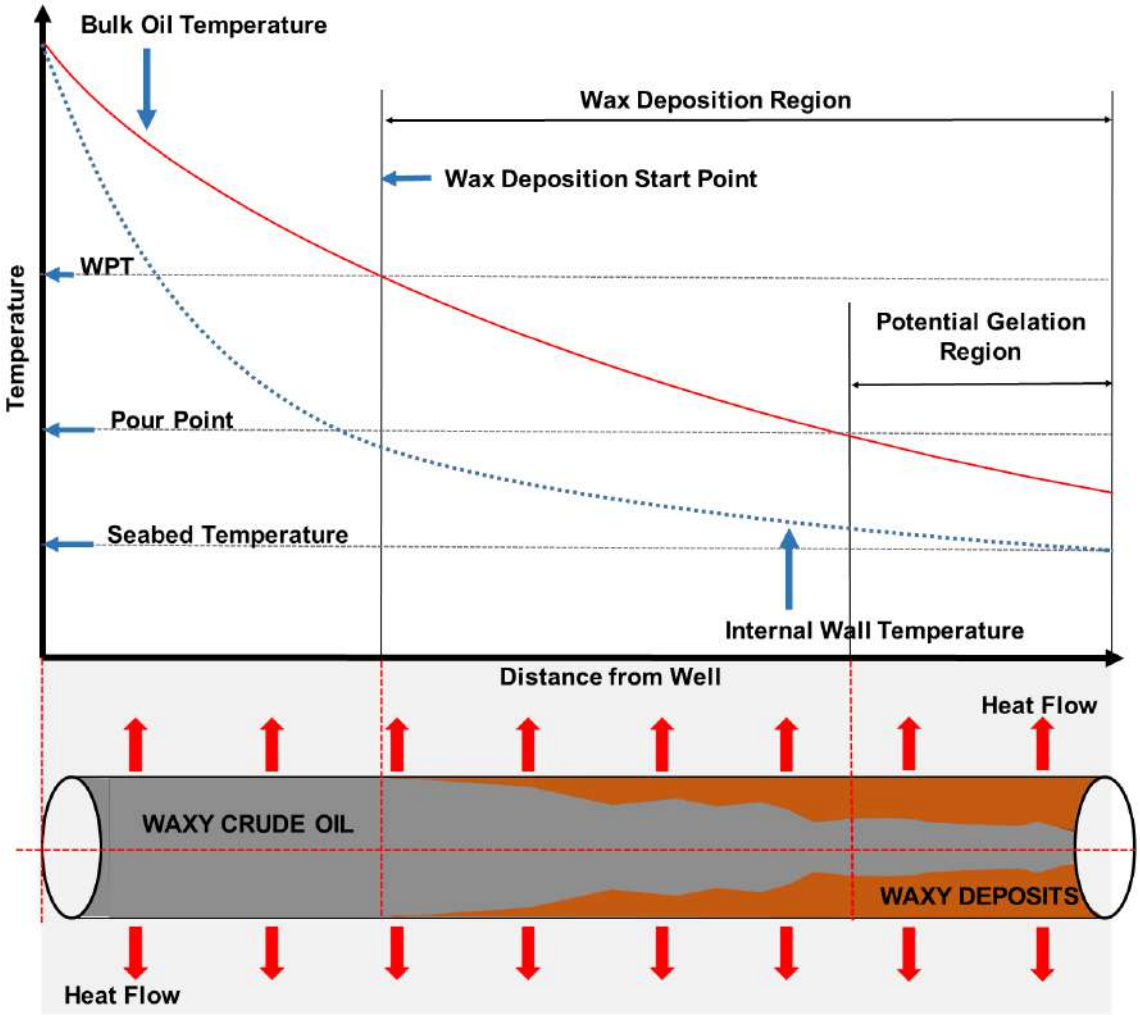


Figure 4 - Schematic representation of wax deposition along a pipe portion in contact with a low-temperature surrounding. As the temperature drops below the WPT, the precipitation and deposition start (adapted from Mendes [51]).

It is common knowledge that crude oil flowing in a pipeline in a cold environment is not necessarily at risk of blockage owing to gelation, provided that the system is kept in

movement [48]. In this sense, the oil flow rate also interferes with wax solubility: the lower the flow rate, the longer the oil stays inside the pipeline, which favors heat exchange with the external environment. Also, the thickness, hardness, and profile of wax deposition show dependence on the flow velocity of the circulating oil [31]. Matzain et al. [52] used a high-pressure multiphase flow test facility to measure wax deposits under different conditions for two-phase gas-oil flow. In horizontal flow, the thickness of deposits varied around the circumference of the pipe depending on flow pattern, as shown in Figure 5. The authors account for the different distributions by describing how, in stratified flow, only the lower part of the wall will be in contact with the oil phase, and the heat transfer rate will be highest at the bottom part of the pipe, resulting in decreasing deposit thickness in a crescent shape (Figure 5A). In the case of wavy stratified flow, the wavy gas-oil interface is cooled because of the waves, increasing heat transfer rate and, thus, deposit thickness along with the interface (Figure 5B). For the intermittent flow, the passing of liquid slugs induced high shear force and stress along the bottom of the test pipeline and shearing of wax deposits, resulting in thinner deposits at the bottom of the pipe (Figure 5C). With annular flow, the wax thickness is uniform around the circumference, as oil is uniformly in contact with the entire wall surface (Figure 5D).

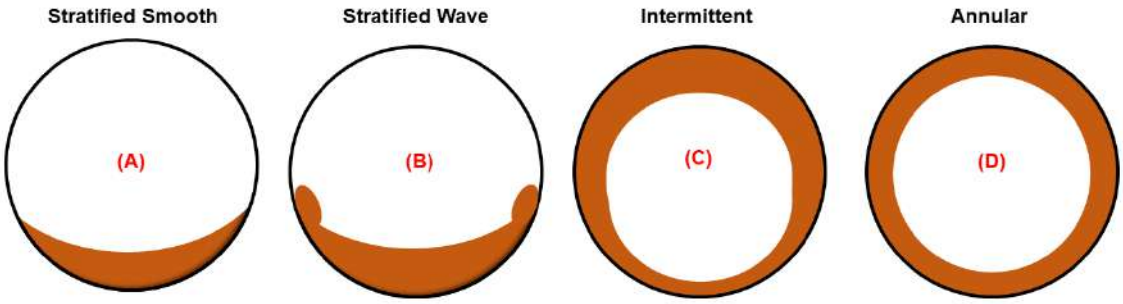


Figure 5 - Different profiles of wax thickness distribution for various horizontal flow patterns of the two-phase gas-oil stream (adapted from Matzain et al. [52]).

At offshore petroleum production, the presence of water leads to the unavoidable water-in-oil emulsion formation, as crude oils contain natural surfactants molecules [53]. Crude oil emulsions can pose significant flow assurance risks. Due to the little propensity to wet the oil-water interface the waxy molecules enmesh via London-Van der Waals interactions during a cooling process to form a crystal network that stabilizes the emulsions by physically encasing the dispersed phase [54]. According to Visintin et al. [38], in a water-in-waxy-oil emulsion, the structure of a load-bearing gel includes water droplets, which enables the appearance of a volume-spanning wax crystal network. Also, emulsion stabilization is achieved when waxy crystals prevent coalescence by hindering

the drainage and rupture of water droplets. Results regarding the influence of water content at gelled water-in-oil emulsions are described elsewhere [41], [55], [56].

The physical aging of a wax crystal network will also greatly affect the rheology of a gelled oil. As they age, growing wax crystals will further enmesh, resulting in a material that is stiffer and more brittle [54]. This aging process involves the molecular diffusion of wax molecules from the bulk fluid into the occluded liquid within the deposit, where the components subsequently precipitate, causing an increase in the solid fraction of the deposit with time, consequently increasing its hardness [2]. Therefore, a long-term shutdown of a production line containing waxy crude oil represents a high loss of revenue and also an increased risk for the restart pumping operations.

Once the waxy crude is in a gel state, its yielding behavior is composed of three main characteristics: the elastic response, the slow deformation, and the sudden and dramatic material fracture [35]. These characteristics would all influence the behavior during pipeline start-up and would determine the nature of a line clearing model. Chang et al. [18] came up with the same reasoning, attesting that the yielding of waxy crude oil occurs by an initial elastic response, followed by viscoelastic creep and a final fracture. Therefore, in order to restart the oil flow, the gelled structure must be disrupted by a large pressure drop across the pipeline.

The most effective way of dealing with the problem of wax deposition in crude oil pipelines would be to prevent it from occurring in the first place. In this regard, chemical additives are widely used since co-crystallization might induce the formation of weak points in the crystal structure [31]. Thus, wax inhibitors are employed to maximize oil production potential by preventing deposition/restriction in flowlines and tubular, providing flow assurance. Also, to reduce or eliminate downhole depositions, increasing production and reduce the pour point of waxy crude oils to meet contract specifications or improve flow [57]. Although, the efficacy of commercially available inhibitors tends to be limited, and has to be evaluated for each specific situation [58]. Thermal methods and pigging procedures are other options. Nonetheless, the availability and/or feasibility of these techniques may be limited [29].

The gelation of waxy oils represents a major challenge to safe and economic oil production. To determine suitable operational conditions at production petroleum fields located in low-temperature environments is therefore crucial to understand the formation, resistance and breakage process of waxy gelled oil. For the successful operation of a pipeline, the designer must understand the yielding behavior of gelled oils to determine

the pump design and power required to achieve flow and also the time required to fully clear the line. It is no doubt a challenge to flow assurance techniques.

## 2.2 Waxy Gels

Waxes are natural constituents of crude oil, typically soluble in the liquid oil phase at the reservoir conditions. The high pressure (8,000 to 15,000 psi) maintains the light compounds solubilized in the crude oil, which favors the solubilization of waxes in the fluid [45], [59]. The high temperature (70 to 150°C) precludes the wax precipitation. These conditions ensure low viscosity and Newtonian fluid behavior for crude oil [60].

The waxes may be divided into two main classes: macro and microcrystalline. Macrocrystalline wax is regarded as the main responsible for deposition and gelation problems during petroleum production. It is constituted primarily by n-alkanes with few or no branches, H/C ratios between 1.96 and 2.05, exhibiting carbonic chains with 20-50 atoms length and melting point ranging to 40-60°C [61]. On the other hand, microcrystalline waxes are aliphatic hydrocarbon compounds containing a lot of branches and rings, exhibiting also a broader carbon number distribution ~ 30-70 carbon atoms. Due to the lack of large-scale crystallinity, they present a wider melting point range, approximately 60-90°C [62].

In terms of intermolecular interactions, nonpolar molecules, such as the waxes, have no measurable dipole moment, and the dipole-dipole attractive force between two alkane molecules is exceedingly small [63]. The principal contributor to intermolecular attraction in alkanes is an induced-dipole-induced-dipole attraction, which is a very weak force. Therefore, interactions between waxes mainly result from the weak attractive London-Van der Waals forces [64].

Solid wax crystals form by nucleation in the bulk fluid phase [65]. The phenomenon named gelation occurs when growing waxy crystals, precipitated from the oil, interlock and form a volume-spanning network of crystal-crystal bonding interactions. The liquid oil phase becomes entrained within the network and the crude oil rheological behavior turns from a simple Newtonian to much more complex behavior [5],[36]. Depending on the wax chemical structure and sample shear and thermal histories, different gelled material may emerge due to a cooling process [67]. Figure 6 exhibits an artist's rendition from images of waxy crystals in solution representing a loose and a highly connected crystal network, i.e., a gelled system.

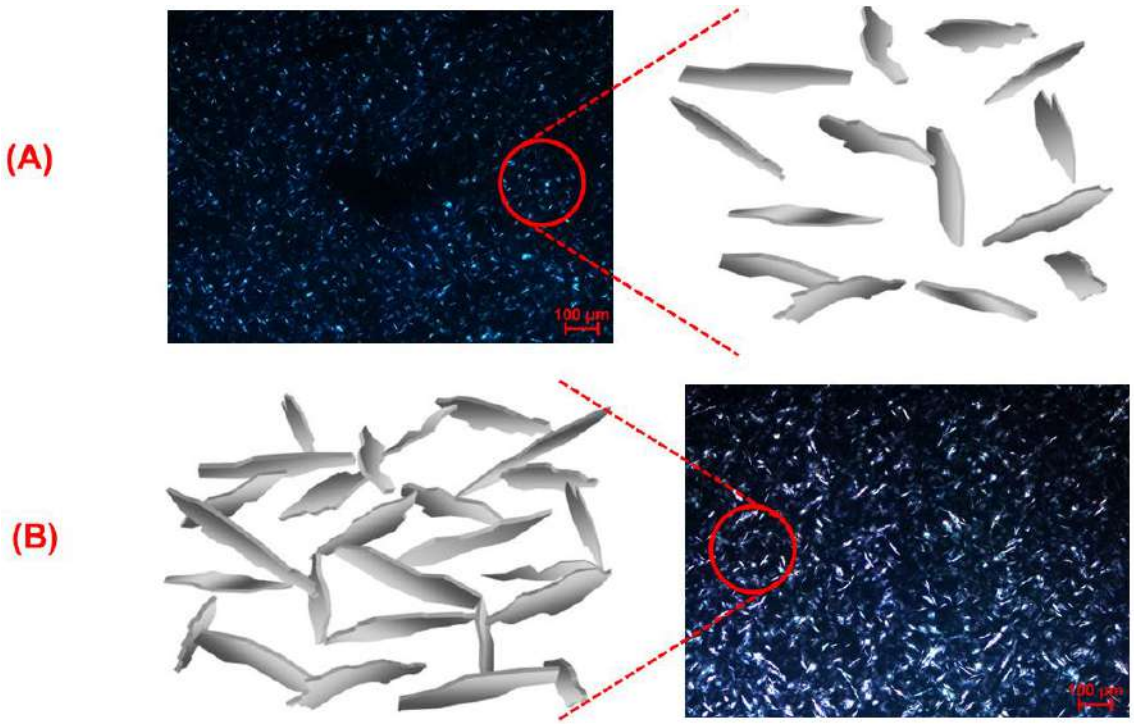


Figure 6 - An artistic concept of a loose network of waxy crystals (A) and a highly connected waxy crystal network (B) (adapted from Paso et al. [2]). The microscopic images were generated throughout this investigation.

In the literature, the term ‘gel’ is used so indiscriminately that it has become ambiguous. Hence, it is important to define and restrain the use of the term to materials which are solid or solid-like, composed of two or more components, one of which is liquid, present in substantial quantity. Furthermore, solid-like gels, as the waxy gels investigated, are rheologically characterized by a storage modulus (G’) exhibiting a pronounced plateau when sheared quite below its yield stress and by a loss modulus (G’’) considerably smaller than the storage modulus in the plateau region [68]. Roughly speaking, the storage modulus measures the elastic response and the loss modulus measures the viscous dissipation per cycle of sinusoidal deformation of a sample [69]. Figure 7 illustrates the difference between a gelled material and a viscoelastic fluid. It exhibits the storage and loss modulus resulting from an oscillatory logarithmic stress ramp performed at 25 $^{o}$C at a controlled-stress rheometer. The only difference between the two prepared samples is the wax composition: the first has 5.0 wt% macrocrystalline wax resulting in G’’ higher than G’ whereas the other has 15 wt% wax resulting in G’ higher than G’’ for the range of oscillatory stress assessed (5 to 30 Pa).

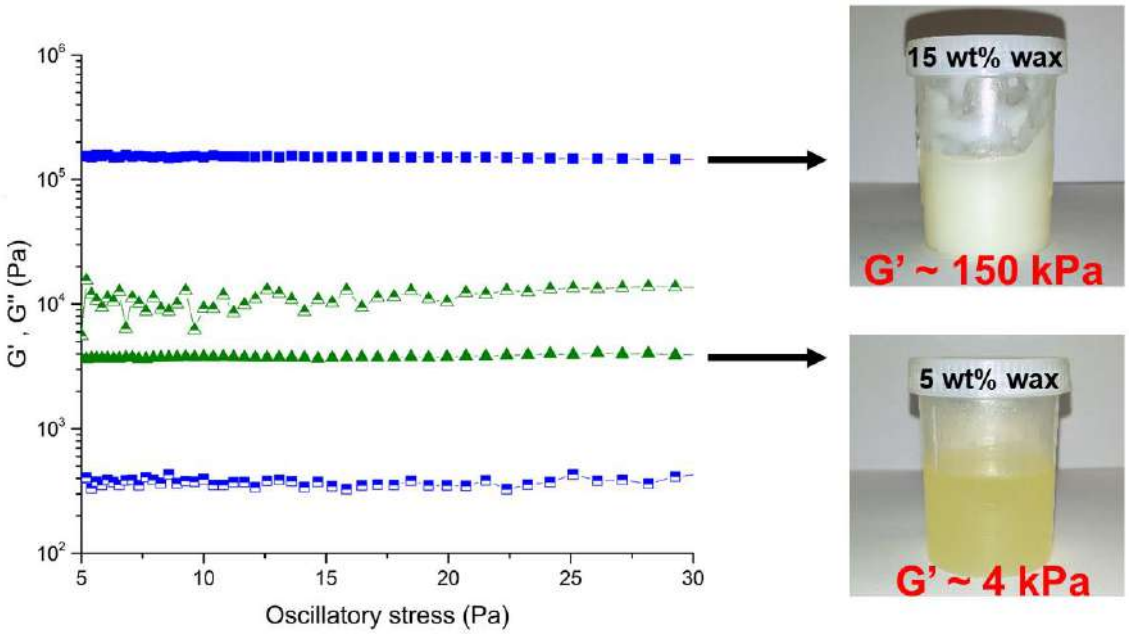


Figure 7 - Storage and loss modulus measurements for model oils containing wax at 5.0 wt% (triangles) and 15 wt% (squares) at 25 ºC. The macroscopic aspect of each sample is shown on the right.

Several mechanisms of deposit formation have been proposed, namely molecular diffusion, shear dispersion, Brownian diffusion, and gravity settling. However, the first is universally acknowledged as the dominant one, whereas the other mentioned mechanisms have been identified to have an low impact on the phenomenon [70]. The wax deposition process, driven by molecular diffusion, starts due to the precipitation of dissolved wax molecules and formation of an incipient deposit layer on the cold pipe wall surface. This process generates a radial concentration gradient of dissolved waxy components, which results in the diffusion of wax molecules from the bulk oil toward the wall. The precipitation of waxy components on the surface of the existing deposit contributes to the growth of its thickness [31]. Also, the trapped oil in the wax deposit causes counter-diffusion of dewaxed oil out of the gel deposit. The diffusion and counter-diffusion lead to the hardening of the gel and increases the size and the amount of wax in the deposit. This process is called aging, the second stage of wax deposition. Therefore, molecular diffusion is critical to the aging and hardening of wax gel deposits [71].

Due to petroleum multicomponent nature and variable composition, a key feature to be considered is the ability to assess structural and morphological properties of wax crystals [72]. In this regard, cryogenic scanning electron microscopy (Cryo-SEM) was employed

by Miyazaki and Marangoni [28] to obtain striking images of model oils of straight-chain paraffin wax-oil mixtures and polyethylene wax-oil mixtures. During the analysis, the temperature was maintained below −150°C and the oil trapped inside was removed in order to obtain a clear picture of the crystal network structure. The results are presented below. Figure 8A and Figure 8B regards a 10 wt% straight-chain paraffin and 10 wt% polyethylene wax-oil mixture, respectively. Figure 8C and Figure 8D regard a 20 wt% straight-chain paraffin before and after a uniaxial compression up to its yield stress.

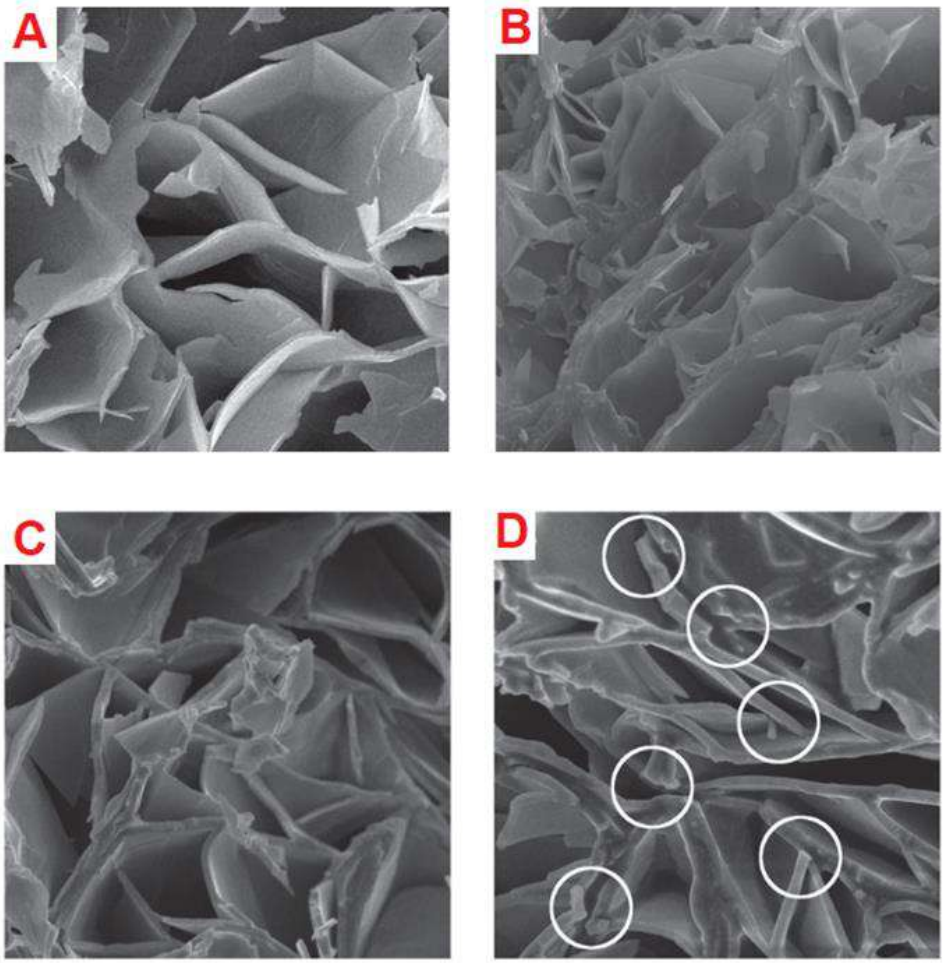


Figure 8 - Cryo-SEM technique employed to obtain images of 10 wt% of a straight-chain wax (A) and polyethylene wax (B) prepared in isotridecyl isononanoate matrix. In addition, images of a 20 wt% of a straight-chain wax before (C) and after (D) yielding (extracted from Miyazaki and Marangoni [28], with permission).

By observing Figure 8 it is clear that all gels consist of a 3D, interconnected, crystalline wax-platelet network. This closed-cell structure partially explains the high oil-trapping ability of wax crystal networks. Also, in Figure 8D it is possible to identify the rupture of the solid occurring at the edges of the cells. Thus, these wax-oil crystal networks yielded mechanically at the links between cells; the cell faces did not change after yielding,

indicating that the walls retained their integrity. The obtained results highlight the fact that wax chemical structure is one factor of absolute importance in liquid oil structuring.

Han et al. [73] investigated structural effects of precipitated wax crystals, ranging from $C_{18}$ to $C_{45}$, on the yield stress of six wax-decane gels. According to the authors, for precipitated multi $C_n$, the n-alkane polydispersity results in co-crystallization among molecules of different chain length. Therefore, not all the $C_n$ molecules show “all-linear conformation style” in wax crystal. In a molecule stacking layer, some long alkane molecules need to bend to a short-chain partner to be accommodated, resulting in the “end-gauche” defect. The crystalline lattice *c*-parameter detected by X-ray diffraction (X-RD) was employed to provide information on the conformation disorder of n-alkanes. It was found that the precipitated $C_n$ with a higher degree of polydispersity favors a more significant conformation disorder. Thus, the competing effect on yield stress was quantitatively identified between the degree of n-alkane polydispersity and the amount of precipitated $C_n$. A schematic view of the “end-gauche” defect is presented in Figure 9.

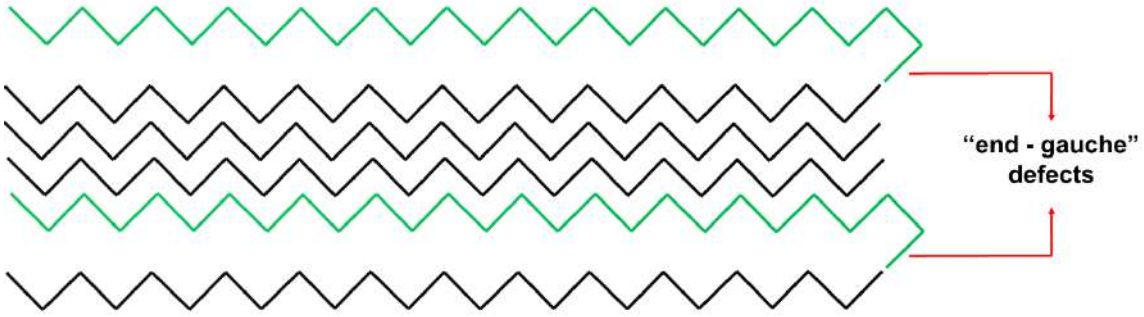


Figure 9 - The schematic of n-alkanes co-crystallization highlighting the “end-gauche” defect (adapted from Han et al. [73]).

In terms of crystal morphology, Cazaux et al. [74] employed optical microscopy and observed anisotropic particles having the shape of needles with length varying between 1 and 10 µm and diameter of the order of 2 µm for the crude oils assessed. Also, an orthorhombic crystal system with long-range order was devised by X-ray scattering results. It can be also found elsewhere that polydisperse distributions of n-paraffin components dissolved in crude oil or other organic solvents assume orthorhombic equilibrium structural phases [75], [76]. In fact, optical microscopy is a representative technique in flow assurance studies. From the cross-polarized light technique, the sample contrast comes from the rotation of polarized light through the crystalline material contained. Crystal length, aspect ratio, and fractal dimension can be obtained from microscopic images[4], [8], [74].

Létoffé et al. [79] investigated model oils and reported a typical crystal size between 1 to 3 µm. The slower the cooling rate, the longer the needles. Paso et al. [4] obtained crystal lengths in the range of 10-20 µm for model oils consisting of n-paraffin waxes dissolved in mineral oil. Srivastava et al. [80] observed the waxes crystals from crude oil with a phase contrast microscope. Their samples had a very high crystalline content, up to 96%. Two types of crystals were reported: a long rod and a thin plate type, the former corresponding to the orthorhombic lattice and the latter to a hexagonal structure. According to Singh et al [81], the network of interacting wax crystals shows complex morphology and this is due to the flocculation of orthorhombic crystallites, creating a highly porous and rigid structure full of entrapped oil. It is also reported in the literature that wax crystal size depends directly on the length of the paraffin chains [79].

Physicochemical characterizations are essential to disclose the wax chemical structures and relate them to the rheological response of gelled oils. Zaky and Mohamed [82] conducted a study on this subject. The authors extracted high melting point macro and microcrystalline waxes from crude residues of El-Ameria and Alexandria Oil Company. They were able to characterize samples through multiple techniques such as gas chromatography with flame-ionization detection (GC-FID), X-RD, differential scanning calorimetry (DSC), thermal gravimetric analysis (TGA), SEM, and $^{1}$H nuclear magnetic resonance ($^{1}$H NMR) and verified differences in their n-paraffin contents, crystallinity, thermal characteristics, degrees of branching and crystal sizes. It was found that microcrystalline wax exhibited melting point and thermal stability higher than those obtained for macrocrystalline wax due to its higher boiling point range and molecular weight. Also, macrocrystalline wax crystals appear in large and loose needle form comparing to microcrystalline wax which crystallized in needle form however as smaller crystals. The degree of crystallinity and degree of branching (expressed as $CH_3$ wt%) for the waxes assessed were respectively 63% and 4.96% (macro) and 83% and 14.7% (microcrystalline).

Doan et al. [83] described the major chemical components of seven natural waxes by high-performance liquid chromatography used in conjunction with evaporative light scattering detector (HPLC-ELSD) and gas chromatography-mass spectrometry (GC-MS) followed by evaluation of their oil structuring properties through oscillatory rheology. Model oils were prepared ranging from 1.0 to 5.0 wt% wax. The gel strength was evaluated in terms of average storage modulus at the linear viscoelastic region and yield stress. Not surprisingly, it was found that the main component dictating the gel strength are hydrocarbons, i.e., waxes. Free fatty alcohols and wax esters also had a positive

correlation with rheological properties, however, less pronounced.

Differential scanning calorimetry (DSC) is another major technique applied to the studies of wax precipitation in the flow assurance context. This technique measures the heat flow from or to the sample when the sample is heated or cooled. Since crystallization will give out heat, it will show up in the DSC curve as an exothermic peak during cooling [84]. Thus, it is possible to quantify the thermal effects and to measure thermodynamic data for waxes. DSC is traditionally utilized to evaluate wax inhibition by heat flow [85], [86], WPT measurement [86], [87] or to determine the mass fraction of crystals formed during cooling under quiescent conditions as a function of temperature [88].

Claudy et al. [89] employed DSC to obtain the crystallization temperature of diesel fuels, which occurred in the temperature range of 30°C to - 20°C. They compared the results with ASTM and standard European tests and reproducibility were always better with DSC. The thermal characterization of 17 North Sea crude oils has been carried out by Hansen et al. [1]. The authors considered a broad range of temperatures (+70 to -140 °C) and find out that the glass transition is correlated with the concentration of the light components in each particular oil matrix. On the other hand, wax precipitation, and wax dissolution temperatures were much more closely correlated with the wax content and with the dissolution temperatures on the average being 13°C. From DSC results Létoffé et al. [90] estimated that only about 2 wt% of wax is responsible for oil gelation for the 14 different crude oils analyzed. A value of 200 J/kg for the enthalpy of precipitation was also obtained. Cheng et al. [91] developed a method based on empirical relations to improve the accuracy in determining the amount of precipitated wax in a waxy crude oil at different temperatures. Fourteen crude oils used in this work cover a large range of fluid compositions and properties. Zaho et al. [86] used DSC to investigate the effect of cooling rate, wax content, asphaltene, and chemical additive on the wax precipitation temperature of model waxy oils and crude oils. The results indicated that WPT increases with increasing the wax content. This confirms bigger precipitation in samples with higher wax content during the gelation process. Although, the effect of pour point depressants on WPT was greater than the other factors investigated.

Waxy gels have a flow behavior completely different from their predecessors. From a rheological standpoint, during the gelation process, the storage modulus increases as a result of the increasing junction zones density between wax crystals. After the rapid increase in elasticity within the gel, G’ keeps increasing slightly and continuously as a result of the reinforcement of the network by slower formation and rearrangement of elastic active bonds/junction zones, reaching a pseudo plateau region, meaning a

continuous reorganization of the particulate network [92]. This process is depicted in Figure 10, which exhibits the storage modulus evolution during a cooling process followed by a time sweep step of a model oil 3.0 wt% composed by macrocrystalline wax and spindle oil. It is possible to observe the buildup of the waxy network structure mostly concentrated between 23°C and 10°C.

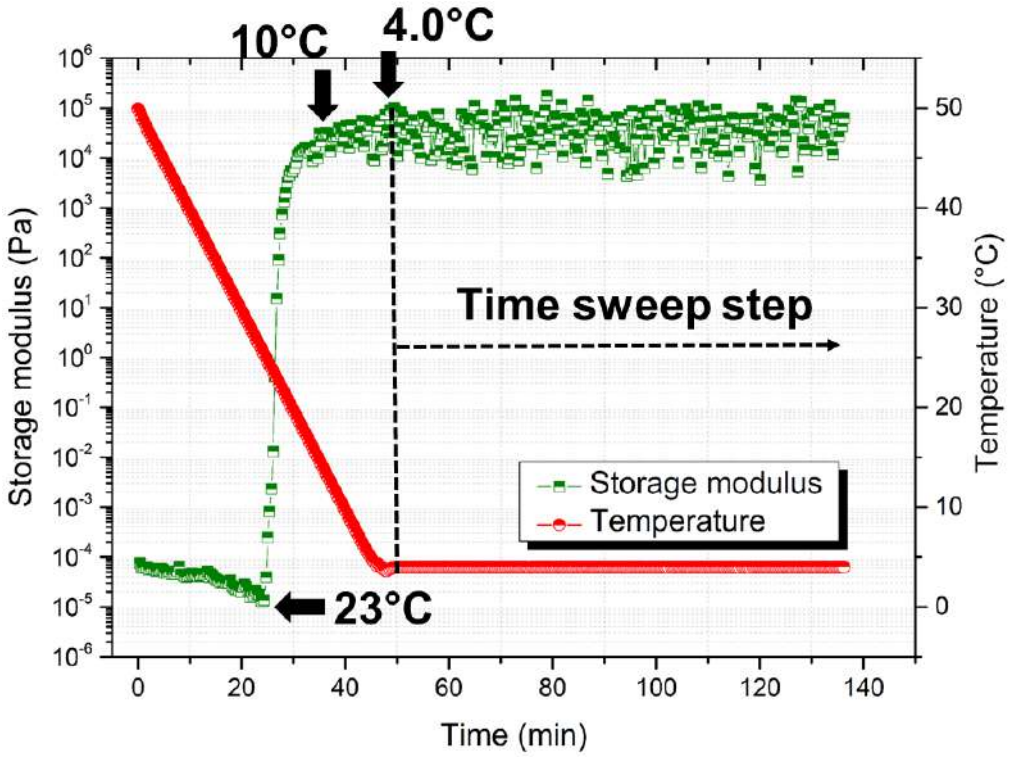


Figure 10 - Storage modulus for model oil 3.0 wt% measured at two subsequent steps: oscillatory cooling from 50°C to 4°C (cooling rate of 1.0°C/min) followed by a time sweep (stress 0.1 Pa and frequency 0.2 Hz) of 100 minutes at 4°C.

The aging effect also plays a role in the waxy gels features, which become harder, richer in heavier waxes and with lower amounts of entrapped oil. As they age, growing wax crystals will further enmesh with quiescent duration, becoming harder and more stable. This greatly affects the rheology of a gelled oil [54]. Therefore, a long-term shutdown of a production line containing waxy crude oil may represent a high loss of revenue and also an increased risk for the restart pumping operations. According to Paso et al. [2], this aging process involves the molecular diffusion of wax molecules from the bulk fluid into the occluded liquid within the deposit, where the components subsequently precipitate, causing an increase in the solid fraction of the deposit with time, consequently increasing its hardness. Accordingly, the reinforcement of the network by aging is explained by the formation of stacks of crystalline lamellar structures. However, there is evidence for another aging mechanism involved in the process. Coutinho et al. [84] used

polarized light microscopy combined with DSC and X-ray diffraction to show that the aging of the wax deposits takes place even for samples kept under isothermal conditions, indicating Ostwald Ripening (a mechanism by which the large crystals grow at the expenses of the melting of smaller crystals of higher energy) as another aging mechanism of wax deposits.

The waxy gel formation has also an impact on emulsion stabilization. Emulsions can be defined as dispersions of two immiscible liquids, generally oil and water. Additionally, a third component is needed, the emulsifier, which acts decreasing the interfacial tension between oil and water and stabilizing the droplet against coalescence, once it is formed [41]. Coalescence requires four steps: flocculation, thin film drainage, film rupture and merging of droplets. In a water-in-waxy-crude-oil emulsion, the number, shape, and size of the crystals located at the interface will dictate differences in film drainage and rupture [93]. According to Hodge and Rousseau [55], the degree of droplet coalescence could be markedly reduced by the presence of waxy crystal at water-in-oil (W/O) interface. It is most likely that the emulsion stabilization against coalescence is a function of the crystal structure of the wax as influenced by this change in crystallization conditions. The authors also concluded that rapid crystallization of wax in the continuous phase of a water-in-oil emulsion following emulsification proved to be an effective means of enhancing long-term system stability.

Haj-Shafiei et al. [54] demonstrated the effect of the solid wax content, SWC, precipitated from water-in-oil model emulsions. For systems with initially low SWC (2.9 wt%), the amount of wax was insufficient to fully stabilize the aqueous phase present. Had the emulsions been stored for 28 days, it is likely that there would have been continued crystal growth as a result of Ostwald ripening, which led to fewer, larger crystals. Systems prepared with initial SWC at 4.2 wt% did not exhibit signals of phase separation which suggests that the amount of wax was sufficient to fully stabilize the aqueous phase.

## 2.3 Yield Stress

Fluid materials, by definition, are systems which flow when subjected to any stress. In general, systems with a uniform phase, such as a solution or a pure substance, are referred to as simple fluids. Differently, materials which contain more than one phase, such as solid particles dispersed in a liquid, are considered structured fluids since their rheological behavior is essentially dominated by different interactions between the constituents [94]. According to Barnes [14], structured material can exhibit the transition

from very high viscosity, greater than $10^6$ Pa.s, to mobile liquid (~ 0.1 Pa.s or less) over a single order of magnitude of stress.

In the flow assurance context, in case of unscheduled production shutdowns, the quiescent cooling of waxy oils can lead to the formation of a two-phase wax-oil gel with a strong waxy crystal interlocking network, which is accompanied by a drastic change in rheological properties, such as yield stress appearance. This causes pipeline clogging, irreparable damage to equipment and hampering to the restart pumping process [15], [31]. Therefore, in case of a pipe filled with gelled material, engineers are most interested in the stress value when the fracture occurs, because it effectively determines the pump capacity required to initiate flow and ensure pipeline restart. This fact highlights the yield stress extreme importance to flow assurance. In practical terms, the pumping of a waxy gelled material is connected to the yield stress as in Equation 1 [17].

In rheological measurements, the stress is proportional to the force applied to the test material, the strain is proportional to the relative displacement of the bounding surfaces, whereas the shear rate is proportional to the relative velocity [94]. At stress levels below the yield stress the viscoelasticity of the network gelled structure can be evaluated using oscillatory rheology by applying sinusoidal stress [34] as in Equation 2:

$$\tau = \tau_0 \sin(\omega t) \qquad \text{Eq. (2)}$$

Where $\tau_0$ represents the maximum applied stress amplitude, $\omega$ is the angular velocity, and $t$ is time. In case of sample within the linear viscoelastic region the measured strain is a sinusoidal function taking the form of Equation 3:

$$\gamma = \gamma_0 \sin[(\omega t + \delta)] \qquad \text{Eq. (3)}$$

where $\gamma_0$ represents the maximum strain amplitude and $\delta$ is the phase shift or, in other words, the degree of which the strain is out of phase with the applied stress. The ratio of the maximum applied stress to the maximum strain is called the complex modulus, $G^*$ (Equation 4):

$$G^* = \frac{\tau_0}{\gamma_0} \qquad \text{Eq. (4)}$$

It turns out that $G^*$ can be divided into an elastic and viscous portion, representing the magnitude of the strain in-phase and out-of-phase with the applied stress, as in Equation 5:

$$G^* = G' + iG'' \quad \text{Eq. (5)}$$

where $i$ represents the imaginary unit. The elastic component is the so-called the storage modulus, G' (Equation 6), and the viscous component is called the loss modulus, G'' (Equation 7). The phase shift is expressed as the ratio of the two moduli as in Equation 8.

$$G' = G^*\cos(\delta) \quad \text{Eq. (6)}$$

$$G'' = G^*\sin(\delta) \quad \text{Eq. (7)}$$

$$\tan(\delta) = G'/G'' \quad \text{Eq. (8)}$$

A material perfectly elastic exhibits no phase shift between the applied stress and resultant strain, that is $\delta$ = 0. Conversely, a perfectly viscous material is 90° out-of-phase with the applied stress and $G^*$ = G'' [95].

Materials such as gelled waxy oils that do not flow until the applied stress exceeds a certain critical value are said to be exhibiting yield flow behavior. According to Wardhaugh and Boger [35], the yield stress can be determined at oscillatory tests in rheometers by steadily increasing the amplitude of oscillation and noting the applied stress at which the response ceased to be elastic. The application of constant stress to a sample of gelled waxy crude provides an experimental condition similar to the pipeline itself. This occurs because most flowlines operate using centrifugal pumps, which apply a controlled pressure drop, rather than a fixed rate of flow [96].

Chang et al. [18], following the previous work by Wardhaugh and Boger [35] defined three different yield stresses to characterize the yielding of a waxy crude oils: the elastic-limit yield stress, below which the material exhibits a linear elastic response (i.e., ceased the stress the sample is able to recover its original shape), the static yield stress, defined as the stress at the starting point of immediate fracture or flow, and the dynamic yield stress, an extrapolated shear stress obtained from the flow curve after the structure of the sample is ultimately broken through sustained shear. It is important to note that the definition of yield stress adopted in this investigation is consistent with the static yield stress defined by Wardhaugh and Boger [35] and Chang et al. [18] (further information in section 2.6).

The elastic limit and static yield stress can be obtained from a logarithmic stress ramp at oscillatory tests. According to Chang et al. [18], for small stress, the storage modulus of

a waxy gel sample is virtually independent of the stress. When the loaded stress increased above a certain value, G′ decreases noticeably. However, the strain exhibits a non-linear increase, meaning that the gelled structure is partly destroyed by the loaded stress. This fact marks the departure from the linear viscoelastic region. A further increase in stress leads to an abrupt decrease in storage modulus. Also, a striking increase in the percentage strain is registered, representing the material fracture.

Whenever oscillatory rheological experiments are employed to determine yield stress, it is important to note that test frequency can influence the measurement, depending on the relaxation behavior of the material under test. Because the storage modulus generally decreases with decreasing frequency for complex fluids, then yield stress tends to follow a similar trend. While lower frequencies will give a better indication for properties at rest, performing an amplitude sweep at such low frequencies can greatly increase the time of the test. Consequently, values between 0.1 to 10 Hz are commonly employed [97].

In waxy gels, yielding is a complex process which is ultimately determined by the strength of the attractive interactions and the micromechanical rearrangements allowed by the network [14]. Figure 11 exhibits a representative yielding behavior captured by the oscillatory rheological test. The gel was prepared using spindle oil and macrocrystalline wax 7.5 wt% during a specific cooling protocol and submitted to logarithmic stress ramp at the temperature of 4 °C. It can be observed that the fracture of the material occurred after a sharp increase in the percentage strain in a very small range of oscillatory stress.

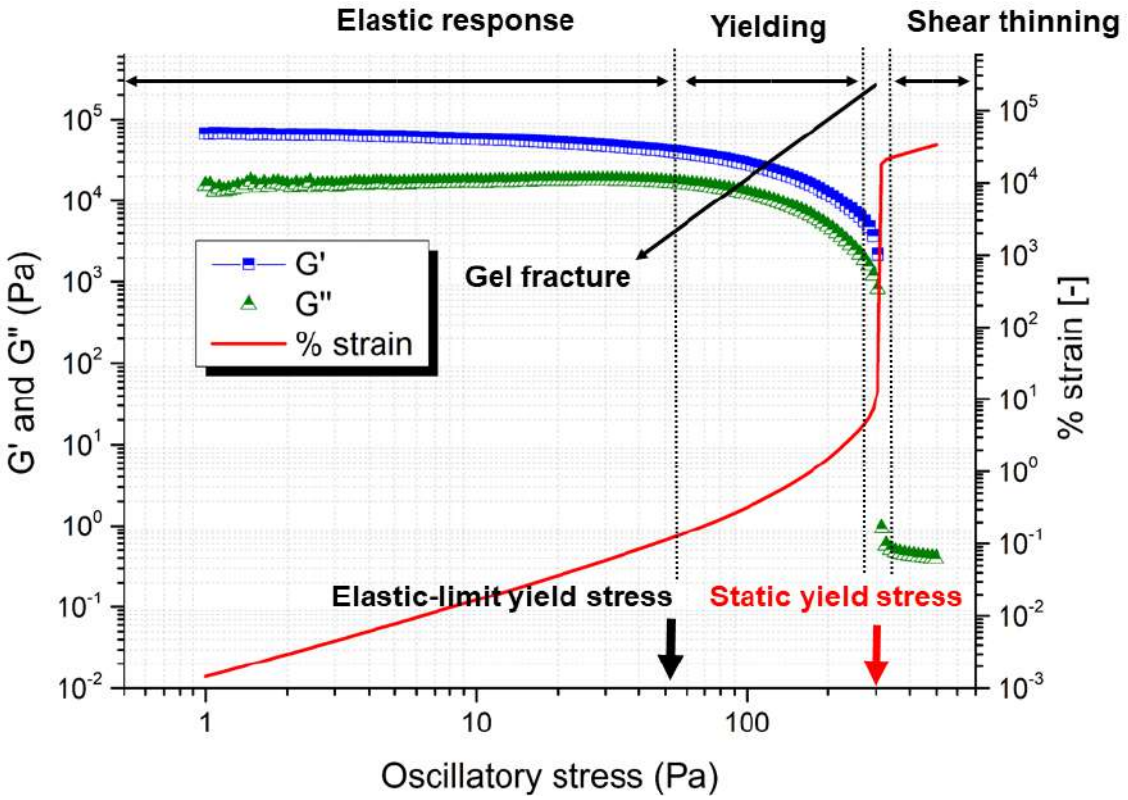


Figure 11 - Typical yielding behavior for waxy gel sample analyzed in this investigation when submitted to logarithmic stress ramp with frequency 0.1 Hz and temperature 4°C.

A number of testing techniques are available for measuring and analyzing the yield stress using a rheometer. According to Walls et al. [98], the best way to do it is to directly measure the stress required to initiate measurable flow by using oscillatory experiments. The authors list some advantages:

1. oscillatory rheology experiments can provide, simultaneously, information about a sample's viscoelastic properties and/or microstructure, and the yield stress;
2. a priori estimation of a material's yield stress is not required;
3. reliable data are obtained both above and below the yield stress, as opposed to the large uncertainties obtained at low shear rates for the steady shear flow experiments;

Another approach is to use steady stress measurements to determine the yield stress of structured material. In a viscosity plot, this property remains constant for small stress values and is generally referred to as the "zero shear viscosity". At some stress level, the material starts to flow, as the viscosity decreases many orders of magnitude over a narrow range of shear stress. The yield stress, then, is estimated as the stress at which viscosity just starts to exhibit a rapid drop in value [99], as can be seen in Figure 12(A). For plots of shear stress versus shear rate, two approaches to data analysis are considered. The first is to use a linear plot and fit the data to one of several models that

contain a yield stress parameter, such as the classic Bingham (Figure 12B) or Herschel-Bulkley (Figure 12C) models. However, fitting the data to a yield stress model can lead to overestimation and not all materials comply with common yield stress models [14], [100], especially waxy gels. The second approach is to use a log-plot which typically shows Newtonian behavior at very high shear rates and stress plateaus at low stresses. These plateaus are then taken as the yield stress (Figure 12D). In all previous cases, it is a challenge to find the point of largest applied shear stress before material flow occurs. One confounding problem is the very large uncertainties that are observed at shear stresses and shear rates below the yield stress [98].

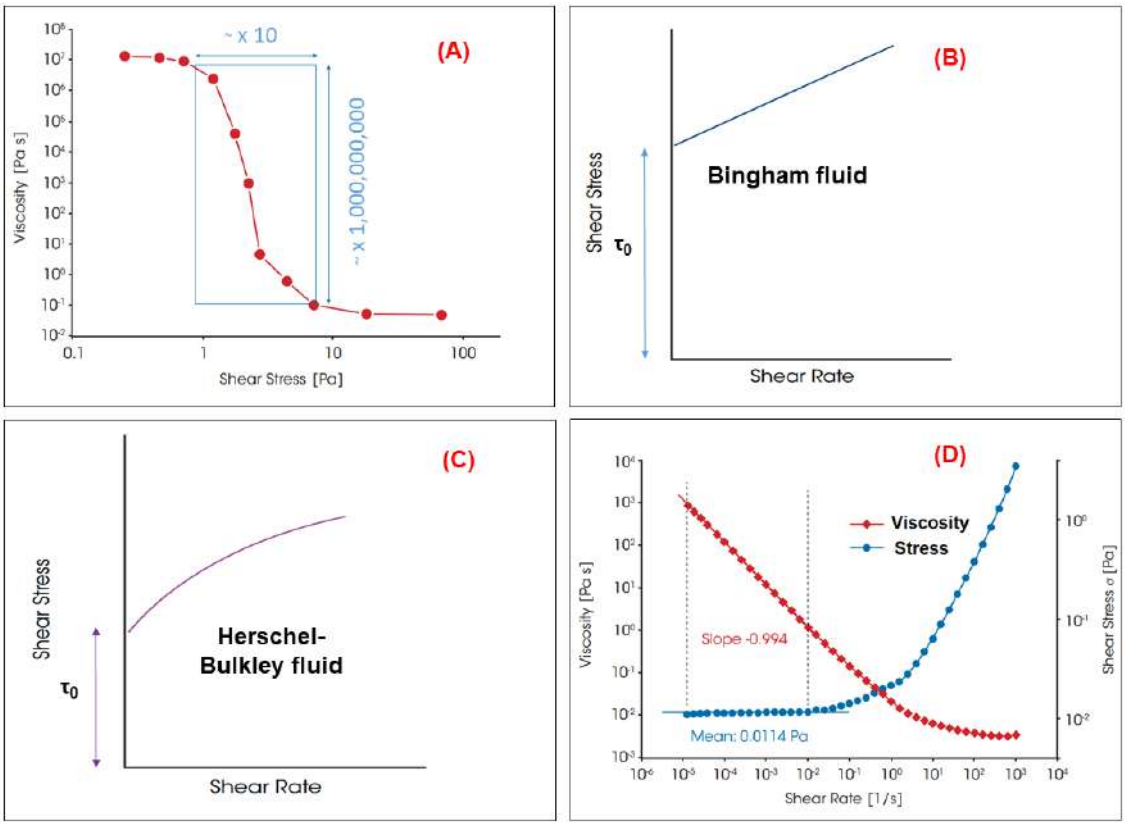


Figure 12 - Different yield stress determination method: (A) viscosity plot of 10 wt% bentonite suspension, shear stress-shear rate behavior of (B) Bingham fluid (C) Herschel-Bulkley fluid and (D) a blue ink sample (adapted from Barnes [101]).

Apart from oscillatory and steady-state rheological tests, an alternative to measuring yield stress is called creep test, in which constant stress is first applied to the system and the strain (the relative deformation) is recorded as a function of time. Below the yield stress, the sample responds to the applied stress by approaching a constant strain value. Above the yield stress, the strain increases rapidly and achieves a constant slope in a plot of strain versus time [102]. Generally, a time ranging from two to ten minutes is

usually sufficient for such test, but longer times can be required if the material relaxes over a longer period [95]. In principle, creep tests would produce more reliable measurements of yield stress in the flow assurance context: supposing a pipeline blocked by waxy gel when the pump is turned on there is a sudden increase in the stress which is transmitted to the entire line. Therefore, the loading stress rate in a real situation of flow restart is better represented by a creep test [14]. Nonetheless, this procedure is very time consuming since it is necessary several experiments to obtain one single curve. Thus, it is helpful to have an estimate of the yield stress before beginning the tests [94].

Figure 13 exhibits a yield stress measurement of a waxy gelled oil based on a creep test performed at a temperature of 4°C. The sample is composed of spindle oil and macrocrystalline wax 3.0 wt%. For stresses up to 190 Pa, the gelled structure is maintained along the experimental time, which is translated in negligible angular velocity. As the experiment is repeated, each time with a new sample, however increasing the stress to 195 Pa, an acute angular response is captured at 11 seconds. Increasing the stress to 200 Pa the time response is shortened to ~ 5 seconds. Thus, the yield stress is considered to be within the range of 190 to 195 Pa.

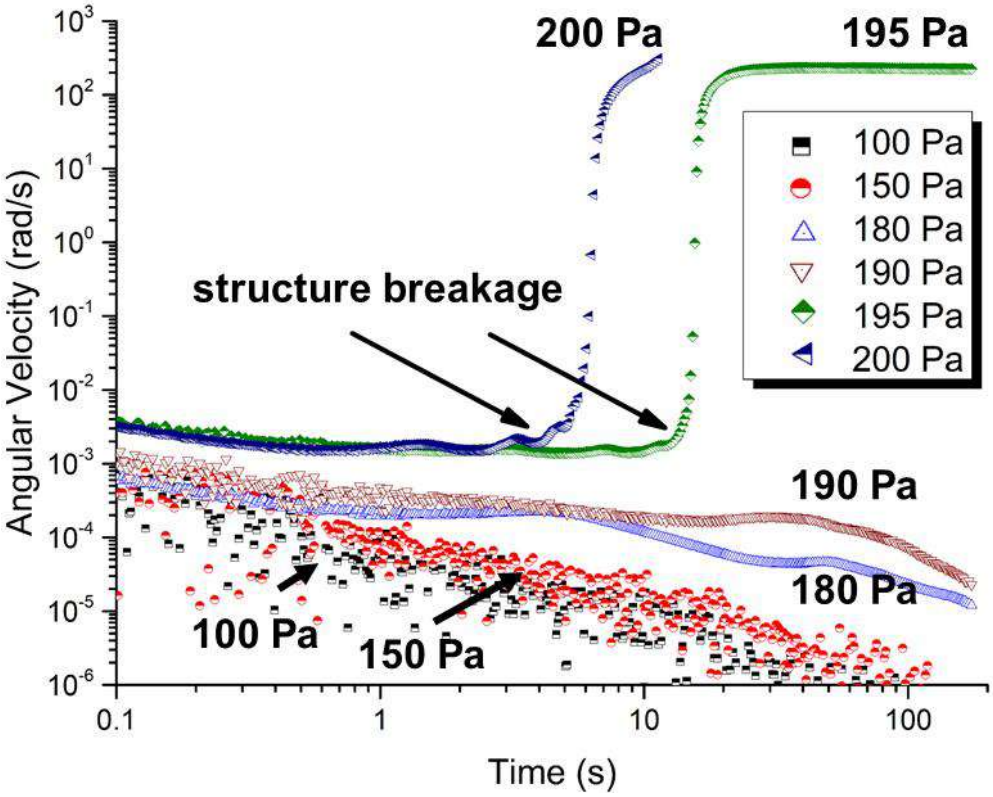


Figure 13 - Creep experiment for yield stress determination of a waxy gelled oil. The test temperature was 4°C with 2 minutes duration and repeated with new samples for increasing stress values. The structure breakage occurs at levels of 190 to 195 Pa.

Despite the number of techniques available, there is no standard test for defining the yielding quantity of waxy crude oils in the petroleum industry [103]. In fact, conflicting results of yield stress are not uncommon, depending on the technique employed, the criterion on which it is based, and often the patience of the investigator as well [37]. Canet et al. [104], for instance, compared different methods for measuring the yield stress of concentrated suspensions of potato purée with the different preparation process. The authors calculated the yield stress from flow curve data through Herschel-Bulkley, Casson, and Bingham models and compared to the data generated from oscillatory measurements. They noted large differences, though trends were fairly correlated. Haj- Shafiei et al. [54], working with W/O model emulsions with different wax content, also observed differences in yield stress for steady and oscillatory rheological measurements. Calculated from the Herschel-Bulkley model, the samples yield stress ranged from 5.0 to 40 Pa whereas in the oscillation study it ranged from 0.1 to 8.0 Pa. However, once more, both methods presented similar patterns for all employed samples.

In case of waxy oils, one possible reason for conflicting yield stress values is that the sample strongly depends not only on what the sample is going through but also on what the sample had gone through, such as thermal and shear history. According to Yi and Zhang [105], thermal histories have a pronounced effect on the rheological behavior of waxy crudes. Thus, prior to any rheological characterization, the authors removed thermal and shear histories by heating the specimens to 80°C and holding at this temperature for two hours. Next, the specimens were kept at room temperature to cool statically for at least 48 hours before being used in rheological experiments. Marchesini et al. [5] also demonstrated the importance of devising an experimental protocol to ensure well-defined thermal and shear histories of waxy crude samples. The authors followed a three-step procedure: the first consists of heating the crude oil at 50 °C for three hours in an open bottle, then raising the temperature to 60 °C and continue heating for another one hour. In this step the light ends of crude oil evaporate, thus ensuring a stable composition during testing. The second step is an isothermal holding time, performed to dissolve all wax crystals in the oil and the third is the cooling process, to which each sample should be submitted immediately before the beginning of any rheological test. Thus, in order to avoid a biased response, the same shear and thermal history must be adopted for all samples prior to the tests [35]. This recommendation was followed for all rheological tests in this investigation.

Despite the possibility of obtaining yield stress from rheometer measurements, it cannot be directly applied to pipeline design because this property also depends on the stress loading rate applied [18]. Therefore, different loading rates can be an important factor

and a source of misleading comparisons among different techniques employed to obtain yield stress. Also, the shear rate range employed is an element to be considered. In this regard, a simple example is given by Tadros [95] who reported the yield stress of a latex suspension using Bingham model extrapolation. When the shear rate was increased from 20 $s^{-1}$ to 160 $s^{-1}$ the obtained yield stress was 9.5 Pa. In contrast, when the flow curve was obtained in the range of 1.0 $s^{-1}$ to 6.0 $s^{-1}$, the yield stress was 5.0 Pa.

As an exception, Pal [41] related a good agreement at yield stress measurements of high internal phase O/W emulsions (i.e., emulsion for which the volume fraction of the dispersed phase exceeds the maximum packing volume). When such highly concentrated emulsions are subjected to small shear deformation, they exhibit a strong elastic response and yield stress. The author conducted three different types of rheological tests, namely: steady shear, oscillatory shear, and creep experiments. The yield stress obtained for the same emulsion showed good agreement for different techniques, increasing exponentially with the increase in the dispersed-phase concentration. However, this unusual result may reflect the fact that a substantial amount of papers has been published on the rheology of dilute and moderately concentrated emulsions whilst little attention has been given to high internal phase systems.

Another aspect that can potentially lead to inaccurate results in rheological measurements is the sample loading, especially at parallel and cone and plate geometries. To illustrate this fact, the effect of sample underfill on parallel-plate and cone-plate geometries were examined by Hellström et al. [106]. The authors demonstrated that even small changes in the sample radius can cause significant errors in the apparent viscosity (up to 7%). Sample underfill can be caused by the incomplete filling of a sample or loss of fluid during a test by, for example, evaporation. In the latter case, a solvent trap can be used to mitigate this effect. Figure 14 exhibits images of mineral oil loading in three distinct situations: correct loading, overfilled and underfilled sample. The use of a solvent trap is also shown.


Figure 14 - Three different situations of sample loading of using a parallel plate geometry 40 mm. A schematic representation of solvent trap, used to mitigate solvent evaporation, is also shown.

The correct geometry choice must also be considered to obtain high-quality rheological data. The cone and plate geometry, for example, are a suitable option for several samples. However, the presence of precipitated wax crystals may introduce measurement errors because characteristic dimensions of the crystals are generally of the same order of magnitude of the geometry gaps, especially in the vicinity of the cone tip [5]. This drawback may also occur with other structured fluids than gelled oil. Some food materials, for instance, have particles with characteristic dimensions in the order of magnitude of the gap available for flow in the conventional rheometers. Placing a sample of such fluid in these geometries may result in the partial destruction of the internal structure. In other situations, phase separation of the basic constituents of the fluid to characterize occurs while the measurement is in progress [107]

Parallel plate geometry is an option with adjustable gap size. Barbato et al. [53] conducted an extensive investigation in order to improve reproducibility in the procedure to determine the yield stress of W/O emulsions of waxy oils. The authors came up with the conclusion that the geometry of cross-hatched parallel plates is the most suitable for the yield stress measurements. Although, this geometry is not suitable for very low viscous samples. Thus, depending on the sample nature and initial test conditions, e.g. high temperature, this geometry is unfeasible for sample loading. In this case, concentric cylinders geometry is indicated due to its enhanced superficial area [101].

## 2.4 Apparent Wall Slip

As mentioned in the previous section, conflicting results of yield stress measurements are not uncommon in the rheology of complex fluids. Among the possible sources of poor repeatability, it can be included the so-called apparent wall slip [108]. On one hand, this

phenomenon is a fundamental component of the way that yield stress fluids respond to mechanical deformation [109]. It is desirable in many natural and industrial processes, as the ability of some materials to slip onto smooth surfaces allows them to move readily and efficiently. From food digestion [110] to fresh concrete pumping over a long distance [111], the transport is facilitated by the slippage. On the other hand, apparent wall slip is clearly an obstacle to access bulk rheological properties by experimental activity since it systematically underestimates the value of rheological measurements [112].

Apparent wall slip emerges in a context of different flow heterogeneities that yield stress materials might exhibit [109]. Figure 15 presents schematics of velocity profiles in simple shear for homogeneous flow, shear-banded flow, (true) slip flow, and apparent slip flow. In the first case, the velocity profile varies linearly between the shearing surfaces and the resulting local shear rates are equal to the macroscopic shear rates (Figure 15A). Shear banding denotes a broad class of phenomena of different origins (e.g. material instabilities), which are associated with the spatial localization of the strain or shear rate into one or several layers of finite thickness (Figure 15B) [113]. Slip, by it turns, represents an extreme realization of strain localization, where most of the deformation occurs near the confining walls whereas the material bulk behaves more or less like a rigid body with negligible deformation. It is important to distinguish the true slip phenomenon, where the slip layer has a molecular dimension (Figure 15C), from apparent wall slip, where the local velocity varies over a finite, albeit small, mesoscopic distance (Figure 15D) [114]. True slip is relevant for polymers melts or solutions whereas slip of high solid dispersions is generally classified as apparent slip [14].

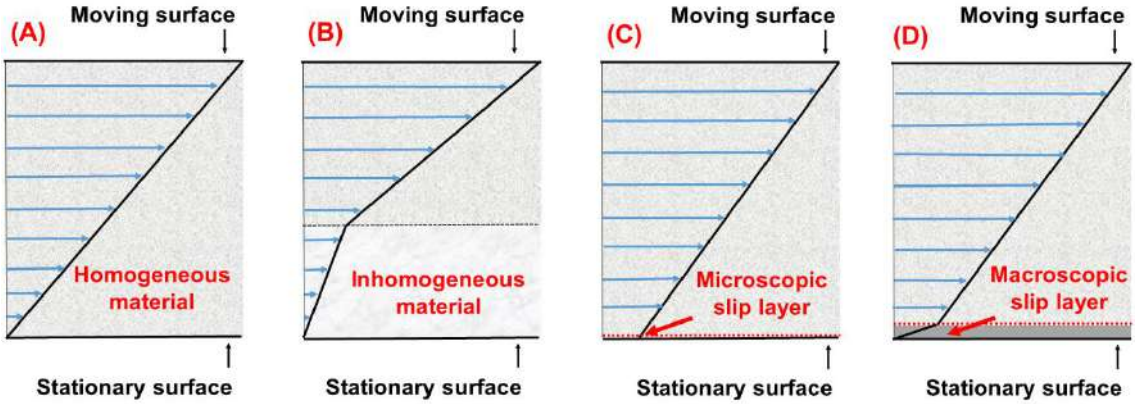


Figure 15 - The velocity profile for yield stress materials: (A) non-slip conditions, (B) shear banding phenomenon (material inhomogeneity is one possible cause), (C) true slip, and (D) apparent wall slip (adapted from Cloitre and Bonnecaze [109]).

The question of the physical nature of apparent wall slip remains somewhat open, and

the answer might depend on the material type. In case of colloidal systems such as waxy gels, apparent wall slip is likely to be caused by the development of a solvent-rich layer at the sample-wall interface, also termed as the “depleted layer” [34], [112], [115]. The general belief is that this layer develops due to the displacement of particles away from the walls with the particles either not interacting with the wall or interacting weakly [114]. The resulting lubricating effect makes the flow easier and not representative of the bulk material, and a discontinuous system is expected where the sample composition near the wall is different than the bulk composition. In extreme cases, the particle-lean fluid near the wall flows, while the bulk material does not deform at all. When stresses smaller than the yield stress are applied, since we do not expect any bulk flow, only viscoelastic effects or apparent wall slip can induce motion [98], [109].

Regarding the depleted layer, Zhang et al. [116] investigated the slippage of various systems (emulsions, bentonite suspensions, Carbopol gels, etc…) and concluded that its thickness varies in a narrow range (35 ± 15 nm) at these systems. The authors also proposed a method to evaluate the variation of slip velocity as a function of the shear stress and found that it essentially follows a straight line of slope ~ 1, suggesting a Newtonian behavior of the slip layer.

According to Barnes [115], slippage is the result of static and dynamic effects. The former arises from the physical depletion of suspended particles away from the area next to the walls. This depletion is assumed to be the result of both particle-packing characteristics and the disruption of Brownian motion near the solid boundaries. Other effects, e.g. electrostatic and steric effects, can also arise between the walls and the particles due to a variety of physical and chemical forces acting. On the other hand, the dynamic effects are due to hydrodynamic forces moving particles away from the walls when torque is applied. As the torque is increased, a shear force gradient develops, contributing to the slip phenomenon.

Lee et al. [117] investigated the waxy gels breaking mechanism at various temperatures and cooling rates using a laboratory-scale pipeline system and a controlled stress rheometer. The authors’ results indicated two distinct mechanisms: cohesive and adhesive failure. The former may result from the breakdown of the gel structure itself whereas the later may occur because of the breakage at the sample-wall interface. It suggests that when modeling the restart of a pipeline, the nature of the gel-wall interactions must be considered in detail since for cohesive failure occurs, it is reasonable to suppose that slippage effects are absent.

The conditions that favor the apparent wall slip are encountered when low shear rates,

large components in the disperse phase, smooth walls, and small dimensions are present [115]. Waxy gels, as belonging to this class of materials, have a complicated transition from the slippage regime to the homogeneous bulk flow regime; beyond the yield stress, apparent wall slip effects and localized shear flow may coexist within the material. Although, for greater applied stress the slippage effects become negligible as compared to bulk flow [118]. Below the yield stress, several other features have been observed with these materials: false Newtonian plateau or decreasing flow curve, hysteresis in increasing–decreasing stress ramps, shear banding in cone-plate geometry and kinks in the flow curves [115], [118].

Figure 16 exhibits schematic representations of apparent wall slip in a rheological test for the parallel plate and Couette flow. A solvent-rich layer presenting low viscosity and small thickness, identified as the “depleted layer”, causes the shear rate experienced by the bulk fluid to differ from the shear near the walls. In fact, for similar stress, the shear rate in the depleted layer is greater than that slightly farther from the wall, in the homogeneous region, therefore most of the deformation occurs near the solid boundaries.

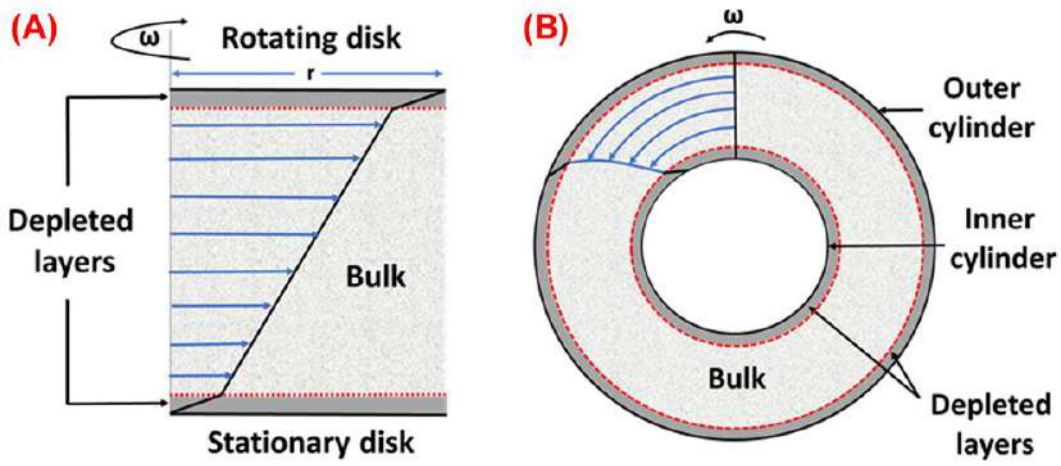


Figure 16 - Schematic representation of apparent wall slip phenomenon in (A) parallel plates (adapted from Russel and Grant [119]) and (B) Couette flow, where the outer cylinder is rotated at angular velocity ω relative to the bob (adapted from Yoshimura et al., [120]).

The detection of apparent wall slip in suspensions and colloidal gels, including its physical description and correction methods, has already been subjecting of study for several researchers. A common technique to prevent or, at least, to mitigate the phenomenon is to roughen the surface of the wall to disrupt the “depleted layer”. It is generally assumed that apparent wall slip is negligible when the roughness of the wall becomes much greater than the typical element size [118]. Another alternative is the use of a vane geometry, as

the blades are designed to shear the material bulk, and hence no depleted layer is expected to form [115]. Thus, the suitable geometry choice is a fundamental part of the rheological analysis of systems prone to slip.

Walls et al. [98] performed a series of yield stress measurements with colloidal gels. Several different test geometries were used, comprising two groups: smooth surfaces (cone and plate geometries) and grooved surfaces (parallel plates with ridged surfaces). Results for the same sample composition measured with serrated plates show excellent agreement at both dynamic and steady rheology experiments. Yet, in the presence of cone and plate geometries, the silica gels show evidence of apparent wall slip. A decrease in yield stress of approximately 60% was observed when compared to serrated plates geometry. Neither increasing the fumed silica content nor adding salt affects this slip behavior.

Saak et al. [34] investigated the influence of apparent wall slip on the yield stress of cement paste using a rotational rheometer with smooth-walled concentric cylinders and a vane geometry. The results showed that the concentric cylinders suffer from a slip during yield stress measurements due to the formation of a water-rich layer at the walls of the cylinders. According to the authors, the use of a vane eliminates slip since shearing occurs within the material.

Marchesini et al. [121] performed an experimental investigation of different rheometric flows of water-based Carbopol dispersions. The smooth Couette, the vane-in-cup and all-grooved Couette (a bob-in-cup with vertical grooves both on the inner and on the outer cylinder) geometries were employed. The detailed flow curves analysis of a Carbopol dispersion 0.17 % indicated the presence of apparent slip below a threshold stress value of ~ 150 Pa. Also, it was observed that the phenomenon occurred only at the outer wall, which is smooth for both the vane-in-cup and the smooth Couette geometries. Therefore, for the range of concentrations investigated by the authors, it was concluded that the all-grooved geometry was successful in suppressing apparent wall slip.

Barbato et al. [53] investigated the influence of several experimental variables in the yield stress of water-in-oil emulsions (50% v/v) prepared with crude oils, including the measurement geometry. The authors observed a significant dependence upon the measuring geometry used (from 100 to 500 Pa). The geometries grooved parallel plate (D = 60 mm) and grooved cylinder measured the highest yield stress. The phenomenon of apparent wall slippage was detected in rheological tests performed with smooth

cylinder, sandblasted parallel plates, parallel plates with smooth surfaces and parallel plates with surfaces attached with sandpaper.

Dimitrou et al. [49] prepared model systems composed by paraffin-wax and mineral oil and evaluated the effect of varying surface roughness on the flow restart of gelled samples. Rheological measurements were performed with roughened upper and lower geometries and with smoother test fixtures. The measured apparent viscosity for the samples in contact with the smooth geometry is much lower than expected, regardless of system composition. The material response indicates that surface roughness can act as slip inhibitors and prevent the gelled wax-oil systems from slipping against them. Bulk deformation and more rapid breakdown of the gel structure are expected for non-slipping samples, due to the larger stress required to achieve steady flow and consequently more power dissipated into the material.

Figure 17 exhibits some geometry elements that can be combined to adjust the roughness level of the solid walls in a rheometer. Smooth cylinder, grooved cylinder, 4-bladed vane, smooth parallel plate, and grooved parallel plate are the moving parts, whereas the smooth cup, the grooved cup, and the smooth Peltier plate are the stationary parts.

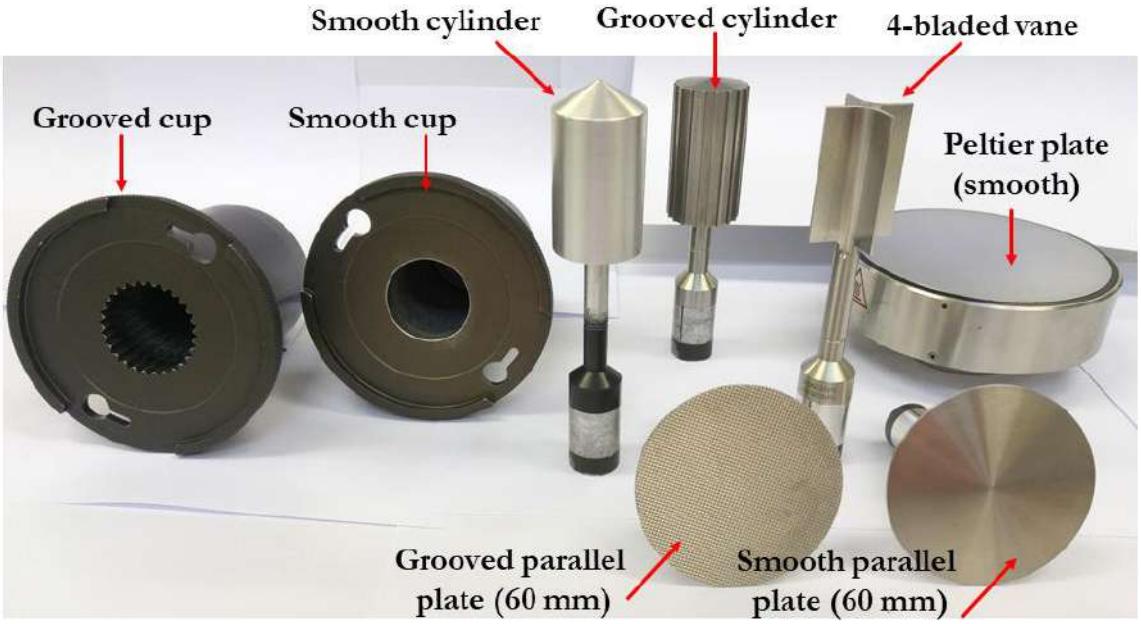


Figure 17 – Geometry elements that can be used for adjustable roughness in the controlled-stress rheometer. Different assemblies can be employed by combining these elements.

The vane tool is designed to replace the cylindrical bob under certain circumstances and is often recommended for concentrated dispersions and emulsions, which are prone to

slippage. According to Saak et al. [34], the use of a vane eliminates slip since shearing occurs within the material, and also it is easier to fabricate, compared with a carefully grooved cylinder. When using the vane with highly structured samples, the material moves like a solid plug, which may tend to slip when using a cylindrical smooth cup. However, as observed for Kaur and Jaafar [108], one limitation of the vane is for low-viscosity liquids, where inertial effects become important, and simple concentric flow-lines becomes distorted in some way. Barnes and Nguyen [122] conclude that one can simply calculate the yield stress of structured material using a vane on the basis of an equivalent solid cylinder, defined by the circumscribing circle formed by the tips of the blades. The authors suggested that the vane method is most suitable for measuring yield stress values greater than ~ 10 Pa.

## 2.5 Scaling Models

The structural properties of colloidal gels, such as gelled waxy oils, can be investigated through scaling models combined with rheology and DSC techniques. Essentially, scaling models are mathematical equations derived to relate material structure to mechanical properties of some class of material [123].

In view of the similarities of wax particle aggregation and polymerization reactions, Shih et al. [69] developed a scaling theory for the elastic properties of colloidal gels by applying scaling concepts that proved to be successful with polymer gels, as previously reported by Gennes [124]. The basic concept of the scaling model for polymer gels is to relate the elastic properties of a gel to its network structure. Shih et al. [69] extended this general scaling model to colloidal gels by considering the structure of the gel network as a collection of flocs, which are fractal objects closely packed throughout the sample. The structural development of the samples can be well monitored by measuring the elastic properties variation of the gels with increasing particle concentration [125].

According to Tang and Marangoni [126], a colloidal gel is a special state of flocculated systems in which a continuous network of particles is formed with the suspension having a very high viscosity and a finite shear modulus. The term colloidal gel refers to a coherent dispersed system comprised of at least two components, one of which is a liquid present in a significant amount that displays solid-like linear viscoelasticity and a series of yielding properties, such as yield stress. When there are attractive interactions between the particles, the gels can form even at very low volume fractions and the particles form fractal clusters: the dispersed component extends continuously

throughout the whole system, which ultimately percolates to form space-filling networks [6].

For a gelled crude oil, the gel structure is formed mainly by the interactions of wax crystal flocs. Therefore, these systems can be treated as colloidal gels with fractal nature. The fractal flocs pack closely and fill the sample volume as repeating units of the colloidal gel network [127]. A schematic representation of colloidal gels is shown in Figure 18. By assuming a fractal structure for colloidal gels that are well above the gelation threshold, a simple but systematic scaling theory can be derived. Microscopic structural characteristics can be obtained through the relations between the storage modulus in the linear viscoelastic region ($G'_{LVR}$), the critical elastic strain ($\gamma_E$), and the mass fraction of precipitated wax crystals ($\phi_w$) [69].

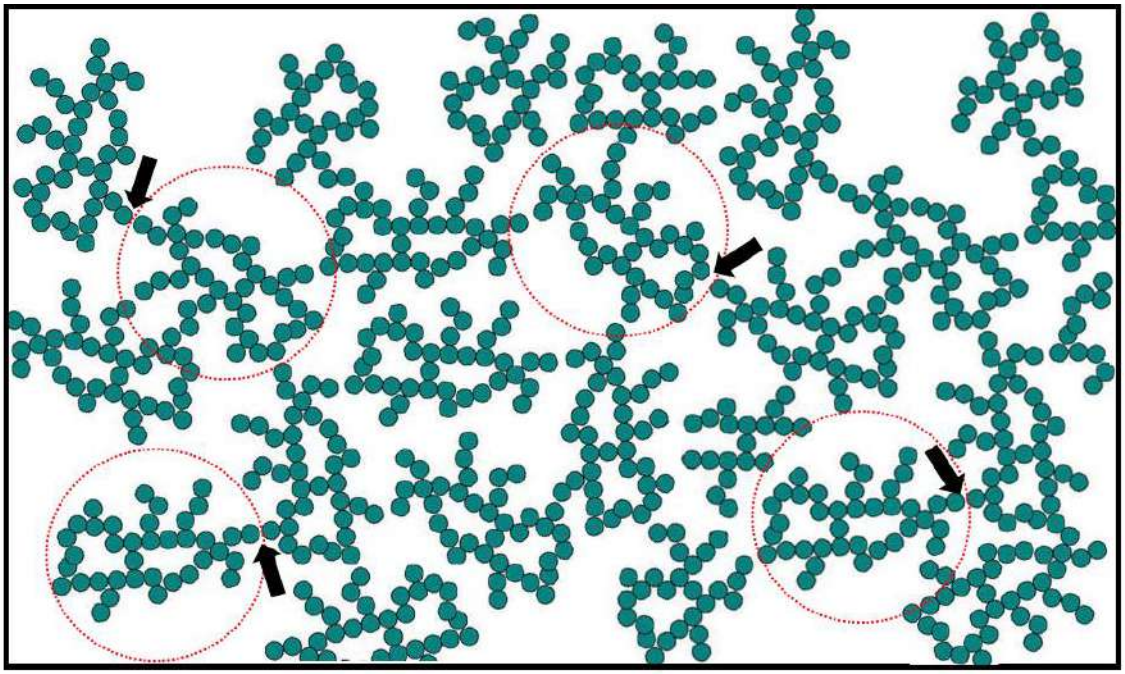

Figure 18 - Schematic structure of a colloidal gel: the circles indicate fractal floc size and the arrows indicate regions of interfloc links (adapted from Shih et al. [69]).

In general, there can be two types of scaling behavior for colloidal gels: the strong-link and the weak-link behavior. The scaling of both the storage modulus and the critical elastic strain depends on whether the interfloc links are stronger than the flocs itself. In the strong-link regime, for instance, the breaking of bonds occurs within a floc and the macroscopic elasticity of the gel is given by that of intralinks. In the weak-link regime, flocs are more rigid when compared to the interfloc connection and the elasticity of the interfloc links determines the elasticity of the gel [69]. In other words, the strong-link and

weak-link regime denote whether the yield behavior of a flocculated network occurs by internal failure either within the floc or between flocs, respectively.

In order to determine the mechanism of mechanical failure and possibly elastic deformation of wax-oil crystal networks, Miyazaki and Marangoni [28] produced impressive images (see Figure 8). Observing the image details it is possible to identify rupture points of the solid at the edges of the structures: the faces did not change after yielding, indicating that the walls retained their integrity. Therefore, we can assume that the system is mechanically in a weak-link regime, where the link between flocs is weaker than the flocs themselves.

There are also other differences in the two link regimes. The elastic constant (represented by the storage modulus) increases more slowly in the weak-link than in the strong-link regime. Also, the critical elastic strain increases with increasing particle concentration in the weak-link, however, it presents opposite behavior in the strong-link regime [63]. A colloidal gel may cross from the strong-link to the weak-link regime with increasing particle concentration. This occurs because since the elastic constant of the individual flocs can vary widely depending on the floc size, the elastic constant of the links between flocs may be different from that of the flocs [69].

Assuming that colloidal aggregates behave as a stochastic mass of fractals on a scale that is large compared to the primary crystal size, both the storage modulus and the critical elastic strain are expected to scale as a function of the particle concentration according to specific power law [125]. A typical scaling for colloidal gels is represented by an equation with the form of Equation 9:

$$M = {\phi_w}^{\mu} \qquad \text{Eq. (9)}$$

where $M$ represents the material's mechanical response and $\mu$ is the scaling exponent. The main parameter of the scaling exponent is a property named fractal dimension, which is an extended Euclidean dimension. It describes the combined effects of morphology and spatial distribution patterns of the crystal clusters in the colloidal crystal networks and is used to quantify the microstructure of the crystal networks [126]. The advantage of fractal dimension is the independence of the measurement yardsticks over a given range of length scales. By using this simple parameter, the high complexity of projection morphologies of waxy crystal clusters can be described rather than having to use several parameters [78].

The increase in solid fraction content due to sample cooling of colloidal gels is followed by an increase in storage modulus, which is explained by the increment in the number of interfloc links. This has an impact in the sense that more developed gel structures present a higher fractal dimension [126]. On the other hand, the shear stress is able to destroy the crystal-crystal interactions due to breakage of London-Van der Waals forces between molecules. As a result, the fractal dimension of wax crystals decreases when the wax aggregates are broken, as observed by Yi and Zhang [105].

In the framework of scaling theory, the fractal dimension also increases as the gelled material changes from the strong-link regime (fractal dimension ~ 1.7 to 2.0) to a transition type (~ 2.2 to 2.5) and finally to the weak-link regime (~ 2.6 to 2.8). This is consistent with the fact that the transition from strong-link to weak-link gel occurs as the particle mass fraction increases [69]. Gao et al. [78] observed that, when the crude oil temperature is lowered, the precipitated wax amount is increased, and the grain size is augmented. Simultaneously, the aggregation of wax crystals is observed and, as a result, the corresponding fractal dimension increases. The authors calculated a chance in fractal dimension for a specific crude oil sample from 1.278 to 1.595 when the temperature is lowered from 24°C to 4 °C.

Jiang et al. [64] employed fractal dimension analysis for quantitative characterization of the structure of clusters in model oils composed by n-octacosane in diesel fuels. The results indicated that changes in the morphology and structure of the particles were accurately reflected in the value of the fractal dimension. For a small amount of precipitated material (< 0.2 wt %), the particles were dispersed uniformly and the fractal dimension was small. In contrast, as the wax content increased, the particles assembled as aggregates or masses with higher fractal dimensions and more intricate structures. This indicates that changes in the wax content of the samples took place, and changes in the fractal dimension show that the size and aggregation state of the particles also changed. It is important to observe that values of fractal dimension larger than three are unrealistic and, in general, the fractal model can be applied only for particle volume fractions up to 20% [127].

All fractal objects exhibit a self-similar or self-affine character, which means that the geometric pattern of a fractal object is repeated at different length scales. In this respect, despite the highly disordered structure of colloidal gels, there is much experimental evidence that in certain length scales they are often self-similar and can be described in terms of fractal geometry [28], [127]. According to Yi and Zhang [63], with the fractal dimension of gelled microstructures, one may develop a correlation between rheological

parameters and the microstructure. Further, the fractal model explains the elastic properties of waxy crystal networks by the summed stiffness of the interfloc links. Thus, a suitable method to quantify the structure of colloidal gels is fractal analysis, which is very sensitive to the order in the spatial distribution of an object's mass in space. Figure 19 exhibits different fractal images, including a microscopy image of gelled model oil obtained in this investigation.

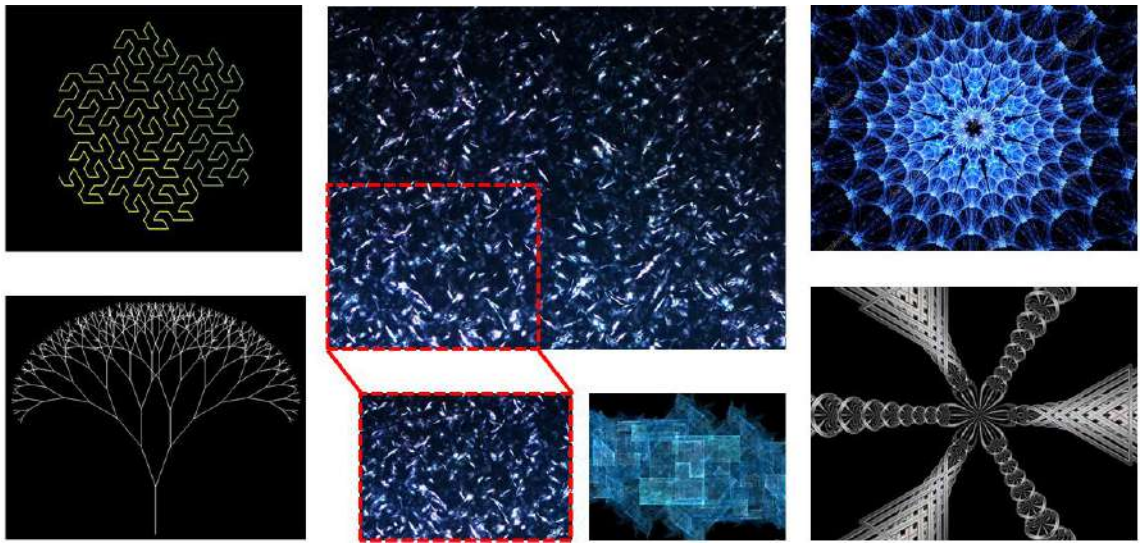

Figure 19 - Examples of fractal images, including clusters of waxy crystals in a gelled model oil (image generated in this investigation). On microscopic examination, their morphology and structures geometrically exhibit self-similarity to a certain degree.

The scaling model has been applied to gelled waxy crudes because of its colloidal nature and the fractal character of the waxy crystals. In this regard, Yang et al. [128] systematically analyzed the structural properties of gelled model waxy oils with different wax concentrations (5−20 wt%) on the basis of the DSC, rheological data, and scaling theory. The structure of the samples, similar to the structure of colloidal gels, transited from a strong-link regime to a weak-link regime with the increase of the mass fraction of precipitated wax crystals. In the strong-link region, $G'_{LVR}$ increases while critical elastic strain decreases with an increasing $\phi_w$. In the weak-link region, both $G'_{LVR}$ and $\gamma_E$ increased with an increasing $\phi_w$. In addition, the fractal dimension increased with increasing $\phi_w$ indicating the uninterrupted development of the gelled crude oils microstructure with increasing mass fraction of wax crystals.

In a similar study, however employing waxy crude samples instead of model oils, Yang et al. [125] investigated the structural characteristics of three oils by using scaling theory. In this case, the structure of the gelled waxy oils transited from a strong-link regime to a weak-link regime with the increasing $\phi_w$, with a transition point varying from 0.98 to 2.39

wt%. The fractal dimension also increased with an increasing $\phi_w$. For values below 0.2 wt%, a very low fractal dimension was obtained for crude oil C (0.790, compared to 2.413 for oil A and 2.282 for oil B), indicating a very porous and loose microstructure. The lack of resin and asphaltene for oil C, as characterized by SARA analysis, also favors the formation of a porous microstructure, which reinforces the result obtained from the fractal analysis. In Figure 20 it is exhibited the relationship between $G'_{LVR}$ and $\gamma_E$ as a function of the mass fraction of precipitated wax crystals for one of the samples assessed by Yang et al. [125].

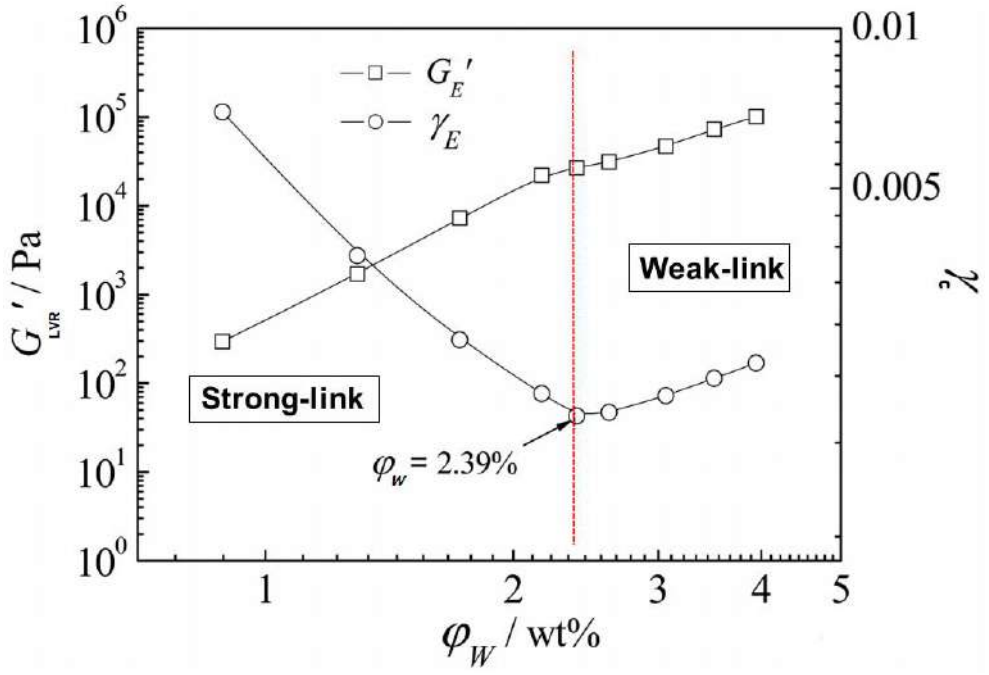


Figure 20 - $G'_{LVR}$ and $\gamma_E$ as a function of $\phi_w$. The mass of precipitated wax crystals was calculated on the basis of DSC experiments (extracted from Yang et al. [125], with permission).

From the left part of Figure 20, it is possible to observe that $G'_{LVR}$ increases as $\Phi_w$ is increased, whereas $\gamma_E$ decreases. According to the scaling theory, this pattern is compatible with the strong-link region. In the weak-link region, both $G'_{LVR}$ and $\gamma_c$ increases with $\Phi_w$. As predicted by Shih et al. [69] in his adapted theory, the waxy gel structured crossed from the strong-link to the weak-link regime with increasing particle concentration.

Scaling models may also encompass a thermodynamic approach. Marangoni [129] derived a general formulation for the relationship between the storage modulus and the microstructure of high volume fraction colloidal networks, represented in Equation 10.

$$E = \frac{12\left(\frac{\Delta U_\xi}{(l_0 - l)}\right)}{\pi a \xi \varepsilon} \Phi_v{}^{1/(d-D)} \quad \text{Eq. (10)}$$

In the above equation, $E$ represents Young's modulus of the crystal networks, $\Delta U_\xi$ corresponds to the change in the internal energy per floc-floc bond, $l_0$ is the equilibrium distance between flocs, $l$ corresponds to the distance between flocs under some applied stress, $a$ is the diameter of the particles (supposed spherical) within a floc, $\xi$ is the diameter of the flocs, $\varepsilon$ is the compressive strain of the network, $\Phi_v$ is the volume fraction of the aggregates of the network, $d$ is the Euclidean dimension of the embedding space, and $D$ is the fractal dimension for the arrangement of particles within the network. According to the author, by substituting $\Delta U_\xi$ with inter-particle interaction energy in a specific network, this extended model is suitable to study any soft material structured as a particle network at high volume fractions.

The general model contained in Equation 10 was adapted by Marangoni and Rogers [130] to study the yield stress as a function of solid volume fraction for blends of milk fat, cocoa butter, and modified palm oil through rheological experiments. The obtained expression is exposed in Equation 11:

$$\tau_0 = \frac{6\delta}{a} \Phi_v{}^{1/(d-D)} \quad \text{Eq. (11)}$$

In this equation $\tau_0$ represents the sample yield stress and $\delta$ is the solid-liquid surface energy (or the crystal-melt interfacial tension). The experimental results obtained by the authors agreed well with the derived model, as can be seen in Figure 21. The constants $\delta, D$, and $a$ were set to 0.01 J/m$^2$, 2.79, and 130 nm, respectively.

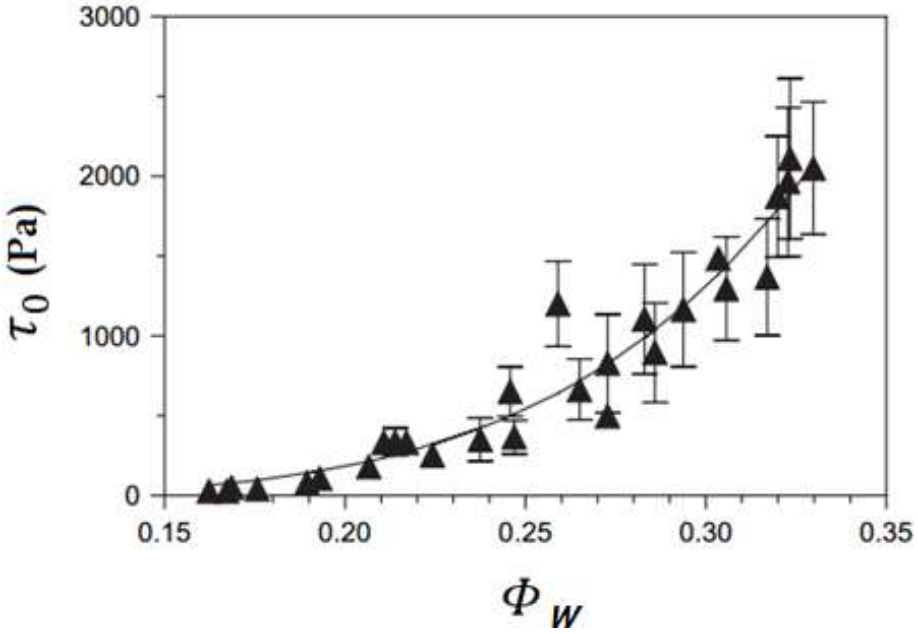


Figure 21 - Scaling behavior for the yield stress of soft material as a function of the volume fraction. The sample is a mixture of milk fat with canola oil crystallized for 24 h at 5.0 °C (extracted from Marangoni and Rogers [130], with permission).

Kane et al. [131] investigated the relationship between the rheological properties and the structure of waxy crude oils cooled in quiescent and flow conditions. An equation for the viscosity as a function of crystals volume fraction was established and analyzed in the framework of colloidal gels with a fractal structure (Equation 12):

$$\eta = \eta_s \left[1 - \frac{\psi}{\phi_m}\left(\frac{\sigma}{\sigma_c}\right)^{-(3-D)/3}\right]^{-[\eta]\phi_m} \quad \text{Eq. (12)}$$

where $\eta_s$ is the solvent viscosity, $\psi$ is the real volume fraction of primary particles, $\sigma$ is the shear stress, $\sigma_c$ is the cohesion stress, $[\eta]$ is the intrinsic viscosity of the particles, $\phi_m$ is the maximum volume fraction for packing, and $D$ is the fractal dimension of an aggregate.

Silva and Coutinho [92], by assuming the wax aggregates as fractals, calculated the fractal dimensions for three cured wax oil gels through scaling theory and rheological measurements, in terms of Equation 13:

$$G' = \lambda \Phi_v^{\beta/(d-D)} \quad \text{Eq. (13)}$$

In this equation, $G'$ represents the storage modulus, $\Phi_v$ is the particle volume fraction, $d$ is the Euclidean dimension of the system, $D$ is the fractal dimension of the flocs, β is a

constant and $\lambda$ is a pre-exponential factor in the power-law scaling. The fractal dimensions for three waxy oils were calculated as 1.7, 1.9, and 2.2. The authors affirmed that the low fractal dimension indicates elongated substructures with network arrangement with a high degree of porosity: a lattice of wax crystals with large spaces among them filled by the oil and non-precipitated material. A higher fractal dimension was related to a greater degree of order in the crystal packing within the aggregates, resulting in a coarser network.

According to Yang et al. [131], there are several experimental techniques available to analyze fractal structures in gel aggregates, such as rheology, microscopy and light scattering. Scattering techniques are probably the most reliable, according to the authors, although they are mostly used in dilute systems with particle volume fractions substantially smaller than 1.0%. At larger particle volume fractions, the techniques based on rheological measurements are better suited to characterize the structure of gels. Gao et al. [78] also presented a direct fractal characterization approach based on micrographs of wax crystals by applying the box-counting method, implemented in ImageJ software. A comparative result between the direct-image approach and the calculation based on rheological measurements is presented in Figure 22 for two waxy oil samples.

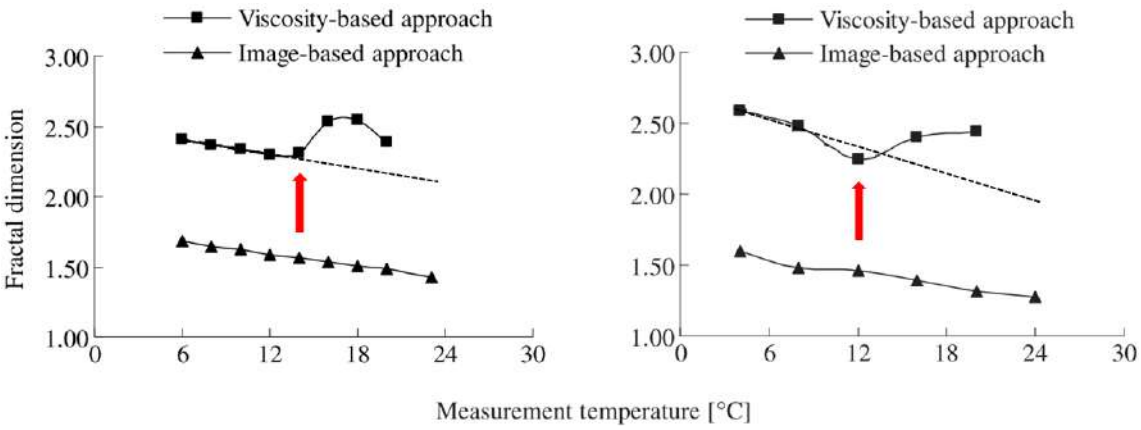


Figure 22 - Comparison between fractal dimension values obtained by the direct image-based approach and by rheological measurements for two crude oil samples at different temperatures. The divergence point is indicated by the arrow (extracted from Gao et al. [78], with permission).

By observing Figure 22 is possible to conclude that the viscosity-based approach fails in higher temperatures (above ~12°C) for both samples. However, as pointed by Gao et al. [78], one drawback of all image-based methods is that the image is the two-dimensional

projection of the actual morphology and structured, which intrinsically yields lower values for the fractal dimension.

## 2.6 Literature Critical Review

In this section, it is presented some author's perspective regarding the assessed literature consulted to compose this Thesis. Despite a large number of studies already published, flow assurance remains an active investigation field, primarily due to oil industry interest in safe and economic drilling. This concern is, to a great extent, responsible for the investigation on the rheological behavior of gelled waxy oils.

The microscopic structural characteristics of gelled waxy crude oils are greatly important in the explanation of the rheological changes at different conditions. However, studies on this aspect were limited because of the complicated nature of the oils and the defects of microscopic observation techniques. More fundamental knowledge of microstructural characteristics is necessary for better understanding the complex rheological changes of gelled waxy crude oil in order to appropriately scale laboratory measurements to field conditions and obtain useful forecasts.

To establish a systematic study on the flow behavior of gelled waxy oils, the first step is to select a suitable technique to assess the rheological data of the material being studied. The knowledge of pipeline flow characteristics and temperature gradient conditions are often difficult to reproduce in laboratory settings. According to Wardhaugh and Boger [35] the nonlinear pressure distribution, together with the effects due to the compressibility of the petroleum transport pipes, the porosity of the wax structure, and contraction effects, should make the capillary viscometer or pilot scale pipeline not suitable for understanding the yielding behavior of gelled waxy oils. On the other hand, dynamic and steady shear rheology are convenient choices for this study.

Yield stress materials are ubiquitous, yet the best way to obtain the value of the yield stress for any given material has been the subject of considerable debate. In fact, rheometry presents several difficulties for complex fluids [34], [98], [115], [119] and performs accurate measurements it is not a straightforward task. Apparent wall slip is a source of the difficulty. In fact, the two main causes of errors in rotational rheometer measurements are due to edge failure and radial migration, both associated with the dynamics of the interface at the rim [100], [132]. In this regard, yield stress measurements may be limited, as the slip phenomenon creates uncertainty in the bulk flow behavior, which is required for effective transport system design. This uncertainty

propagates to constitutive models derived from the questionable experimental observations. Therefore, it is vital to investigate the effect of apparent wall slip on the rheology of waxy gels and eliminate or mitigate the phenomenon in order to estimate its extension on the assessed data.

Slippage phenomenon is a potential risk to the quality of rheological data. Even though there still many authors who give little attention or simply ignore this issue. For example, one common approach is to consider that wall slip or apparent wall slip was eliminated by the use of one roughened surface. Nonetheless, we must consider that a sample in a rheometer is in contact with two solid surfaces, i.e., the moving part and the stationary part (see Figure 17). Thus, for yield stress materials, the slippage may take place at both surfaces and it is clear that both should be roughened in order to eliminate the slippage effects. This represents a simple but effective mean of measuring the properties of gelled oils that would otherwise display large slip effects at smooth walls. It is not reasonable to assume that only one portion of the sample is prone to slip unless one has evidence to support it.

The physics behind the non-Newtonian and time-dependent behavior presented by the colloidal gel is not completely understood. Despite that, according to the consulted literature, the gelling process of waxy crudes is governed by a large number of parameters, such as the cooling rate, the stress loading rate, and aging time, as well as the shape and structure of the wax crystals. Thus, there should be an effort to consistently apply similar conditions for model pipelines and controlled stress rheometer experiments.

Significant research on the industrial and academic level has been dedicated to developing proper additives to mitigate the gel deposits formation. However, little work has been devoted to understanding how the composition of the oil itself affects the formation of this wax-oil gel. While the costs of remediation, usually via mechanical pigging and/or the addition of a wide array of fluids, inhibitors, and additives, can be quite high, these costs are dwarfed by the production losses incurred by flow reductions and/or pipeline shutdowns and maintenance needed because of wax deposition. Greater insight into how the composition of crude oil can influence the gelation characteristics could be crucial in developing more accurate deposition models that could also incorporate such properties as the gelation temperature and the yield stress.

Different techniques can be employed to estimate the yield stress of a particular sample. As exposed in section 2.3, in the flow assurance context creep tests would produce more reliable measurements of yield stress, in principle. Although, obtaining a single value of yield stress from creep measurements is exceedingly time-consuming since to gather

one curve several experiments are needed. In this sense, oscillatory experiments are a more suitable option for an extensive investigation.

In the mid-'80s, multiple definitions of yield stress have been proposed. One may find yield stress defined as "the stress below which the substance is an elastic solid and above it is a liquid with a plastic viscosity" or, alternatively, "the stress below which no flow can be observed under the experiment conditions" [133]. However, it is reasonable to argue that the yield stress is, in fact, an idealization since, given sufficient accurate measurements (or sufficient patience), no yield stress would exist. In other words, if a material flows at high stresses it will also flow, however barely and slowly, at low stresses. In addition, according to Barnes [37], all materials can flow on long enough timescales and consequently many materials, which are considered to have true yield stress, are actually very high viscosity liquids. On the other hand, the question of whether yield stress exists as a real phenomenon is not relevant in engineering practice. For process timescales such as production, transportation, and storage of waxy crude oil the yield stress is a practical reality.

At low stresses, the waxy gels are very viscous, resembling an elastic solid. Over a very narrow stress range, the viscosity drops several orders of magnitude and macroscopic flow occurs. The critical stress range is very small and often designated as a single point, called the yield stress. In this investigation a practical definition of yield stress is adopted: the stress at G' and G'' crossing point at oscillatory amplitude sweep. This definition matches with the static yield stress definition by Wardhaugh and Boger [35] in their seminal paper and provides a reasonable and fast method to probe a wide experimental range. Despite being arbitrary criteria, the definition essentially represents the point at which, when increasing the applied stress, the solid first shows liquid-like behavior, i.e. continual deformation.

In the flow assurance context yield stress is a key parameter. The storage modulus has not the same relevance. However, in the case of waxy gels, both properties arise from the same phenomenon (precipitation, deposition, and further enmeshment of wax crystals). Thus, it is reasonable to assume that storage modulus is strongly correlated to yield stress for these systems. In this regard, scaling models may be useful in relating elastic properties of waxy gels to its network structure.

Scaling models can be applied to further understand the relationship between rheology and microstructure for the gelled waxy crude oils. On the basis of the results exposed in section 2.5, it is possible to conclude that the morphology and structure of wax crystals can be effectively characterized as a whole via the fractal dimension either from

scattering, rheological or direct-image techniques. Fractal dimensions calculated by different methods are sensitive to different structural features of the crystal network. Regardless of the method employed, there is an agreement among these authors that a larger fractal dimension represents a higher complexity of the wax crystal morphology.

# 3 Materials and Methods

This chapter is intended to provide a detailed, clear, and precise description of the experimental procedures performed in this Thesis and also a description of the materials used.

## 3.1 Materials

Model waxy oils were the focus of this investigation. Four different waxes were acquired to compose it: **$L_{24}$** (Fluka Analytical Reagents, Brazil), **$L_{29}$** (Sigma-Aldrich, USA), **$B_{37}$** (Fluka Analytical Reagents, Brazil) and **$B_{53}$** (GM Waxes, Brazil). The capital letter **L** stands for (predominantly) linear wax whereas **B** stands for branched wax. The numbers subscripts indicate the average carbon number.

The solvent adopted for model oil preparation is alkane mineral oil, free of crystallizable waxes at the temperatures assessed in the rheological tests (50 °C to 4 °C). The boiling point ranges from 261°C to 511°C, the density at 20°C is 852 kg/m$^3$, and the viscosity at 20°C is $2.39 \times 10^{-5}$ Pa.s. The oil was kindly supplied by Petrobras S.A and henceforward it will be referred to as spindle oil.

## 3.2 Methods

The waxes and spindle oil were physicochemically characterized by means of $^{13}$C-NMR, X-RD, FT-IR, DSC, GC-FID, SAXS, and optical microscopy. The details of each technique are presented in the following.

### 3.2.1 $^{13}$C Nuclear Magnetic Resonance ($^{13}$C-NMR)

Waxes spectrums were obtained with Mercury 300 (Varian, USA) equipment at 75 MHz. 10 mm tubes and deuterated chloroform was employed (125 mg of wax : 2.5 ml of solvent). Pulse width and delay were 90° and 1 second, respectively. Prior to analysis, waxes were solubilized at 120 °C inside closed tubes. For **$L_{24}$** and **$L_{29}$** the temperature of the experiment was held at 40°C whilst 50 °C was employed for **$B_{37}$** and **$B_{53}$**.

### 3.2.2 X-Ray Diffraction (X-RD)

The waxes X-ray diffraction patterns were recorded in the range 2Θ = 5 to 60° with a step size of 0.05 2Θ/s in a MiniFlex (Rigaku, Japan) powder x-ray diffractometer. The equipment employs a copper anode source (λ = 0.154 nm) and voltage set at 30 kV. The θ-θ goniometer set-up used a 0.57 divergence slit, 0.57 scatter slit, and 0.3 mm receiving slit. For the experiments, the samples were melted at a circulating oven (120 °C, 10 minutes) and poured into homemade sample holders to crystallize at room temperature. Samples were then transferred to the x-ray sample holder, and scans were performed from at scanning rate of 1.0° $min^{-1}$ and 20ºC temperature.

### 3.2.3 Fourier Transform Infrared Spectroscopy (FT-IR)

IRaffinity-1 (Shimadzu, Japan) equipment with a DTGS-KBr detector, 2.0 $cm^{-1}$ resolution, and Happ-Genzel apodization was employed to obtain the spectrums of the waxes and spindle oil. Sixteen sample scans were performed in the range of 4,000 to 500 $cm^{-1}$.

### 3.2.4 Differential Scanning Calorimetry (DSC)

A DSC 8500 (Perkin-Elmer, USA) was employed for thermal characterizations of spindle oil, waxes and also model oils. $N_2$ at 50 ml/min was used as the purge gas. Samples of 15 to 25 mg were placed in aluminum pan with pierced cover. The experimental procedure for **$L_{24}$**, **$L_{29}$**, **$B_{37}$**, **$B_{53}$** waxes, and spindle oil comprised five steps:

Step [1] Heating ramp from 25°C to 80°C at 20°C/min;

Step [2] 10 min conditioning at 80°C;

Step [3] Cooling ramp from 80°C to 4°C at 1.0°C/min;

Step [4] 10 minutes conditioning at 4°C;

Step [5] Heating ramp from 4°C to 80 at 1.0°C/min.

Samples of 27.5 to 29 mg were used for the specific investigation by scale models (section 4.5). The procedure adopted for **$L_{29}$** and **$B_{53}$** waxes and also for the model oils comprised three steps:

Step [1] Heating ramp from 25°C to 80°C at 10°C/min;

Step [2] 10 min conditioning at 80°C;

Step [3] Cooling ramp from 80°C to -10°C at 10°C/min;

Among other information, the generated data provided means to calculate the mass fraction of precipitated wax at different temperatures. The higher cooling rate of 10°C/min provided a better DSC signal in view of the small amount of wax present in ~ 29 mg of model oils 7.5 wt%.

### 3.2.5 Gas Chromatography Flame Ionization (GC-FID)

Gas chromatography was employed with spindle oil and wax samples. The boiling point distribution was performed by a 6890N GC (Agilent Technologies, USA) with electronics pneumatic control (EPC), configured with a flame ionization detector (FID) and a 10 m x 530 µm x 2.65 µm $DB^{-1}$ capillary column. The experimental procedure was based on ASTM D2887. The same equipment was employed for carbon number distributions. A melted silica capillary column with 100% methyl silicone stationary phase was selected. The experimental procedure was based on ASTM D5442.

### 3.2.6 Small Angle X-Ray Scattering (SAXS)

The SAXSpoint 2.0 (Anton Paar GmbH, Austria) was used to investigate model oil samples. The equipment configuration is: Primux 100 microfocus X-ray source, which provides X-ray flux with high spectral purity (99.9%) at a low power range of 50 W, AXO montel (dual bounce) with custom optics, TC 150 with 1 mm capillary and Dectris Eiger R 1M detector (1M pixels, 75 micron pixel size). The samples have been warmed at 80°C for 10 minutes and loaded with a pipette into a warmed-up capillary. The capillary was then cooled to 4 °C (cooling rate of 1.0°C/min). Next, 30 minutes of isothermal holding at 4°C was applied and then the SAXS measurement was started (30 min, 6 x 5 min frames).

### 3.2.7 Model Oils Preparation

Wax solutions were prepared inside a 150 ml beaker, placed on a C-MAQ HS7 heating plate (IKA, China) at a constant temperature of 120°C at 15 minutes under magnetic stirring to ensure homogeneity and solubility. Total wax content ranged from 2.5 to 15 %wt, 30g for each preparation. These values were based on waxy crude oil compositions

commonly encountered worldwide [134]. In order to departure from the same thermal and shear history, the samples were freshly prepared immediately before each rheological test. Previous rheological measurements showed that these model oils reproduce essential features of crude oil gels, exhibiting a low-temperature gel-like mechanical response to an imposed low-frequency oscillatory stress.

### 3.3 Rheological Experiments

Rheometry was the main technique employed in this Thesis. The different protocols for the rheological tests performed with model waxy oils are described in details in the following.

#### 3.3.1 Investigation on the Effect of Apparent Wall Slip

The apparent wall slip phenomenon was judiciously investigated through rheological tests employing geometries with different roughness. After preparation, model oils with 3.0 wt% or 7.5 wt% $\mathbf{L_{29}}$ wax were immediately placed in the rheometer. A DHR-3 (TA Instruments, USA) equipment was used. The initial temperature was set to 50°C for all tests.

Three types of experiments were performed: oscillatory, creep and steady-state flow tests. In the case of oscillatory tests, all experiments were run in triplicate. The 95% confidence interval was provided by the Student's t-test.

The rheological protocol comprises 4 steps. The first 3 steps were identical to all experiments:

Step [1] - conditioning at 50°C for 5 minutes to favors the sample thermal equilibration;

Step [2] - quiescent cooling from 50°C to 4°C at 1.0°C/min;

Step [3] - 30 minutes of isothermal holding at 4°C to obtain a gelled material;

(a) In the case of oscillatory tests, the last step was:

Step [4a] - logarithmic stress sweep at 4°C and 1 Hz, from 1 Pa to 500 Pa (3.0 wt% systems) or 1 Pa to 2,700 Pa (7.5 wt% systems). The yield stress was defined at the G' and G'' crossing point.

(b) In the case of creep tests, the last step was:

Step [4b] - sample holding for 2 minutes at 4 °C under a constant stress value. The yield stress was defined as the first stress value able to promote a sharp increase in the angular velocity of the rotor.

(c) In the case of steady-state flow tests, the last step was:

[4c] – flow curves with the shear rate varying logarithmically from $10^{-3}$ to $10^{3}$ $s^{-1}$, equilibration time of 150 seconds and 30 seconds sampling.

Figure 17 exhibits all the geometry elements employed in the apparent wall slip investigation. Smooth cylinder, grooved cylinder, 4-bladed vane, smooth parallel plate, and grooved parallel plate are the moving parts, whereas the smooth cup, the grooved cup, and the smooth Peltier plate are the stationary parts.

Seven different assemblies were used in the rheological tests:

**SPP** – **S**mooth **P**arallel **P**late (with smooth Peltier plate)

**GPP** – **G**rooved **P**arallel **P**late (with smooth Peltier plate)

**SC + SC** – **S**mooth **C**ylinder + **S**mooth **C**up

**SC + GC** – **S**mooth **C**ylinder + **G**rooved **C**up

**GC + SC** – **G**rooved **C**ylinder + **S**mooth **C**up

**GC + GC** – **G**rooved **C**ylinder + **G**rooved **C**up

**V + GC** – **V**ane + **G**rooved **C**up

The dimensions for each geometry are detailed:

- smooth cylinder and grooved cylinder: bob diameter 28.05 mm, bob length 50.00 mm;

- smooth cup and grooved cup: 30.50 mm diameter;

- vane: four-bladed elements equally distributed at the bar that connects to the rheometer, 1.20 mm thickness, 41.9 mm height;

- smooth and grooved parallel plates: 60 mm in diameter. In this case, both geometries were assembled with a smooth Peltier plate and a fixed gap of 800 µm.

Table 1 lists rheological tests performed, according to the experiment type, system composition, and geometry assembly.

Table 1 - Rheological tests according to the composition and geometry employed

| Experiment type | 3.0 wt% | 7.5 wt% |
|---|---|---|
| Oscillatory tests | SPP<br>GPP<br>SC + SC<br>SC + GC<br>GC + SC<br>GC + GC<br>V + GC | SC + SC<br>SC + GC<br>GC + SC<br>GC + GC |
| Creep tests | SC + SC<br>GC + GC | -<br>- |
| Steady-state flow tests | SC + SC<br>GC + GC | SC + SC<br>GC + GC |

### 3.3.2 Investigation on the Effect of Experimental Variables

In order to assess the effects of important experimental variables at yield stress of gelled oils, a protocol was defined. The rheological tests were based on a $2^{6-1}$ factorial experimental design with 37 experiments, including 5 central points. Six independent variables were selected: cooling rate ($x_1$), **$L_{29}$** weight percent ($x_2$), **$B_{53}$** weight percent ($x_3$), shear rate along cooling ($x_4$), final cooling temperature ($x_5$), and aging time ($x_6$).

Model oils were composed of a blend of predominantly linear and branched paraffin-wax (**$L_{29}$** and **$B_{53}$**, respectively). Total wax content ranged from 2.5 to 7.5 wt%. Individual compositions are shown in Table 2. All samples were prepared prior to the rheological test in order to avoid different thermal or shear histories.

Table 2 - Compositions used in the investigation of the experimental variables

| **$L_{29}$** wax (wt%) | **$B_{53}$** wax (wt%) | Total wax (wt%) |
|---|---|---|
| 1.25 | 1.25 | 2.5 |
| 3.75 | 1.25 | 5.0 |
| 1.25 | 3.75 | 5.0 |
| 2.50 | 2.50 | 5.0 |
| 3.75 | 3.75 | 7.5 |

Independent variables included in the experimental design and the respective levels are listed in Table 3. The yield stress was assigned as a dependent variable.

Table 3 - Factorial experimental design $2^{6-1}$: independent variables and levels

| Variable | -1 | 0 | +1 |
|---|---|---|---|
| $x_1$ - cooling rate (°C/min) | 0.50 | 0.85 | 1.20 |
| $x_2$ - **$L_{29}$** weight percent (wt%) | 1.25 | 2.50 | 3.75 |
| $x_3$ - **$B_{53}$** weight percent (wt%) | 1.25 | 2.50 | 3.75 |
| $x_4$ - shear rate along cooling ($s^{-1}$) | 0 | 0.80 | 1.60 |
| $x_5$ - final cooling temperature (°C) | 4 | 8 | 12 |
| $x_6$ - aging time (min) | 0 | 30 | 60 |

The selected levels for the independent variables were chosen in order to approximate the experimental conditions to the field operational conditions of offshore waxy oil production. It is also important to mention that when the aging time variable ($x_6$) is equal to zero, it does not mean that the aging process is not occurring on the rheological test. The time needed to break the waxy gelled structure is certainly higher than zero. Thus, during the stress sweep step the material is aging. Although, the aging time variable ($x_6$) intends to assess the effect of isothermal structure development before the yield stress measurement, which reflects the structural evolution of gelled waxy systems under quiescent and isothermal conditions.

An empirical equation (Equation 14) was used for fitting the generated data, according to the standard data analysis for this design. The dependent variable, the yield stress, was obtained from the last step of the rheological procedure (described below).

$$\boldsymbol{\tau_0 = a_0 + \sum_{i}^{6} a_i x_i + \sum_{i<j}^{6} a_{ij} x_i x_j} \qquad \text{Eq. (14)}$$

In Equation 14 $a_0$ is the independent term; $\mathbf{a_i}$ and $\mathbf{a_{ij}}$ are the regression coefficients related to the main effects and the second-order interactions, respectively, and $\mathbf{x_{i,j}}$ are the independent variables, normalized to [-1, 1] interval.

One important assumption for the rheological tests is that the standard deviations of the error terms for yield stress are considered constant, independent on the $\mathbf{x_{i,j}}$ values and

equal to the central point. In other words, homoscedastic error distribution was assumed. Table 4 summarizes the different conditions of the experimental design.

Table 4 - Experimental conditions for the rheological tests performed

| Run # | $x_1$ (°C/min) | $x_2$ (wt%) | $x_3$ (wt%) | $x_4$ ($s^{-1}$) | $x_5$ (°C) | $x_6$ (min) |
|---|---|---|---|---|---|---|
| 1 | 0.50 | 1.25 | 1.25 | 0 | 4.0 | 0 |
| 2 | 1.20 | 1.25 | 1.25 | 0 | 4.0 | 60 |
| 3 | 0.50 | 3.75 | 1.25 | 0 | 4.0 | 60 |
| 4 | 1.20 | 3.75 | 1.25 | 0 | 4.0 | 0 |
| 5 | 0.50 | 1.25 | 3.75 | 0 | 4.0 | 60 |
| 6 | 1.20 | 1.25 | 3.75 | 0 | 4.0 | 0 |
| 7 | 0.50 | 3.75 | 3.75 | 0 | 4.0 | 0 |
| 8 | 1.20 | 3.75 | 3.75 | 0 | 4.0 | 60 |
| 9 | 0.50 | 1.25 | 1.25 | 1.60 | 4.0 | 60 |
| 10 | 1.20 | 1.25 | 1.25 | 1.60 | 4.0 | 0 |
| 11 | 0.50 | 3.75 | 1.25 | 1.60 | 4.0 | 0 |
| 12 | 1.20 | 3.75 | 1.25 | 1.60 | 4.0 | 60 |
| 13 | 0.50 | 1.25 | 3.75 | 1.60 | 4.0 | 0 |
| 14 | 1.20 | 1.25 | 3.75 | 1.60 | 4.0 | 60 |
| 15 | 0.50 | 3.75 | 3.75 | 1.60 | 4.0 | 60 |
| 16 | 1.20 | 3.75 | 3.75 | 1.60 | 4.0 | 0 |
| 17 | 0.50 | 1.25 | 1.25 | 0 | 12 | 60 |
| 18 | 1.20 | 1.25 | 1.25 | 0 | 12 | 0 |
| 19 | 0.50 | 3.75 | 1.25 | 0 | 12 | 0 |
| 20 | 1.20 | 3.75 | 1.25 | 0 | 12 | 60 |
| 21 | 0.50 | 1.25 | 3.75 | 0 | 12 | 0 |
| 22 | 1.20 | 1.25 | 3.75 | 0 | 12 | 60 |
| 23 | 0.50 | 3.75 | 3.75 | 0 | 12 | 60 |
| 24 | 1.20 | 3.75 | 3.75 | 0 | 12 | 0 |
| 25 | 0.50 | 1.25 | 1.25 | 1.60 | 12 | 0 |
| 26 | 1.20 | 1.25 | 1.25 | 1.60 | 12 | 60 |
| 27 | 0.50 | 3.75 | 1.25 | 1.60 | 12 | 60 |
| 28 | 1.20 | 3.75 | 1.25 | 1.60 | 12 | 0 |
| 29 | 0.50 | 1.25 | 3.75 | 1.60 | 12 | 60 |
| 30 | 1.20 | 1.25 | 3.75 | 1.60 | 12 | 0 |

| | | | | | | |
|---|---|---|---|---|---|---|
| 31 | 0.50 | 3.75 | 3.75 | 1.60 | 12 | 0 |
| 32 | 1.20 | 3.75 | 3.75 | 1.60 | 12 | 60 |
| CP1 | 0.85 | 2.50 | 2.50 | 0.80 | 8.0 | 30 |
| CP2 | 0.85 | 2.50 | 2.50 | 0.80 | 8.0 | 30 |
| CP3 | 0.85 | 2.50 | 2.50 | 0.80 | 8.0 | 30 |
| CP4 | 0.85 | 2.50 | 2.50 | 0.80 | 8.0 | 30 |
| CP5 | 0.85 | 2.50 | 2.50 | 0.80 | 8.0 | 30 |

CP = Central Point

The rheological tests were performed at DHR-3 rheometer (TA Instruments, USA) equipped with grooved concentric cylinders (bob diameter 28.05 mm, bob length 50 mm; cup diameter 30.50 mm). It was found in our previous study that the grooved geometry was successful in eliminating apparent wall slip during the rheological tests. Peltier elements were employed for temperature control. The initial temperature was set to 50°C for all tests performed. This temperature is 20°C higher than the wax precipitation temperature for the most concentered systems (**$L_{29}$** 3.75 wt% + **$B_{53}$** 3.75 wt%), according to our previous results [67]. The experimental procedure is depicted in Figure 23.

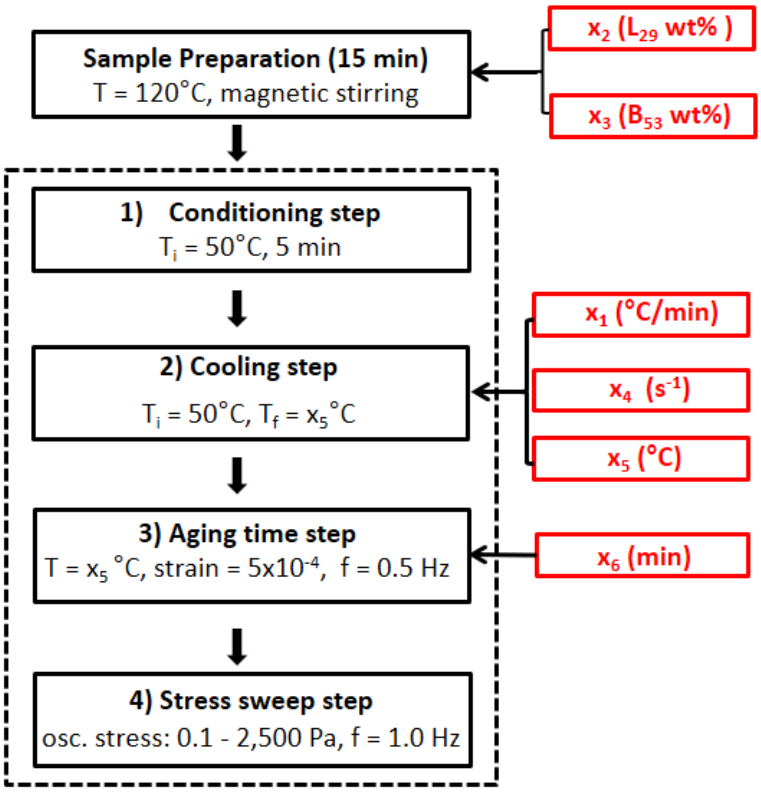


Figure 23 - Procedure adopted for the rheological experiments. Independent variables are assigned to $x_1$ to $x_6$ (see Table 3).

Conditioning step intended to promote thermal equilibration between the sample and the cylinder walls. Cooling was a dynamic step and the viscosity as a function of temperature was obtained for the conditions where the shear rate was different from zero. Aging was an oscillatory step and G' and G'' were captured as a function of time. The values for strain and frequency were chosen in order to promote the smallest disturbances and keep the sample within the linear viscoelastic regime since it is reported that waxy gelled systems are quite sensitive to the applied strain in the beginning of network building-up [53], [135]. The yield stress was obtained using a logarithmic stress ramp, ranging from 0.1 to 2,500 Pa at a frequency of 1 Hz.

### 3.3.3 Investigation on the Effect of Chemical Structure

To study the effect of different chemical structures in the yield stress four waxes were acquired to prepare model oils: $\mathbf{L_{24}}$, $\mathbf{L_{29}}$, $\mathbf{B_{37}}$, and $\mathbf{B_{53}}$. The composition was set to 7.5 wt% for single and blended wax solutions. For blended systems, 3.75 wt% of each wax was used. In order to departure from the same thermal and shear history, the samples were freshly prepared before each run.

The rheological tests were carried out at DHR-3 (TA Instruments, USA) equipped with grooved concentric cylinders (Bob diameter 28.05 mm, cup diameter 30.50 mm, Bob length 50.00 mm) to avoid apparent wall slippage phenomenon, which may underestimate yield stress values. The initial temperature was set to 50°C prior to analysis.

The procedure comprised of 4 steps:

[1] conditioning at 50°C for 5 minutes to favors the sample thermal equilibration;

[2] dynamic cooling from 50°C to 4 °C at 1.0°C/min and a shear rate of 0.8 $s^{-1}$;

[3] time sweep at 4°C for 15 minutes at oscillatory stress of 0.1 Pa and frequency 0.2 Hz to favor structure build-up;

[4] logarithmic stress ramp ranging from 0.1 to 1,000 Pa at 0.1 Hz frequency. All experiments were run in triplicate. The 95% confidence interval was provided by the Student's t-test.

### 3.3.4 Rheological Experiments to Derive Scaling Models

Scaling models were used to assess the effect of the wax concentration and microstructure characteristics on the mechanical response of **$L_{29}$** and **$B_{53}$** 7.5 wt% model oils. The rheological tests performed to derive the scaling models were carried out at DHR-3 (TA Instruments, USA) equipped with grooved concentric cylinders (Bob diameter 28.05 mm, cup diameter 30.50 mm, Bob length 50.00 mm).

The gelation points of model waxy oils were obtained through the temperature sweeping test under oscillatory mode. The procedure comprised of 2 steps:

[1] conditioning at 80°C for 5 minutes (well above the WPT of the oils);

[2] oscillatory cooling from 80°C to 4°C, 1.0°C/min, frequency of 1Hz and %strain of 0.5

During the cooling process, the storage modulus and the viscous modulus were measured under a fixed oscillatory frequency and a fixed shear strain. The gelation point was defined as the temperature at which G' begins to become larger than G'' [48], [81].

The critical elastic strain, $\gamma_E$, which is the value of maximum shear strain in the linear elastic region [95], [125] and the storage modulus in the linear viscoelastic region, $G'_{LVR}$, were obtained through the stress sweeping test under oscillatory mode. The procedure comprised of 4 steps:

[1] conditioning at 50°C for 5 minutes;

[2] quiescent cooling from 50°C to the specific test temperature (below the gelation point) at 1.0°C/min;

[3] time sweep at the specific test temperature for 20 minutes at oscillatory stress of 0.1 Pa and frequency 0.2 Hz to favor structure build-up;

[4b] logarithmic stress ramp ranging from 0.1 Pa to 500 Pa at a frequency of 1 Hz.

## 3.4 Optical Microscopy

Polarized light microscopy was adopted for morphological characterization of precipitated waxy crystals. Visualizations were made at inverted Axio Imager 2 microscope (Carl Zeiss, Germany) equipped with MRc5 Axiocam (5.0 megapixels) and temperature controller (Linkan T95-PE) with 20x objective lens (200x magnification).

Before visualization, the samples were solubilized inside a 50 ml beaker, placed on a C-MAQ HS7 heating plate (IKA, China) at a constant temperature of 120°C at 15 minutes

under magnetic stirring. Then, a small volume (~ 0.05 mL) was placed on viewing slides positioned on the thermal stage of the microscope preheated at 50°C for 5 minutes. Next, the sample was cooled at a 1.0°C/min.

All images were taken and analyzed with Axio Vision 4.8 software. The crystal lengths and aspect ratio (defined here as the ratio of the major and minor axis) were averaged for 25 random measurements.

# 4 Results and Discussion

This chapter is intended to expose, interpret and discuss the relevant results generated in this investigation, to justify the adopted approach and critically evaluate the study, considering the existing knowledge about the subject.

Five major sections are presented:

- Section 4.1 - Materials Physicochemical Characterization
- Section 4.2 - Apparent Wall Slip Phenomenon
- Section 4.3 - Influence of Experimental Variables at Yield Stress
- Section 4.4 - Influence of Wax Chemical Structures at Yield Stress
- Section 4.5 - Scaling Models for Gelled Waxy Oils

In section 4.1 it was investigated **$L_{24}$**, **$L_{29}$**, **$B_{37}$** and **$B_{53}$** wax samples, spindle oil, and also model oils of single and blended waxes at fixed composition 7.5 wt%.

Section 4.2 encompassed samples of gelled waxy oils **$L_{29}$** 3.0 wt% and 7.5 wt%.

In section 4.3 it was presented and discussed the rheological behavior of gelled model oils composed by a blend of **$L_{29}$** and **$B_{53}$** waxes with the composition varying from 2.5 wt% to 7.5 wt%.

In Section 4.4 model oils composed of single and blended waxes at a fixed composition of 7.5 wt% were prepared. Ten different samples were used: **$L_{24}$**, **$L_{29}$**, **$B_{37}$**, **$B_{53}$**, **$L_{24} + L_{29}$**, **$L_{24} + B_{73}$**, **$L_{24} + B_{53}$**, **$L_{29} + B_{37}$**, **$L_{29} + B_{53}$**, and **$B_{37} + B_{53}$**.

Section 4.5 encompassed samples of model oils **$L_{29}$** and **$B_{53}$** at 7.5 wt% and 15 wt%.

At the end of each chapter is presented a conclusion that reiterates the most important findings and synthesizes the discussion.

## 4.1 Materials Physicochemical Characterization

The results obtained from physicochemical characterizations of the waxes by different analytical techniques are summarized in Table 5. As already mentioned (section 3.1), the capital letter **L** stands for (predominantly) linear whereas **B** stands for branched wax. The subscripted numbers indicate the average carbon number calculated from GC-FID data.

Table 5 - Waxes structural and physical features

| Feature | $\mathbf{L_{24}}$ | $\mathbf{L_{29}}$ | $\mathbf{B_{37}}$ | $\mathbf{B_{53}}$ |
|---|---|---|---|---|
| Melting point range (°C)[(a)] | 42 - 50 | 50 - 58 | 56 -75 | 41 - 68 |
| Avg. fusion enthalpy (J/g)[(a)] | 135 | 187 | 152 | 91 |
| Avg. crystallization enthalpy (J/g)[(a)] | 133 | 203 | 167 | 116 |
| $CH_2/CH_3$ molar ratio (%)[(b)] | 24 | 25 | 44 | 57 |
| $CH/CH_2$ molar ratio (%)[(b)] | 0.0 | 0.0 | 6.36 | 4.41 |
| Branches per linear chain[(b)] | 0.0 | 0.0 | 2.79 | 2.51 |
| Average carbon number[(c)] | 24 | 29 | 37 | 53 |
| Branched wax content (wt%)[(c)] | 10.4 | 15.2 | 35.3 | 32.5 |
| Crystallinity degree (%)[(d)] | 50.1 | 31.7 | 51.0 | 35.8 |

Data from: [(a)]DSC, [(b)]$^{13}$C-NMR, [(c)]GC-FID, [(d)]XRD experiment (Avg. stands for average)

### 4.1.1 Differential Scanning Calorimetry

The thermal behavior of spindle oil and waxes was investigated by DSC technique. The melting range and average enthalpies of fusion and crystallization were obtained (see Table 5). For $\mathbf{L_{24}}$ and $\mathbf{L_{29}}$ waxes, the melting temperature ranged from 43 to 54°C and 50 to 58°C, respectively. For $\mathbf{B_{37}}$ and $\mathbf{B_{53}}$ waxes, it ranged from 56 to 75°C and 40 to 62°C, respectively. One can observe a narrower range in melting for $\mathbf{L_x}$ (~ 10°C) compared to $\mathbf{B_x}$ (~ 20°C). The wax structure is responsible for such differences. Indeed, broader melting ranges indicate a higher degree of polydispersity, a microcrystalline wax feature. The absence of a narrow melting region is also related to the presence of isoalkanes and/or cycloalkanes [136]. The average enthalpies of fusion ranged from 91 to 187 J/g whereas the average crystallization enthalpies were among 116 to 203 J/g. The very high wax polydispersity combined with isoalkanes and/or cycloalkanes presence may lead to small values of enthalpy [62], as occurred to $\mathbf{B_{53}}$ wax.

In addition to completely amorphous or completely crystalline materials, there are of course materials that are partially crystalline. In this type of materials, crystalline and amorphous regions coexist [76]. In **$L_{29}$** thermograms (Figure 24) there are smaller peaks marked with dotted ellipses. This can be due to amorphous precipitation or, more likely, a transition between crystalline modifications of paraffin waxes, while the more intense peaks are assigned to melting and crystallization. Regarding **$B_{37}$** thermogram (Figure 25), the smaller peak is not seen, which is likely due to a relatively high branch content and crystallinity degree (see Table 5). Spindle oil did not exhibit any thermal response at the range of temperatures assessed. Figures 24 and 25 exhibits the thermograms for heating and cooling programming for **$L_x$** and **$B_x$** waxes.

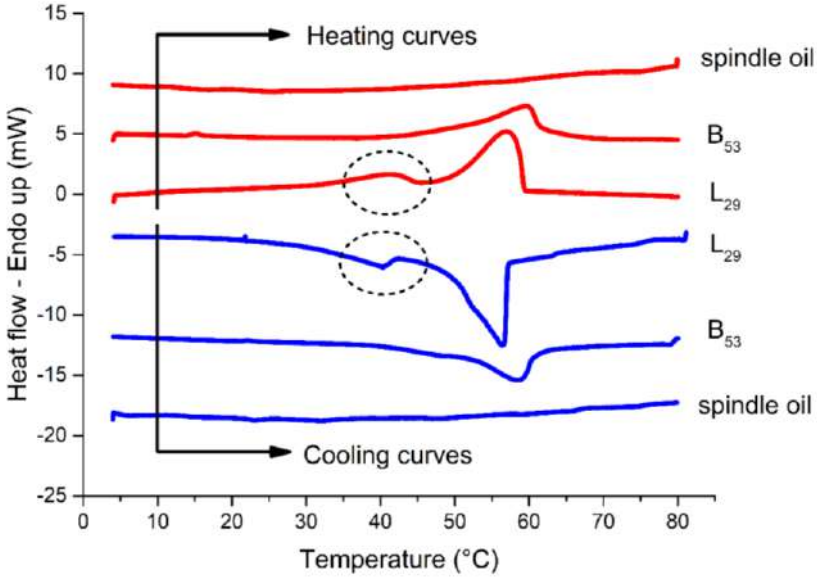


Figure 24 - Thermal characterization by DSC for spindle oils and **$L_{29}$** and **$B_{53}$** waxes.

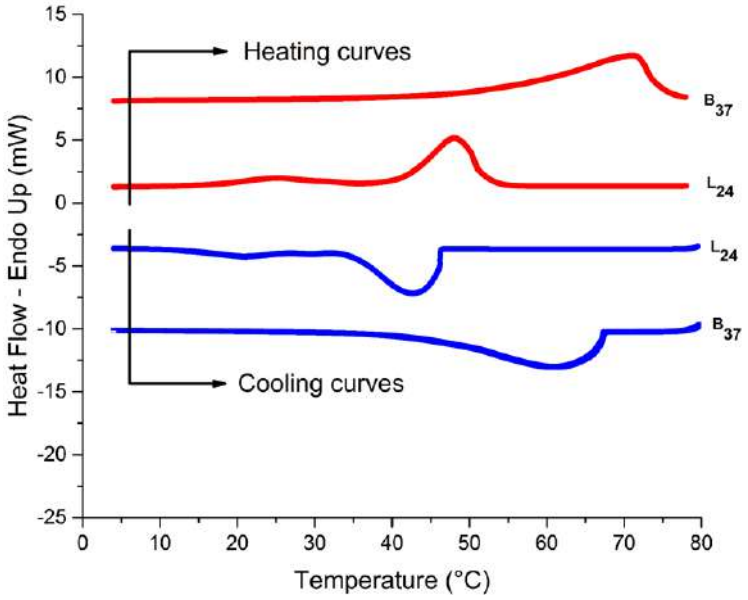


Figure 25 - Thermal characterization by means of DSC for **$L_{24}$** and **$B_{37}$** waxes.

### 4.1.2 $^{13}$C Nuclear Magnetic Resonance

Waxes $^{13}$C-NMR spectra were obtained and exhibited in Figure 26 and Figure 27. From the normalized areas, a dimensionless $CH_2/CH_3$ ratio can be calculated. Details on this calculation can be found elsewhere [137]. This number relates the carbons at the carbon main chain to the primary carbons and provides an estimative for the chain length [137]. As can be seen from Table 5, the results from GC-FID regarding average carbon number (24, 29, 37 and 53) and the respective ones from $^{13}$C-NMR (24, 25, 44 and 57) are comparable. The better agreement for $\mathbf{L_x}$ waxes probably due to their simpler $^{13}$C-NMR spectra.

Another ratio, the $CH/CH_2$, provides a relative estimative for tertiary carbons presented in the sample (in molar basis). In the case of $\mathbf{B_{37}}$, 6.36% of carbons are due to branches. Comparing to $\mathbf{B_{53}}$, which has 4.41% of tertiary carbons, the former wax is smaller and presents more branches per molecule. From $CH_2/CH_3$ and $CH/CH_3$ molar ratio it is possible to estimate the number of branch points for each linear main chain. This number is about 2.79 for $\mathbf{B_{37}}$ and it is smaller for $\mathbf{B_{53}}$ (2.51). In the case of the predominantly linear waxes, $\mathbf{L_{24}}$ and $\mathbf{L_{29}}$ did not present signals for tertiary carbons (the analysis were repeated twice, leading similar results). This fact does not necessarily indicate the absence of branches. Indeed, as shown in Table 5, $\mathbf{L_{24}}$ and $\mathbf{L_{29}}$ waxes have non-negligible branching contents, according to GC-FID data. However, the characteristic signal associated with tertiary carbons for these particular waxes (~ 32.5 ppm) [137] could not be detected by the NMR equipment. This is a result expected for a macrocrystalline wax, as already mentioned.

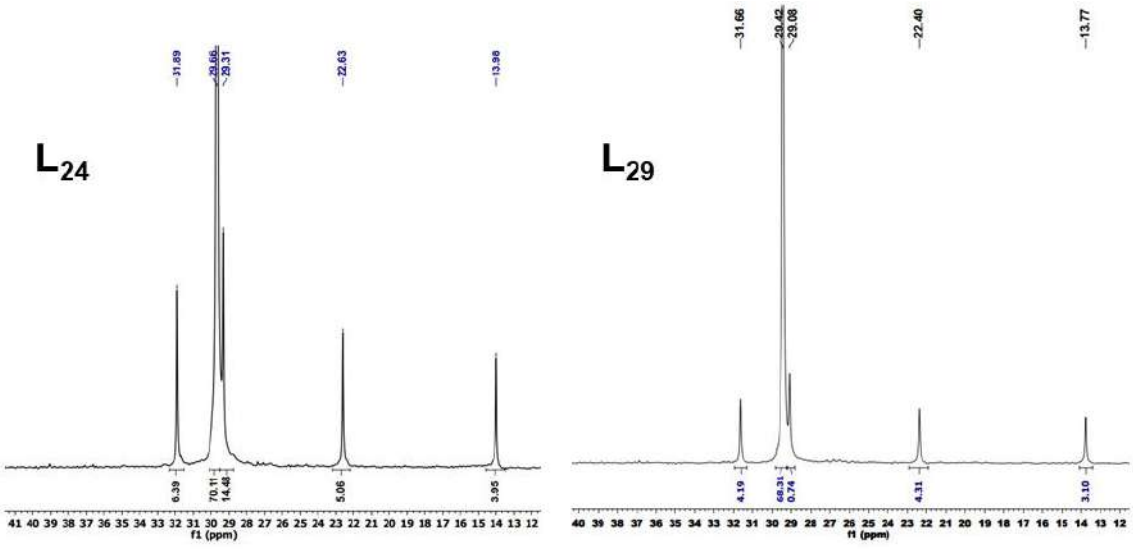


Figure 26 - Detailed $^{13}$C-NMR spectra of $\mathbf{L_{24}}$ and $\mathbf{L_{29}}$ waxes.

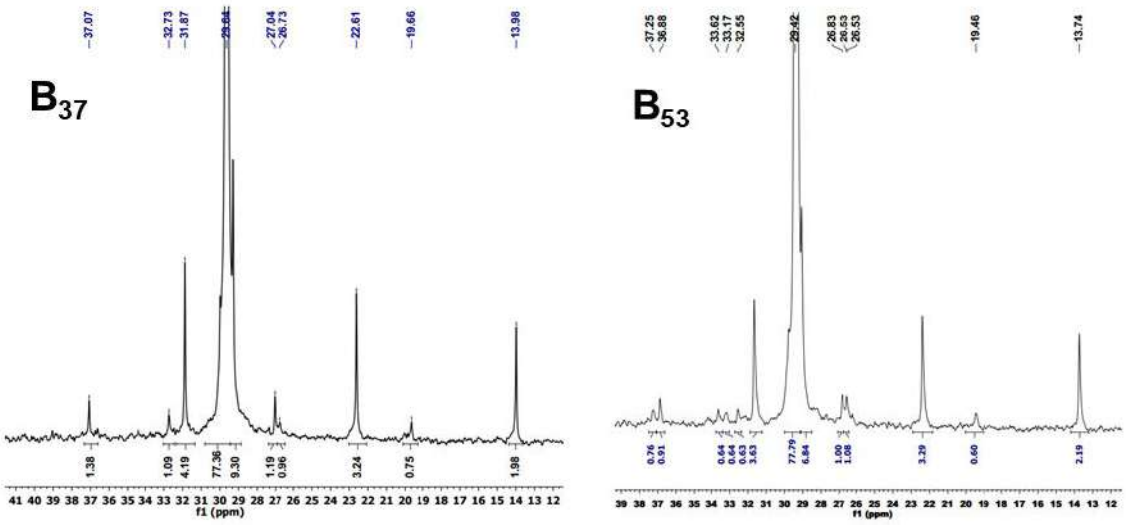


Figure 27 - Detailed $^{13}$C-NMR spectra of **$B_{37}$** and **$B_{53}$** waxes.

### 4.1.3 Gas Chromatography Flame Ionization

Carbon number distribution was obtained from CG-FID data. Spindle oil, **$L_{24}$**, and **$L_{29}$** wax presented an average carbon number of 23, 24, and 29, respectively. **$B_{37}$** and **$B_{53}$** wax presented an average carbon number of 37 and 53, respectively. For spindle oil, **$L_{24}$**, and **$L_{29}$** wax the distribution ranged from $C_{15\text{-}39}$, $C_{17\text{-}30}$, and $C_{18\text{-}60}$, respectively. In the case of branched waxes, **$B_{37}$** has a distribution ranging from $C_{22\text{-}56}$, whereas **$B_{53}$** distribution ranges from $C_{14\text{-}78}$. In Figure 28 it is possible to observe the carbon number distribution for the waxes and spindle oil.

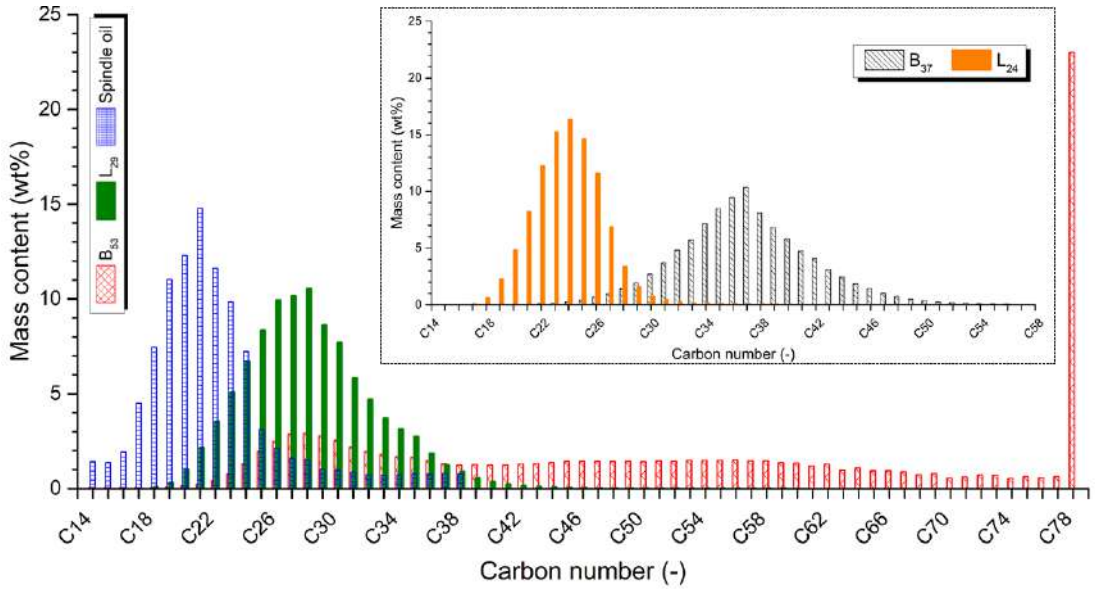


Figure 28 - Carbon number distributions for spindle oil and **$L_{29}$** and **$B_{53}$** waxes.

Table 5 contains the information of branched content of each wax. **$L_{24}$** and **$L_{29}$**, regarded as predominately linear waxes, have 10.4 wt% and 15.2 wt% due to branched carbons, respectively. Therefore, it is expected that waxes interactions would be dominated by its crystalline character. **$B_{37}$** and **$B_{53}$**, on the other hand, has 35.3 wt% and 32.5 wt% assigned to branched carbons, being, therefore, considered non-linear branched molecules. The combined results from $^{13}$C-NMR and GC-FID suggests that **$B_{37}$** has more tertiary carbons per linear chain and longer branches, based on the higher mass of branched carbons encountered. It is worth mentioning that the equipment used for the analysis has a detection limit at $C_{78}$ however **$B_{53}$** wax has 23 wt% assigned to larger carbon chains. The average carbon number of 53 was calculated assuming that all remaining carbon chains have 79 atoms, which is a conservative estimation, especially when compared to $^{13}$C-NMR results of 57 atoms (see Table 5) for **$B_{53}$**.

The boiling range for the spindle oil was also assessed. The oil starts to boil at 261°C, with 0.5 wt% of weight loss, and evaporates totally at 511°C, with 99.5 wt% of weight loss. Thus, stable compositions are expected for temperatures much higher than the preparation temperature of model oils employed in this investigation (120°C). The distribution is exhibited in Figure 29.

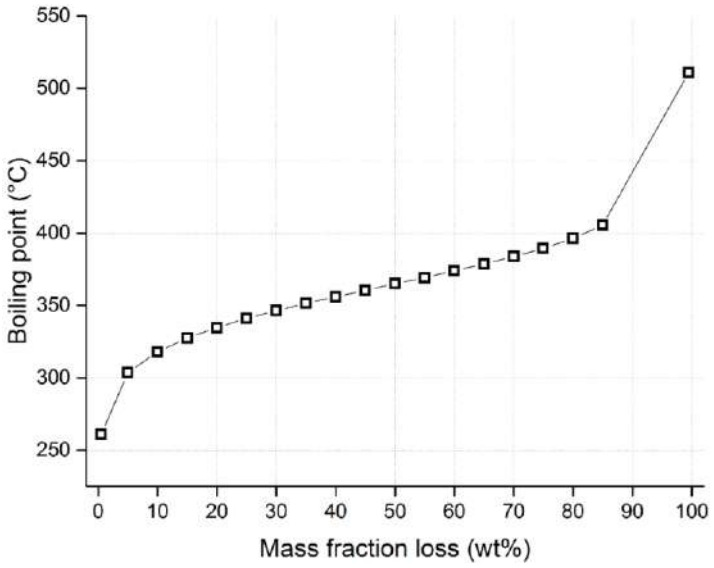


Figure 29 - The range of boiling points for spindle oil.

### 4.1.4 X-ray Diffraction

The diffraction pattern for all waxes was similar and the most intense peaks were located at 2Θ ~ 21.50° and 2Θ ~ 23.50°, which represent materials crystallized with orthorhombic shapes [73]. Assuming a first-order X-ray reflection, i.e. n = 1 from Bragg's Law, the

distance between the parallel planes of atoms are estimated to be 0.413 nm and 0.378 nm according to the more intense and narrow peaks.

All the waxes showed clear peaks with similar intensities at the low angle region of 2Θ ~ 12°, providing evidence for lamellar packing [83]. According to Zaky and Mohamed [82], the peak at 2Θ = 36.07°, more intense at **$L_{24}$** wax, is characteristic of macrocrystalline waxes. The crystallinity degree (calculated dividing the area under Bragg peaks by the total area under the diffractogram) for **$L_x$** and **$B_x$** waxes are shown in Table 5. A low degree of crystallinity indicates carbon chains highly non-linear, presenting obstacles for the regular packing of chains. Also, wide molecular weight distribution may contribute to this reduced crystallinity [82]. In this sense, the relatively small enthalpy values for **$B_{53}$** wax is corroborated by the low XRD crystallinity value.

The XRD results of crystallinity degree for **$L_{29}$** and **$B_{37}$** (31.7 % and 51.0 %) could not be explained satisfactorily since one might expect an increased crystallinity for predominantly linear waxes. Due to this, the $^{13}$C-NMR and XRD experiments were repeated, although yielding similar results. The diffraction patterns for **$L_x$** and **$B_x$** waxes are exhibited in Figure 30.

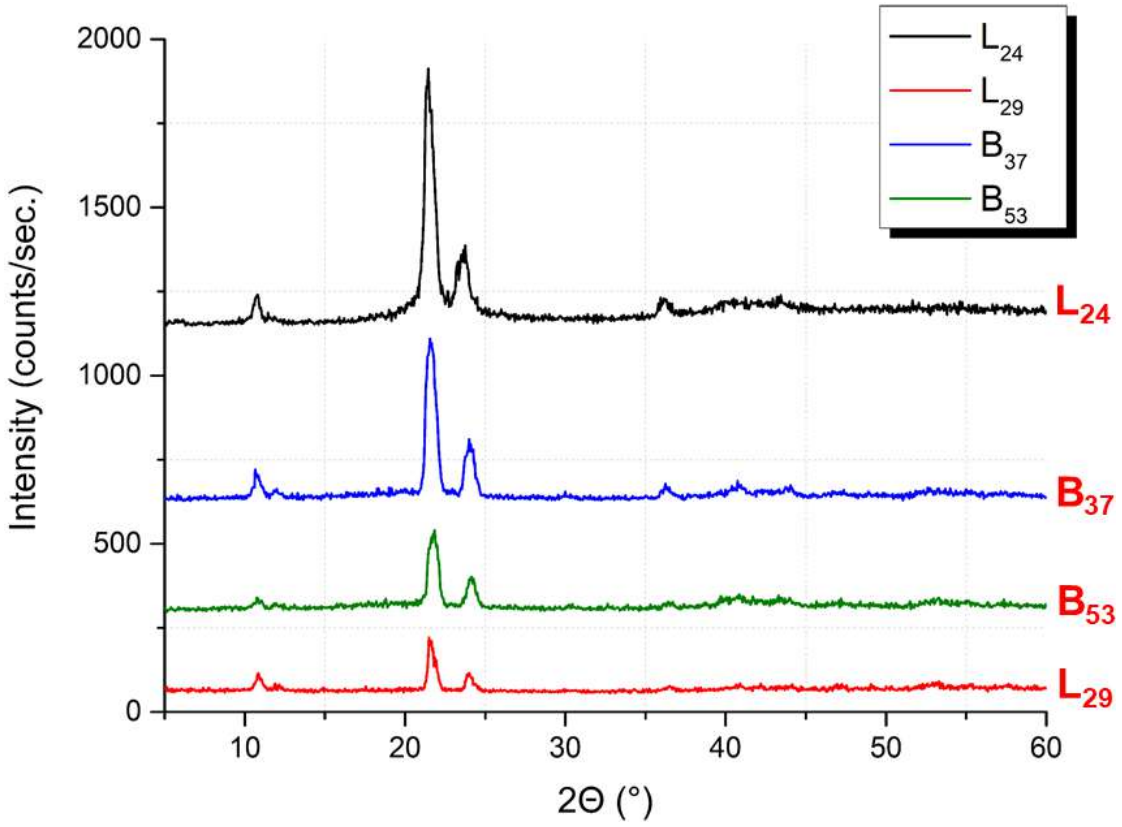


Figure 30 - X-ray diffraction patterns for **$L_x$** and **$B_x$** waxes. From top to bottom: **$L_{24}$**, **$B_{37}$**, **$B_{53}$**, and **$L_{29}$**.

### 4.1.5 Small Angle X-Ray Scattering

Four model oils were analyzed by small-angle X-ray scattering (SAXS) experiments to probe for structural differences. The selected systems were **$L_{29}$**, **$L_{29}$** + **$B_{37}$**, **$L_{29}$** + **$B_{53}$** and **$L_{29}$** + **$L_{24}$**. The composition was set to 7.5 wt%. Blended systems employed 3.75 wt% of each wax. All samples were heated to 80°C for 10 minutes to solubilize all wax crystals prior to the experiment and cooled to 4°C at the rate of 1.0°C/min. Next, 30 minutes of isothermal holding at 4°C was applied and then SAXS measurements started.

When a crystalline material is irradiated by monochromatic X-rays with a specific wavelength, a diffraction pattern can be collected by an area detector which is perpendicular to the beam and located at a fixed distance downstream from the sample [138]. If the samples present a distance between the planes of atoms (d-spacing) in the order of nanometers, the corresponding diffraction pattern appears in small angle range due to the scattering waves interference, which produces distinct spots or rings [139].

Figure 31 exhibits SAXS experimental images of the model oils assessed. All samples presented a diffuse scatter that decreases in intensity radially and (except for **$L_{29}$** + **$B_{53}$** model oil) a diffraction maximum along the meridional and equatorial axis, spread out into an evident arc. According to Tadimalla et al. [140] scattering patterns with these components are characteristic of soft matter. Considering model oil **$L_{29}$** 7.5 wt% as the base material, it is possible to conclude by the images that all additives (i.e., **$B_{37}$**, **$B_{53}$**, and **$L_{24}$** wax) modified the waxy gelled structure. For **$L_{29}$ + $B_{53}$** model oil, the intense diffuse scattering may be related to the fact that **$B_{53}$** wax has a vast carbon number distribution (see section 4.1.3), indicating multiple length scales.

It is well known that the d-spacing is one of the main parameters characterizing a crystalline sample. Based on the primary peak position of the scattering intensity function for **$L_{29}$**, **$L_{29}$** + **$B_{37}$**, and **$L_{29}$** + **$L_{24}$** model oils, shown in Figure 32, the d-spacing was calculated as 4.2 nm, 4.8 nm, and 4.0 nm, respectively. As an illustration, Kané et al. [8] observed a thin lamellar structure, with d-spacing between 1.5 and 3.0 nm for the samples assessed (namely crude oils and model oils), when crystallized by a controlled cooling process. Sample **$L_{29}$** + **$B_{53}$** did not present a clear peak, thus it was unable to calculate this property precisely.

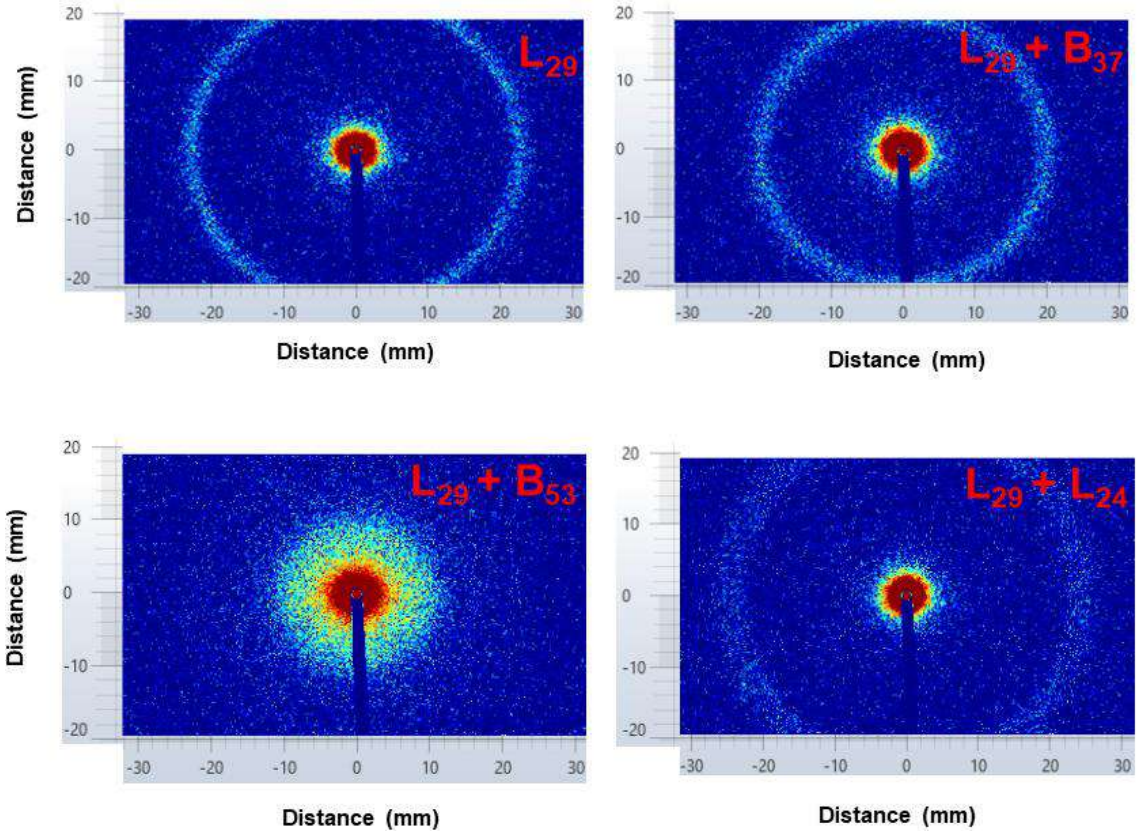


Figure 31 - 2D SAXS images of waxy gels model oils model recorded with a Dectris Eiger R detector. The sample-to-detector distance is about 2.7 m.

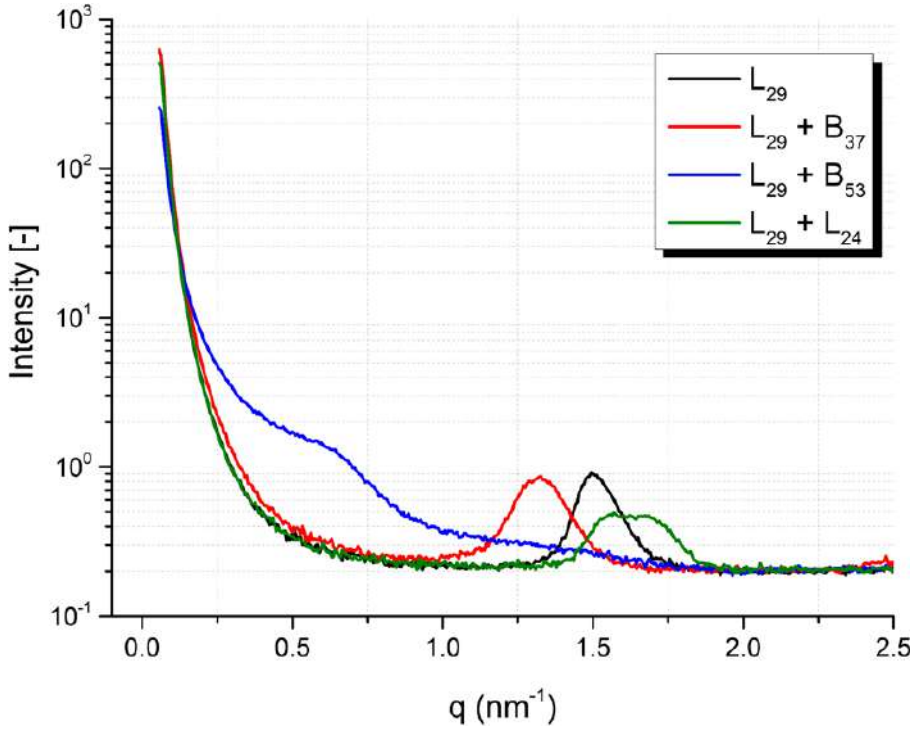


Figure 32 - Distributions of intensities of scattered X-rays for 7.5 wt% model oils at a temperature of 4°C: at small scattering vector amplitude the profiles obtained are virtually superimposed.

Since d-spacing represents the distance between planes of atoms that give rise to diffraction peaks, it is possible to note that the blended system **$L_{29}$** + **$B_{37}$** presented the highest value, probably due to the presence of a branched wax. Also, d-spacing for model oil **$L_{29}$** is about 10 times higher than that calculated by the X-RD data for **$L_{29}$** pure wax (see section 4.1.4). This indicates structural differences after solubilization of the wax in the oil matrix.

Nanometer-scale information on the wax crystals surface can be obtained by SAXS data in Porod's region, where the scattering vector is in the range $2x10^{-4}$ $nm^{-1}$ to $2x10^{-3}$ $nm^{-1}$. The slope of the log-log plot of the SAXS intensity I($q$) as a function of $q$ in this region signifies the smoothness of the crystal surface; the closer the slope is to −4, the smoother the surface of the crystal [141]. The slope obtained for **$L_{29}$**, **$L_{29}$** + **$B_{37}$**, **$L_{29}$** + **$B_{53}$** and **$L_{29}$** + **$L_{24}$** model oils were -3.98, -3.70, -2.95, and -3.59, respectively. This result indicates that the surface of the wax crystals in **$L_{29}$** + **$B_{53}$** waxy gel is less ordered on a nanometer scale. Despite that, as will be presented in section 4.4.3, this model oil presented the highest yield stress among the four systems evaluated here. In this regard, Imai et al. [142] investigated waxy gels consisting of a solid paraffin wax ($C_{32}$) solubilized in different oil matrices. The slope of Porod's plot for gels of $C_{32}$ in caprylic acid triglyceride (TnC) and $C_{32}$ in n-tetradecane were −3.1 and −3.5, respectively. The authors obtained a similar trend, i.e. the higher was the slope the higher was the gel hardness (measured on a Rheoner RE-3305 at 20 °C by inserting the cylindrical plunger into the gel). They also generated high-quality SEM images of dried waxy crystals which clearly showed a smooth surface for $C_{32}$/$C_{14}$ system and a rougher surface with a stratified lamellar structure for the $C_{32}$/TnC gel. It is highly likely that this particular lamellar structure enabled the crystals to enmesh with each other more tightly, and consequently producing a harder gel.

### 4.1.6 Fourier Transform Infrared Spectroscopy

The structure that develops in the gelled oils is dependent on the wax content and also on the presence of other materials that may reduce the crystallinity of the structure. To certify for the presence of possible impurities FTIR experiments were performed and results are exhibited in Figure 33 for waxes and spindle oil. Similar spectra were observed for all samples. The most intense peaks can be found at 3,000 to 2,840 $cm^{-1}$ region which indicates stretching vibrations for C-H bonds of $sp^3$ carbons, i.e. the alkane or cycloalkane chemical signature. Peaks between 1,473 $cm^{-1}$ to 1,461 $cm^{-1}$ and 1,378 $cm^{-1}$ to 1,377 $cm^{-1}$ are due to scissoring molecular vibrations at methylene groups of C-

H bonds and symmetrical bending vibrations for C-H ($sp^3$ carbons), respectively. The peak at 720 $cm^{-1}$ is associated with straight chain methylene at least four units long [143], [144]. Thus, none impurity seems to be present in waxes and oil samples. Also, the FTIR spectrum for spindle oil is identical to the commercial available nujol™ paraffinic oil [143], suggesting that spindle is a paraffinic oil.

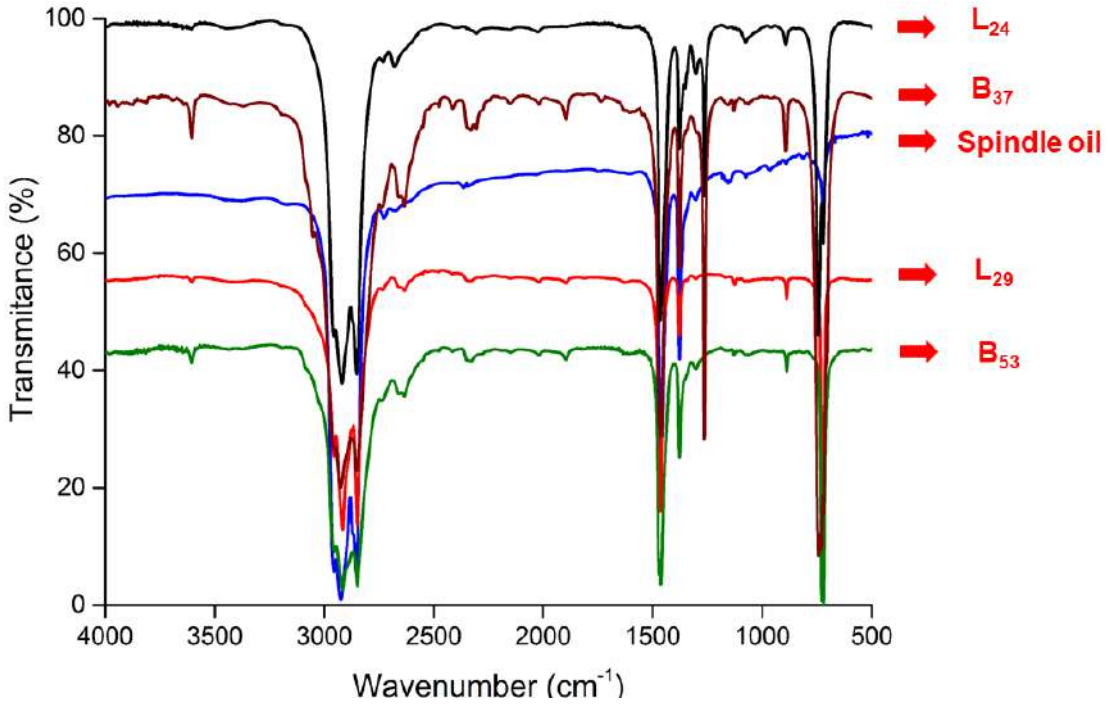


Figure 33 - FTIR spectra for spindle oil, $\mathbf{L_x}$, and $\mathbf{B_x}$ waxes.

### 4.1.7 Rheology of Spindle Oil

The rheological behavior of spindle oil was investigated since it is the common solvent for all model oils. Figure 34 exhibits the flow curve and the viscosity curve at two representative temperatures, with a shear rate ranging from 0.1 $s^{-1}$ to 1,000 $s^{-1}$ (10 points per decade; each point had 80 seconds of equilibration and 40 seconds averaging). The steady-state values of viscosity and the straight lines for shear stress indicate a simply Newtonian fluid. The oil viscosity is $7.29 \times 10^{-3}$ Pa.s at 50°C and $4.06 \times 10^{-2}$ Pa.s at 4°C. Comparatively, at 50°C, the oil is 26 times more viscous than water and at 4°C, it is 13 times more viscous.

The fluid viscosity is determined both by collision among particles and by the force fields which determines interactions among molecules. The theoretical description of viscosity is therefore quite complex. Nonetheless, it is common knowledge that viscosity varies with temperature, generally becoming smaller as the temperature is elevated. This trend

occurs because the increased kinetic motion at higher temperatures promotes the breaking of intermolecular bonds between adjacent layers [145]. Figure 35 exhibits the viscosity variation of spindle oil during a cooling program from 50°C to 4°C at 1.0°C/min and a shear rate of 1.6 $s^{-1}$.

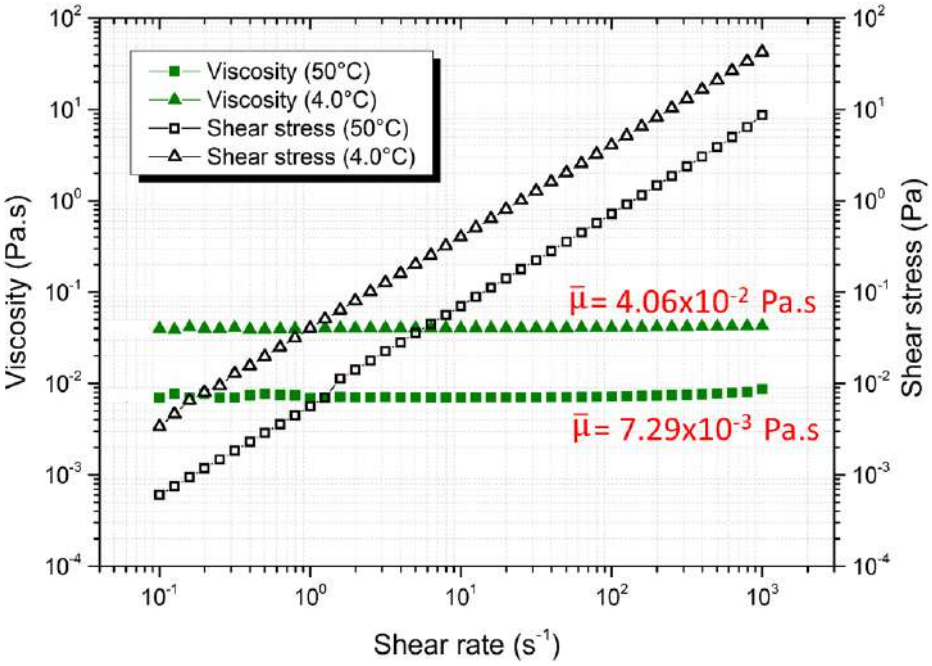


Figure 34 - Flow curve and viscosity curve for spindle oil at 50°C and 4°C (sweep from 0.1 to 1,000 s-1 with 80 seconds of equilibration and 40 seconds averaging).

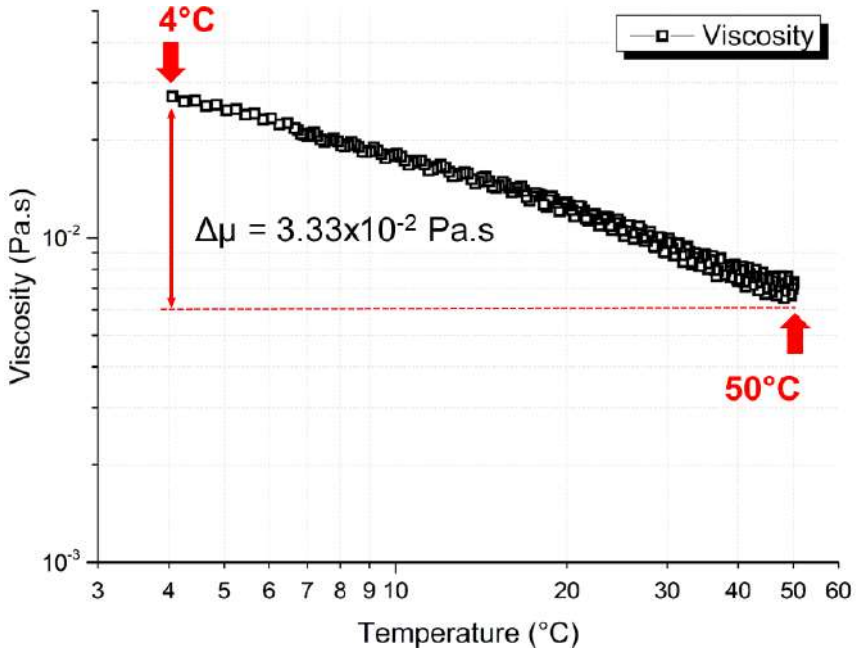


Figure 35 - The viscosity of spindle: due to cooling process the viscosity increased 5.6x from an initial temperature of 50°C to 4°C (cooling rate of 1.0°C/min, shear rate 1.6 $s^{-1}$).

According to Haj-Kacem et al. [146], the temperature dependence of viscosity can be fitted frequently with the Arrhenius-type equation for numerous Newtonian fluids. For most of the organic solvents, the logarithm of viscosity deviates slightly to the linearity against the reciprocal of absolute temperature (1/T). In fact, the data from spindle oil plotted as the natural logarithm of viscosity (in Pa.s) against the reciprocal of temperature (in $K^{-1}$) lies on a straight line with $R^2 = 0.96$.

### 4.1.8 Waxes Morphology

Optical microscopy was employed to investigate the size and shape of waxy crystals precipitated from model oils. The composition was set to 7.5 wt% for single and blended systems. The polarized light was the adopted technique and samples were cooled from 50°C to 4°C at 1.0°C/min. The images were obtained after 15 minutes at the final temperature and some interesting aspects of wax crystal morphologies can be devised in Figure 36.

The morphology and structure of the wax crystals play an important role in the flow properties of waxy crude oils. Clusters of self-assembled crystals might form an aggregate in different ways leading to a stronger or weaker gel [64]. The network of interacting waxy crystals showed complex morphology and according to Singh et al. [13], it is due to the flocculation of orthorhombic wax crystallites, creating a highly porous and rigid structure full of entrapped oil. In Figure 36 all systems presented needle-like crystals amassed into clusters of varying sizes and patterns. For single model oils, the highest yield stress was obtained with **$L_{29}$** wax, as will be discussed in section 4.4.2. This was achieved in the image with fewer unoccupied space, despite the highest crystal size and aspect ratio being achieved by **$L_{24}$** wax. Although, this same trend is not valid for blended systems. **$L_{24}$** + **$L_{29}$** model oil presented the largest crystals (25.8 µm) whilst **$B_{37}$** + **$B_{53}$** the smallest (9.04 µm). The aspect ratio was also the smallest for **$B_{37}$** + **$B_{53}$**, indicating a more rounded shape. Indeed, is clear the presence of very tiny crystals for this system.

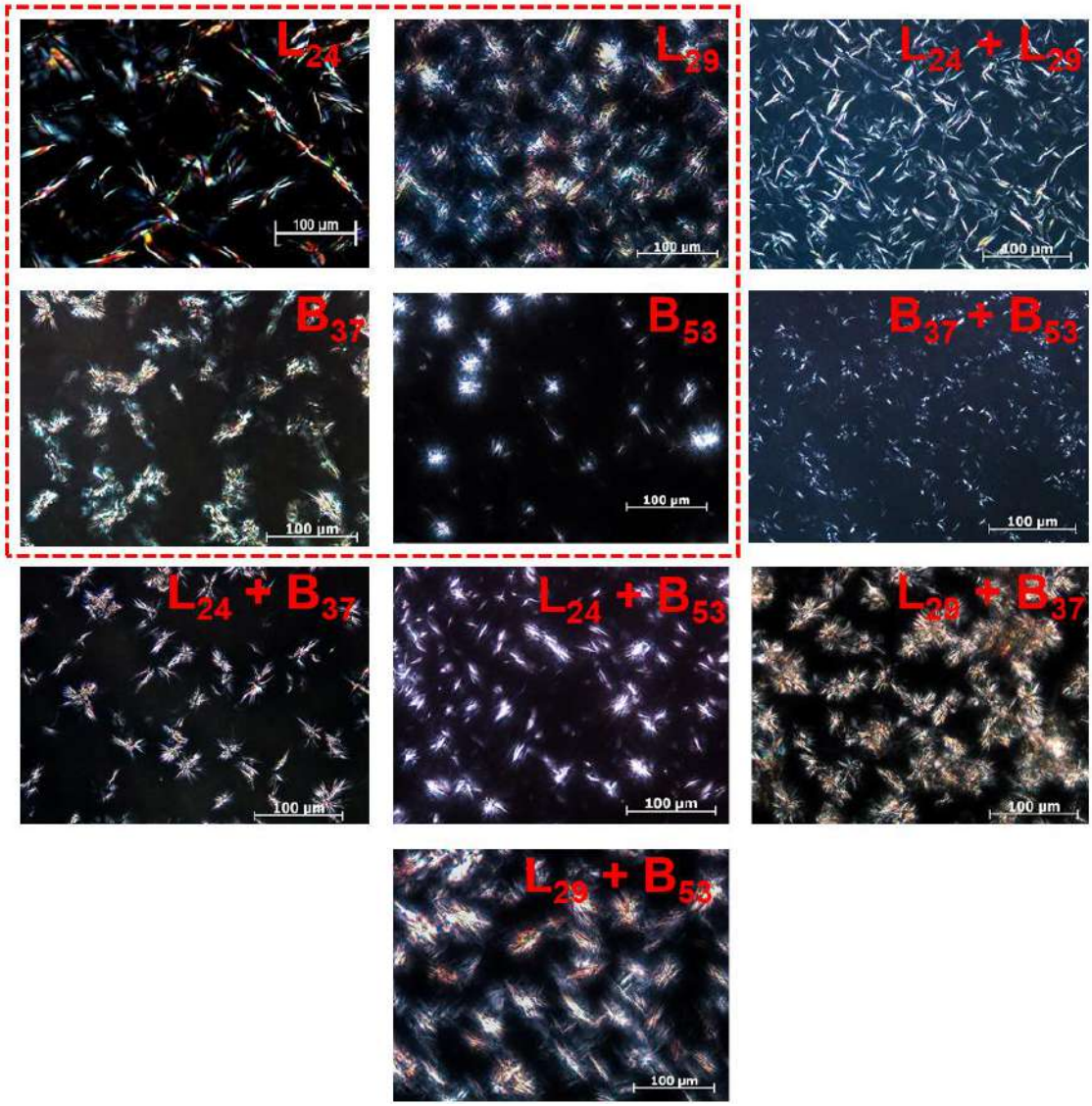


Figure 36 - Microscopy images of precipitated wax crystals from freshly prepared model oils cooled from 50°C to 4°C at 1.0°C/min (200x magnification). Single systems are highlighted.

Table 6 exhibits the average length and aspect ratio of waxy crystals from different model oils. According to Zaky and Mohamed [82], macrocrystalline waxes appear at large and loose needle form. Meanwhile, the microcrystalline waxes crystallize in needle form despite smaller in size. Paso et al. [2] obtained crystal lengths in the range of 10-20 µm for model fluids consisting of n-paraffin waxes dissolved in mineral oil which is in agreement with the lengths obtained in this study. We note that the micrometer-sized wax crystals formed, and their marked tendency to associate into dense crystalline masses, together with the low concentration of wax solids required for gelation, provide important clues that waxy gels belong to the broad family of attractive colloidal gels.

Table 6 - Morphological features for wax crystals of $\mathbf{L_x}$ and $\mathbf{B_x}$ model oils

| Model oil | Average length (μm) | Aspect ratio |
|---|---|---|
| $\mathbf{L_{24}}$ | 72.3 | 9.09 |
| $\mathbf{L_{29}}$ | 24.0 | 12.5 |
| $\mathbf{B_{37}}$ | 12.5 | 7.33 |
| $\mathbf{B_{53}}$ | ---* | ---* |
| $\mathbf{L_{24}}$ + $\mathbf{L_{29}}$ | 25.8 | 9.09 |
| $\mathbf{B_{37}}$ + $\mathbf{B_{53}}$ | 9.04 | 4.54 |
| $\mathbf{L_{24}}$ + $\mathbf{B_{37}}$ | 18.9 | 5.55 |
| $\mathbf{L_{24}}$ + $\mathbf{B_{53}}$ | 17.2 | 5.88 |
| $\mathbf{L_{29}}$ + $\mathbf{B_{37}}$ | 14.8 | 7.69 |
| $\mathbf{L_{29}}$ + $\mathbf{B_{53}}$ | ---* | ---* |

*at these images it was not possible to precisely devise isolated crystals

Despite the efforts to devise useful patterns from microscopic images, quantitative characterization of their morphology and structure is difficult, due to the high complexity and irregularity of wax crystal microstructures. In view of the literature, as far as the author concern, attempts to bring out a clear idea on the type of the crystals naturally occurring in crude oils and relate it directly to yield stress via morphological aspects were not successful.

### 4.1.9 Conclusions

Section 4.1 encompassed the results from the physicochemical characterization of spindle oil, $\mathbf{L_x}$ $\mathbf{B_x}$ waxes and distinct model oil compositions. Several experimental techniques were employed with this purpose: DSC, $^{13}$C-NMR, GC-FID, X-RD, FT-IR, SAXS, rheology and optical microscopy.

The combined results indicate that $\mathbf{L_x}$ is macrocrystalline and predominately linear waxes, whereas $\mathbf{B_x}$ is microcrystalline branched wax with a substantial presence of isoalkanes and/or cycloalkanes in its structures. Among the branched waxes, $\mathbf{B_{37}}$ is smaller and present more ramification points (6.36% of carbons, on a molar basis, are due to branching) compared to $\mathbf{B_{53}}$, which has 4.41% of tertiary carbons. $\mathbf{L_{24}}$ and $\mathbf{L_{29}}$, regarded as predominately linear waxes, has 10.4 and 15.2 wt% due to branched carbons, according to GC-FID experiments, although it was not detected by $^{13}$C-NMR. This number is around 33 wt% for $\mathbf{B_x}$ waxes. Also, all the waxes showed X-RD peaks

with similar intensities at the low angle region of 2Θ ~ 12°, providing evidence for lamellar packing.

The differences in the scattering pattern in the SAXS experiments for the model oils, $\mathbf{L_{29}}$, $\mathbf{L_{29}}$ + $\mathbf{B_{37}}$, $\mathbf{L_{29}}$ + $\mathbf{B_{53}}$ and $\mathbf{L_{29}}$ + $\mathbf{L_{24}}$ indicate structural differences. The highest value of the slope of Porod's plot for $\mathbf{L_{29}}$ + $\mathbf{B_{53}}$ is correlated to its rough surface [142]. The d-spacing values for $\mathbf{L_{29}}$, $\mathbf{L_{29}}$ + $\mathbf{B_{37}}$, and $\mathbf{L_{29}}$ + $\mathbf{L_{24}}$ model oils were 4.2 nm, 4.8 nm, and 4.0 nm, respectively. The branched $\mathbf{B_{37}}$ wax is likely to be responsible for the highest spacing between successive atomic planes.

The FTIR results indicated none impurity present in waxes and oil samples. Also, spindle oil has a spectrum identical to the commercial available nujol™ paraffinic oil suggesting that spindle is also a paraffinic oil.

The rheology of spindle oil was obtained, and the results indicated Newtonian fluid behavior in the range of temperatures assessed at rheological tests (50°C to 4°C). Also, the Arrhenius-type dependence of viscosity with temperature was detected. Through the optical microscopy, it was possible to observe differences in wax morphology for different model oil compositions, although the technique has some limitations. First, the microscopic images could not display a complete 3D microstructure. In addition, the images at temperatures below gelation point often cannot show a clear network structure. Thus, a more complete and unequivocal characterization is needed in order to unveil possible relations between images and rheological properties.

## 4.2 Apparent Wall Slip Phenomenon

In the flow assurance context, yield stress plays a major role. Thus, it is vital to obtain correct estimations of this property. The idea of yield stress was introduced in the 1920s by the pioneering work of Bingham, and since then, its concept and definition have been continuously debated, especially after Barnes and Walters [133] challenged its existence in their article “The Yield Stress Myth?”. Although, the question of whether yield stress exists as a real phenomenon has little relevance in engineering since for process timescales such as production, transportation, and storage of waxy crude oil the yield stress is a practical reality.

Apparent wall slip, on the other hand, is one of the main challenges reported in the rheological characterization of structured materials. In this investigation, the viscoelastic properties and flow characteristics of gels consisting of $\mathbf{L_{29}}$ macrocrystalline wax 3.0 wt% and 7.5 wt% were assessed and the phenomenon of apparent wall slip was investigated. The quality of rheological data obtained with smooth and grooved geometries was also compared and there is evidence that apparent wall slip plays a major role in this regard. The gels were formed *in situ* in a stress-controlled rheometer and several rheological properties were obtained. Seven different geometry configurations with varying roughness, including parallel plates, concentric cylinders, and vane were used. Results from oscillatory, creep, and steady-state rheology tests were obtained. An important assumption for all tests is that a continuous fluid layer is always in contact with the wall, thus the no-slip boundary conditions are not violated. However, prior to discussing these results, it is convenient to consider the importance of aging time step in the rheological experiments performed and also the yield stress frequency dependence for oscillatory experiments.

### 4.2.1 Aging Time

Rheological measurements performed after a suitable aging time are less subject to the system structural variations over time, providing more reproducible results in terms of yield stress [53]. Thus, the purpose of this step is to provide a sufficient time by which all the samples achieve similar levels of structuring, enhancing the repeatability of the tests (considering samples departing from the same initial conditions). In this regard, in the case of waxy crude oils, the increase of storage modulus is attributed to the appearance and expansion of a crystalline network, composed mainly by waxy crystals [147]. Therefore, the plot of storage modulus as a function of time can indicate whether or not

the system has reached structural equilibrium. In this investigation an isothermal holding time of 30 minutes at 4°C, also named as aging time, was adopted prior to yield stress evaluation (see details in section 3.3.1).

The particular choice for 30 minutes as aging time relies on the fact that, for the two compositions investigated, the average value of storage modulus increases relatively slowly along this period, considering that aging time is a step applied after cooling the samples until 4°C. To illustrate this fact, G' was measured for a **$L_{29}$** 3.0 wt% system during two subsequent steps: oscillatory cooling from 50°C to 4°C (dT/dt = 1.0°C/min, oscillatory stress = 0.1 Pa, frequency = 1 Hz) followed by a time sweep step of 100 minutes. Before temperature reaches 23°C the major part of the wax crystals were completely solubilized in the oil matrix, reflecting in very low values of G' ($10^{-5}$ Pa to $10^{-4}$ Pa), which indicates that no structured material is present in the sample. Then, a sharp increase in G' was observed, indicating that 23°C is the temperature from which the precipitated wax crystals is able to build a spanning waxy network that ultimately will lead to fluid gelation. As cooling proceeds, the abrupt change in storage modulus vanishes at a temperature of 10°C, i.e., before the system reaches the final cooling temperature. The "aging" begins when the temperature reaches 4°C. At this point, G' has increased about nine orders of magnitude comparing to its value in the initial temperature, at 50°C. Although, there is not a significant change during the aging. In fact, it seems that G' oscillates around an equilibrium value, indicating that the structure build-up process is concentrated before aging. Considering 100 minutes of aging, the average value of G' is $2.2 \times 10^4$ Pa, only 16% higher than 30 minutes of aging. Thus, 30 minutes was adopted as a suitable aging time. Figure 37 summarizes the above description.

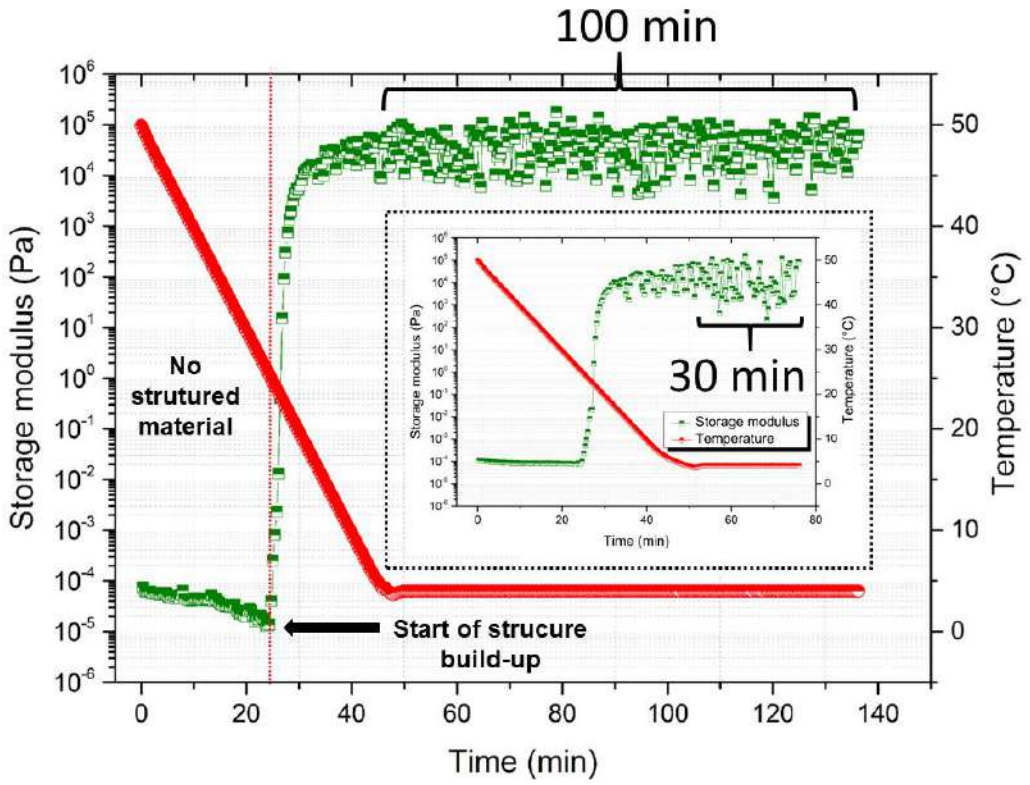


Figure 37 - Oscillatory cooling step from 50°C to 4°C of 3.0 wt% **$L_{29}$** wax (dT/dt = 1.0°C/min) followed by a time sweep step of 100 minutes. In detail, the same rheological procedure is depicted, although with a time sweep of 30 minutes.

### 4.2.2 Yield Stress Frequency Dependency

One important issue to consider with respect to using oscillatory rheology to measure yield stresses is the frequency effect. To evaluate the influence of this parameter it was performed a series of yield stress measurements with **$L_{29}$** wax 3.0 wt% (details in section 3.3.1) and frequencies of 0.1 Hz, 0.5 Hz, and 1 Hz. GC + GC geometry was used in these tests. The yield stress was found to vary less than the uncertainty for the range of frequencies assessed, with values of 272 ± 18 Pa, 262 ± 32 Pa and 259 ± 26 Pa, respectively. Waals et al. [98] obtained similar results for the yield stress of colloidal silica gels when tested frequencies of 0.1 rad/s, 1 rad/s, and 5 rad/s (0.016 Hz, 0.16 Hz, and 0.79 Hz, respectively) were employed. Thus, in the face of these results, the frequency of 1 Hz was selected for all logarithmic stress sweep tests in this Thesis.

In addition, frequency sweep tests indicate that the analyzed material is a true gel in low-frequency values. These tests were performed by changing the step 4[a] (see section 3.3.1) for a frequency sweep from 0.1 to 10 Hz and strain levels at 0.1% or 1%. Figure 38 summarizes the results. It is possible to observe that in the range of 0.1 to 1 Hz

storage modulus is higher than loss modulus and the values are similar regardless of the percentage strain. Nonetheless, for frequencies higher than 2 Hz there is a change in the G' increasing rate for the strain of 0.1% and a shift from elastic to viscous behavior for the strain of 1%. The yield stress values obtained in the previous experiments is also depicted in Figure 38.

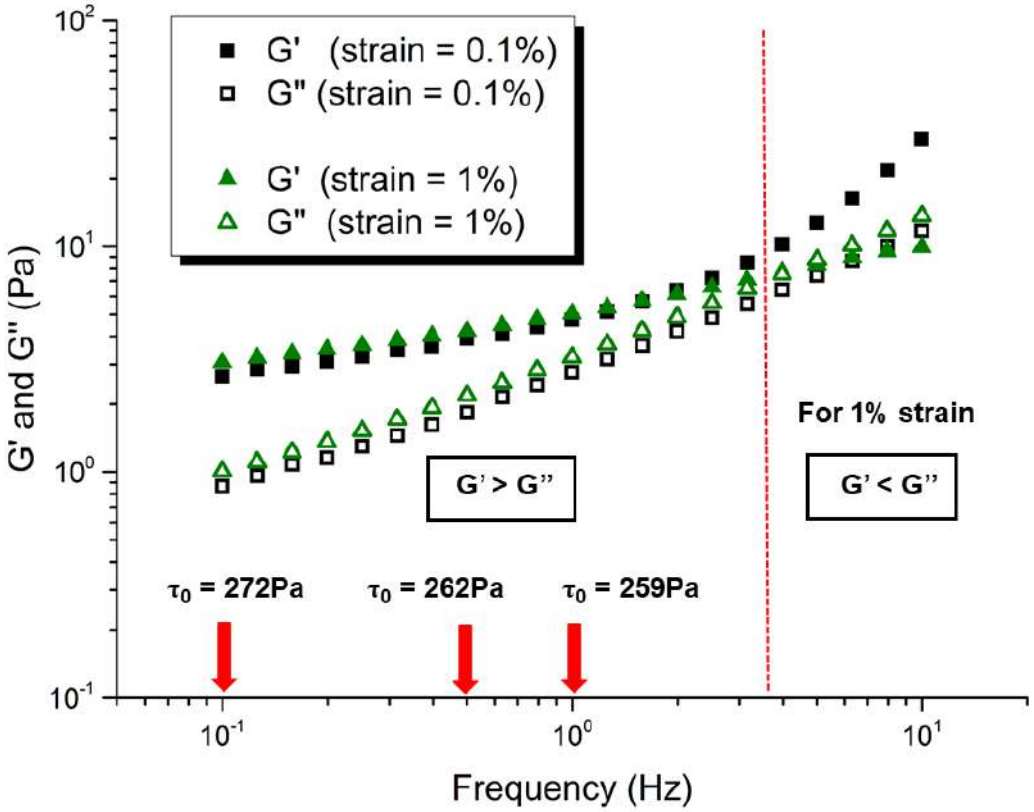


Figure 38 - Frequency sweep tests for **$L_{29}$** 3.0 wt% waxy gels at 4.0°C in the range of 0.1 to 10 Hz and different strain values (0.1% and 1%).

### 4.2.3 Viscoelastic Properties and Apparent Wall Slip

Viscoelastic properties were obtained from the oscillatory rheological experiments for **$L_{29}$** wax 3.0 wt% and 7.5 wt% with seven different geometry assemblies. The abbreviation and description of each geometry are given in Table 7 (see also Figure 17):

Table 7 - Geometries used in the apparent wall slip investigation

| Abbreviation | Description |
|---|---|
| **SPP** | **S**mooth **P**arallel **P**late (with smooth Peltier plate) |
| **GPP** | **G**rooved **P**arallel **P**late (with smooth Peltier plate) |
| **SC + SC** | **S**mooth **C**ylinder + **S**mooth **C**up |
| **SC + GC** | **S**mooth **C**ylinder + **G**rooved **C**up |
| **GC + SC** | **G**rooved **C**ylinder + **S**mooth **C**up |
| **GC + GC** | **G**rooved **C**ylinder + **G**rooved **C**up |
| **V + GC** | **V**ane (4 Blades) + **G**rooved **C**up |

The results of yield stress, relative percentage error of yield stress ($\tau_0$ RPE) and storage modulus at the linear viscoelastic region ($G'_{LVR}$), measured by different geometry configurations, are exhibited in Table 8. When the V+GC, GC+SC and GC+GC geometries are used, it is assumed that the flow is the same as the one that occurs in the smooth Couette geometry, i.e. the material between blades/grooves moves rigidly together with the solid surfaces.

Table 8 - Yield stress, $\tau_0$ RPE* and $G'_{LVR}$ for two different model oils composition

| **$L_{29}$** 3.0 wt% model oils | | | |
|---|---|---|---|
| Geometry | $\tau_0$ (Pa) | $\tau_0$ RPE* (%) | $G'_{LVR}$ (kPa) |
| SPP | 40 ± 15 | 37.5 | 13 ± 1.4 |
| SC+SC | 40 ± 8 | 20 | 74 ± 7.1 |
| SC+GC | 42 ± 10 | 23.8 | 67 ± 2.0 |
| GC+SC | 64 ± 25 | 39 | 86 ± 9.8 |
| GPP | 106 ± 34 | 32.1 | 25 ± 1.9 |
| GC+GC | 259 ± 26 | 10 | 109 ± 1.3 |
| V+GC | 259 ± 24 | 10.8 | 61 ± 1.3 |
| **$L_{29}$** 7.5 wt% model oils | | | |
| SC+SC | 488 ± 102 | 20.1 | 259 ± 23 |
| SC+GC | 696 ± 130 | 18.7 | 254 ± 8.5 |
| GC+SC | 1,454 ± 210 | 14.4 | 523 ± 66 |
| GC+GC | 2,700 ± 252 | 9.33 | 682 ± 37 |

*$\tau_0$ RPE was defined as the yield stress uncertainty (provided by the Student's t-test) divided by its average value

For the 3.0 wt% system, the yield stress captured by geometries with smooth moving parts SPP, SC+SC, and SC+GC had an excellent reproducibility (~ 41 Pa).

Nevertheless, this value is 84% lower than those obtained for the all-grooved geometries (259 Pa) GC+GC and V+GC, i.e., the geometries where the moving and stationary parts are rugged. This result clearly indicates the presence of apparent wall slip in the measurements performed with SPP, SC+SC, and SC+GC geometries. According to Lee et al. [117], the restart of a pipeline blocked with gelled oil may result from the breakdown of the gel structure itself (cohesive failure), or it may occur because of the breakage at the pipe–gel interface (adhesive failure). The cohesive yielding of the gel occurs when the applied stress exceeds the mechanical strength of the wax-oil gel structure, thus this process occurs without wall slippage. Since it is very difficult to predict the failure mechanism in a real production scenario the estimative of yield stress in terms of cohesive failure is extremely relevant because it's more conservative. For the all-grooved geometries, besides the excellent reproducibility, there is a clear gain in terms of repeatability as the average of $\tau_0$ RPE for GC+GC and V+GC is 10.4%, comparing to 27.1% for the geometries with smooth moving parts SPP, SC+SC, and SC+GC.

Another worth noting aspect emerges from the comparison of yield stress obtained with smooth parallel plates, SPP, and grooved parallel plates, GPP. In this case, from SPP to GPP there was an increase in the roughness of the geometry moving part, whereas the stationary part remains smooth. Nevertheless, an increase of 165% in the yield stress was detected with GPP, as can be seen in Table 8. Identical reasoning can be applied to the smooth cylinder + smooth cup, SC+SC, and grooved cylinder + smooth cup, GC+SC, since it was observed the same increasing trend. This indicates that the slippage effects were mitigated by introducing grooved moving surfaces. However, if we compare the yield stress measured with GPP (106 Pa) to the yield stress from all-grooved geometries (259 Pa), an increase of 144% is obtained. When the same comparison is made for GC+SC (64 Pa) the increase is of 300%. Therefore, it is clear that the trade between a smooth to a grooved moving part mitigates but do not eliminate apparent wall slip, as slippage still occurr whenever smooth surfaces are present. This may seem a trivial observation, yet as far as the author's concern, there is no general theory enabling one to predict the exact conditions and extent under which apparent wall slip occurs. For example, Buscall et al. [112] demonstrated that concentrated colloidal dispersion weakly flocculated (specifically nonaqueous polymer latex dispersed in a mixture of high-boiling hydrocarbons) show slip flow when sheared between smooth concentric cylinders. Although, no apparent slip occurred at the outer cylinder. Comparisons of flow curves obtained using smooth and roughened cylinders showed that slip only occurs at the inner cylinder, and also that bulk flow is re-established at higher stresses where the dispersions start to shear thin. However, Barnes [148]

suggested as a way of coping with the depletion problem, the addition of a slender gauze basket inserted inside the outer cylinder to eliminate apparent slip at the outer wall as slippage effects were observed in rheological measurements of some structured materials using the vane-in-cup geometry.

Taking into account the results for yield stress obtained with SC+GC (42 Pa), GC+SC (64 Pa), and GPP (106 Pa), it is possible to infer that slippage phenomenon is more intense when the moving part of the geometry is smooth. Finally, as the yield stress captured by GC+SC and GPP is an intermediate value between all-smooth and all-grooved geometries, it clearly indicates that apparent wall slip is not fully remediated by serrated plates or grooved cylinders unless the roughness of the stationary part is also increased. Figure 39 summarizes these findings for **$L_{29}$** 3.0 wt% system.

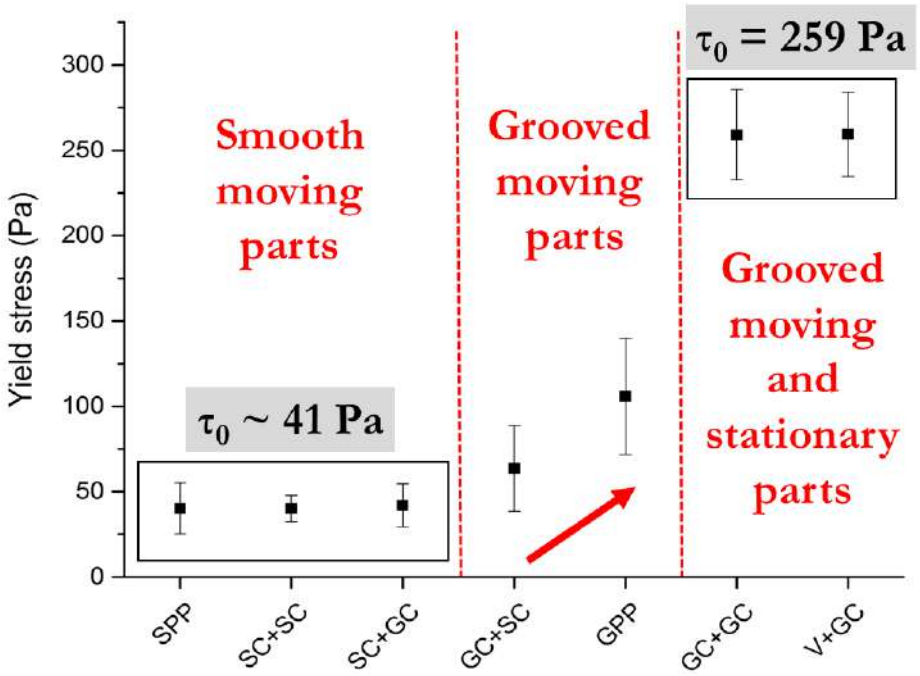


Figure 39 - Yield stress results for model oil composed of 3.0 wt% **$L_{29}$** wax with seven different geometry assemblies.

Regarding 7.5 wt% model oils, four representative geometries were employed, namely SC+SC (all-smooth), SC+GC with a smooth moving part + grooved stationary part, GC+SC with a grooved moving part + smooth stationary part and GC+GC (all-grooved). Analyzing Table 8, the same reasoning for 3.0 wt% systems can be applied here regarding the yield stress results. For example, if one compares the values for SC+SC geometry (488 Pa) to GC+GC (2,700 Pa), there is an 82% decrease when the all-smooth geometry is used. It is approximately the same decrease in yield stress calculated for 3.0 wt% systems, indicating in this case that apparent wall slip is not composition-

dependent (at least in the range assessed) and affects systems in the same extent when all-smooth and all-grooved geometries are compared. The repeatability is also enhanced for GC+GC geometry ($\tau_0$ RPE 9.33%), compared to SC+SC ($\tau_0$ RPE 20.1%).

In addition, it is observed intermediate values between the lowest and highest yield stress. From SC+GC (696 Pa) to GC+SC (1,454 Pa) there was an increase in yield stress, once again indicating that he slippage phenomenon is more intense when the moving piece of the geometry is smooth. Figure 40 summarizes these findings, highlighting the same qualitative behavior of yield stress for both compositions. It is worth noting that yield stress strongly depends on the total amount of wax in the oil [77], [149]. Interestingly, in this investigation the yield stress for 7.5 wt% model oils are about 10 times higher when compared to 3.0 wt%, thus 10-fold increase was observed when the amount of wax increased by 2.5x.

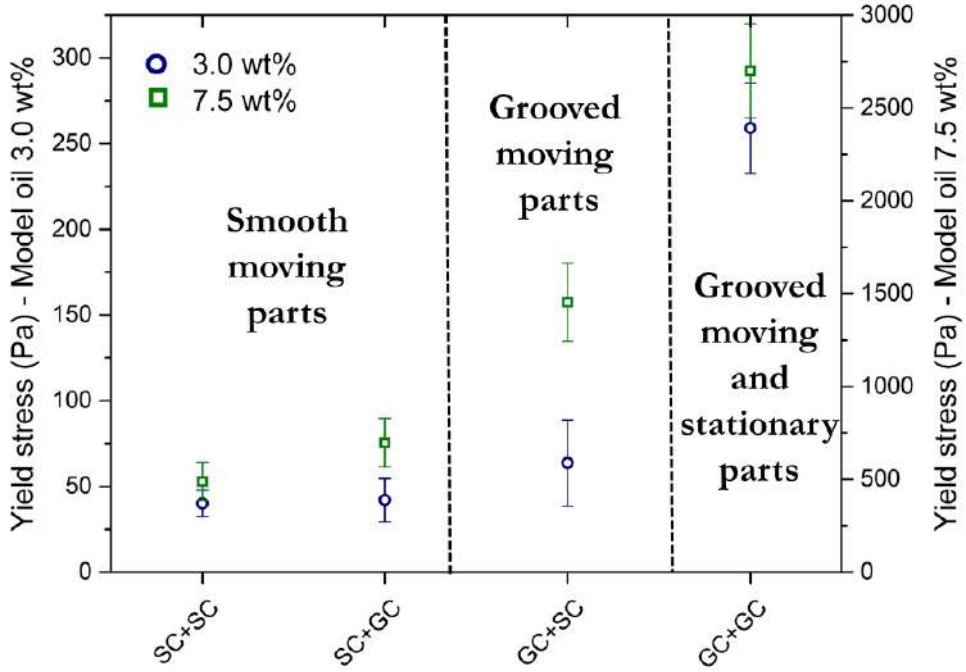


Figure 40 - Yield stress results for model oils with 3.0 wt% **$L_{29}$** wax (blue circles) and 7.5 wt% (green squares) measured with four representative geometries.

In this investigation yield stress is certainly a suitable metric for apparent wall slip quantification. Nonetheless, the storage modulus was also evaluated. Despite having the same unit, these two quantities are not necessarily correlated. However, in the particular case of waxy gels, both properties arise from the same phenomenon, that is, the oil gelation. Thus, in principle, one could expect similar results.

The analysis was based on the average of storage modulus in the linear viscoelastic region ($G'_{LVR}$) and values are exhibited in Table 8. When concentric cylinder geometries

are compared (SC+SC, SC+GC, GC+SC, and GC+GC) the $G'_{LVR}$ behavior is a clear function of geometry the roughness, regardless of the system composition. Thus, the same trend observed for yield stress is followed here: (1) when a geometry with a smooth moving part is employed, $G'_{LVR}$ has the lowest value; (2) an intermediate value is achieved when a grooved moving part is used with a smooth stationary part; (3) the highest $G'_{LVR}$ is obtained for the all-grooved geometry. In addition, when all-smooth SC+SC geometry is compared to all-grooved GC+GC, the decrease in $G'_{LVR}$ is of 32% for 3.0 wt% and 62% for 7.5 wt% systems. Thus, apparent wall slip has a clear influence in the storage modulus since it is underestimated when measured by geometries with smooth parts. Figure 41 exhibits these findings. Also one may note similar qualitative behavior when comparing Figure 39 and Figure 40.

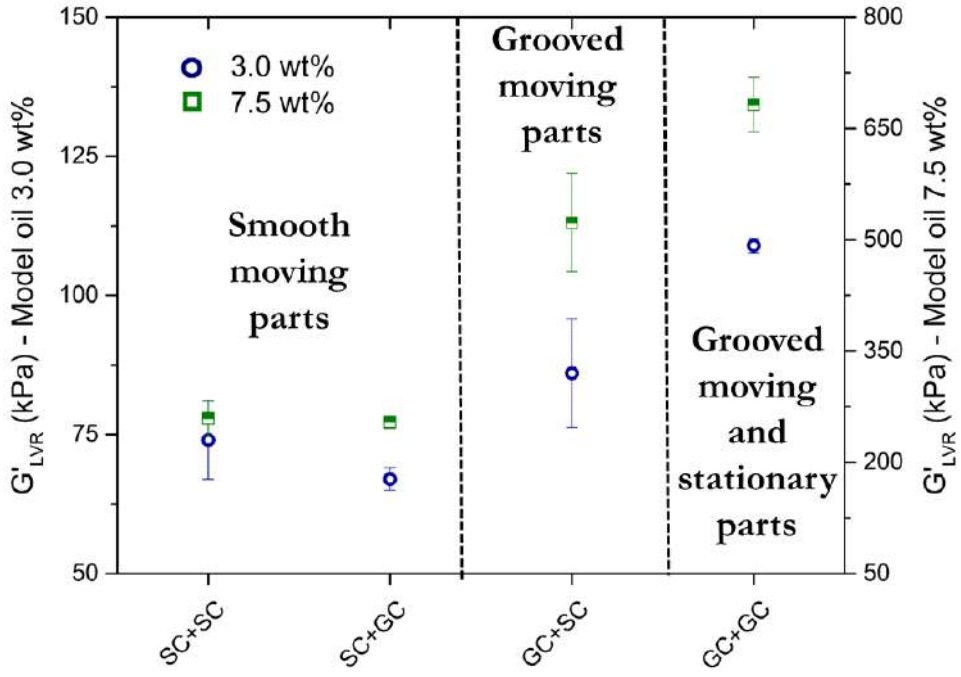


Figure 41 - Storage modulus in the linear viscoelastic region ($G'_{LVR}$) for 3.0 wt% model oils (blue circles) and 7.5 wt% (green squares) measured with four representative geometries.

Regarding different fracturing conditions of the waxy gels, Figure 42 provides data for a meaningful analysis. It exhibits the results for the logarithmic stress sweep step of 3.0 wt% systems obtained with seven different geometries (step [4a], section 2.2). The storage modulus (G'), loss modulus (G'') and %strain were plotted as a function of the oscillatory stress. From the images, one can clearly observe that after G' and G'' crossing point the storage modulus still being captured for all geometries, except for the all-grooved GC+GC and V+GC. Also, there is a kink in the %strain curve for all geometries, once again, except for the all-grooved GC+GC and V+GC. Certainly the definitions of G'

and G'' are only valid at the linear viscoelastic region. However, the fact that storage modulus is still being captured after G' and G'' crossing point indicates the presence of slippage effects, since only geometries with a smooth part were able to capture it. Thus, the fracture of the gel due to the increasing oscillatory stress is captured more accurately by the all-grooved geometries GC+GC and V+GC, reflecting in a %strain curve very sharp near the breakage point and without kinks after breakage. This fact indicates cohesive failure mechanism, i.e., the gelled structure was in fact fractured, instead of sliding on the geometry walls. In addition, the storage modulus vanishes (as expected) after the breakage.

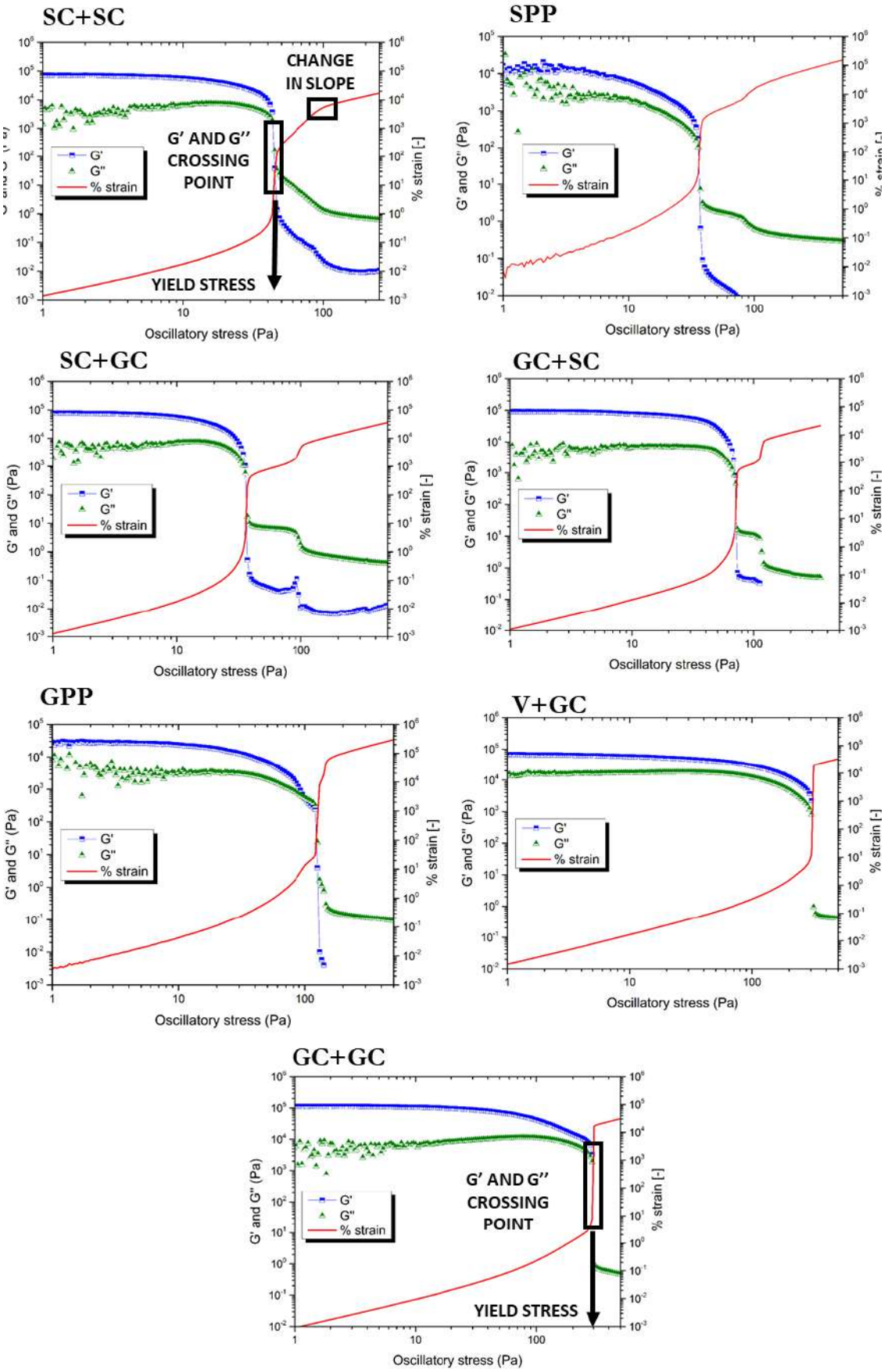


Figure 42 - Logarithmic stress sweep (4°C and 1 Hz, from 1 Pa to 500 Pa) for **$L_{29}$** 3.0 wt% model oil performed with seven different geometries assemblies. It is possible to

observe that after G' and G'' crossing point the storage modulus still is captured for all geometries, except for the all-grooved GC+GC and V+GC. Also, there is a kink in the %strain curve for all geometries except for GC+GC and V+GC.

Similar behavior was reported by Walls et al. [98], when investigating the apparent wall slip of colloidal gels and verified a second plateau for G' at oscillatory rheological tests with smooth surfaces, which was absent with grooved geometry. The authors presumed that at moderately high stress amplitudes that correspond to the second G' plateau, apparent wall slip may occur due to a thin layer of particle-lean fluid near the walls deforming more than the bulk of the material. At sufficiently large stress amplitudes the gel structure is entirely disrupted and the bulk material begins to flow and approaches the behavior observed with grooved geometry assessed (serrated parallel plates). An alternative explanation brought up by the authors for the presence of two G' plateaus was the existence of two types of microstructures in the colloidal gels. The disruption of each structure would correspond to the catastrophic drop in G' (this is seen in Figure 42 for SC+SC and SC+GC geometry). However, if such a scenario existed, the dual plateau and drop-off behavior would have remained with the use of grooved geometries.

Another perspective is given by Barnes [115]. According to the author, for materials as attractive colloids, when a smooth surface is present, apparent wall slip occurs for stress levels lower than the yield stress. When yield stress is exceeded, the slippage tends to become negligible. Considering this reasoning and assuming that yield stress for the 3.0 wt% systems is correctly measured with all-grooved geometries (259 Pa, Table 8), once more we came to the conclusion that slippage effects are present for geometries with smooth parts (SC+SC, SC+GC, GC+SC, SPP, and GPP), even after G' and G'' crossing point, as can be observed in Figure 42. This reflects in kinks in %strain curves and storage modulus extended capturing.

Lastly, if one considers the storage modulus, the higher the extension of G' plateau, the higher is the yield stress. This value is a clear function of geometry surface roughness. Nonetheless, for the all-grooved geometries GC+GC and V+GC, the data scattering is less pronounced, which indicates a higher quality measurement. Also, the repeatability is clearly improved as can be seen in the detail of Figure 43. For example, the standard deviation of $G'_{LVR}$ is 18.9 kPa for SC+SC geometry and 3.4 kPa for GC+GC. Thus, apparent wall slip has an effect not only on the accuracy but also on the repeatability of the measurement.

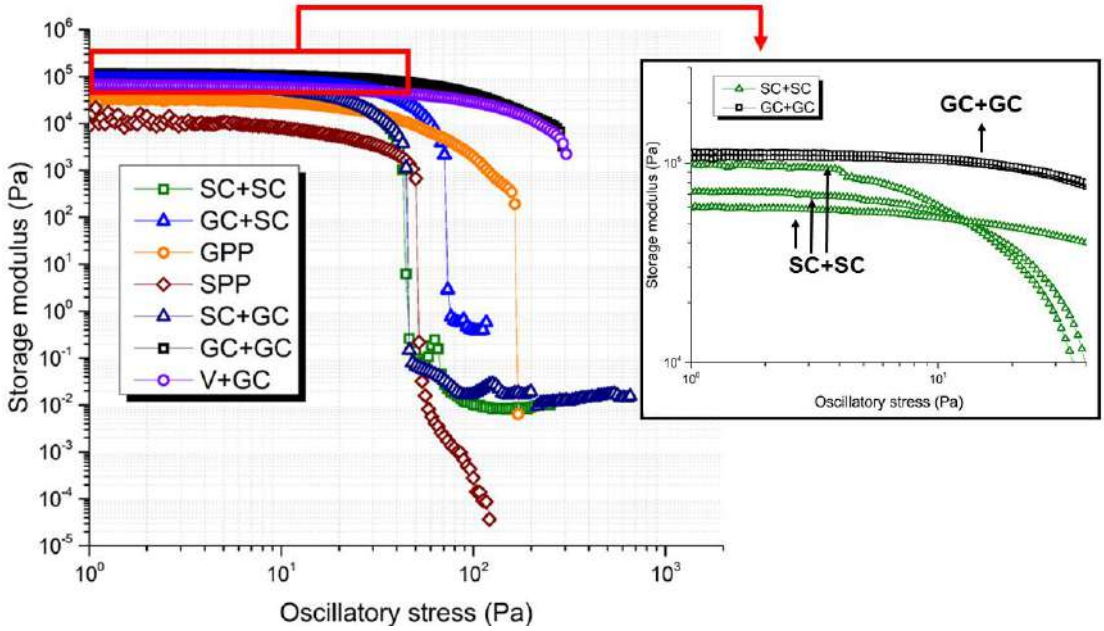


Figure 43 - Storage modulus for **$L_{29}$** 3.0 wt% systems measured during logarithmic stress sweep (4°C and 1 Hz, from 1 Pa to 1,000 Pa) for different geometry assemblies. The triplicates for SC+SC and GC+GC tests are shown in details.

### 4.2.4 Creep tests

Creep experiments were performed with SC+SC and GC+GC geometries for **$L_{29}$** 3.0 wt% system, according to the protocol exposed in section 3.3.1. These geometries produced, the lowest and the maximum values of yield stress respectively, according to oscillatory tests (see Table 8), regardless of system composition. Thus, the values obtained with oscillatory measurements were used as a guide to probe stress levels corresponding to the yield stress determined by creep experiments.

The series of creep experiments began with low stress applied (lower than yield stress) at which the system behaves similarly to a viscoelastic solid. The stress was gradually increased such that several creep curves are obtained. The yield stress was defined as the first value of stress that causes a marked increase in the geometry angular speed, as in creep experiments the gel breakage can be associated with a sudden increase in the rotor angular velocity [150]. The results are exposed in Figure 44.

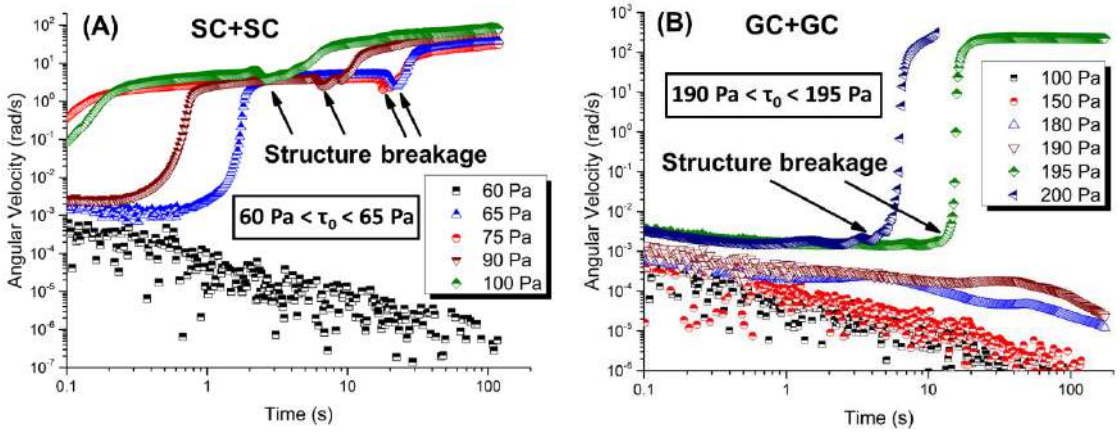


Figure 44 - Creep tests for model oils **$L_{29}$** 3.0 wt% at (A) all smooth SC+SC geometry and (B) all-grooved GC+GC geometry. The procedure comprises holding the sample for 2 minutes at 4 °C under a constant stress value.

It can be seen from Figure 44(A) that the yield stress captured with SC+SC geometry is in the range of 60 to 65 Pa. The reasoning is as follows: when smaller stress values are applied to a material in a Couette geometry with smooth surfaces, the resulting rotation velocity is negligible up to a critical deformation beyond which the materials start to flow by slippage. For stress levels of up to 60 Pa, the gelled structure is maintained virtually intact, which is translated by the negligible angular velocity (less than $10^{-3}$ rad/s) during the test. As the experiment is repeated, this time increasing the stress to 65 Pa, an acute angular response is captured, first at 0.6 seconds as the angular velocity increased from ~ $10^{-3}$ rad/s to 3.2 rad/s, and next at 28 seconds with an increase from ~ 3.2 rad/s to 85 rad/s. This leads to the interpretation that the waxy gelled structure was completely disrupted in 28 seconds as the moving cylinder of the SC+SC geometry was able to move practically freely. The most probable points of structure breakage are indicated by black arrows in Figure 44(A). The first sharp increase of angular velocity for the stress level of 65 Pa suggests that immediately after applying stress, the waxy gel slides in the geometry walls in the first two seconds. The same behavior is repeated for stress levels larger than 65 Pa, although at higher imposed stress values the gel fracture occurs at shorter time intervals. It is also interesting to note that near the breakage point there is a kink in the curve, which much less pronounced for the GC+GC geometry (Figure 44B).

Comparing the yield stress for SC+SC geometry produced with creep tests (60 Pa < $\tau_0$ < 65 Pa) to that produced by oscillatory tests ($\tau_0$ ~ 40 Pa) one may note a difference. This is likely to be due to the dependence of yield stress on the loading stress rate in the case of waxy gels. The loading rate dependency of the stress-strain curve is closely related to behaviors such as stress relaxation time and viscoelasticity [18], [35].

Figure 44(B) exhibits creep tests with al-grooved GC+GC geometry. It is possible to observe that stress levels of up to 190 Pa cause negligible angular velocity (less than $10^{-3}$ rad/s), indicating that the yielding of this sample requires higher stress to occur. When the test is repeated with 195 Pa, the angular velocity increases about four orders of magnitude to more than 600 rad/s after 14.9 seconds. For 200 Pa this response is shortened to 5.8 seconds, with angular velocity reaching the equipment speed limit. Thus, according to the adopted definition for yield stress in the creep test, the value is between 190 Pa and 195 Pa, indicating an average decrease of 68% if measurements are made with SC+SC geometry. Nonetheless, there is a difference not only in the value but in the behavior of the curves, comparing Figure 44(A) and Figure 44(B). For GC+GC there is only one unequivocal sharp increase in angular velocity when the stress level is 195 Pa or 200 Pa, indicated by a black arrow. This is the point of gel breakage when completely roughened surfaces are used. Thus, it is plausible to suppose that apparent wall slip plays a role not only on yield stress underestimation but in the angular vs time curve format shape, which is much easier to interpret for all-grooved geometries.

### 4.2.5 Flow curves

The flow behavior of **$L_{29}$** waxy gels 3.0 wt% and 7.5 wt% was investigated through steady-state rheological experiments, employing smooth SC+SC and grooved GC+GC geometries. Due to apparent wall slip, bulk rheological properties are no longer accurately measured leading to an underestimation of the true viscosity of structured materials [115]. In a slippage boundary, if the stress distribution is not perfectly homogeneous, one might expect that under a given torque some regions will flow while others will remain at rest because the yield stress has not been overcome in the latter [118]. Thus, for samples prone to slip, steady-state rheological experiments also require a judicious preparation.

Prior to discussing the main results, two points of concern are highlighted:

1) To obtain a reliable flow curve the equilibration time must be considered, as it is expected that each point in the curve reflects the system in a particular steady-state. In Figure 45 it is exhibited the flow behavior for a **$L_{29}$** model oil 7.5 wt% at a test temperature of 4°C during the logarithmic sweep from $10^{-3}$ to $10^{3}$ $s^{-1}$ with GC+GC geometry at two different situations. In the first case, it was employed 15 seconds for sample equilibration and 15 seconds averaging the viscosity. Then it was employed 150 seconds for equilibration and 30 seconds averaging viscosity. It is clear that not only the stress values

are different but also repeatability increased by enlarging equilibration time. Thus, 150 seconds it was adopted as a suitable equilibration time.

2) Despite being possible to increase the range of shear rates assessed, it is very difficult to obtain reliable data points at values lower then $10^{-3}$ $s^{-1}$ as steady shear response in the low-stress limit is often quite difficult to delineate and some uncertainty persists [119].

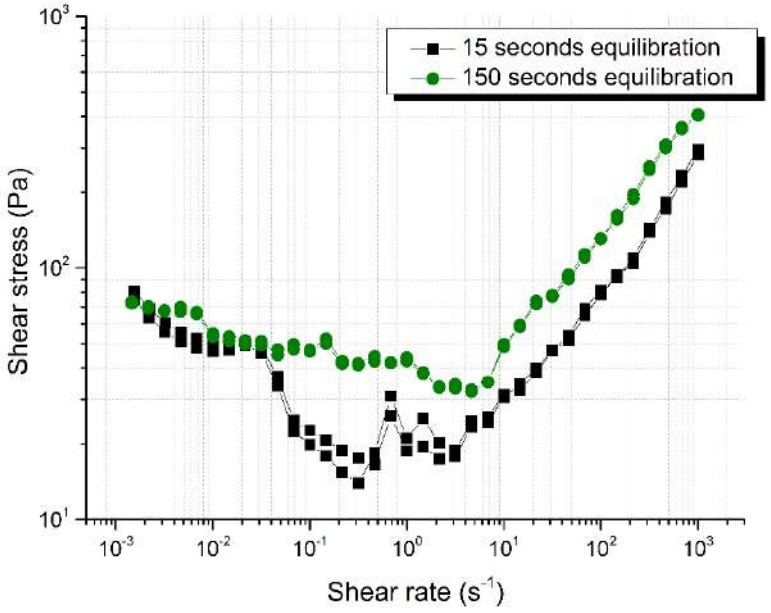


Figure 45 - Flow curves of model oil **$L_{29}$** 7.5 wt% at 4°C with GC+GC geometry employing two different equilibration times: (■) 15 seconds and (●) 150 seconds.

The viscosity curve and the flow curve for **$L_{29}$** 3.0 wt% system were obtained with the smooth Couette (SC+SC) and the grooved Couette (GC+GC) geometry. Figure 46 summarizes the results. As can be observed, the repeatability is clearly enhanced with GC+GC. Above shear rates of ~ 1.0 $s^{-1}$, the curves for both geometries are nearly coincident. Specifically, much lower stress values are obtained with the SC+SC geometry for shear rates lower than 1.0 $s^{-1}$ (Figure 46B), reflecting in lower values of viscosity. This is likely to be caused by an apparent wall slip. For the GC+GC geometry, under a steady imposed shear rate, the inhibition of slippage effects can result in larger stress required to achieve steady flow and consequently more power being dissipated into the material [151]. Also, at the viscosity plot, a clear kink is observed in the curve pertaining to the SC+SC smooth Couette geometry, indicating the presence of apparent wall slip effects [121]. The kink in the flow curve is a familiar characteristic of material slippage, which in this case is mitigated by the use of grooved geometry. In addition, while apparent wall slip alters the characteristics of the curves at low shear rates, the effect becomes less important for values larger than ~ 1.0 $s^{-1}$. Sánchez et al [152] investigated the influence of the preparation method on apparent wall slip of model

emulsions with smooth and rough surface geometries and obtained similar results in terms of reproducibility. The authors noticed that the region in which apparent wall slip is more pronounced corresponds to a region of low reproducibility in the flow curve obtained with smooth surfaces. On the contrary, the flow curve obtained by using geometries with rough surfaces were highly reproducible and accurate.

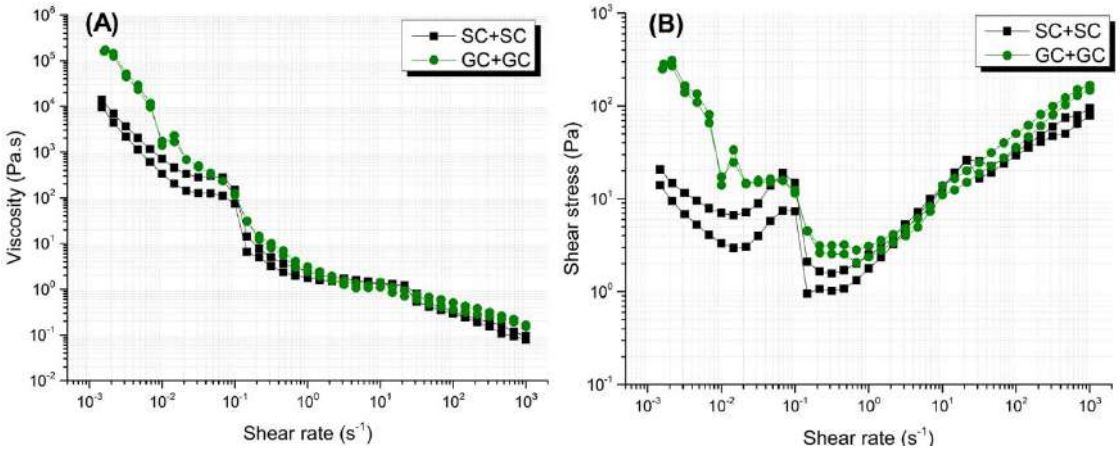


Figure 46 - Model oil **$L_{29}$** 3.0 wt%: (A) viscosity curve and (B) flow curve at 4°C (from $10^{-3}$ to $10^{3}$ $s^{-1}$) for (■) all smooth and (●) all-grooved geometries.

Figure 47 exhibits the viscosity and flow curve for a 7.5 wt% system at 4°C. The same reasoning exposed for the 3.0 wt% system can be applied here, however, the convergence of the curves was postponed for much higher values of shear rate (around $10^{2}$ $s^{-1}$). This is likely to be caused by the stiffer structure developed by a system which contains more waxy in its composition. For both 3.0 wt% and 7.5 wt% systems, the flow curves are nearly coincident after the breakage of the gelled structure and the samples start to flow most likely as a Newtonian fluid. Since the 7.5 wt% system is mechanically more resistant the apparent wall slip effects are extended to higher values of shear rate.

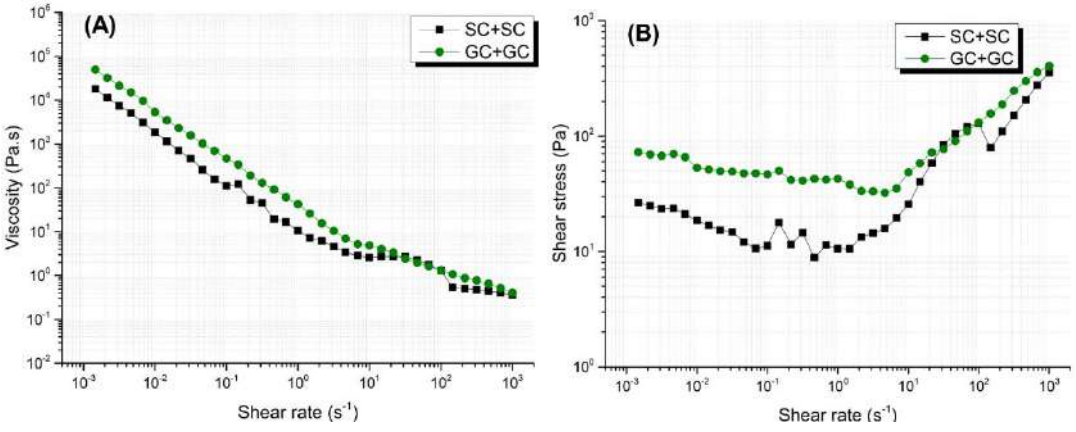


Figure 47 - Model oil **$L_{29}$** 7.5 wt%: (A) viscosity curve and (B) flow curve at 4°C (from $10^{-3}$ to $10^{3}$ $s^{-1}$) for (■) all smooth and (●) all-grooved geometries.

Lastly, as apparent wall slip causes a decrease in the viscosity measurement, it can be quantified as the relative difference between the areas under the flow curves obtained using geometries with smooth and grooved surfaces [152]. For the 3.0 wt% system, the areas were calculated as 203.2 Pa/s (SC+SC) and 266.1 Pa/s (GC+GC). Thus, a decrease of 24% can be computed. For 7.5 wt%, the areas were 672.4 Pa/s (SC+SC) and 969 Pa/s (GC+GC), and a decrease of 31% is calculated. These results show that the viscosity of waxy gels is affected by apparent wall slip approximately to the same extent, regardless of the system composition.

### 4.2.6 Conclusions

In this section, the viscoelastic properties and flow characteristics of gels consisting of **$L_{29}$** macrocrystalline wax 3.0 wt% and 7.5 wt% were assessed. Seven different geometry configurations were used, containing combinations of smooth and grooved walls, at oscillatory, creep and steady-state rheological experiments. First, it was discussed the importance of aging and time sweep step prior to the yield stress measurements. In the following, there was an analysis of the apparent wall slip effects on the viscoelastic properties of waxy gels, namely storage modulus and yield stress, provided by oscillatory tests. The strategy is to depart from similar stable gels and assess these rheological properties varying the geometry roughness. Thus, the effect of apparent wall slip can be analyzed and quantified by comparing the results from geometries progressively more rugged. The yield stress obtained by oscillatory rheology was compared with results from creep tests, confirming the trend previously observed. For creep tests two representative geometries were selected, the smooth cup smooth cylinder Couette and the grooved cup grooved cylinder Couette. Finally, the flow behavior of waxy gels is assessed with the two representative geometries, showing how viscosity curves are affected by apparent wall slip. Flow curves were also used to quantify apparent wall slip was as the relative difference between the areas under the curves obtained using geometries with smooth and grooved surfaces.

From oscillatory rheological measurements, a decrease of ~ 80% in yield stress was calculated for different system compositions. Creep tests also indicated an average decrease of 68% if measurements are made with smooth Couette geometry. There is also evidence that slippage is more pronounced when moving part of the geometry is smooth. When all-grooved geometries were used, not only the reproducibility but repeatability of yield stress was improved.

Apparent wall slip has also a clear influence in the storage modulus since this property is underestimated when measured by geometries with smooth parts. For geometries with a smooth part, the property was captured even when the system is far from the linear viscoelastic region, which was not the case for all-grooved geometries. Thus, the storage modulus measurement may provide indirect evidence of apparent wall slip.

Flow curves also exhibited much lower stress values when smooth Couette geometry was employed, reflecting in lower values of viscosity. This is likely to be caused by an apparent wall slip. For the all-grooved geometry, under a steady imposed shear rate, the inhibition of slippage effects resulted in larger stress required to achieve steady flow. The results also showed that the viscosity of waxy gels is affected by apparent wall slip approximately to the same extent, regardless of the system composition.

It became clear that the trade between a smooth to a grooved surface mitigates but do not eliminate apparent wall slip. In order to do so, a completely grooved geometry must be used. Since there is no general theory enabling one to predict the exact conditions and extent under which apparent wall slip occurs, this study addresses the importance of the correct geometry choice in order to assess the bulk rheological properties of waxy gels. Thus, to obtain high-quality rheological data, for systems prone to slip it is mandatory the use of grooved surfaces at both moving and stationary parts of the rheometer.

## 4.3 Influence of Experimental Variables at Yield Stress

In this section, we present and discuss the rheological behavior of gelled model oils composed by a blend of **$L_{29}$** and **$B_{53}$** waxes with the composition varying from 2.5 wt% to 7.5 wt%. The experimental procedure is given in details in section 3.3.2. The main goal is to evaluate the influence of six experimental variables on the rheological behavior of samples under gelling conditions. In the literature, substantial effort is devoted to modeling crude oil intricate rheological behavior as a function of variables such as temperature, cooling rate, shear stress (or shear rate), disperse phase volume, and aging time [11], [12], [22], [33], [70], [77], [153], [154]. The major experimental variables are assessed in this study. The system is composed of a well-characterized but polydisperse waxes dissolved in spindle oil (see section 4.1 for complete physicochemical characterizations). In order to cope with a large number of effects simultaneously, a $2^{6-1}$ statistical experimental design was used. The waxy crystal morphologies, the relationship of storage modulus and yield stress and the sensitivity to shear and partial recovery of gelled oils are also discussed. In addition, an experimental equation is proposed to predict yield stress.

The experimental conditions and results are summarized in Table 9 and discussed in the following. The yield stress is the response variable of this experimental design. In fact, there exist different criteria for detecting the yielding of structured materials. In this investigation, as already commented, it was defined as the oscillatory stress at the crossing point of storage modulus and loss modulus. This definition provides a reasonable and fast method to measure yield stress in a wide experimental range [155].

Table 9 - Experimental conditions, yield stress, storage modulus and final viscosity

| Run # | $x_1$ (°C/min) | $x_2$ (wt%) | $x_3$ (wt%) | $x_4$ ($s^{-1}$) | $x_5$ (°C) | $x_6$ (min) | $\tau_0$ (Pa) | $G'_{LVR}$ (kPa) | $\eta_F$ (Pa.s) |
|---|---|---|---|---|---|---|---|---|---|
| 1 | 0.50 | 1.25 | 1.25 | 0 | 4.0 | 0 | 20 | 2.57 | *--- |
| 2 | 1.20 | 1.25 | 1.25 | 0 | 4.0 | 60 | 63 | 11.2 | --- |
| 3 | 0.50 | 3.75 | 1.25 | 0 | 4.0 | 60 | 630 | 450 | --- |
| 4 | 1.20 | 3.75 | 1.25 | 0 | 4.0 | 0 | 1,995 | 530 | --- |
| 5 | 0.50 | 1.25 | 3.75 | 0 | 4.0 | 60 | 158 | 24.1 | --- |
| 6 | 1.20 | 1.25 | 3.75 | 0 | 4.0 | 0 | 99 | 15.2 | --- |
| 7 | 0.50 | 3.75 | 3.75 | 0 | 4.0 | 0 | 1,000 | 261 | --- |
| 8 | 1.20 | 3.75 | 3.75 | 0 | 4.0 | 60 | 794 | 242.8 | --- |
| 9 | 0.50 | 1.25 | 1.25 | 1.60 | 4.0 | 60 | 3.2 | 2.11 | 1.13 |

| | | | | | | | | | |
|---|---|---|---|---|---|---|---|---|---|
| 10 | 1.20 | 1.25 | 1.25 | 1.60 | 4.0 | 0 | 0.5 | 0.033 | 1.26 |
| 11 | 0.50 | 3.75 | 1.25 | 1.60 | 4.0 | 0 | 7.9 | 6.9 | 8.51 |
| 12 | 1.20 | 3.75 | 1.25 | 1.60 | 4.0 | 60 | 1,258 | 447 | 11.20 |
| 13 | 0.50 | 1.25 | 3.75 | 1.60 | 4.0 | 0 | 0 | 0.018 | 1.60 |
| 14 | 1.20 | 1.25 | 3.75 | 1.60 | 4.0 | 60 | 16 | 11.3 | 3.48 |
| 15 | 0.50 | 3.75 | 3.75 | 1.60 | 4.0 | 60 | 20 | 20.1 | 12.87 |
| 16 | 1.20 | 3.75 | 3.75 | 1.60 | 4.0 | 0 | 3.2 | 3.72 | 11.40 |
| 17 | 0.50 | 1.25 | 1.25 | 0 | 12 | 60 | 1.6 | 0.42 | --- |
| 18 | 1.20 | 1.25 | 1.25 | 0 | 12 | 0 | 5 | 0.20 | --- |
| 19 | 0.50 | 3.75 | 1.25 | 0 | 12 | 0 | 632 | 138.9 | --- |
| 20 | 1.20 | 3.75 | 1.25 | 0 | 12 | 60 | 1,584 | 678.3 | --- |
| 21 | 0.50 | 1.25 | 3.75 | 0 | 12 | 0 | 158 | 25 | --- |
| 22 | 1.20 | 1.25 | 3.75 | 0 | 12 | 60 | 125 | 15.79 | --- |
| 23 | 0.50 | 3.75 | 3.75 | 0 | 12 | 60 | 630 | 304.8 | --- |
| 24 | 1.20 | 3.75 | 3.75 | 0 | 12 | 0 | 398 | 68.5 | --- |
| 25 | 0.50 | 1.25 | 1.25 | 1.60 | 12 | 0 | 0 | 0.001 | 0.41 |
| 26 | 1.20 | 1.25 | 1.25 | 1.60 | 12 | 60 | 8 | 1.57 | 0.57 |
| 27 | 0.50 | 3.75 | 1.25 | 1.60 | 12 | 60 | 316 | 218.5 | 4.21 |
| 28 | 1.20 | 3.75 | 1.25 | 1.60 | 12 | 0 | 199 | 90.3 | 4.16 |
| 29 | 0.50 | 1.25 | 3.75 | 1.60 | 12 | 60 | 5 | 3.20 | 1.52 |
| 30 | 1.20 | 1.25 | 3.75 | 1.60 | 12 | 0 | 6.3 | 1.04 | 2.68 |
| 31 | 0.50 | 3.75 | 3.75 | 1.60 | 12 | 0 | 1.6 | 3.33 | 5.82 |
| 32 | 1.20 | 3.75 | 3.75 | 1.60 | 12 | 60 | 76 | 92.49 | 6.68 |
| CP1 | 0.85 | 2.50 | 2.50 | 0.80 | 8.0 | 30 | 50 | 36.48 | 7.15 |
| CP2 | 0.85 | 2.50 | 2.50 | 0.80 | 8.0 | 30 | 50 | 40.21 | 8.42 |
| CP3 | 0.85 | 2.50 | 2.50 | 0.80 | 8.0 | 30 | 40 | 34.37 | 6.82 |
| CP4 | 0.85 | 2.50 | 2.50 | 0.80 | 8.0 | 30 | 40 | 29.42 | 8.46 |
| CP5 | 0.85 | 2.50 | 2.50 | 0.80 | 8.0 | 30 | 40 | 37.22 | 8.21 |

*--- viscosity is not available, because shear rate during cooling was set to zero
CP = Central Point

### 4.3.1 Viscosity Increase during Cooling

Prior to discussing the effect of each experimental variable, the viscosity behavior during the cooling process is considered. It is well-known that the viscosity of waxy oils depends on the applied shear rate. However, the following analysis and comparisons are

applicable for the samples tested with a fixed shear rate of 1.6 $s^{-1}$, which encompasses experiments 9 to 16 and experiments 25 to 32 (see Table 9). The starting temperature for the rheological tests is 50°C; at this condition, all model oils and the spindle oil have approximately the same viscosity ~ $5x10^{-3}$ Pa.s. As the temperature is reduced, with an imposed shear rate of 1.6 $s^{-1}$ an increase of up to 100,000 times is observed for the model oils viscosity. Even systems exhibiting negligible yield stress ($\tau_0 < 1$ Pa) presented an increase of up to ~ 10,000 times. However, the viscosity of spindle oil, measured in the same temperature range, increased only 10 times. Figure 48 illustrates the case for experiments 10, 12 and spindle oil. It is possible to observe curves superimposition until approximately 25°C. Below this temperature, the viscosity of experiments 10 and 12 presented a sudden change, evident on a linear scale plot and defined by Japper-Jaafar et al. [39] as the Wax Precipitation Temperature. This behavior was observed for all experiments.

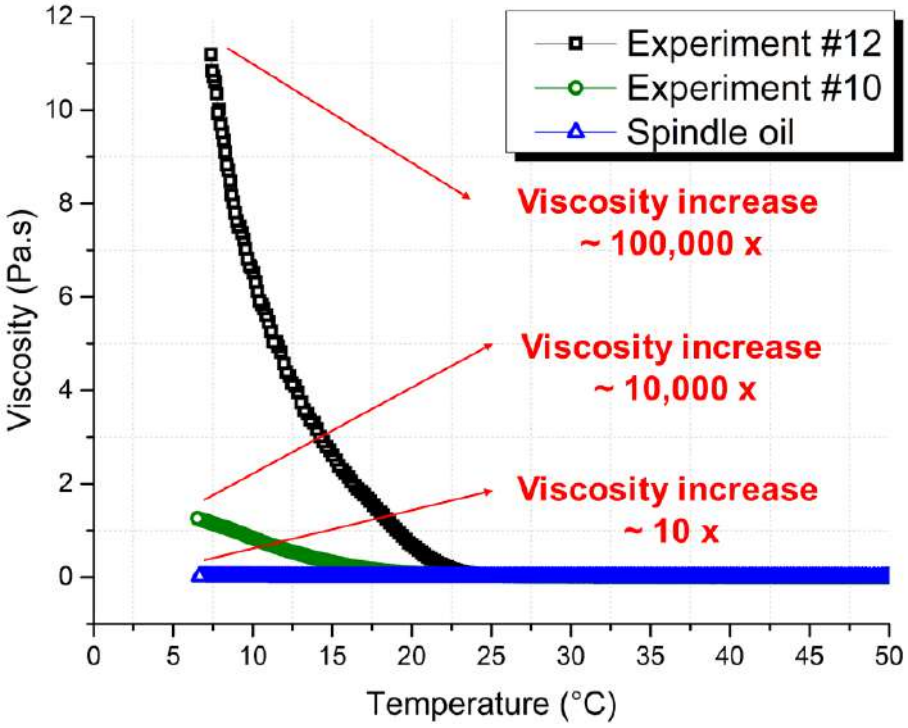


Figure 48 – Viscosity profile along the cooling step for experiment 12 (◧), experiment 10 (●) and spindle oil (▲). The cooling rate was 1.2°C/min and shear rate of 1.6 $s^{-1}$.

The smallest viscosity increase was registered in experiment 25 (78 times). As model systems are composed exclusively of waxes and spindle oil, the results clearly indicate that wax precipitation occurred for all the systems assessed and it is responsible for viscosity increasing. As a consequence of the continuous precipitation, crystal-crystal interactions may lead to a strong waxy-gel network formation. Thus, it is reasonable to assume that higher viscosity would lead to higher yield stress. Table 9 includes the

values of the viscosity measured in the last temperature of the cooling step (named final viscosity). Contrary to expectations, for the conditions tested in this investigation, there is virtually no correlation among yield stress and final viscosity ($R^2$ = 0.16). This might be consequence of the shear rate of 1.6 $s^{-1}$ employed. On the other hand, the system compositions and also the test conditions vary from test to test after the cooling step. Thus, this poor correlation may indicate that yield stress is highly affected by the composition ($x_2$ and $x_3$) and/or aging time ($x_6$), because these are the variables not involved in the cooling step (see Figure 23 for a clear picture). The relative importance of each variable is discussed in the next session.

### 4.3.2 Cooling Rate Effect

The influence of the experimental variables on yield stress and their mutual interactions can be established by the parameters of Equation 14 ($\boldsymbol{\tau_0 = a_0 + \sum_i^6 a_i x_i + \sum_{i<j}^6 a_{ij} x_i x_j}$). A multiple linear regression analysis was employed for computing the parameters, using the sum of squared residuals (SS Residuals/(n-1)) as the experimental error estimate. Statistical significance was set to p-level ≤ 0.05. If this value was greater than 5%, the parameter was removed from the Equation. Significant parameters are exhibited in Table 10 ($_{L29}$ and $_{B53}$ = linear and branched waxes, respectively, $_{SR}$ = shear rate).

Table 10 - Significant parameters calculated for Equation 14

| Parameter | Value | Percentage contribution* |
|---|---|---|
| $a_0$ | 319 ± 21 | - |
| $a_{\text{Cooling Rate}}$ | 95 ± 21 | 8 |
| $a_{L29}$ | 277 ± 21 | 23 |
| $a_{B53}$ | -101 ± 21 | 9 |
| $a_{\text{SR during Cooling}}$ | -199 ± 21 | 17 |
| $a_{\text{Cooling Rate x L29}}$ | 96 ± 21 | 8 |
| $a_{\text{Cooling Rate x B53}}$ | - 124 ± 21 | 10 |
| $a_{\text{L29 x B53}}$ | -130 ± 21 | 11 |
| $a_{\text{L29 x SR during Cooling}}$ | -162 ± 21 | 14 |

*the parameter $a_0$ was not included in the percentage contribution because it is not associated with any experimental variables

The cooling rate is associated with the parameter $a_{\text{Cooling Rate}}$ in Table 10. The positive value indicates that yield stress is favored by faster cooling conditions. It is worth

mentioning that the effect of this variable was extensively studied in the literature and apparently different conclusions were drawn. It has been reported that the cooling rate may increase [156], [157], decrease [4], [15] or have a non-monotonic effect on the yield stress [117], [158]. Nonetheless, it does not seem appropriate to compare the effect of a single variable on the yield stress between investigations that applied different experimental protocols.

Analyzing Table 9, from the five highest values of yield stress obtained four presented a cooling rate of 1.2°C/min. On the other hand, from the five smallest yield stress obtained, only experiment 10 presented a cooling rate of 1.2°C/min. Although, as the cooling was performed in two different ways (quiescent and non-quiescent), it is important to consider the associated effect of shearing the samples.

If one divides the experimental design into two equal parts (a) containing only the results for quiescent cooling and (b) only the results for the disturbed cooling (shear rate = 1.6 $s^{-1}$), the analysis indicates that for data in (a) there is no trend, except that already commented: the faster the cooling the higher the yield stress. Accordingly, a halt in oil production would be less problematic for smaller cooling rates, considering the pumping restart operations. For data in (b), there is no clear trend for the cooling rate of 1.2°C/min, however the rate of 0.5°C/min concentrates the smaller yield stress values. This is clearly seen in the yield stress distribution for each cooling rate, in both cases (quiescent and non-quiescent), as shown in Figure 49. A high standard deviation ($\delta$ > 300 Pa) indicates a disperse distribution of yield stress for a particular cooling rate. Thus, no trend is devised (Figure 49A). However, for the disturbed cooling (Figure 49B), the rate of 0.5 °C/min concentrates smaller values of yield stress, with relatively low dispersion. This behavior can be explained by considering the effect of the applied shear rate during the cooling process. The disturbance tends to break up the crystal network as it forms. A lower cooling rate implies that the sample is subjected to the disturbance for a longer time. According to Kané et al. [8], Venkatesan et al. [159], and Lin et al. [15], whenever disturbances along the cooling step are present, the yield stress is favored by fast cooling rates.

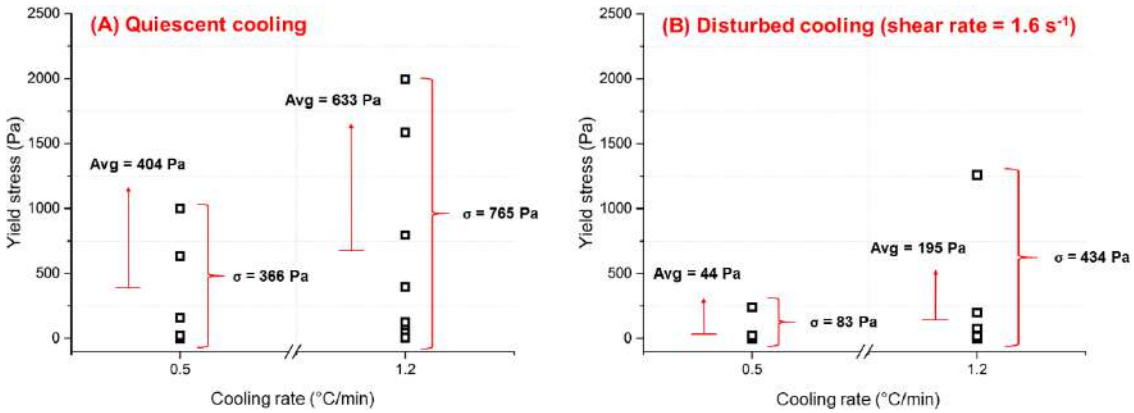


Figure 49 - Yield stress distribution for 0.5°C/min and 1.2°C/min cooling rates at two conditions: (A) quiescent and (B) disturbed cooling. Avg stands for the average value of yield stress and σ represents the standard deviation.

The parameters $a_{\text{Cooling Rate x L29}}$ and $a_{\text{Cooling Rate x B53}}$ were also significant, with percentage contributions to the response variable of 8% and 10%, respectively. They quantify the combined effect of the variables, taken in pairs and they presented opposite signs. As will be discussed in the next session, these results are likely to be due to the structural properties of the waxes involved in the cooling process. Despite being significant, the cooling rate itself has a relatively low influence on the yield stress, with a percentage contribution of only 8%.

### 4.3.3 Wax Content Effect

Wax content is associated with parameters $a_{L29}$ and $a_{B53}$ in Table 10. The influence of wax precipitation in yield stress is well known in the literature; the network of interacting paraffin wax crystals are responsible for the yield stress appearance [8], [15], [38]. Indeed, **$L_{29}$** wt% is the most influent variable, which means that yield stress is enhanced by the increase of **$L_{29}$** wax content. On the other hand, **$B_{53}$** wt% presented a negative effect. Since samples comprised mineral oil and blend of waxes, one might suppose a large and positive effect for the **$B_{53}$** wt% variable; however, it was not the case.

The obtained results are due to structural differences among the waxes, as demonstrated in section 4.1. **$L_{29}$** wax comprises mainly linear saturated aliphatic chains and few obstacles are present for favored interactions. **$B_{53}$** is a branched wax that presents a huge hindrance when trying to approximate to other wax molecules, thus the co-precipitation with **$L_{29}$** may generate a network with many voids, resulting in the weak gelling. This is reflected in the negative value of the $a_{L29 \text{ x } B53}$ parameter (see Table 10),

which presents a percentage contribution of 11%. According to this result, the increase of both **$L_{29}$** and **$B_{53}$** wax content will lead to a decrease in the yield stress. Figure 50 shows microscope images of precipitated waxes from **$L_{29}$** and **$B_{53}$** 5 wt%, and **$L_{29}$** + **$B_{53}$** 2.5 + 2.5 wt% to illustrate this fact. The samples were cooled from 50°C to 4°C at 1.0°C/min at the microscope thermal stage. Then, an isothermal holding time of 60 minutes was applied under a constant temperature of 4°C. All pictures were taken immediately after the isothermal holding time.

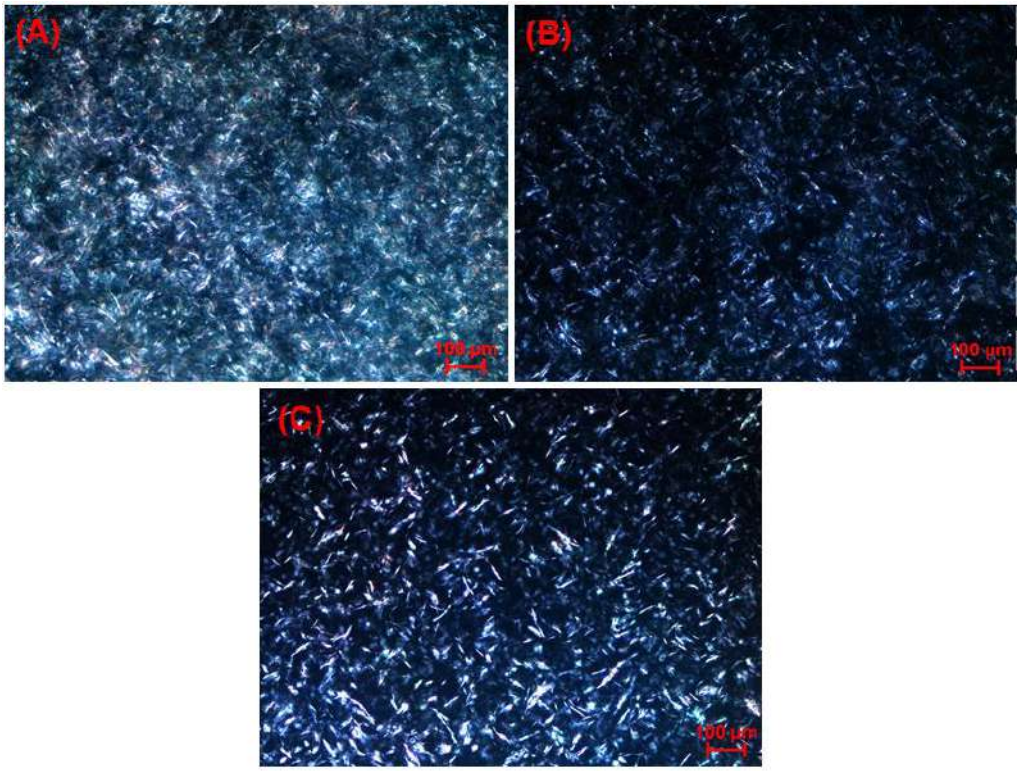


Figure 50 - Microscopy images for (A) **$L_{29}$** 5 wt%, (B) **$B_{53}$** 5 wt% and (C) **$L_{29}$** + **$B_{53}$** 2.5 + 2.5 wt% systems, taken after an isothermal cooling of 60 minutes at 4°C. The samples were previously cooled from 50°C to 4°C at 1.0°C/min.

One can observe that the clustering pattern varied widely from system to system. **$L_{29}$** wax (Figure 50A) presented fewer unoccupied space, making difficult to devise individual crystals. **$B_{53}$** presented a pattern similar to **$L_{29}$** in terms of shape, however, there are clear voids in the image (Figure 50B), indicating a more loose network with less crystal-crystal interactions. The blended system (Figure 50C) presented the highest crystal length, amassed into clusters of varying size. Although, it is clear that the network presented some voids and it is not completely superimposed as for **$L_{29}$** wax.

Also, additional rheological experiments employing single wax systems were performed in triplicate. Model oils were prepared to contain 7.5 wt% of **$L_{29}$** wax and 7.5 wt% of **$B_{53}$**

wax and they were tested under a two-step rheological procedure: cooling from 50°C to 4°C at 1.0°C/min and 0.8 $s^{-1}$ shear rate, following by yield stress measurement. The results were 199.5 ± 31.2 Pa for **$L_{29}$** and 26.7 ± 5.5 Pa for **$B_{53}$** wax. Therefore, it indicates that the predominately linear wax employed was able to form a stronger interlocking network, comparing to the branched wax, leading to higher yield stress. These results are in accordance with Zhao et al. [77] and Bai and Zhang [29].

### 4.3.4 Shear Rate During Cooling

The parameter associated with the shear rate during cooling ($a_{SR\ during\ Cooling}$, Table 10) presented a large and negative value, indicating that yield stress increases when the shear rate is reduced. In fact, it was the second most important effect, with a percentage contribution of 17%. It is assumed that the disturbance applied as shear rate during the cooling process acts against crystals clusters formation, preventing strong interactions that lead to spanning gelled network structures [77]. Thus, is more likely to observe high yield stress for the quiescent cooling conditions. To illustrate this, one may recall Figure 49 and observe average yield stress at quiescent cooling conditions of 404 Pa for experiments performed with 0.5°C/min and 633 Pa for 1.2°C/min. For the disturbed cooling, the average values were 44 Pa and 195 Pa, respectively.

In order to probe the effect of small disturbances along cooling in more details, additional rheological tests were performed in triplicate employing a waxy crude oil (0.892 $g/cm^3$@20°C and 5.0 ± 0.1 total wax content measured by UPO method 46-85) and the respective W/O emulsion (50 wt%). Samples were cooled from 25 to 4.0 °C at two distinct scenarios: at zero shear stress and 1.0 Pa shear stress disturbance. The results indicated a yield stress decrease from 87.4 ± 13.4 Pa to 47.9 ± 11.2 Pa for waxy crude and 488.6 ± 25.4 Pa to 412.8 ± 29.1 Pa for the W/O emulsion. It represents a yield stress reduction of 45% for the waxy crude and 16% for the W/O emulsion. It demonstrates that even small variations in cooling conditions were able to affect the yield stress either for waxy crude and W/O emulsions.

The parameter $a_{L29\ x\ SR\ during\ Cooling}$ was computed as significant and had a percentage contribution of 14%. Even though the big positive effect of **$L_{29}$** wt%, the interaction between the shear rate and the **$L_{29}$** wax content was negative, which means that a simultaneous increase of both variables will correspond to a decrease in yield stress.

### 4.3.5 Final Cooling Temperature

The parameters associated with the “final cooling temperature” variable in Equation 14 were not significant. In Figure 51 it is exhibited the yield stress distribution according to the final cooling temperature. Considering the results of the experimental design, the average yield stress value is comparable for each temperature assessed (379 Pa for 4°C and 259 Pa for 12°C). It is also possible to find high values of yield stress for the temperature of 12°C and the data dispersion, represented by the standard deviation, is close in both cases. Nonetheless, there are 4 values of yield stress in the range of 500 to 1,500 Pa for the temperature of 4.0°C and only 1 value for the temperature of 12°C in the same range. Also, the highest yield stress is assigned to an experiment with this final cooling temperature. Albeit small, there is a trend for yield stress increase at smaller temperatures.

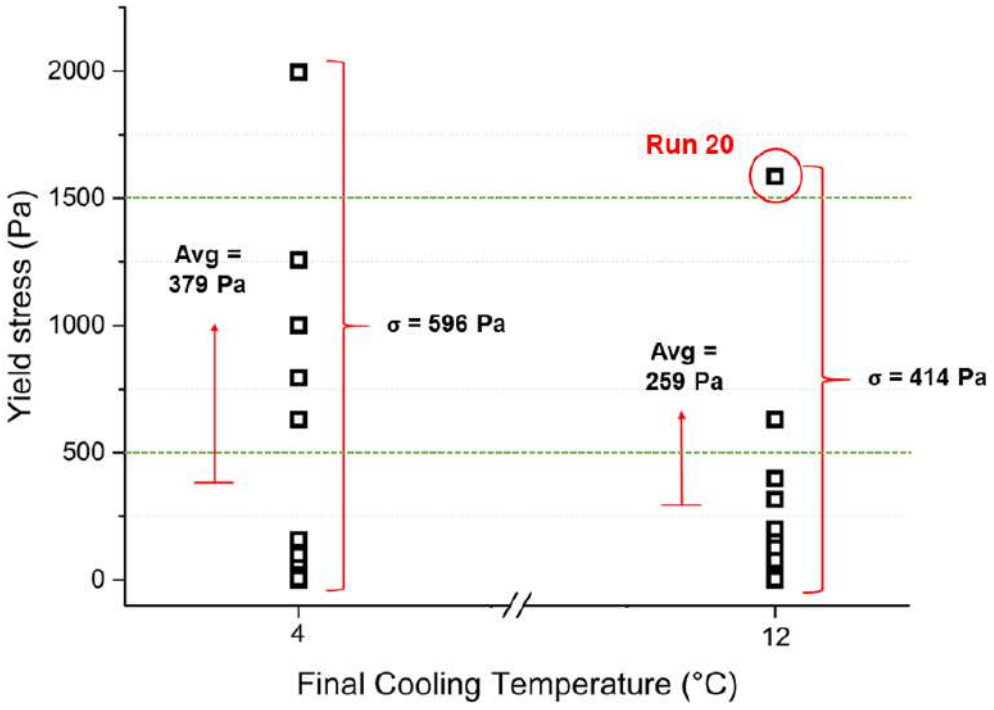


Figure 51 - Yield stress distribution for final cooling temperatures of 4°C and 12°C. Avg stands for the average yield stress and σ represents the standard deviation.

In terms of parameter estimation, the fact that “final cooling temperature” is not quantifiable is related to the spread of yield stress values at 4°C and also the very high value of 1,584 Pa at 12°C (experiment 20). However, there might be a possible explanation in physical terms: all model oils might have reached the gelled state in temperatures above 12°C. If this was the case, it is plausible that “final cooling temperature” has little impact on the yield stress. To illustrate this, Table 11 exhibits the

Wax Precipitation Temperature, as defined in Japper-Jaafar et al. [39], for samples with shear rate during cooling equals 1.6 $s^{-1}$. As can be observed, the smaller WPT value is 21°C (experiment 25), which means that this entire subset of experiments reached a gelled state before 12°C. It is feasible to assume that other samples on the experimental design also reached a gelled state before 12°C, mainly because they were cooled in quiescent conditions. It is also possible to observe that the highest WPT values in Table 11 (≥ 32 °C) are associated with systems compositions of 7.5 wt% wax in total. The higher amount of wax guarantees the formation of a gel in early stages of cooling, however it does not guarantee the highest yield stress values, because, as exposed, $\mathbf{B_{53}}$ has a negative contribution. This is reflected in the fact that WPT and yield stress are uncorrelated ($R^2 < 0.2$).

Table 11 - WPT for the tests with shear rate during cooling set to 1.6 $s^{-1}$

| Run # | $x_1$ (°C/min) | $x_2$ (wt%) | $x_3$ (wt%) | $x_5$ (°C) | $x_6$ (min) | WPT (°C) |
|---|---|---|---|---|---|---|
| 9 | 0.5 | 1.25 | 1.25 | 4 | 60 | 26.8 |
| 10 | 1.2 | 1.25 | 1.25 | 4 | 0 | 25 |
| 11 | 0.5 | 3.75 | 1.25 | 4 | 0 | 26.1 |
| 12 | 1.2 | 3.75 | 1.25 | 4 | 60 | 23 |
| 13 | 0.5 | 1.25 | 3.75 | 4 | 0 | 28 |
| 14 | 1.2 | 1.25 | 3.75 | 4 | 60 | 29.7 |
| 15 | 0.5 | 3.75 | 3.75 | 4 | 60 | 33 |
| 16 | 1.2 | 3.75 | 3.75 | 4 | 0 | 32 |
| 25 | 0.5 | 1.25 | 1.25 | 12 | 0 | 21 |
| 26 | 1.2 | 1.25 | 1.25 | 12 | 60 | 21.6 |
| 27 | 0.5 | 3.75 | 1.25 | 12 | 60 | 26.5 |
| 28 | 1.2 | 3.75 | 1.25 | 12 | 0 | 25 |
| 29 | 0.5 | 1.25 | 3.75 | 12 | 60 | 30.9 |
| 30 | 1.2 | 1.25 | 3.75 | 12 | 0 | 25.8 |
| 31 | 0.5 | 3.75 | 3.75 | 12 | 0 | 34.5 |
| 32 | 1.2 | 3.75 | 3.75 | 12 | 60 | 33.9 |

Another analysis is based on microscopy images. Figure 52 exhibits waxy crystals precipitated from $\mathbf{L_{29}}$ + $\mathbf{B_{53}}$ 2.5 + 2.5 wt% systems at three different isothermal holding times: 0 min, 30 min, and 60 min. The samples were cooled from the starting temperature of 50°C at 1.0°C/min until 12°C or 4°C. Figure 52(A), Figure 52(B), and Figure 52(C) refer to the final temperature of 4 °C whereas Figure 52(D), Figure 52(E), and Figure

52(F) refer to 12 °C. It is possible to observe similar crystal shapes and clustering patterns from both cases, nevertheless for the final temperature of 4°C fewer voids can be detected. An image with less unoccupied spaces indicates more wax precipitated, which, in principle, would translate in higher yield stress. These images indicate that when samples are submitted to the same experimental protocol, the final cooling temperature translates in differences at microscopy level.

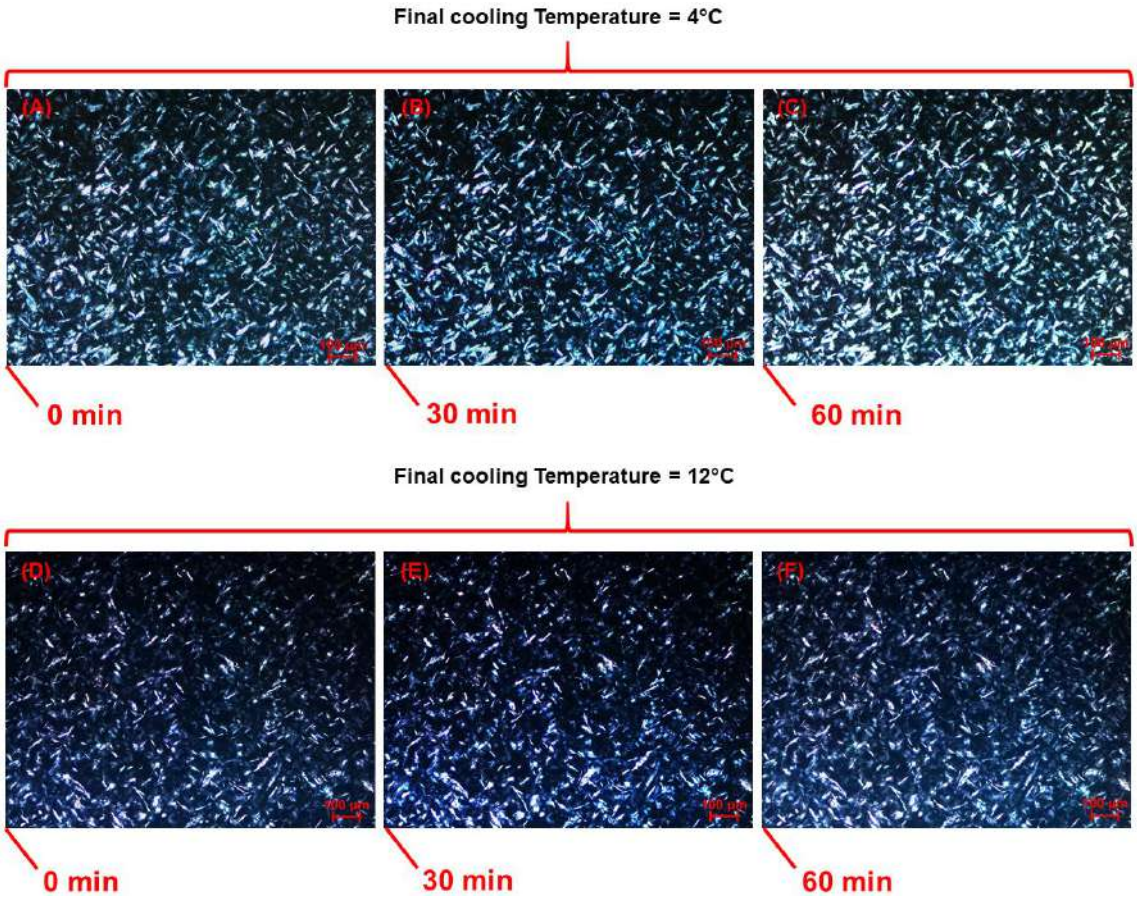


Figure 52- Microscopy images for a system of $\mathbf{L_{29}}$ + $\mathbf{B_{53}}$ 2.5 + 2.5 wt% cooled until 4.0°C at three different isothermal holding times: (A) 0 min, (B) 30 min, and (C) 60 min. The same composition was used to prepare and cool a model oil until 12°C at three different isothermal holding times: (D) 0 min, (E) 30 min, and (F) 60 min. The samples were cooled from the starting temperature of 50°C at 1.0°C/min.

### 4.3.6 Aging Time Effect

The parameters associated with the aging time in Equation 14 were not significant. In principle, it is not an expected result. According to Lopes-da-Silva and Coutinho [44] and Jia and Zhang [135], even at the end of the cooling step, the oil-gel may still be out of equilibrium, allowing further isothermal rearrangements. Visintin et al. [10] also studied

the influence of the aging time and concluded that the aging process affects the material properties, especially in the first minutes. The structure build-up of the waxy gelled network can be followed in a plot of G' vs time, during the isothermal holding step (i.e., the aging step). In this case, storage modulus increases as a result of the increasing junction zones density between wax crystals. Thus, the structural development of waxy gelled crudes can be monitored by measuring the elastic features of the samples [125]. After the rapid increase in elasticity within the gel, G' keeps increasing slightly and continuously as a result of the reinforcement of the network by slower formation and rearrangement of elastic active bonds/junction zones, reaching a pseudo plateau region, meaning a continuous reorganization of the particulate network [92].

In this investigation, the plot of G' vs time is shown in Figure 53 for experiments with aging time variable set to 60 minutes. It is possible to observe a huge increase in the storage modulus, of up to two orders of magnitude, in the first 10 minutes of aging. After 30 minutes, the changes are limited, and G' reaches a plateau. The profiles were similar for all 16 experiments with aging time variable different from zero.

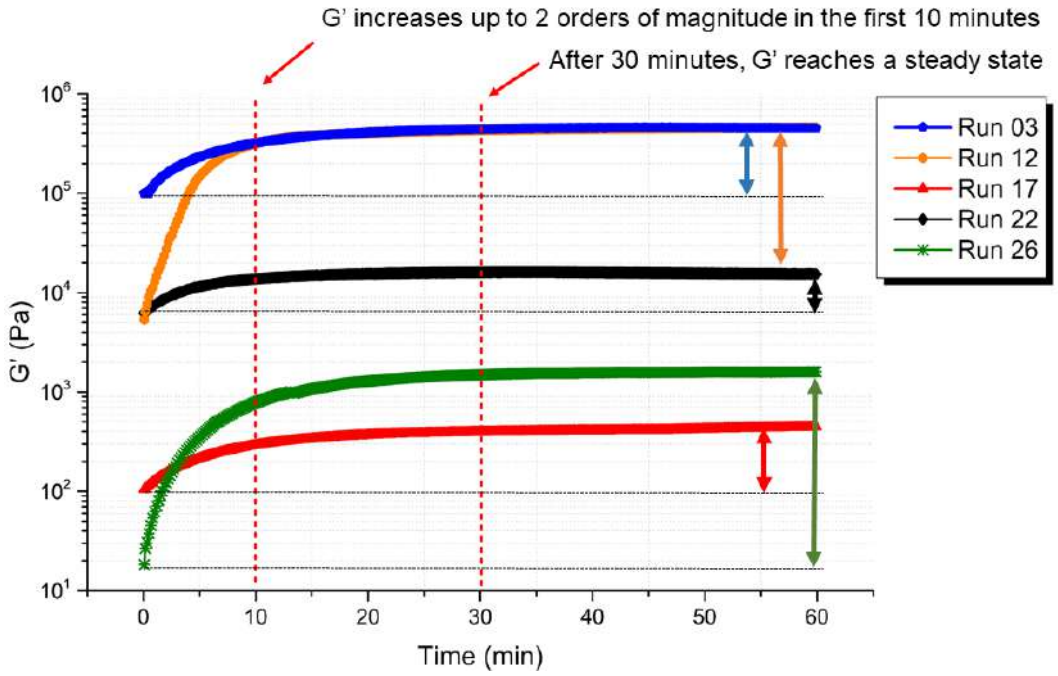


Figure 53 - Storage modulus evolution in the isothermal holding time step (strain $5x10^{-4}$ and frequency 0.5 Hz) for five experiments. The first 10 minutes establish the major structural changes. The relative increase is represented by the double arrows.

If there was a clear structure build up during the aging, why it was not translated in yield stress increase when compared to experiments without aging time? In other words, why

this variable was computed as not significant? This fact might indicate that the cooling conditions are decisive for the gel waxy structure. If the conditions are unfavorable for the structure development (e.g., a small amount of linear wax, high amount of branched wax and shear rate during cooling), the aging time will not provide a relevant impact on the yield stress. See, for example, experiment 9 ($\tau_0$ = 3.2 Pa), experiment 26 ($\tau_0$ = 8 Pa) or experiment 29 ($\tau_0$ = 5 Pa), which had unfavorable cooling conditions, aging time of 60 minutes, and presented negligible yield stress. On the other hand, experiment 4 ($\tau_0$ = 1,995 Pa), experiment 7 ($\tau_0$ = 1,000 Pa), and experiment 19 ($\tau_0$ = 632 Pa) had aging time set to zero, however, they presented significantly higher values of yield stress. These results do not imply that aging time is not important in the gelation process: they indicate that if the gel is formed in unfavorable conditions during the cooling step, the aging time will not impact or will impact weakly on yield stress. Another aspect is that the structure build-up is concentrated in the first minutes. Thus, even for the samples without aging time, it is possible to have structure build up in the last step of the rheological procedure, common to all experiments.

The yield stress distribution is given in Figure 54. It is possible to observe the lack of a clear pattern for both levels of aging time, which mathematically explains why this independent variable was computed as not significant in Equation 14. However, the average value of yield stress is 26% higher for 60 minutes of aging time. Also, the standard deviation is lower and more experiments are found inside the range of 500 to 1,500 Pa of yield stress when model oils were aged for 60 minutes. Figure 52 also shed some light on the influence of aging time in the gelation process. Regardless of the final cooling temperature assessed (12°C of 4°C), the same pattern was observed: there is a high amount of wax precipitated on the beginning of the isothermal holding (0 minutes), but If one looks closely in the details, it is possible to see a slight increase of precipitated wax in the images, for further isothermal holding times (30 min and 60 min). Therefore, it indicates rearrangements in the waxy gelled structure during isothermal holding time.

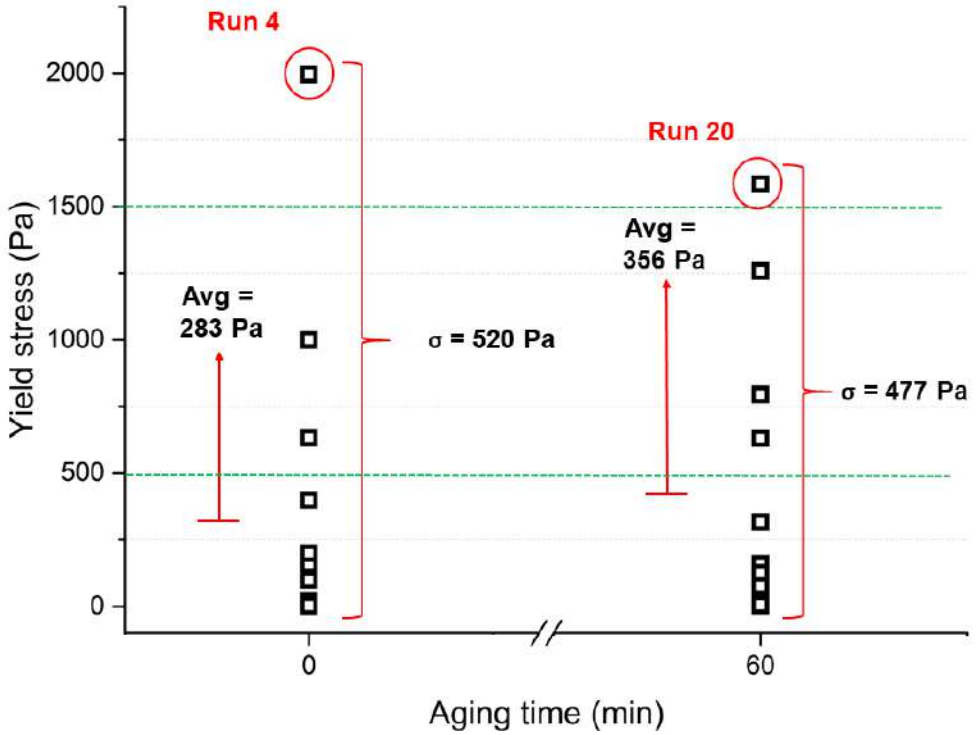


Figure 54 - Yield stress distribution for the aging time variable of 0 min and 60 min. Avg stands for the average yield stress and σ represents the standard deviation.

### 4.3.7 Storage Modulus and Yield Stress Correlation

In the flow assurance context yield stress is a key parameter. The storage modulus, however, has not the same relevance. These two different properties are not necessarily correlated. From a pragmatic engineering standpoint, storage modulus is related to the resistance of some material to being deformed elastically whereas yield stress can be regarded as the highest stress at which no flow is detectable. However, during the oil gelation, both properties are affected by the phenomena. Specifically, in this investigation, the storage modulus and yield stress arise from the interaction of precipitated wax crystals in a gelling fluid, due to the temperature drop. Therefore, it is expected a high correlation among them.

To investigate this assumption, the storage modulus in the linear viscoelastic region ($G'_{LVR}$, Table 9) was obtained. $G'_{LVR}$ was defined as the storage modulus averaged in the linear viscoelastic region, gathered from the last step of the rheological experiments (step 4, section 3.3.2, Figure 23 ). Figure 55 illustrates a typical result from the logarithmic stress ramp, where the yield stress is also obtained. At small values of oscillatory stress, there is a plateau for G' values corresponding to the linear viscoelastic region. Next, for higher values of oscillatory stress, there is a yielding region, corresponding to a

noticeable storage modulus decrease, until the structure ultimately broke, represented by the G' and G'' crossing point. All experiments presented similar profiles.

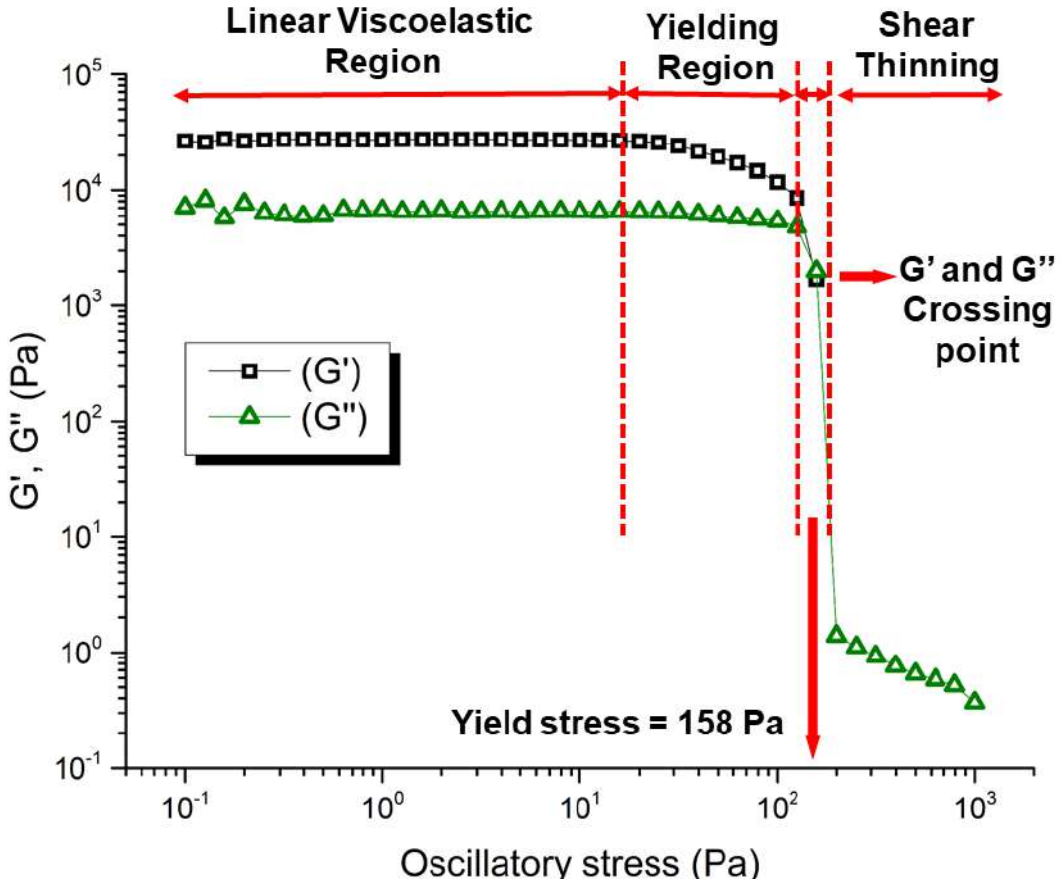


Figure 55 - Typical result from the logarithmic stress ramp (experiment 5, Table 3). $G'_{LVR}$ and yield stress are obtained in this step. The frequency was set to 1 Hz.

The correlation between storage modulus in the linear viscoelastic region and yield stress can be seen in Figure 56, which exhibits an almost linear proportionality. This correlation is more intense for higher values of the properties. The best result was achieved by nonlinear curve fitting with $R^2$ of 0.91. It was not possible to devise specific reasons for the larger deviation of experiments 18 and 31, circulated in Figure 56.

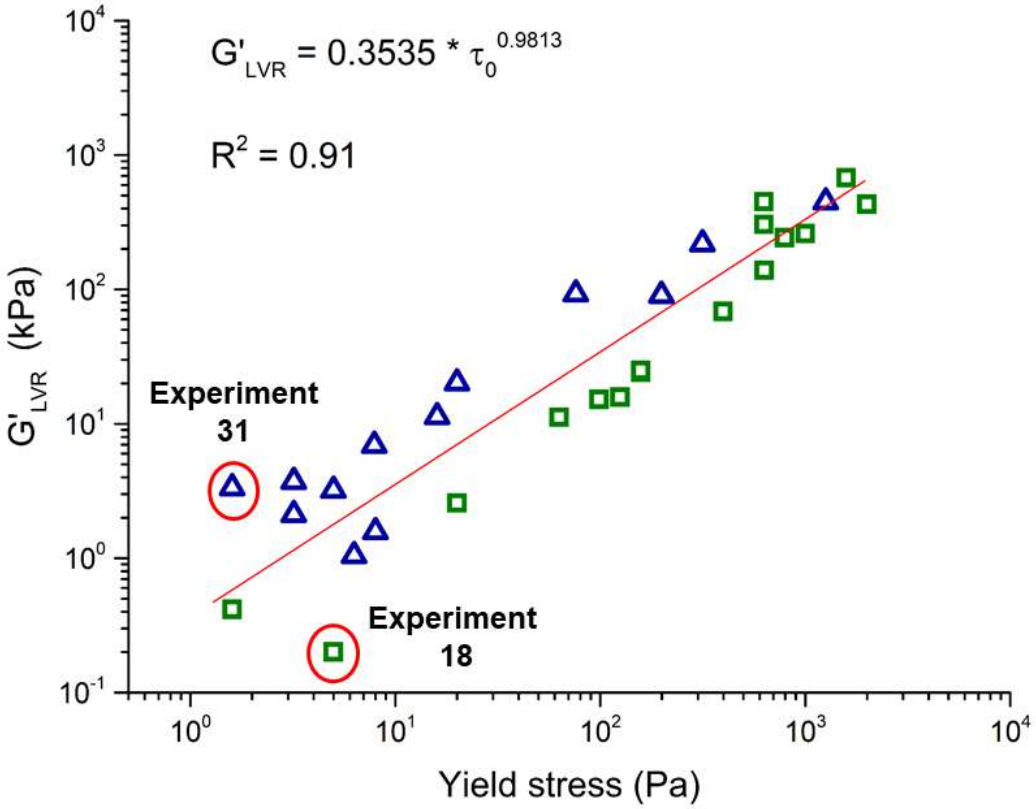


Figure 56 - Model oil yield stress and the respective storage modulus in the linear viscoelastic region. Blue triangles represent experiments with shear rate during cooling equals to 1.6 $s^{-1}$, whereas in green squares quiescent cooling was applied.

The relevance of this correlation lies in the fact that yield stress is not an easy measurement and highly dependent on the employed technique. It is not unusual to find variations in the results obtained from different methods with the same material [54], [160]. On the other hand, storage modulus is a readily obtained property, easier to measure and interpret. Thus, if one has a small data set (e.g. 10 experiments) where these two properties are available, simple equations can be obtained for yield stress estimation, through nonlinear data fitting. This is especially useful when a vast number of experiments need to be performed.

### 4.3.8 Structure Recovery

According to Wardhaugh and Boger [35], once the waxy oil is in a gel state, its yielding behavior is composed of three main characteristics: the elastic response, the slow deformation, corresponding to the yielding region, and the sudden and dramatic material fracture. This description fits well for all assessed model oils, as exposed in Figure 55. At this point, an important question to consider regards to events after the material

fracture. Is it possible that structural recover occurs, once favorable conditions emerge (e.g., isothermal holding time at low temperature and low disturbance)? According to Jia and Zhang [161], once destroyed, it is quite difficult for the waxy crude oil structure to recover to the initial state, because of poor reversibility. As will be discussed, this characteristic can exert great influence during pipeline start-up.

In order to investigate structural reversibility, model oils containing **$L_{29}$** 7.5 wt%, **$B_{53}$** 7.5 wt% and a blend of **$L_{29}$** + **$B_{53}$** (3.75 wt% + 3.75 wt%) wax were prepared and quiescently cooled from 50 to 4°C at 1.0°C/min in the rheometer. Next, the storage and loss modulus were captured for different levels of strain. Figure 57 summarizes the results for the blended system. It is possible to observe that for the 0.5% strain, applied in the first 15 minutes, the sample presented features of a gelled material, due to the high values of G' (~ 232 kPa) and also G' is higher than G''. As the imposed strain increased to 25%, there was a huge and immediate decay of the storage modulus to 89 Pa. In this new situation, G'' was noticeably higher than G', indicating predominant viscous behavior. After 30 minutes, when the strain returned to 0.5 %, both storage and loss modulus increased, although G'' still higher than G', implying that a gelled state was not reached. This profile was similar for the three compositions assessed, thus this behavior does not seem to depend on the wax chemical structures.

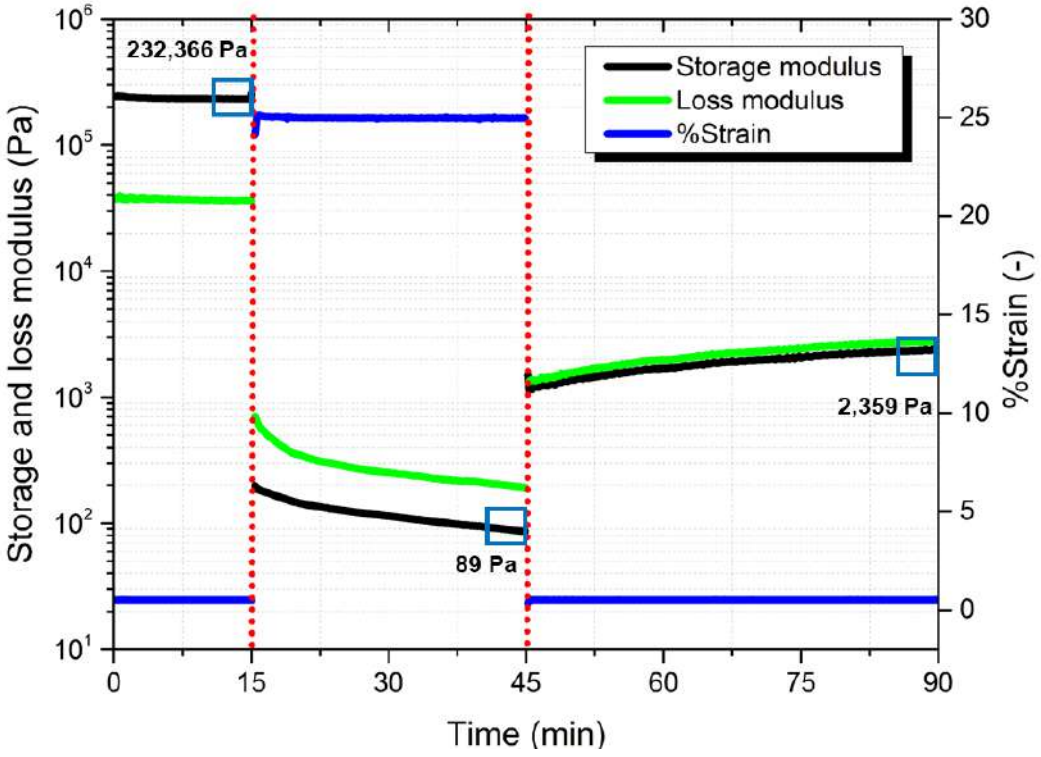


Figure 57 - Storage and loss modulus measured at 4°C at different imposed strain (0.5 % and 25 %) for gelled model oil **$L_{29}$** + **$B_{53}$** 3.75 wt% + 3.75 wt%. The sample was freshly prepared and quiescently cooled from 50 to 4°C at 1.0°C/min and frequency of 0.5 Hz.

The values of storage modulus in the last 5 minutes of each step were also averaged for quantitative analysis. Considering these averages, shown in the details of Figure 57, the recovery of storage modulus by the end of the last step was only 1.0% for the blended system. **$L_{29}$** and **$B_{53}$** model oils presented recovery of 1.4% and 3.9%, respectively. Hence, the obtained results clearly indicate poor structural reversibility, in accordance with Jia and Zhang [161].

In order to investigate if the reversibility was limited by the short time employed in the previous analysis (only 45 minutes for the recovery step), a long term experiment was performed with **$L_{29}$** 7.5 wt% model oil. In this case, after the 3 steps presented in Figure 57 the sample was submitted to an isothermal holding time of 60 hours at 4°C followed by another round of G' and G'' measurements. Next, the sample was submitted to the isothermal holding of 96 hours at 4°C and a final round of G' and G'' measurements were performed. All the results are gathered in Figure 58. One can observe similar results to the previously obtained for the first cycle of experiments regarding the freshly prepared sample. After 60 hours at 4°C, at 0.5% of strain, the storage modulus was slightly higher than loss modulus, indicating a gelled fluid, however about two orders of magnitude lower when compared to the G' for the freshly prepared sample. When the imposed strain is increased to 25% the storage modulus rapidly decreases to levels even lower than that reached by the sample freshly prepared. The same behavior was observed after 96 hours of isothermal cooling. In fact, regardless of the isothermal holding, the recovery in G' is very low, approximately 1.5% compared to the storage modulus of the sample freshly prepared.

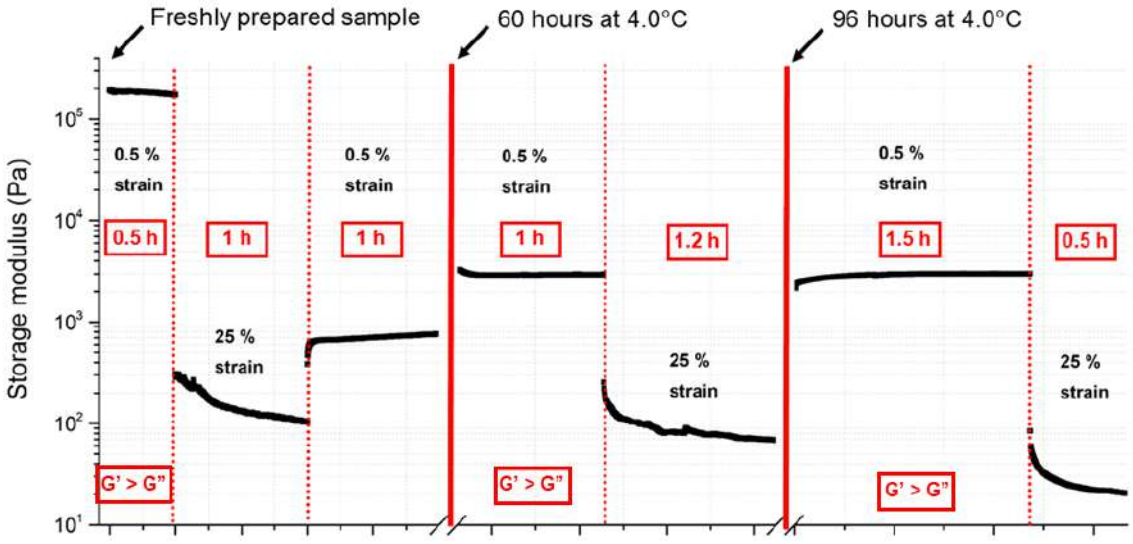


Figure 58 - Long term experiment to compare the storage modulus for a previous gelled

model oil **$L_{29}$** 7.5 wt% at different imposed strains (0.5% and 25%). The duration of each step varied from 0.5 to 1.5 hours and it is presented in the red boxes. The sample was freshly prepared and quiescently cooled from 50 to 4°C at 1.0°C/min and frequency of 0.5 Hz.

As could be observed, the rheological manifestation of structural changes due to the imposition of a strain translates in a variable storage modulus. Poor recovery of G' was obtained even after 96 hours at low temperature. The physical causes of irreversible changes might include the rupture of the strong aggregated waxy particles. The practical importance of this fact is that the storage modulus and yield stress are highly correlated. Thus, once the structure of waxy oils is broken, one might expect that even after a long shutdown period during oil production, the gelled structure will be no longer an obstacle for restart pumping operations.

### 4.3.9 Conclusions

An experimental investigation was performed with model waxy oils under gelling conditions. Two types of wax were employed, a predominantly linear (**$L_{29}$**) and a branched (**$B_{53}$**) wax. Spindle oil was used as a solvent. Experimental variables of cooling rate, wax content, shear rate during cooling, final cooling temperature and aging time were analyzed in rheological experiments. A factorial experimental design was devised in order to cope with a large number of effects simultaneously. The yield stress was set as the response variable. Crystal morphology was assessed through polarized light microscopy.

The effect of each variable was analyzed separately. According to the experimental design analysis, it was concluded that linear wax and branched wax have opposite effects in the yield stress value. **$L_{29}$** wax is able to enhance the yield stress and it was the biggest influence detected. On the other hand, **$B_{53}$**, a branched wax, presents a significant hindrance when trying to approximate to other wax molecules. Therefore, co-precipitation with **$L_{29}$** may generate a network with many voids, resulting in weak gelling. The shear rate during cooling presented a large impact. The higher is the value of this variable, the smaller is the yield stress. These results were confirmed by additional rheological experiments with waxy crude oil and W/O emulsion. The final cooling temperature was computed as a non-significant variable, probably due to the fact that all model oils were already in a gelled state before reaching the upper level of this variable (12°C). By the analysis of aging time variable, it was concluded that the most important

step for yield stress value is the cooling. If unfavorable conditions are present at the cooling stage (e.g. a small amount of wax and/or shearing conditions at cooling), the aging time will not affect the yield stress meaningfully.

It was demonstrated that storage modulus and yield stress have a high correlation. A set of 32 experiments was employed and a fitting equation was proposed with $R^2$ of 0.91. As the storage modulus is a readily obtained property, it can be used as an alternative method to estimate yield stress.

Finally, long term experiments demonstrated that waxy oils have poor structural reversibility. The analysis was conducted in terms of storage modulus, although the conclusions can be expanded to the yield behavior since it was demonstrated that G' and yield stress are strongly correlated. It means that once the structure of waxy oils is broken, one might expect very small yield stress even after long shutdown periods. The obtained results disclose the relative importance of these variables on the viscoelastic properties of the gelled oils. The presented information may be useful for start-up prediction and/or the feasibility of a remediation procedure aimed at helping the removal of wax plugs.

## 4.4 Influence of Wax Chemical Structures at Yield Stress

The rheological properties of waxy gels have important technological implications. Effective strategies to prevent and remediate paraffin deposition and wax plugging, including the developing of more accurate deposition models, demands a solid understanding of the relationship between structure and mechanical properties. Thus, it is important to investigate how the gel characteristics are affected by oil composition.

In order to assess the relationship of the wax chemical structure and viscoelastic properties of waxy gels, model oils composed of single and blended waxes were prepared at a fixed composition of 7.5 wt% and then gelled. The investigation encompassed four different well-characterized commercial waxes (see section 4.1), solubilized in a spindle oil matrix. Among the employed waxes, two are predominantly linear whereas the others are non-linear branched molecules. Previous rheological measurements demonstrated that these systems reproduce essential features of crude oil gels when submitted to a cooling protocol, e.g. gel-like mechanical response. Rheological properties were measured at a controlled-stress rheometer by oscillatory shear experiments. It was found once more (see section 4.3.7) that yield stress and storage modulus are highly correlated ($R^2 = 0.94$).

### 4.4.1 Measurements of WPT, Yield Stress, $G'_{LVR}$ and $\gamma_{CR}$

Model oils composed by $\mathbf{L_{24}}$, $\mathbf{L_{29}}$, $\mathbf{B_{37}}$ and $\mathbf{B_{53}}$ waxes solubilized in spindle oil were employed to evaluate the influence of the chemical structure and provide insight into crystal-crystal interactions. The composition was set to 7.5 wt% for each system. Blended systems employed 3.75 wt% of each wax.

For temperatures above a threshold limit, known as Wax Precipitation Temperature (WPT), the waxy oils behave as simple fluids without elasticity, due to none (or almost none) waxy crystals presence. This scenario corresponds to the step [1] of the rheological tests performed (see details in section 3.3.3). However, the viscosity of the system begins to increase as they undergo a cooling process with the temperature reaching the WPT and further lower values (step [2] of the rheological tests). Different techniques have been developed to measure the WPT based on DSC, near-Infrared spectroscopy, nuclear magnetic resonance spectroscopy, and optical microscopy [39], [86], [162]. In this work, this measurement was based on rheological data. Despite existing comparative studies in the literature suggesting that rheometry measurements underestimate the Wax Precipitation Temperature [39], [163], this fact is not a particular

concern in this study, since we are comparing WPT values based on the same metric. The WPT was defined as the onset temperature where there is a sudden viscosity change evident on a linear scale plot [39]. This behavior is exhibited in Figure 59 for three different model oils. As a consequence of the continuous precipitation (especially at quiescent conditions), the crystal-crystal interactions lead to the formation and spanning of a waxy-gel network (step [3] of the rheological tests). As the cooling rate directly affects the gelation process and consequently the yield stress value [13], it was kept at 1.0°C/min at all rheological tests performed in this section.

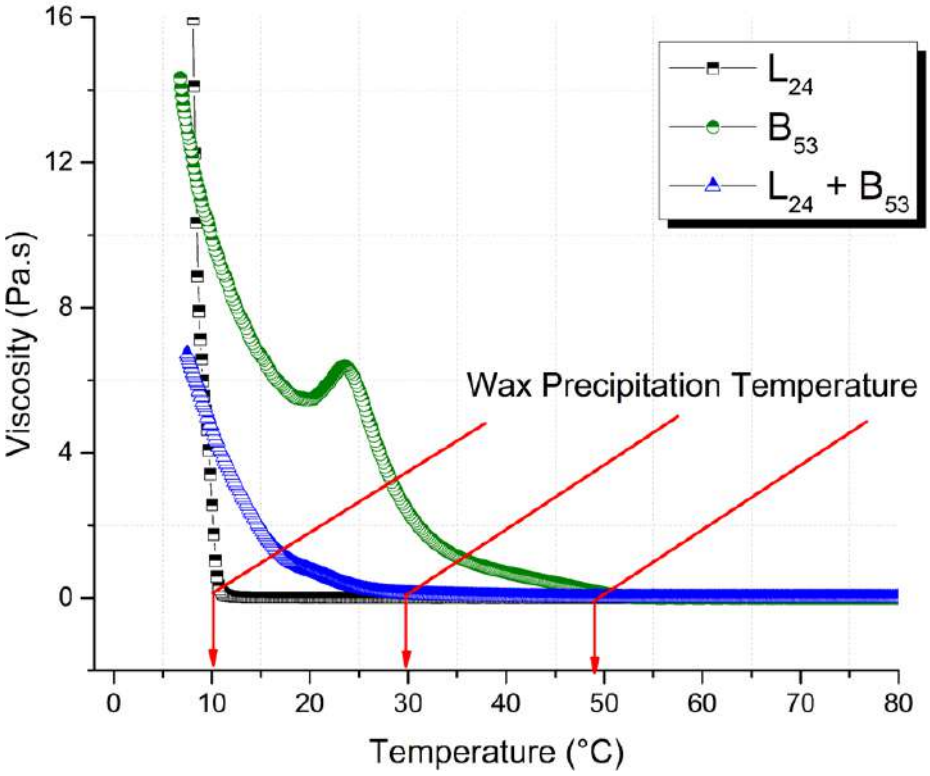


Figure 59 - Viscosity behavior during the cooling process of **$L_{24}$**, **$B_{53}$** and **$L_{24}$** + **$B_{53}$** model oils with 1.0°C/min rate and shear rate of 0.8 $s^{-1}$.

The gelled oils have a viscoelastic structure that responds to the stress exhibiting a yielding region. At oscillatory amplitude sweep tests, this region comprises the onset departure of the storage modulus from the linear viscoelastic region and the crossing point of G' and G''. The yielding of gelled oils can be suitable captured by step [4] of the rheological tests performed and is exhibited in Figure 60.

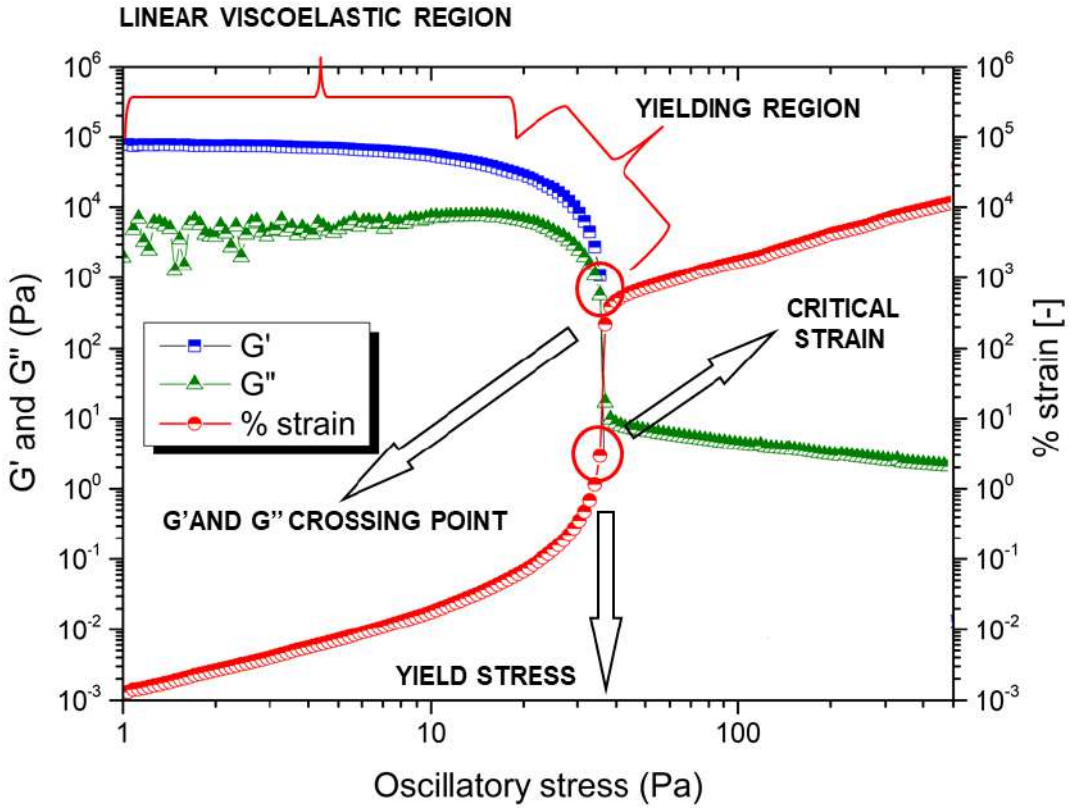


Figure 60 - A profile of the logarithmic stress sweep used to obtain $\tau_0$, $G'_{LVR}$ and critical strain values (oscillatory stress ranging from 0.1 to 1,000 Pa at 0.1 Hz frequency).

In this work, the yield stress is taken as the oscillatory stress for the crossing point of G' and G'' which, as already stated, provides a reasonable and fast method to probe a wide experimental range. Also, it is important to highlight that gelled oils have a viscoelastic structure that responds to the stress exhibiting a yielding region. At oscillatory amplitude sweep tests, this region comprises the onset departure of the storage modulus from the linear viscoelastic region and the crossing point of G' and G''. Thus, there is a region of yielding, not a single point. Despite that, for process timescales such as production, transportation, and storage of waxy crude oil the yield stress is a practical reality and it can be essentially defined as the point at which, when increasing the applied stress, the solid first shows liquid-like behavior, i.e. continual deformation [94].

Another useful property obtained from the step [4] is the storage modulus in the linear viscoelastic region ($G'_{LVR}$). At temperatures larger than WPT $G'_{LVR}$ is very small, meaning that the concentration of precipitated wax crystals is not large enough to build a strong gel structure. With the decrease of the test temperature, the storage modulus increases greatly because of the continuous precipitation of wax crystals.

The method described by Yang et al. [125] for $G'_{LVR}$ calculation implies an obvious decrease in storage modulus and it may be subjected to different perceptions. Thus, a Matlab® code was developed in order to establish a numerical criterion and compare the results of $G'_{LVR}$ with those obtained from visual inspection. The code calculates the property through the average of storage modulus values inside a specified boundary defined and updated on the basis of the current G' value in the vector. The calculation stops when the first G' value is found outside the boundary. This boundary can be adjusted based on a collect criterion (δ). For example: if the collect criterion that defines the boundaries is set to 1.0%, the next $G'_{i+1}$ value must be at most 1.01*$G'_i$ and at least 0.99*$G'_i$. Figure 61 illustrates the Matlab® code developed.

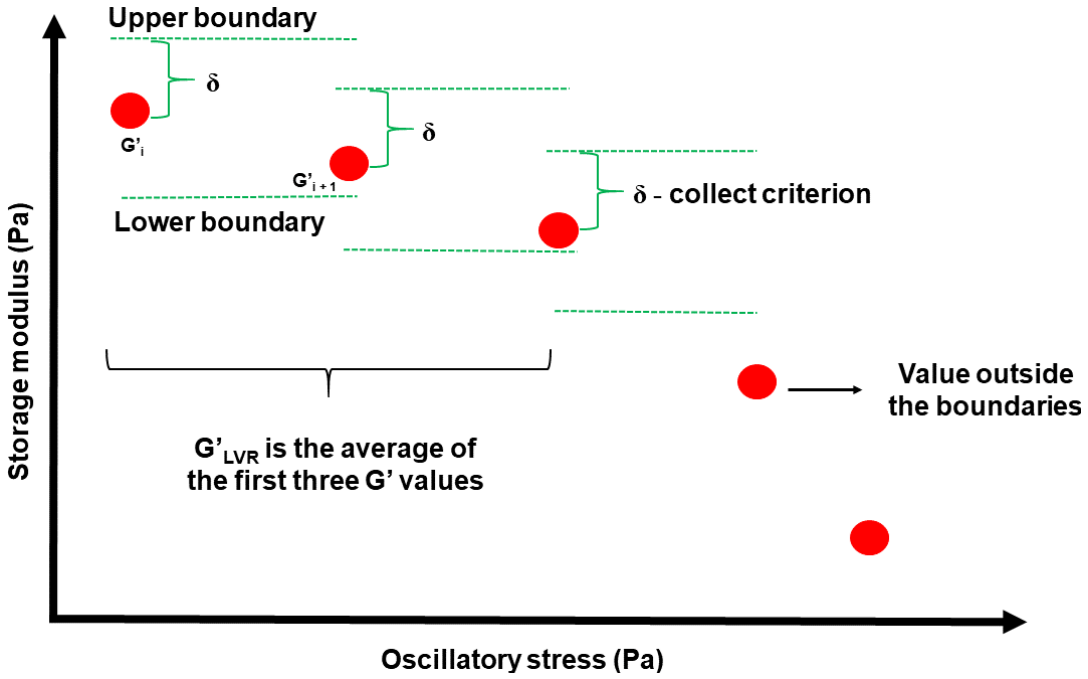


Figure 61 – Graphical representation of Matlab® code used for $G'_{LVR}$ calculations.

Both values of δ = 1.0% and δ = 2.0% produced $G'_{LVR}$ results very similar to those calculated from visual inspection. The good agreement indicates that visual inspection can be a fast and reliable method for $G'_{LVR}$ calculation.

Finally, the critical strain ($\gamma_{CR}$) is defined in this study as the maximum value of shear strain captured before a complete material rupture, which is represented by an abrupt increase of the strain located among the yielding region and G' and G'' crossing point (see Figure 60). When the oscillatory stress is low the strain increases linearly because the material is in the linear elastic region. When the loaded stress increases above a certain value, G′ decreases but the strain increases exponentially, meaning that the gelled structure is partly destroyed. The $\gamma_{CR}$ is, therefore, defined as the maximum shear strain in this yielding region. It is important to note that this definition is slightly different

from the critical elastic strain, which is the value of maximum shear strain in the linear elastic region [95], [125], thus a smaller value than the critical strain.

### 4.4.2 Single Wax Model Oils

Table 12 summarizes the results obtained from rheological tests in terms of yield stress, wax precipitation temperature, storage modulus in the linear viscoelastic region, critical strain and cohesive energy density.

Table 12 - Rheological properties and cohesive energy density ($E_c$) of waxy gels.

| Model oil | Yield stress (Pa) | WPT (°C) | $G'_{LVR}$ (kPa) | Critical strain (%) | $*E_c$ ($J/m^3$) |
|---|---|---|---|---|---|
| **$L_{24}$** | 112.5 ± 10.7 | 10.6 | 82.426 | 0.3795 | 5.934 |
| **$L_{29}$** | 199.5 ± 31.2 | 27.3 | 319.89 | 0.2154 | 7.420 |
| **$B_{37}$** | 8.43 ± 0.92 | 34.3 | 3.304 | 0.3236 | 0.173 |
| **$B_{53}$** | 26.7 ± 5.5 | 48.6 | 14.407 | 0.5311 | 2.032 |
| **$L_{24}$** + **$L_{29}$** | 223.9 ± 27.9 | 21.5 | 305.28 | 0.0910 | 1.265 |
| **$B_{37}$** + **$B_{53}$** | 2.99 ± 0.54 | 35.1 | 1.548 | 0.1017 | 0.008 |
| **$L_{24}$** + **$B_{37}$** | 335.1 ± 30.5 | 20.1 | 179.07 | 0.1876 | 3.152 |
| **$L_{24}$** + **$B_{53}$** | 630.2± 40.4 | 28.2 | 214.64 | 0.1740 | 3.250 |
| **$L_{29}$** + **$B_{37}$** | 134.4 ± 16.9 | 19.7 | 116.01 | 0.1290 | 0.965 |
| **$L_{29}$** + **$B_{53}$** | 266.7 ± 16.3 | 29.2 | 164.40 | 0.1692 | 2.354 |

*cohesive energy density obtained at 4°C, defined according to Equation 15 [95].

For systems prepared with single wax, the yield stress was favored by an increase in chain length for predominantly linear and branched wax when compared separately. This is possible due to the earlier precipitation of longer wax molecules which favors the molecule packing and guarantees more available nuclei for crystallization. In this reasoning, the longer is the saturated linear chain the higher is the WPT, which in fact is observed by comparing the WPT values for **$L_{24}$**, **$L_{29}$**, **$B_{37}$** and **$B_{53}$** (10.6°C, 27.3°C, 34.3°C and 48.6°C, respectively). Although, non-linear alkanes might reduce the gel strength

[31], [77]. As the interlocking network resulting from the gelation process relies on crystal-crystal interactions, it is reasonable to argue that branching points reduce gel strength, since crystal interactions may be hampered. Therefore, the highest WPT value for the branched **$B_{53}$** wax does not guarantee the highest yield stress, which suggests a competitive effect among carbon chain length and tertiary carbons presence. Thus, it is important for further evaluations do not dissociate the impact of these two structural features at rheological properties. In this basis, the very low yield stress for the **$B_{37}$** system might be due to the number of branches (2.71 per linear saturated aliphatic chain) in relatively narrows carbon chains when compared to **$B_{53}$**. Figure 62 exhibits the yield stress as a function of model oil compositions.

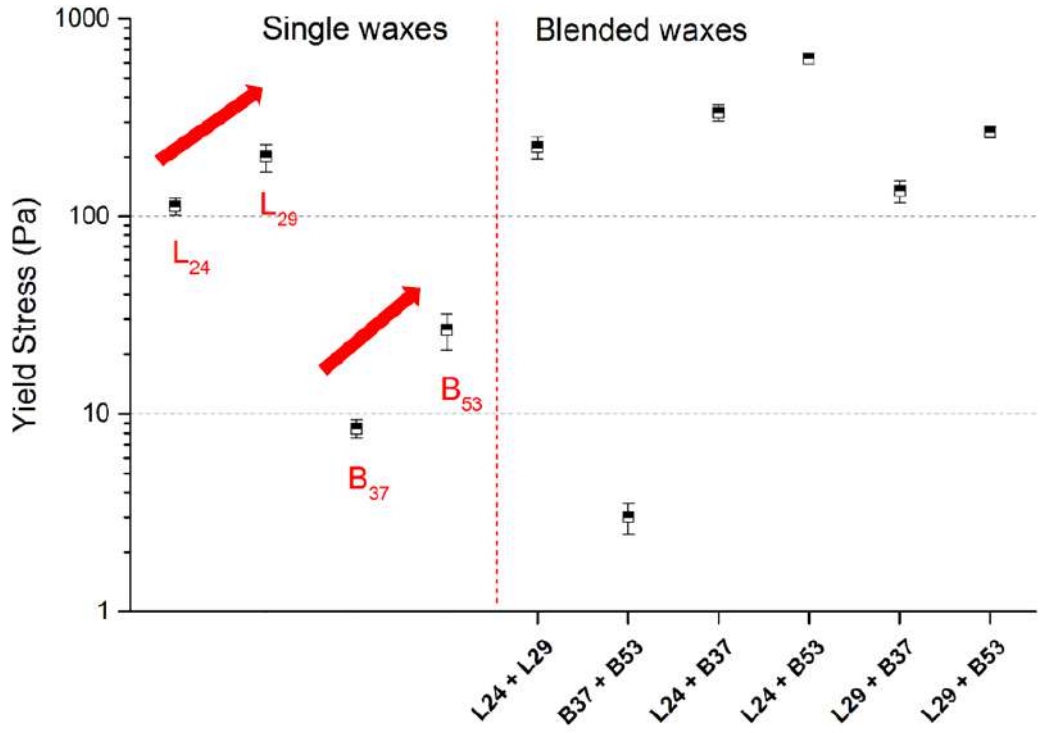


Figure 62 - Model oils yield stress for singles waxes (left) and blended waxes (right).

The correlation of yield stress and storage modulus for the data contained in Table 12 is exposed in Figure 63. As one can observe there is an almost linear proportionality between the yield stress and $G'_{LVR}$ for single and blended model oils since $R^2$ is 0.94 and the fitting equation exponent (1.0801) is very close to the unity. Considering that the storage modulus is also affected by the material internal structure, the previous reasoning applied to yield stress is applicable to $G'_{LVR}$. Similar findings are shown in section 4.3.7 for a bigger data set and different model oil compositions.

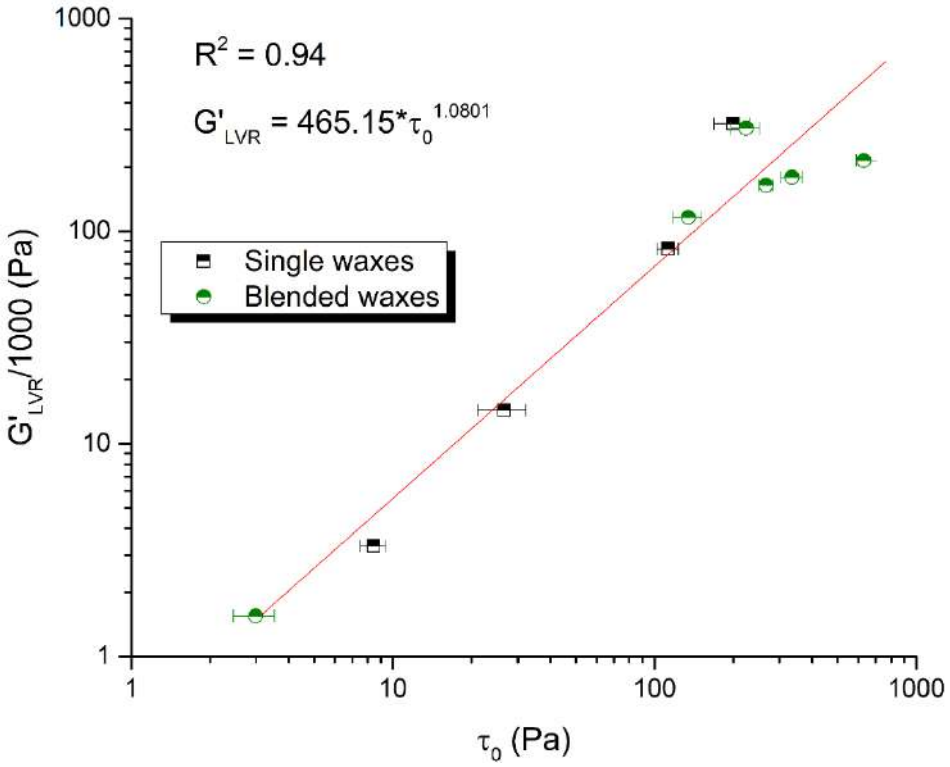


Figure 63 - $G'_{LVR}$ and yield stress correlation for single wax and blended waxes model oils.

An incipient idea of the relationship between storage modulus and yield stress is presented by Lopes-da-Silva and Coutinho [44] in the investigation of the gel structure development under quiescent conditions for three different waxy crude oils. Mendes et al. [12] presented quantitative correlations between G' and yield stress for a Brazilian waxy crude oil, using small amplitude oscillatory tests to obtain the rheological data. The authors observed analogous behavior for G' and gel yield stress development at static cooling conditions. For mixed cooling conditions (i.e., dynamic and static conditions employed during cooling) the linear relation between those two properties was not so clear. Although, it could be devised a global tendency, showing that the higher the storage modulus, the higher the yield stress. The importance of such results is well stated by the authors: "If a relation between G′ and yield stress can be drawn, it can be useful as a method for reducing the number of experiments to detect yield stress tendencies with respect to some cooling parameter". Fernandes et al. [164] also presented similar reasoning for samples of oil-based drilling fluid that exhibits a complex rheological behavior, i.e., elasticity, viscoplasticity, and thixotropy. The authors proposed a correlation between the stress overshoot observed in flow start-up rheometric experiments and the storage modulus, obtained during a low amplitude oscillatory sweep over the aging time. The results showed an excellent agreement for the linear

relationship of these two properties, with error bands of 10% in a range of shear rates varying from 0.5 to 50 $s^{-1}$. At the best authors' knowledge, there are at least three complex materials (drilling fluids, waxy crude oil, and model waxy oil) that presented a correlation between storage modulus and yield stress.

Another analysis can be drawn in terms of cohesive energy. This property is related to the interaction energy among wax crystals molecules and generally, the stronger it is, the higher is the intensity of association formed by hydrophobic groups [165], [166]. Non-linear alkanes do not pack as closely together as linear waxes. Their cohesive energy is thus weaker than those observed for their linear counterparts. Table 12 contains the values of cohesive energy densities, $E_c$, which is essentially the driving force of the ordering transformation from soft to hard wax in the gelation process. These values were calculated from $G'_{LVR}$ and $\gamma_{CR}$ (step 4[c], section 3.3.3) based on Equation 15 [95]:

$$E_c = {}^{1}/_{2} * \gamma_{CR}^{2} * G'_{LVR} \qquad \text{Eq. (15)}$$

It is observed that the values of $E_c$ follow the same trend of yield stress. The branched wax **$B_{37}$** presented the lowest $E_c$ value (0.173 J/$m^3$). This indicates that these wax molecules would be less available to aggregate together, thus significantly lowering their cohesive energy as well as their chances to nucleate wax crystallization. In fact, the structural features of **$L_x$** and **$B_x$** wax affect the yield stress, $G'_{LVR,}$ and the cohesive energy similarly, which can be observed from Table 12. According to Tadros [95], the cohesive energy is also the most sensitive parameter for the assessment of coalescence. Any coalescence will result in a decrease in the number of contact points and cause a reduction in $E_c$.

### 4.4.3 Blended Wax Model Oils

Rheological properties and cohesive energy density are available for blended wax systems in Table 12. As can be noticed, the WPT values for systems containing **$L_{24}$** are approximately the average between the WPT for each wax that composes the respective blend. This is clearly seen in Figure 59: the WPT for **$L_{24}$**, **$B_{53}$** and **$L_{24}$** + **$B_{53}$** model oils are 10.6 °C, 48.6 °C, and 28.2 °C, respectively. Since the WPT is sensitive to the carbon number distribution [8], it is clear that occurred a shift in this distribution for blends containing **$L_{24}$**. It suggests that, in these cases, the waxes were completely associated during the precipitation. However, for the association of **$B_{37}$** + **$B_{53}$**, **$L_{29}$** + **$B_{37}$** and **$L_{29}$** + **$B_{53}$**

it is observed that the WPT corresponds to approximately the same WPT value of the smaller wax in the blend (e.g., the WPT for **$L_{29}$**, **$B_{53}$**, and **$L_{29}$** + **$B_{53}$** model oils are 27.3 °C, 48.6 °C, and 29.2 °C, respectively).

The yield stress for the **$L_{24}$** + **$L_{29}$** blend is statistically equivalent to the single **$L_{29}$** model oil. As **$L_{24}$** and **$L_{29}$** waxes comprise mainly linear saturated aliphatic chains and few obstacles are present for favored interactions (such as branching points) it is comprehensible that the yield stress of this blended system matches the yield stress of the longer wax. Nevertheless, for **$B_{37}$** + **$B_{53}$** the yield stress is negligible. The branched nature of these two waxes associated with an unfavorable combination of main chain lengths is likely to be responsible for this result. It is expected that branched wax molecules with ~ 37 carbon atoms experience a huge hindrance when trying to approximate to wax molecules with ~ 53 carbon atoms, thus a network with many voids is formed resulting in the weak gelling. Similar results were presented by Senra et al. [167]. The authors investigated model oils prepared exclusively from linear wax in dodecane and considered the effect of cocrystallization on the gelation characteristics of the samples. According to them, when two or more materials crystallize together, the crystal formation will not be as perfect as a single material forming a crystal structure because of their differing sizes. The different chain lengths provide defects and weaknesses in the crystal structure. Although, as revealed in the investigation, some compositions are prone to cocrystallize whereas other associations seem to be not affected by the added alkane.

For **$L_{24}$** + **$B_x$**, both blends had an increase in yield stress, comparing to the single **$L_{24}$** model oil. Combined with **$B_{53}$** the yield stress for this blend increased 462 % comparing to the single **$L_{24}$** system. In the case of **$L_{24}$** + **$B_{37}$**, the yield stress is 199 % higher. It is clear that the rheological properties of a waxy gel are influenced by the nature of interactions between the microstructural components occurring at the junction zones, which exist between intersecting crystal branches or entangled crystal lamellas. In this regard, the reasoning is as follows: since **$B_{53}$** has very large carbon main chains, the branches might be located apart from each other. In this case, small linear waxes are able to arrange itself between the branch points, thus the crystal interactions would just be slightly affected by these branches. Considering that **$B_{37}$** is smaller and more branched than **$B_{53}$**, this arrangement is less likely, except for very small chain waxes molecules.

To support the above argument, one can consider the worst possibility (in terms of wax-wax interactions) for the positions of tertiary carbons in a branched molecule: the

branches are equally spaced. In this case, the ratio of main chain length/branches per linear chain provides the space available between branching points. For **$B_{37}$** this ratio is 15.5 and for **$B_{53}$**, 21.9 (calculated from $^{13}$C-NMR data, Table 5). Thus, it is more likely that small molecules (such as **$L_{24}$** wax) would be able to arrange itself among **$B_{53}$** branches, thus enhancing London-Van der Waals interactions (more than at **$B_{37}$**). It can be seen by **$L_{29}$** + **$B_{37}$** blend: as both waxes have carbon chains with similar size, the hindrance is much more pronounced, reflecting a decrease in yield stress of 33 % compared to **$L_{29}$** single systems.

In terms of critical strain, Table 12 provides values for blended model oils. Comparing the critical strain of single and blended systems, one can conclude that waxy gels formed from single wax are more deformable. Interestingly the branched wax **$B_{37}$** and **$B_{53}$** have relatively high critical strain values and low values for storage modulus. On the other hand, **$L_{24}$** + **$L_{29}$** and **$B_{37}$** + **$B_{53}$** blended systems have a very similar critical strain (0.0910 and 0.1017, respectively) and completely different storage modulus (305.28 kPa and 1.548 kPa, respectively). Also, for the single wax samples, there is no clear correlation between the critical strain values and any other property in Table 12. On the other hand, for blended systems, the higher critical strain can account for the higher cohesive energy densities, as these two properties are fairly linearly correlated ($R^2$ = 0.79).

Regarding cohesive energy density, Figure 64 illustrates how this property is related to yield stress for all systems assessed. Single wax and blended systems were divided into two datasets since in both cases the $E_c$ seems to be linearly correlated to the yield stress, however with a different angular coefficient. The $R^2$ value is higher for single wax (0.90) when compared to blended systems ($R^2$ = 0.75), however, the number of points for single wax is smaller, thus it is not easy to state which curve is fitting best. The behavior of $E_c$ for single wax systems is somehow easy to follow: the bigger the linear main chain and the fewer the branches, the higher is the cohesive energy density and yield stress. On the other hand, blended systems were able to achieve the highest yield stress values. It indicates that in terms of cohesive energy the interactions among waxes of the same nature are more favorable.

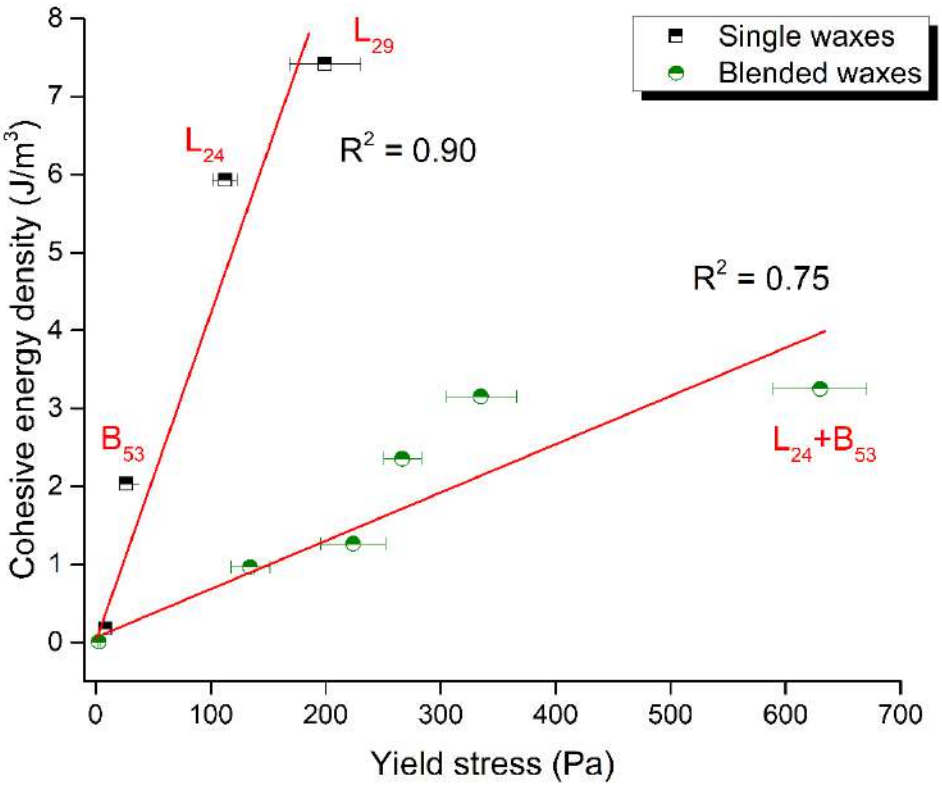


Figure 64 - Cohesive energy density as a function of yield stress for single waxes and blended waxes systems.

For **$B_{37}$** + **$B_{53}$** blend the $E_c$ value is very low (0.008 J/m$^3$), representing a 99.6 % decrease compared to **$B_{53}$** single wax. According to Jang et al. [168] the cohesive energy density of the crystalline wax is much smaller in the presence of molecules that are able to act as an inhibitor of wax crystallization (comb-like polymers in the case studied) and their presence perturbs or retards the ordering transformation of the amorphous wax aggregate into an ordered phase [168]. In this regard, the branched **$B_{37}$** may act as a wax inhibitor for sufficient large wax molecules (e.g. **$L_{29}$** or **$B_{53}$** wax).

### 4.4.4 Conclusions

Model oils consisting of predominantly linear and non-linear branched waxes dissolved in mineral oil were investigated. Rheological measurements showed that these systems reproduce essential features of crude oil gels (e.g. exhibiting a low-temperature gel-like mechanical response to an imposed low-frequency oscillatory stress). Therefore, they were employed to verify and further probe the processes involved in the formation of wax crystal aggregates and the influence of wax chemical structures.

The results indicated that for a better interpretation of yield stress, the chain length and

the degree of branching may not be taken separately. The presence of branch points at the linear saturated aliphatic chains is likely to be responsible for a reduced crystal-crystal interaction, consequently lowering the yield stress. On the other hand, an increase in the chain length showed the opposite effect. Therefore, it is important for further evaluations do not dissociate the impact of these two structural features at rheological properties.

For blended systems the small-chain linear wax was able to interact favorably with the long-chain non-linear wax (**$L_{24}$** + **$B_{53}$**), possibly due to its ability to accommodate within the later molecule, ensuring the highest yield stress value (630.2 Pa). The wax structural arrangement of 37 carbon atoms on average (**$B_{37}$**), including approximately three tertiary carbons, was effective for lowering the yield stress of particular blended systems.

The lowest viscoelastic properties were measured for a blended system composed by non-linear waxes, which was also characterized by the smallest and rounded crystals visible by optical microscopy (see section 4.1.8).

The rheological results indicated that **$B_{37}$** wax may act as a wax inhibitor for sufficient large wax molecules (e.g., **$L_{29}$** or **$B_{53}$**), but increases the yield stress of gels of a shorter wax molecule (**$L_{24}$**). Its presence may perturb or retard the ordering transformation of the amorphous wax aggregate into an ordered phase for large molecules such as **$L_{29}$** or **$B_{53}$**, which are not able to arrange itself linearly among the branch points of **$B_{37}$**. The large branched wax, **$B_{53}$** increased the yield stress of the two predominantly linear waxes, but its interaction with another branched wax **$B_{37}$** did not show any appreciable yield stress enhancement.

## 4.5 Scaling Models for Gelled Waxy Oils

In this section, the effect of the wax concentration, microstructure characteristics and rheological response of gelled waxy oils is discussed from the perspective of the scaling theory. A mathematical model that relates the microscopic structure and the elastic properties of model oils **$L_{29}$** and **$B_{53}$** 7.5 wt% was derived from rheology and DSC results. For gelled waxy oils, the particle concentration is the mass fraction of precipitated wax crystals ($\Phi_w$) which frequently increases with decreasing the oil temperature [1]. Then, the structural development during the cooling process can be monitored by measuring the elastic properties of the sample. In addition, the fractal dimension, which is helpful to better understand the microstructure of gelled oils, can be obtained by discussing the relationships of $G'_{LVR}$ and the critical elastic strain ($\gamma_E$) to the mass fraction of precipitated wax.

It is important to mention that the definitions for the critical strain ($\gamma_{CR}$), presented in section 4.4.1, and the critical elastic strain ($\gamma_E$) are slightly different. As can be seen in Figure 65, which shows the oscillatory stress sweep of a model oil **$L_{29}$** 7.5 wt% at 4°C, the storage modulus remains close to a steady value and the strain increases linearly when the oscillatory stress is in a low range (below ~ 60 Pa). It indicates the linear elastic region. Nonetheless, when the loaded stress increases above a certain value, G′ begins to decrease obviously while strain increases nonlinearly, meaning that the gel structure is partly destroyed by the loaded stress and the gelled oil comes into the nonlinear viscoelastic region. The critical elastic strain is obtained at this moment and defined as the value of maximum shear strain in the linear elastic region [95], [125]. A further increment in the stress ultimately leads to the complete structural breakage, marked by a sharp increase in the strain value.

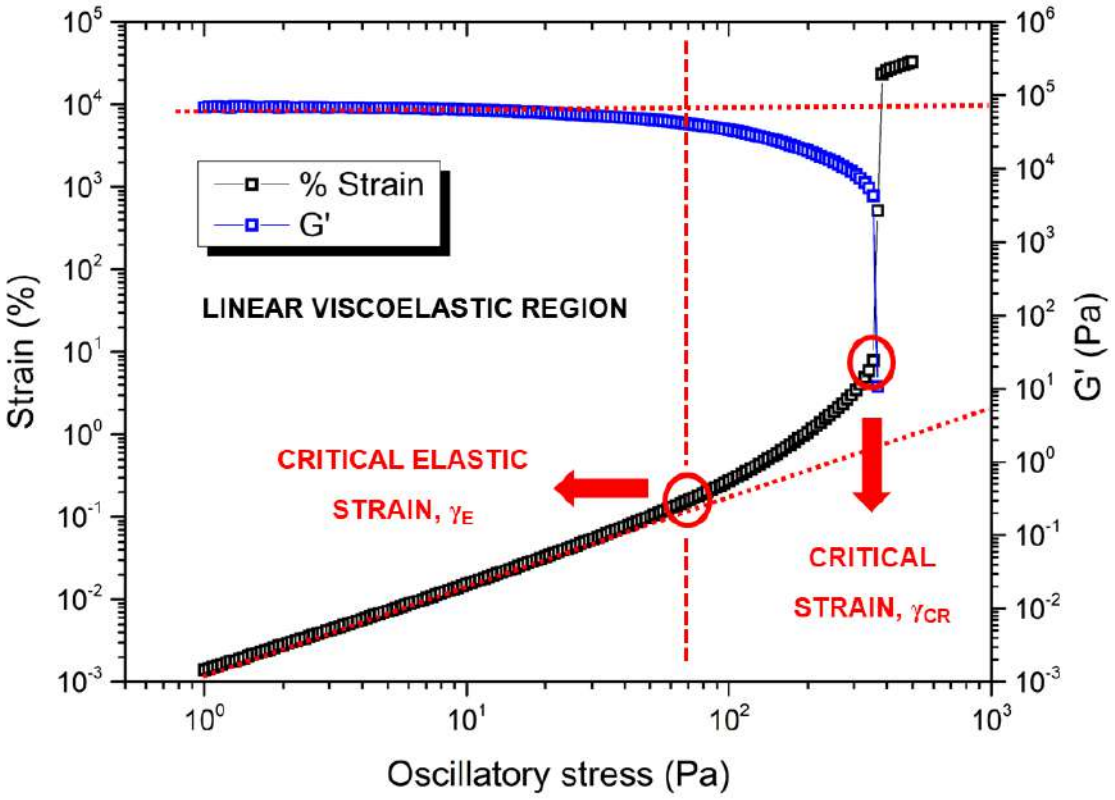


Figure 65 - Strain and storage modulus as a function of oscillatory stress for a gelled model oil **$L_{29}$** 7.5 wt% at 4°C. Oscillatory stress ranged from 0.1 Pa to 500 Pa at a frequency of 1 Hz.

A fundamental assumption to derive the scaling models is that the structure of the gels is constituted by a stochastic mass of fractal flocs, which during gelation aggregate with each other (e.g., see Figure 19). Therefore, both the storage modulus in the linear viscoelastic region and the critical linear elastic strain of the gel are expected to scale as a function of the particle concentration [69]. In the framework of the theory, two regimes are proposed. In the strong-link, the interfloc links are stronger than the intrafloc links, and the macroscopic elasticity of the gel is given by that of intralinks [125]. The relations for the elastic properties in the strong-link regime are presented in Equation 16 and Equation 17 [69]:

$$G'_{LVR} = \Phi_w^{\left(\frac{d+x}{d-D}\right)} \quad \text{Eq. (16)}$$

$$\gamma_E = \Phi_w^{\left(\frac{-1-x}{d-D}\right)} \quad \text{Eq. (17)}$$

where $d$ is the Euclidean dimension (for a 3-D system, $d = 3$), $D$ is the fractal dimension of the flocs, and $x$ is the backbone fractal dimension. Thus, from experimentally measured values of $G'_{LVR}$ and $\gamma_E$ as a function of the mass fraction of precipitated wax crystals, it is possible to estimate the values of the scaling exponents from a log-log plot and obtain the fractal dimension and the backbone fractal dimension. Thus, it is said that scaling theory enables the extraction of structural information from the rheological measurements.

In the weak-link regime, where the elasticity of the interfloc links determines the elasticity of the gel, the scaling behavior for $G'_{LVR}$ and $\gamma_E$ is given by Equation 18 and Equation 19, respectively [69]:

$$G'_{LVR} = \Phi_w^{\left(\frac{d-2}{d-D}\right)} \quad \text{Eq. (18)}$$

$$\gamma_E = \Phi_w^{\left(\frac{1}{d-D}\right)} \quad \text{Eq. (19)}$$

As the Euclidian dimension is three for a 3-D system, the same scaling exponent is considered for both properties. Also, comparing Equation 19 to Equation 17, one can see that in the weak-link regime the critical elastic strain increases with increasing mass fraction, whereas in the strong-link regime it decreases.

The mechanical response is readily given in terms of storage modulus and elastic strain through rheological experiments (see section 3.3.4). On the other hand, the mass fraction of particles at different temperatures can be calculated on the basis of the DSC curves according to the method described by Chen et al. [88]. These authors studied 14 crude oils with wax content ranging from 1 to 27 wt%. Firstly, they obtained the wax content of each sample by a slightly modified version of the standard acetone method (UOP method 46–64). Then, the isolated waxes were used in DSC experiments to demonstrate that the ratio of the "crude oil total thermal effect" to the "isolated waxes total thermal effect", i.e., $Q_{oil}/Q_{wax}$, provided values of wax content equivalent to that obtained by the acetone method, with an absolute average deviation of only 0.82 wt%.

Considering that model oils are much simpler systems, a similar method as described by Chen et al. [88] can be applied. Thus, it is possible to calculate the mass of precipitated wax crystals at some specific temperature (e.g., $T_x$) by computing the ratio of the "model oil thermal effect between the WPT of the model oil and $T_x$" to the "total thermal effect of the pure wax", i.e. $Q_{model\ oil\ at\ Tx}/Q_{pure\ wax}$. The thermal effects can be

computed by integrating the area under the DSC calorimetric signal curve with suitable software. Figure 66 summarizes the procedure described above.

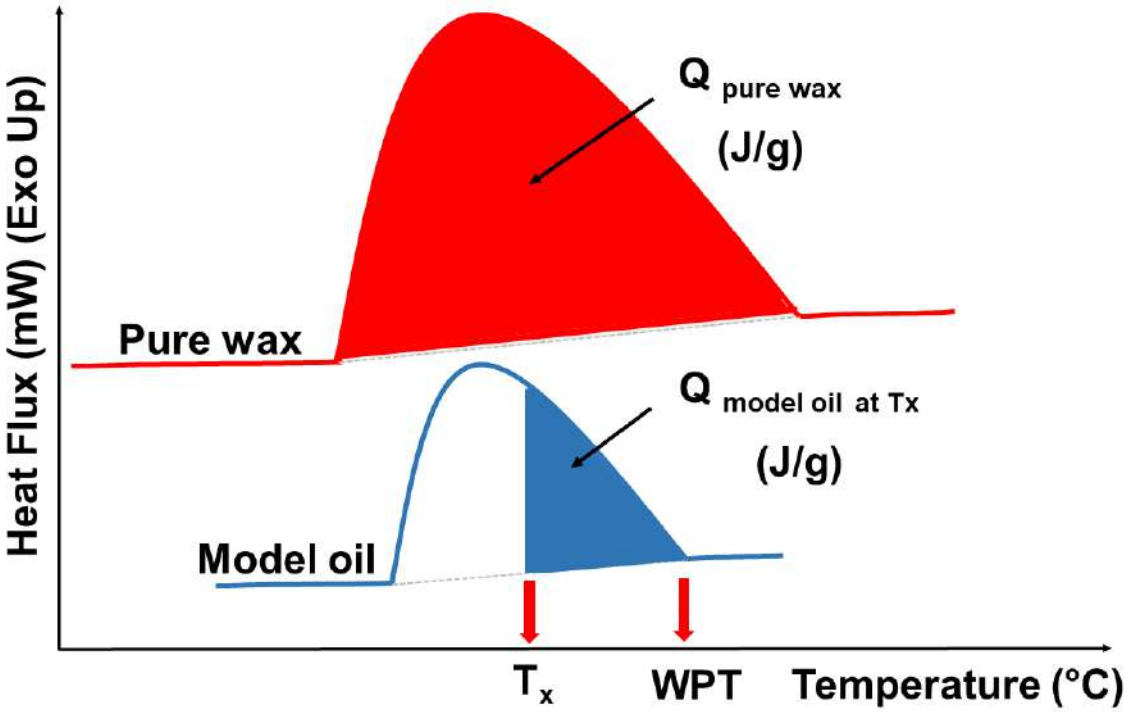


Figure 66 - Hypothetic DSC curves for a pure wax and a model oil prepared by wax solubilization in an oil matrix.

In the following, it is discussed the obtaining process and the relationships of $G'_{LVR}$ and $\gamma_E$ as function of $\Phi_w$ for models oils composed of **$L_{29}$** and **$B_{53}$** wax. Polarized light microscopy was also used to support the investigation.

### 4.5.1 Scaling Models for $L_{29}$ 7.5 wt% Model Oil

To obtain a useful set of data and derive the scaling models the first step was to identify the gelation point of the sample. In rheological terms, it is defined as the temperature at which the storage modulus becomes higher than the loss modulus [13], [48]. In practical terms, it is the point where the concentration of precipitated wax crystals is large enough to form a gel-like structure. Once it was found, rheological experiments that provided $G'_{LVR}$ and $\gamma_E$ were conducted at temperatures close and progressively below the gelation point. Also, the mass fraction of precipitated wax was evaluated at specific temperatures. Then, according to Equations 16 to 19, it was possible to calculate the scaling exponents and to obtain the fractal dimension for each scaling regime.

Figure 67 exhibits the procedure of gelation point determination for the **$L_{29}$** 7.5 wt% model oil. The system was freshly prepared and submitted to an oscillatory rheological test from 80°C to 4°C at 1.0°C/min with a strain set to 0.5% and a frequency of 1 Hz. The structural transition from liquid-like to solid-like occurs with the decrease of the test temperature, which is responsible for continuous precipitation of wax crystals. It is worth mentioning that despite being different properties, according to the adopted definitions the gelation point (25.3°C) is comparable to the WPT (27.3°C, see Table 12) for the **$L_{29}$** 7.5 wt% model oil. It's likely that the absence of contaminants (such as resin and asphaltene) favors the formation of a network structure and it is easier for the wax crystals to grow into large needle-like particles [125]. Since the WPT, as defined in see section 4.4.1, is also dependent on the mass of precipitated crystals, it is expected similar values when compared to the gelation point.

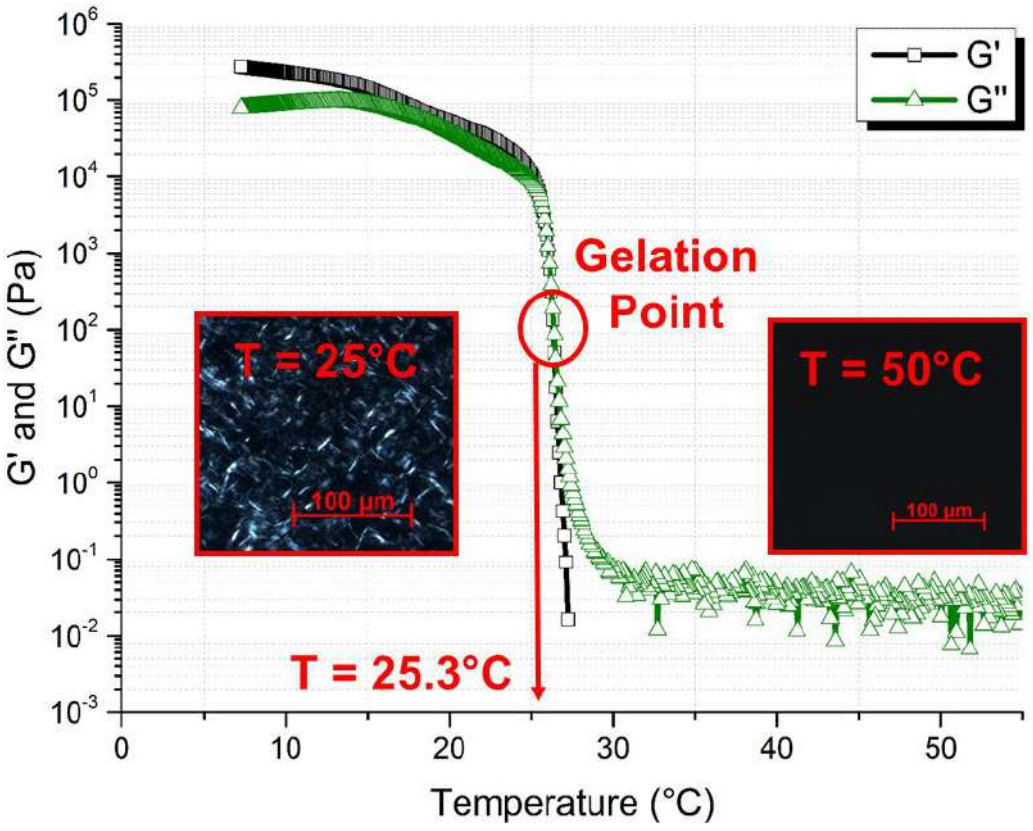


Figure 67 - Oscillatory test for the gelation point determination of **$L_{29}$** 7.5 wt% model oil. The cooling rate was set to 1.0°C/min, frequency of 1 Hz, and %strain of 0.5. Optical microscopy images are shown in details at 50°C and 25°C.

The DSC curves for **$L_{29}$** pure wax and model oil **$L_{29}$** 7.5 wt% is exhibited in Figure 68. The thermal behavior of model oil **$L_{29}$** 15 wt% is also shown, however only for illustrative purposes. In contrast to the **$L_{29}$** pure wax, at temperatures above 40°C, the amount of precipitated material is exceedingly small for both model oils, characterized by the

absence of baseline deviation in the DSC curves. It can be inferred that this small amount of precipitated wax crystals ($\Phi_w$ < 0.3 wt%) has little influence on the structure of the model oils. Therefore, until the gelation point, the model oils show a liquid-like behavior. As the temperature drops, it is possible to observe due to the shape of the curves that these samples release heat very quickly. However, the wax precipitating peak is narrowed when comparing **$L_{29}$** 7.5 wt% to the **$L_{29}$** 15 wt% model oil. Also, it is assumed that most of the waxes precipitate at −10 °C for all samples.

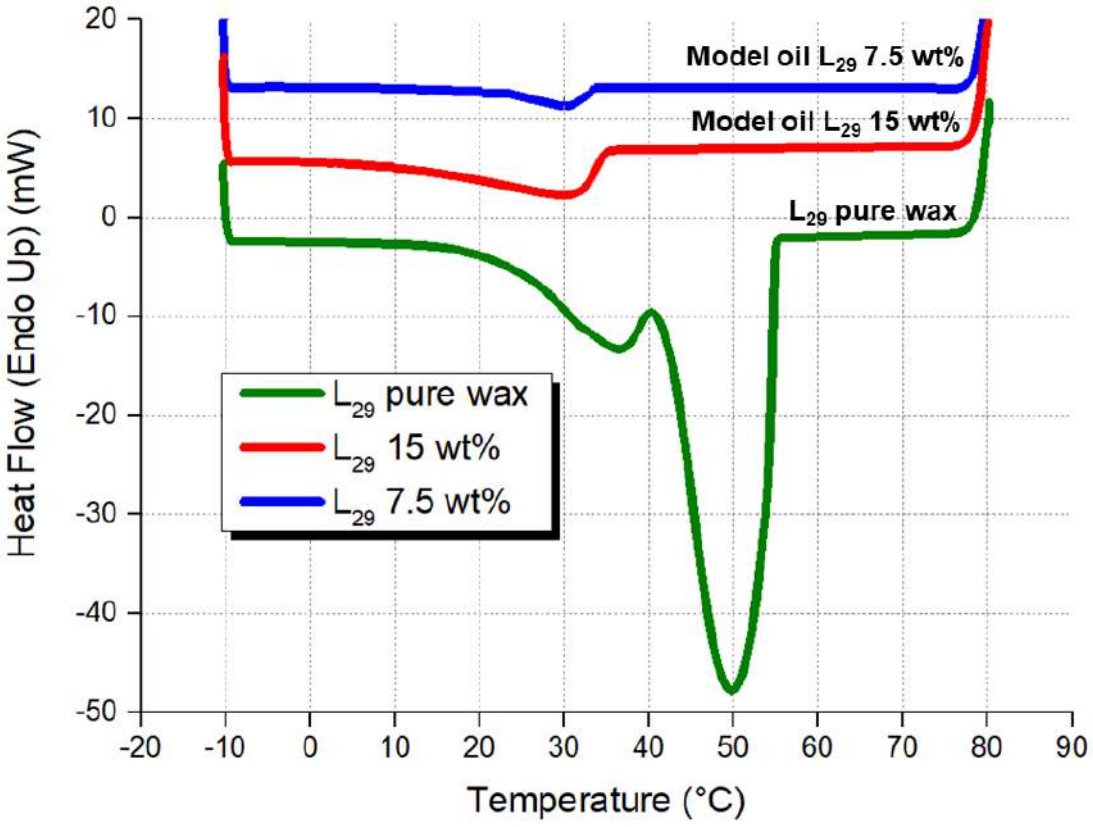


Figure 68 - Thermal behavior of **$L_{29}$** pure wax and model oil **$L_{29}$** 7.5 and 15 wt%. The cooling rate was set to 10°C/min.

On the basis of the DSC results, it was possible to calculate the mass fraction of precipitated wax at different temperatures by the proposed method in Figure 66. The results can be seen in Figure 69 for the model oils **$L_{29}$** 7.5 and 15 wt%. Despite having twice more wax in its composition, the **$L_{29}$** 15 wt% model oil presented much more precipitated material at -10°C: 14.21 wt% compared to 3.18 wt% for the **$L_{29}$** 7.5 wt% model oil. For the 7.5 wt% system, the concentration of precipitated wax crystals increases quickly from 1.28 wt % to 2.04 wt % with the decrease of temperature from 30 to 25°C. At this point the amount of precipitated wax crystals becomes large enough to affect the crude oil structure, thus causing the structure transition from liquid-like to solid-

like. This result indicates that a very small concentration of precipitated wax crystals is able to cause the sample gelation, as also stated by Hansen et al. [162]. Comparing with the 15 wt% system, the concentration of 2.04 wt% is reached at about 33°C. In fact, at room temperature (25°C), the visual aspect and the rheological behavior of this sample is compatible with a gelled material (this is clearly seen in Figure 7).

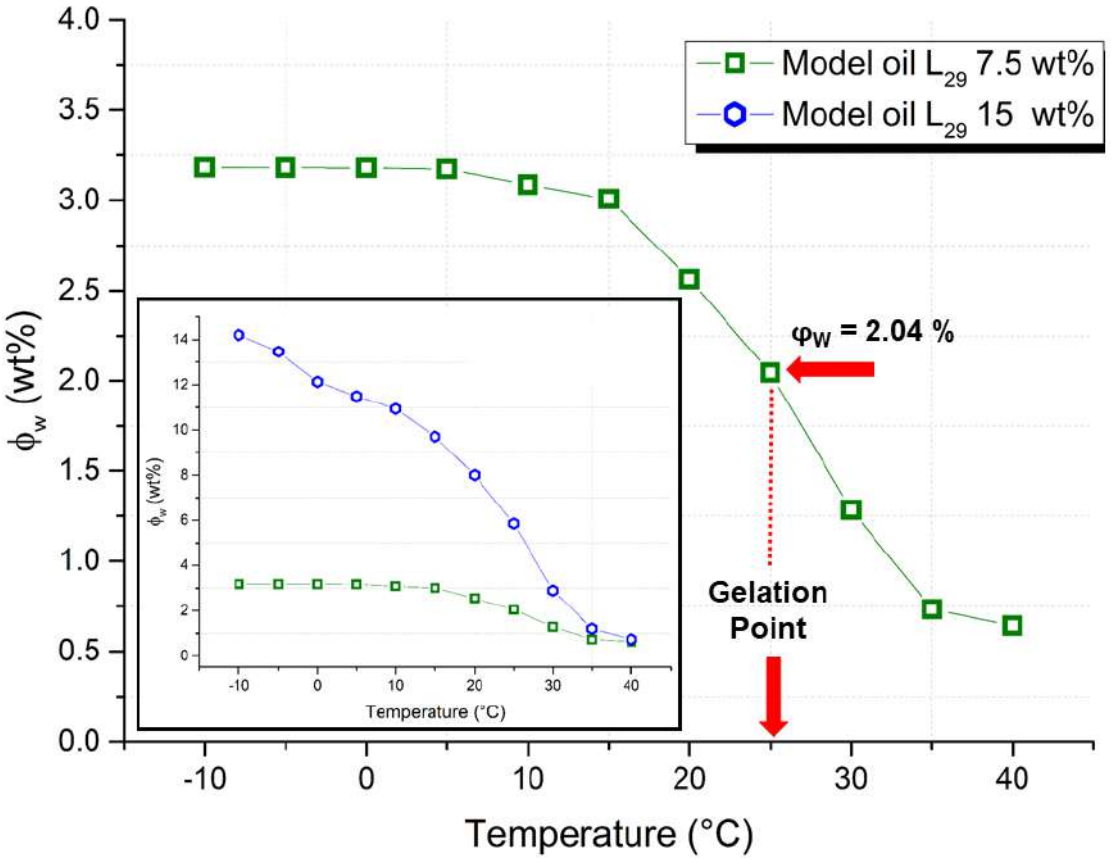


Figure 69 - Mass fraction of precipitated wax crystals for model oils **L29** 7.5 and 15 wt% (detail) under different temperatures calculated from DSC data.

The elastic properties of **L29** 7.5 wt% model oil was accessed through rheology analysis for temperatures ranging from 25°C to 7°C, a total of 10 experiments. Since the system is above the gelation threshold for these temperatures, the scaling is affected mainly by the structure of the individual flocs [69]. In possession of $G'_{LVR}$, $\gamma_E$ and $\Phi_w$ it was possible to plot the elastic properties of gelled oils as a function of the mass fraction of precipitated crystals to analyze the possible strong-link to weak-link regime transition. Each regime denotes whether the yield behavior of the gelled structure occurs by failure either within the floc or between flocs, respectively. Also, according to the scaling theory:

(a) $G'_{LVR}$ increases more slowly in the weak-link regime than in the strong-link regime;

(b) $\gamma_E$ increases with increasing particle concentration in the weak-link regime however it decreases with increasing particle concentration in the strong-link regime. The colloidal gel may cross over from the strong-link regime to the weak-link regime with increasing particle concentration [69], [124].

The results for the **$L_{29}$** 7.5 wt% model oil are summarized in Figure 70. The data were plotted on a logarithmic scale since according to the scaling theory, $G'_{LVR}$ and $\gamma_E$ will scale to $\Phi_w$ in a power-law fashion. By observing Figure 70 it is clear that storage modulus increased monotonically with decreasing temperature, indicating the continuous development of the gelled structure. In addition, it increased more slowly in the weak-link than in the strong-link regime: the average increase was 42.1 kPa/°C in the strong-link against 11.8 kPa/°C in the weak-link. The critical elastic strain decreased from 25°C to 19 °C, indicating the strong-link regime. However, at temperatures below 19°C, $\gamma_E$ gradually increased with the decrease of temperature. Therefore, the major predictions of the scale theory were supported by the data obtained for **$L_{29}$** 7.5 wt% model oil.

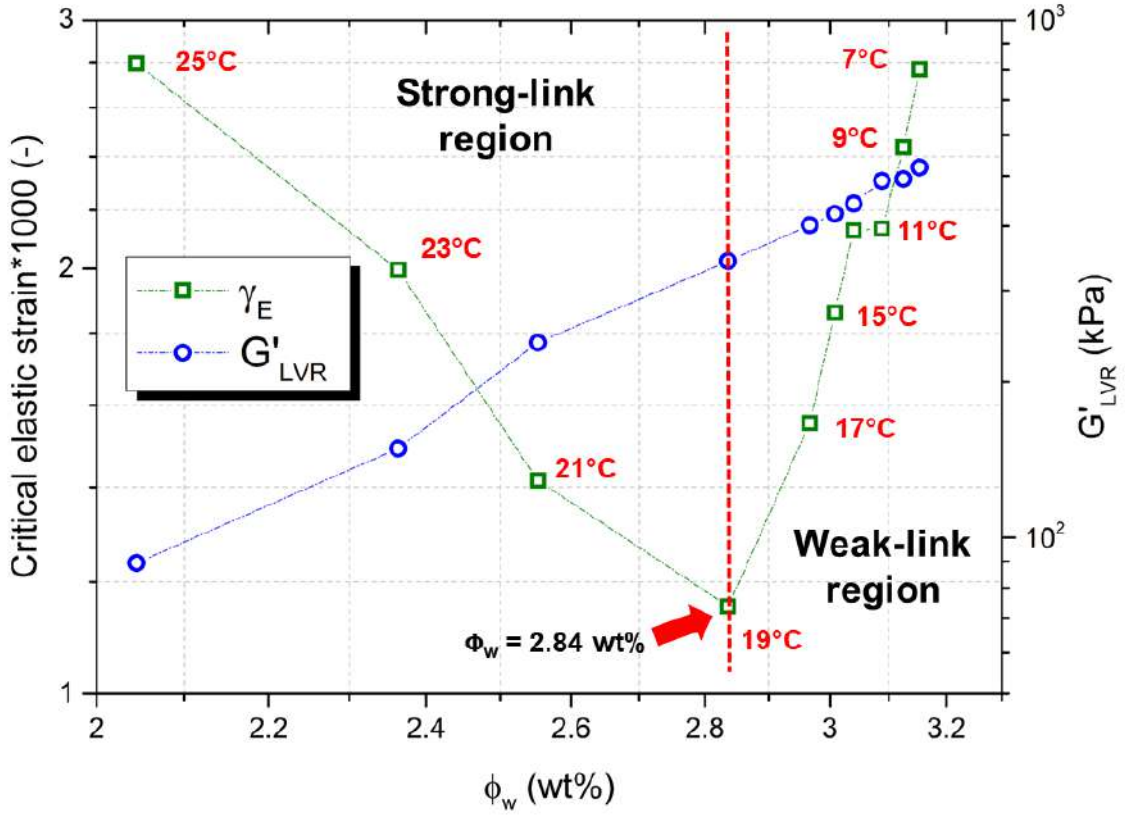


Figure 70 - Elastic properties as a function of mass fraction of precipitated wax crystals for a model oil **$L_{29}$** 7.5 wt%.

According to presented data, it is reasonable to suppose that the structural failure of waxy crude oils in temperatures near to 4°C occurs between the clusters of waxy

crystals, not inside the clusters since in the weak-link regime the flocs are more rigid when compared to the interfloc links. Thus, for a waxy crude in a gelled state at sufficiently low temperature it is expected a mechanical yield between the clusters with the crystals retained their integrity (see Figure 8). Although, it is important to highlight that strong-link and weak-link represent two extreme situations. According to Wu and Morbidelli [127], the transition from one regime to the other with the change in particle concentration is continuous, leading to intermediate situations where both inter and intrafloc links contribute to the overall elasticity of the gel.

The model's parameters for the strong-link and weak-link regimes were calculated and presented in Table 13. The scaling exponents were denoted by $A$ and $B$. They represent the slope value from the log-log plot of $G'_{LVR}$ as function of $\Phi_w$ and the slope value from the log-log plot of $\gamma_E$ as function of $\Phi_w$, respectively.

Table 13 - Parameter values for the scaling model of **$L_{29}$** 7.5 wt% system

| Range of $\Phi_w$ (wt%) | Link regime | $A$ | $B$ | $D$ | $x$ |
|---|---|---|---|---|---|
| $\Phi_w \leq$ 2.84 | strong-link | 4.232 ($R^2$ = 0.96) | -2.810 ($R^2$ = 0.96) | 1.594 | 2.952 |
| 2.84 < $\Phi_w \leq$ 3.18 | weak-link | 4.279 ($R^2$ = 0.97) | - | 2.767 | - |

In the weak-link regime, the fractal dimension was calculated through the $G'_{LVR}$ data because of the better linear relationship between ln($G'_{LVR}$) and ln($\Phi_w$). The value of fractal dimension calculated from $\gamma_E$ is slightly higher ($D$ = 2.887), nevertheless the quality of the linear fit was inferior ($R^2$ = 0.94). Also, the associated scaling exponent presented an exceedingly high value ($A$ = 8.815) when compared to several studies reviewed by Wu and Morbidelli [127], where it does not exceed 5.650.

As can be seen in Table 13, the fractal dimension $D$ in the strong-link regime is 1.594, whereas its value in the weak-link is 2.767. This means that along cooling the wax crystals tend to grow in more and more intricate morphologies and structures and also the microstructure of the gelled oil becomes more compact with the increase of waxy crystal concentration [78], [128]. Considering that the assessed temperatures in the weak-link regime (7 to 19°C) are smaller when compared to strong-link (21 to 25°C), this progressive structural organization was expected. This can be seen clearly in Figure 71, where the morphology and structural evolution of waxy crystals precipitated from **$L_{29}$** 7.5 wt% model oil during the cooling process is presented. The freshly prepared sample was

quiescently cooled in equipment thermal stage from 80°C to 4°C, at 1.0°C/min. At 25°C, very close to the gelation point, it is possible to observe a significant amount of needle-like crystals amassed into clusters of varying sizes. The size and the number of crystals increased due to continuous precipitation of waxes during temperature drop. Also, the floc compactness is visibly affected when the image details at 25°C and 5°C are compared.

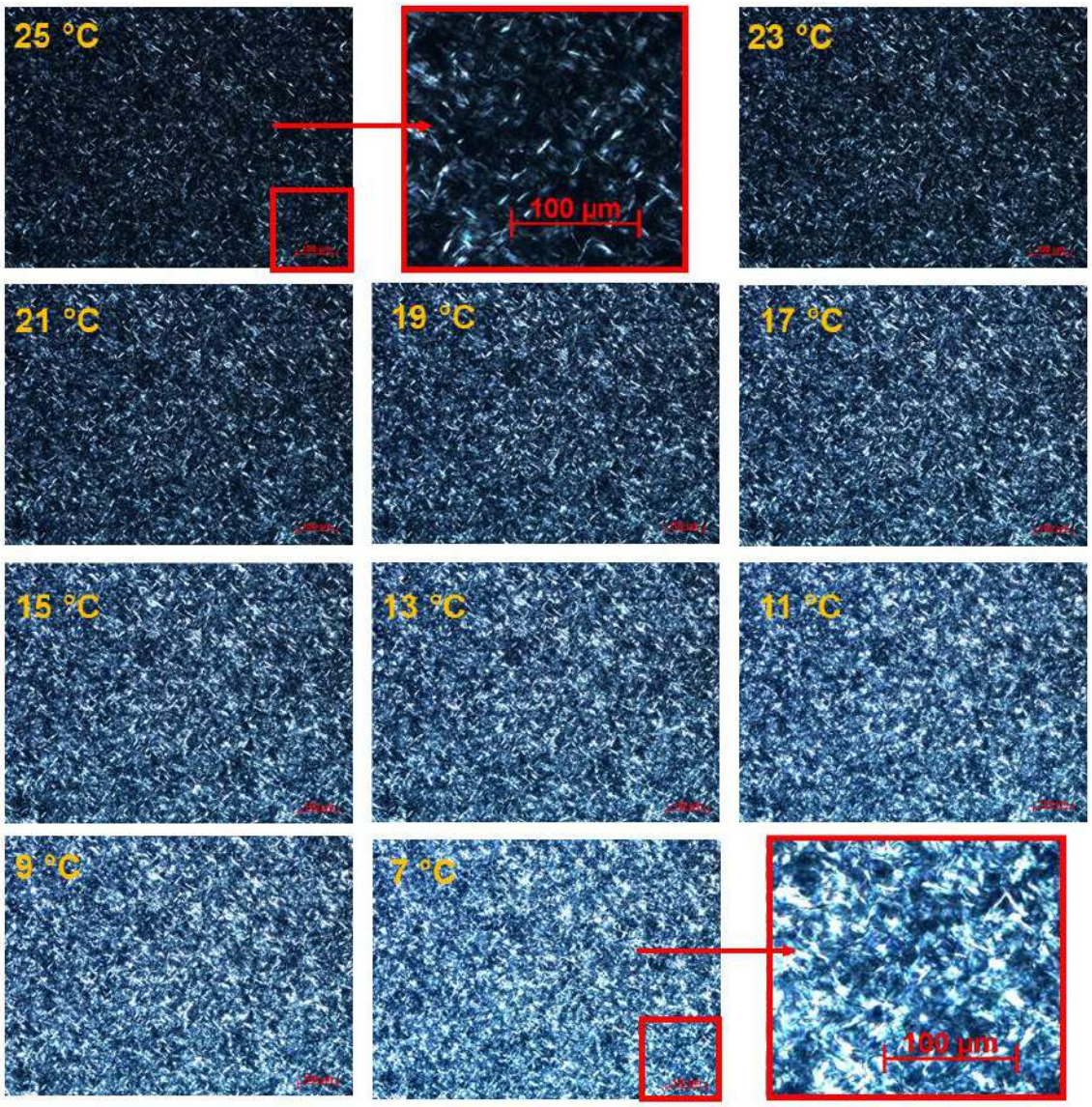


Figure 71 - Precipitated wax crystals from freshly prepared **$L_{29}$** 7.5 wt% model oils cooled quiescently from 80°C to 4°C at 1.0°C/min (200x magnification).

### 4.5.2 Scaling Models for $B_{53}$ 7.5 wt% Model Oil

The methodology for obtaining the scaling models was established in section 4.5.1. Another system was tested following similar steps: model oil containing **$B_{53}$** 7.5 wt%.

Unlike **$L_{29}$**, the **$B_{53}$** is a branched-type wax with approximately twice more carbons in its carbonic chain. Thus, the results from model oils with different structural features can be compared. For a complete characterization of **$L_{29}$** and **$B_{53}$** wax one may refer to sections 4.1.1 to 4.1.8.

Figure 72 exhibits the cooling step of the rheological test used to determine the gelation point of **$B_{53}$** 7.5 wt% model oil. The system was freshly prepared and cooled from 80°C to 4°C at 1.0°C/min with a strain of 0.5% and a frequency of 1 Hz. The gelation point is defined as the temperature where G' becomes higher than G'' for the first time [13], [48]. As highlighted in Figure 72, this temperature is 44.7 °C, fairly close to the WPT for this model oil (48.6 °C, see Table 12). The earlier precipitation of longer wax molecules is likely to be responsible for these values, approximately 20°C higher when compared to **$L_{29}$** 7.5 wt% model oil.

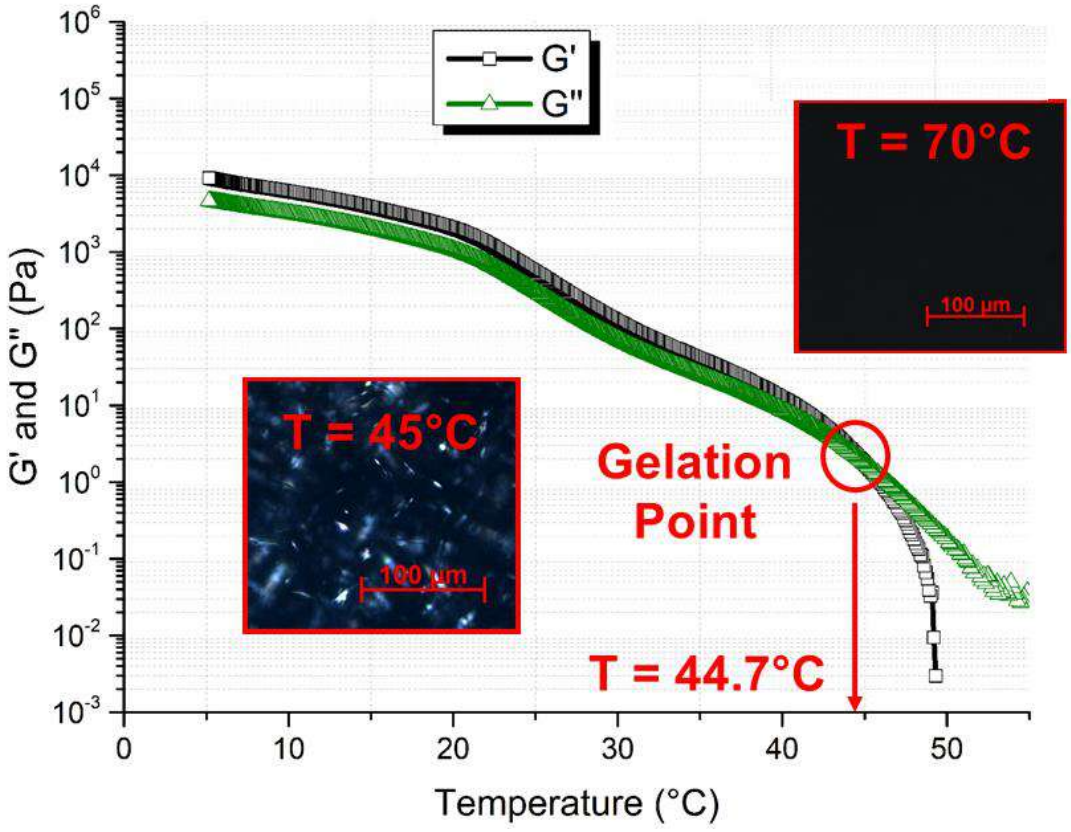


Figure 72 - Oscillatory test for the gelation point determination of **$B_{53}$** 7.5 wt% model oil. The cooling rate was set to 1.0°C/min, frequency of 1Hz, and %strain of 0.5. Optical microscopy images are shown in details at 70°C and 45°C.

The DSC curves for **$B_{53}$** pure wax and model oils 7.5 wt% and 15 wt% are exhibited in Figure 73. In contrast to the **$L_{29}$** results, broader peaks can be observed, characteristic of microcrystalline wax. At temperatures above 65°C, any precipitated material is virtually

absent. As the temperature drops, it is possible to observe two precipitating peaks for each model oil, although they are more intense and occurs earlier for the 15 wt% composition. Also, it is assumed that most of the waxes are precipitated at −10 °C for all samples.

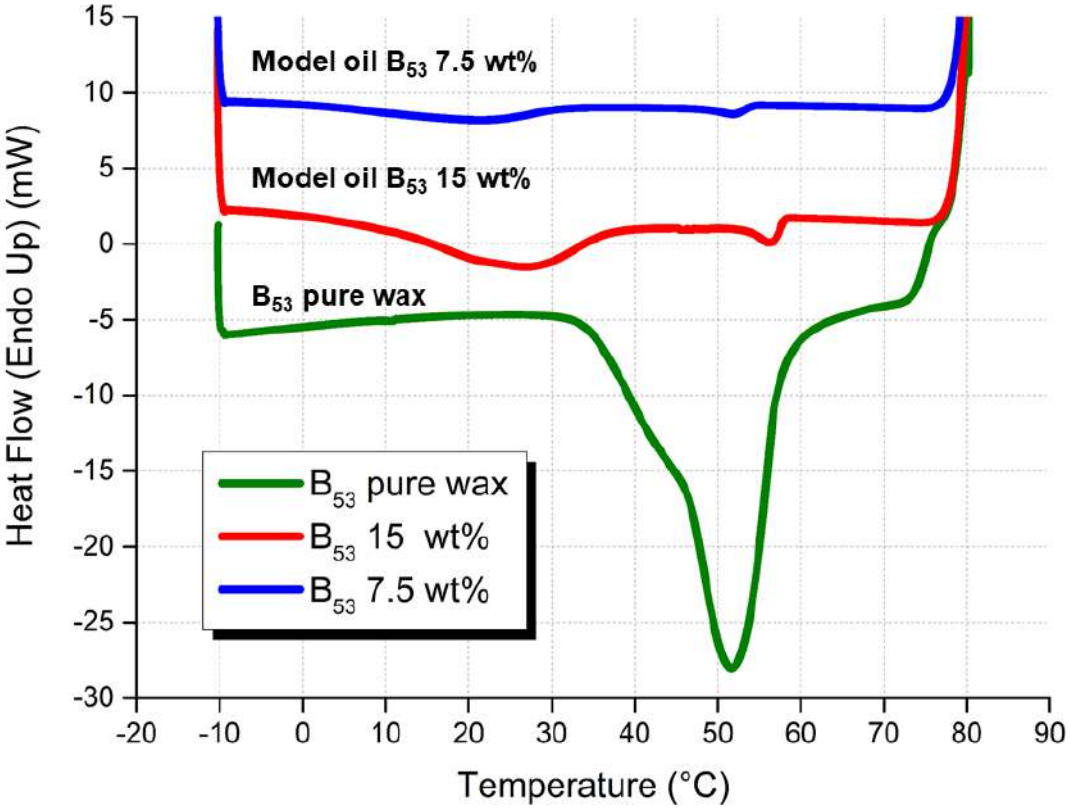


Figure 73 - Thermal behavior of **$B_{53}$** pure wax and **$B_{53}$** 7.5 and 15 wt% model oils. The cooling rate was set to 10°C/min.

On the basis of the DSC results, it was possible to calculate the mass fraction of precipitated wax at different temperatures. The results are exposed in Figure 74 for the model oils **$B_{53}$** 7.5 and 15 wt%. As expected, the 15 wt% system presented more precipitated material at -10°C: 19.24 wt% compared to 7.24 wt% for the **$B_{53}$** 7.5 wt% model oil. For this later system, the gelation point of 44.7°C is reached with a surprisingly low amount of precipitated material, only 1.76 wt%. It implies that the structural transition from liquid-like to solid-like behavior is achieved at temperatures much higher than 25°C. For **$B_{53}$** 15 wt% model oil the concentration of 1.76 wt% is reached at ~ 55°C. In fact, the **$B_{53}$** model oils at 7.5 and 15 wt% achieve a gel-like appearance when stored at room temperature just a few minutes after preparation. Despite that, when compared in similar conditions, the yield stress of **$B_{53}$** model oil is smaller than **$L_{29}$** (see section 4.4.2). Also,

it is possible to observe in Figure 74 regions where the mass fraction of precipitated wax increased faster. These regions are associated with the precipitation peaks of DSC curves in Figure 73: for example, the range of 30°C to 5°C, highlighted by the red dotted lines.

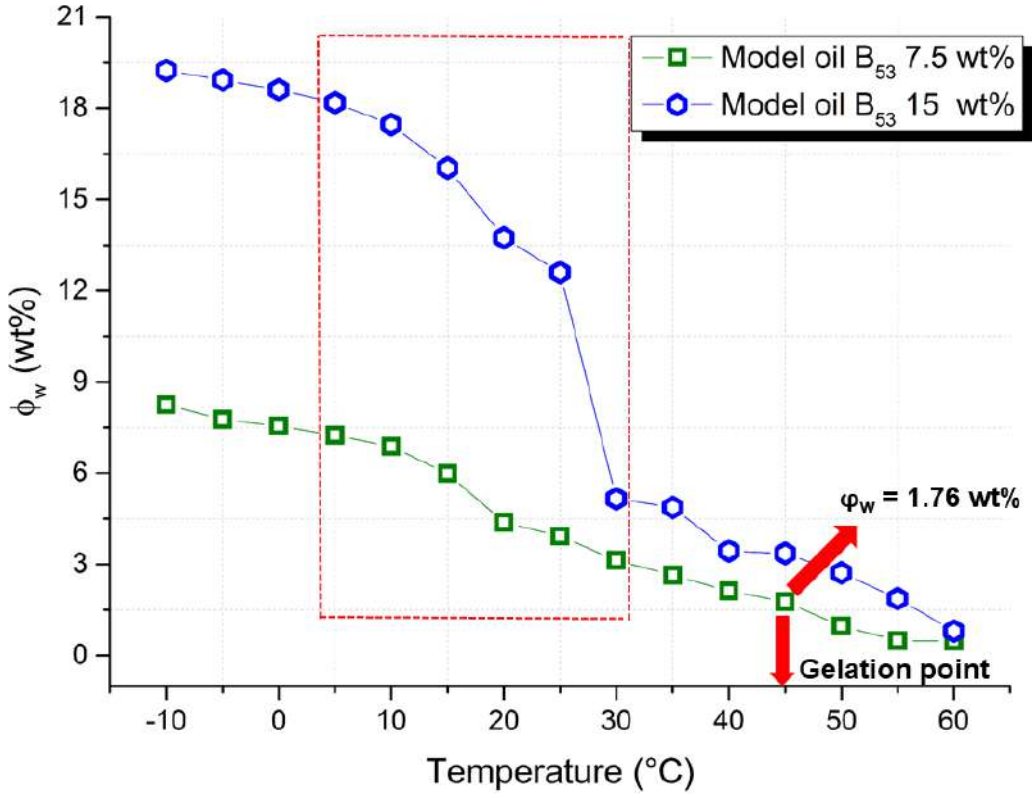


Figure 74 - Mass fraction of precipitated wax crystals of model oils **B53** 7.5 and 15 wt% under different temperatures calculated from DSC data.

The elastic properties of **B53** 7.5 wt% model oil were accessed through rheological measurements for temperatures ranging from 45°C to 21°C, a total of 10 experiments. The obtained values of $G'_{LVR}$ and $\gamma_E$ were plotted as a function of the mass fraction of precipitated crystals in Figure 75. Also, there are the values of yield stress in parenthesis. As can be seen, the critical elastic strain decreased from 45°C to 36 °C, indicating the strong-link regime. However, at temperatures below 36°C, $\gamma_E$ gradually increased with the decrease of temperature. Once more, strong-link and weak-link regimes could be clearly devised, and the temperature of 36°C marked the shift. Thus, the colloidal gel produced by the cooling of **B53** 7.5 wt% model oil presented the qualitative behavior predicted by the scaling theory when the concentration of precipitated wax increases [67],[120]. This reinforces the assumption that at temperatures nearby 4°C the structural failure of waxy gelled materials occurs at interlink connections of crystals clusters (see

Figure 8 for reference). The yield stress is approximately near zero at the gelation temperature and it increases monotonically as the temperature decreases.

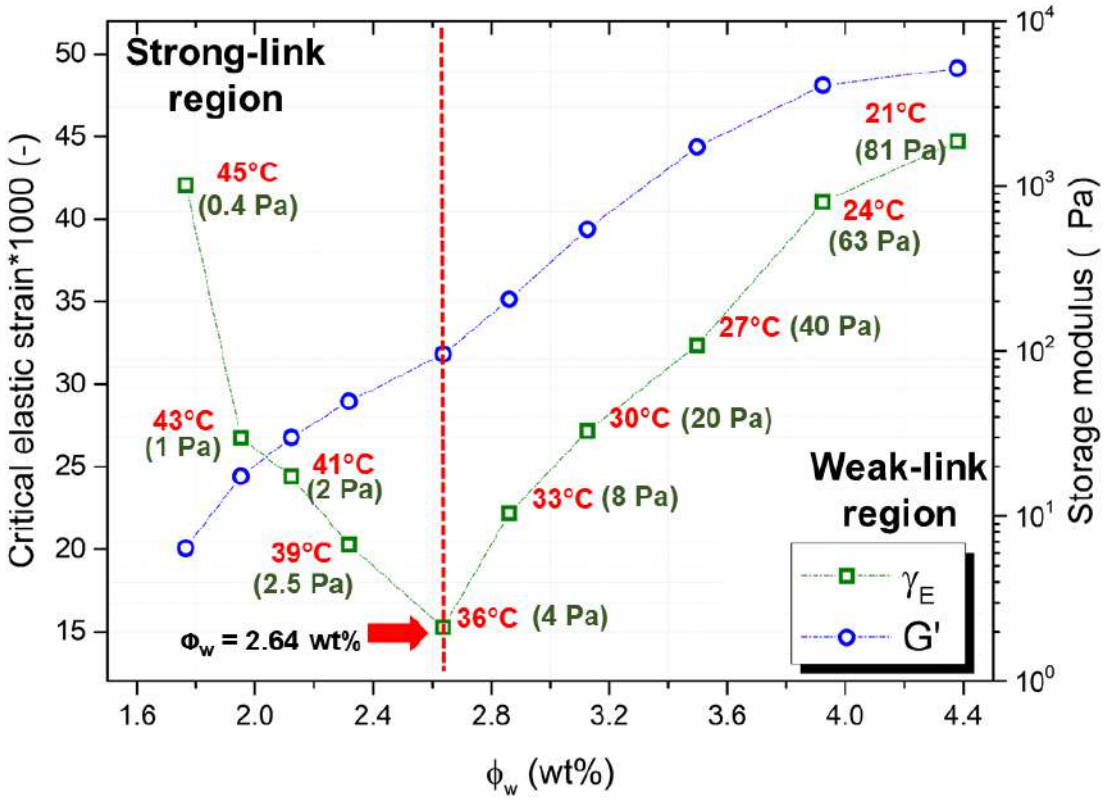


Figure 75 - Elastic properties as a function of mass fraction of precipitated wax crystals for model oil **B$_{53}$** 7.5 wt%.

Compared to the **L$_{29}$** system, the $G'_{LVR}$ values were substantially smaller. However, they increased monotonically with decreasing temperature, indicating the continuous development of the gelled structure. Differently from the **L$_{29}$** system previous analyzed and contrary to the scaling model predictions, the average storage modulus increase was much higher in the weak-link regime: 412.8 Pa/°C against only 6.3 Pa/°C in the strong-link. This could be associated with the fact that **B$_{53}$** model oils reach the gelation point in earlies stages of temperature. However, at these temperatures, the gelled network is weak and poorly developed. For example, at 45°C the value of $G'_{LVR}$ is very small, only 6.41 Pa, meaning that the concentration of precipitated wax crystals is not large enough to build a strong gel structure. As the regime shift also occurred at the relatively high temperature of 36°C, the gelled network development occurred more intensely in the weak-link, reflecting a higher rate of G' increase in this region.

The scaling model parameters for the strong-link and weak-link regimes presented in Equations 16 to 19 were calculated and presented in Table 14. The scaling exponents $A$

and $B$ are represented by the slope of the log-log plot of $G'_{LVR}$ as function of $\Phi_w$ and $\gamma_E$ as function of $\Phi_w$, respectively.

Table 14 - Parameter values for the scaling model of **$B_{53}$** 7.5 wt% system

| Range of $\Phi_w$ (wt%) | Link regime | $A$ | $B$ | $D$ | $x$ |
|---|---|---|---|---|---|
| $\Phi_w \leq$ 2.64 | Strong-link | 4.688 ($R^2$ = 0.96) | -2.365 ($R^2$ = 0.96) | 2.139 | 1.036 |
| 2.64 < $\Phi_w \leq$ 4.38 | Weak-link | - | 1.678 ($R^2$ = 0.98) | 2.404 | - |

In the weak-link regime, the fractal dimension was calculated through the $\gamma_E$ data because of the better linear relationship between ln($\gamma_E$) and ln($\Phi_w$). The values from $G'_{LVR}$ data are higher with $D$ = 2.871, and the scaling exponent $A$ = 7.780. Additionally to this fact, the value of the scaling exponent from $G'_{LVR}$ data is exceedingly high when compared to those from the studies reviewed by Wu and Morbidelli [127], where it does not exceed 5.650.

As can be seen in Table 14, the value of fractal dimension increased from 2.139 in the strong-link region to 2.404 in the weak-link region indicating the continuous development of the microstructure with decreasing temperature (or, reciprocally, by increasing waxy crystal concentration). The progressive structural organization is exhibited in Figure 76. The freshly prepared sample was quiescently cooled in equipment thermal stage from 80°C to 4°C, at 1.0°C/min. At temperatures ranging from 45°C to 36°C, it is possible to observe many voids in the images and a high amount of small crystal clusters. At 21°C, the image is completely filled by the precipitated material and a complex entangled structure can be seen in the detail. By observing Figure 71 and Figure 76 it seems that after a sufficiently long period all of the particles become part of a single cluster.

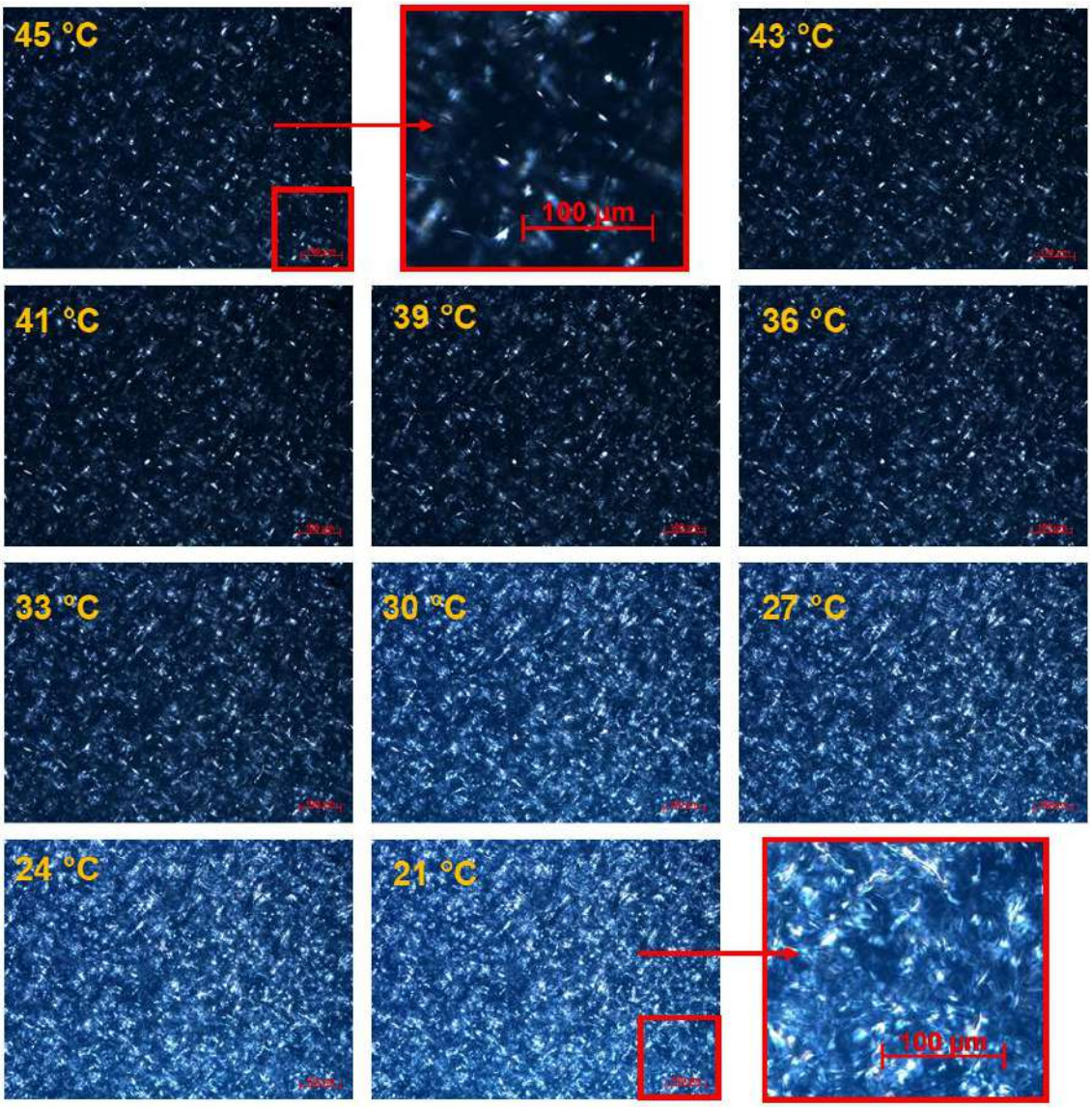


Figure 76 - Precipitated wax crystals from freshly prepared **$B_{53}$** 7.5 wt% model oils cooled quiescently from 80°C to 4°C at 1.0°C/min (200x magnification).

### 4.5.3 Conclusions

Scaling models developed by Shih et al. [69] were applied to describe the scaling of elastic properties of **$L_{29}$** 7.5 wt% and **$B_{53}$** 7.5 wt% model waxy oils employing concepts that proved to be successful with polymer gels [124]. A methodology for deriving the scaling models was successfully devised: first, the gelation point and the mass fraction of precipitated wax crystals were determined. Then, the storage modulus in the linear viscoelastic region and the critical elastic strain of the gelled oils were obtained at temperatures close and progressively below the gelation point. Next, the relationships of $G'_{LVR} \sim \Phi_w$ and $\gamma_E \sim \Phi_w$ were established and the fractal dimensions of the gelled

materials were calculated. Finally, the microstructure of the gelled oils was discussed with the aid of polarized optical microscopy.

From the obtained results is possible to state that the microstructure of the gelled waxy oils analyzed is similar to the microstructure of colloidal gels, which, according to the scaling theory, can be divided into strong-link and weak-link regime. For both model oils investigated a clear regime transition occurred as the mass fraction of precipitated wax crystal increased. Although, differently from the **$L_{29}$** system (and contrary to the scaling model predictions), the rate of storage modulus increase in **$B_{53}$** 7.5 wt% model oil was much higher in the weak-link regime, possibly due to particular structural properties of this wax, as the presence of very long carbonic chains.

The transition from strong-link to the weak-link regime at temperatures of 19° and 36°C for **$L_{29}$** and **$B_{53}$** systems, respectively, suggests that structural failure of waxy gelled materials occurs between the links that connect the clusters of crystals when the gelation temperature is close to 4°C. Similar results that support this statement can also be found in the work of Yang et al. [125], [128]. In this regard, the technique of cryogenic-scanning electron microscopy presented at Miyazaki and Marangoni [28] study would be decisive to clarify this point.

The fractal dimension increased for both model oils as the waxy gels changed from the strong-link type to the weak-link regime. This is consistent with the continuous development of the microstructure of the gelled oils with increasing $\Phi_w$ (in other words, with the temperature decrease). This development is clearly seen at the microscopy images that show more intricate morphologies and structures for successively lower temperatures. The aggregates tend to restructure during the growth, which certainly modifies their appearance.

# 5 Final Remarks

Colloidal systems are very common in our daily lives. It extends beyond the chemical field to areas such as physics, biology, geology, and many others, where small particles under certain conditions aggregate to form large complex structures. If there are enough particles organized in patterns like clusters or flocs, the aggregating system may form a gel structure that gives new properties to the material, e.g. elasticity, scattering, and conductivity. Therefore, there is a significant interest in understanding the structure of colloidal gels to control them for engineering applications. The particular interest in colloidal waxy gels is the core of this Thesis and flow assurance is the main application devised. In this regard, model oils consisting of predominantly linear and branched waxes dissolved in mineral oil were investigated under gelling conditions. A blend of waxes with different structures was necessary to obtain a system that mimics the gelation behavior of crude oils. Though this is not surprising, in the light of findings on the composition of the real crude oils wax [162], there seems to be a lack of discussion on the role of branched waxes on the yielding properties of waxy gels even for model systems.

The primary objective of this Thesis was to relate the macroscopic behavior of gelled waxy oils, in terms of viscoelastic properties, to microstructure and general composition features. Most of the presented results were focused on this objective. Rheology was the main experimental technique employed, followed by differential scanning calorimetry and optical microscopy. These three techniques provide data for the majority of studies concerning the flow assurance of waxy oils. Also, an extensive physicochemical characterization of waxes and the oil matrix was performed to aid in the rheology-to-structure relationship. Results from thermal analysis, $^{13}C$ Nuclear Magnetic Resonance, Gas Chromatography, X-ray Scattering, and Fourier Transform Infrared spectroscopy were presented. Features compatible with predominantly linear macrocrystalline wax were obtained for $\mathbf{L_{24}}$ and $\mathbf{L_{29}}$ waxes whereas branched microcrystalline were assigned to $\mathbf{B_{37}}$ and $\mathbf{B_{53}}$. The number of ramification points was estimated in 6.36% for $\mathbf{B_{37}}$ and 4.41% for $\mathbf{B_{53}}$ wax, in molar basis.

For the model waxy oils prepared, the contaminants (such as resin and asphaltene) were absent and wax crystals were able to grow into large plate-like clusters, which favors the formation of a network structure. Then a very small concentration of precipitated material could lead to the oil gelation. Once the gelled structure is obtained and the temperature

is kept constant, it was verified that the destructive flow had irreversible effects. As pointed out by Mendes [51], it is not possible to state that the conclusions obtained with model oils are valid for any waxy crude oil, but the same qualitative tendencies of the rheological behavior could be expected, as their origin is the basic interaction between wax crystals and a liquid matrix. Thus, the obtained results indicate that if the structure of a gelled waxy crude oil is broken, one might expect that even after a long shutdown period there will be no obstacle for restart pumping operations.

The importance of slippage prevention in rheological tests was established by comparing results from smooth and grooved geometries. It was demonstrated that the use of grooved surfaces, both at the rotating and stationary parts of the rheometer, produced high-quality and more realistic measurements, being highly indicated for investigations with waxy gels. When smooth geometries were employed, a decrease of more than 80% in yield stress was observed for model oils composed either by $\mathbf{L_{29}}$ 3.0 wt% or 7.5 wt% model oils. This deviation has a huge impact on any further calculation based on yield stress. Also, the repeatability of the tests was enhanced by using grooved geometries. This is very important since the yield stress measurements are often difficult to reproduce precisely.

The technique of polarized light microscopy was extensively used in this Thesis, however, it has some limitations. Indeed, the visual analysis is hampered by the high complexity and irregularity of wax crystals, and there is no general agreement in the literature either on the shape (platelet or needle) or the average size (from nanometers to several microns) for this type of material. In this regard, the attempts to correlate morphological aspects to rheological properties (e.g. crystal length to yield stress) were not successful. Despite the adversities, it was possible to devise clusters of self-assembled crystals presenting needle-like features of varying sizes and patterns. The general characteristics resemble those of crude oils: the solid phase appears to be composed of ill-formed, needle-like crystals amassed into clusters which further aggregate to form a space-filling network. The crystals formed by the linear waxes in the absence of the iso-components are longer, suggesting that branched waxes interfered with the regular growth of the wax crystals. The micrometer-sized waxy crystals formed, and their marked tendency to associate into dense crystalline masses, combined with the low concentration required for gelation, provide important clues that these waxy gels belong to the broad family of attractive colloidal gels.

Operational definitions for yield stress, storage modulus in the linear viscoelastic region, critical strain, critical elastic strain, and cohesive energy density were presented. It was

also shown that viscoelastic properties are highly affected by the chemical structure of waxes. The presence of branch points at the carbonic chains is likely to be responsible for a reduced crystal-crystal interaction or a reduced crystal growth, lowering the yield stress. On the other hand, an increase in the chain length showed the opposite effect. Therefore, it is important for further evaluations do not dissociate the impact of these two structural features at rheological properties. The rheological results indicated that **$B_{37}$** wax may act as a wax inhibitor. Its presence may perturb or retard the ordering transformation of the amorphous wax aggregate into an ordered phase for large molecules such as **$L_{29}$** or **$B_{53}$**, which are not able to arrange itself linearly among the branch points of **$B_{37}$**.

The cohesive energy density (and storage modulus) demonstrated to be highly correlated to yield stress. Since these properties raise due to waxy crystals precipitation and interaction, a simple method to estimate yield stress from storage modulus was proposed. Accordingly, a database of oscillatory rheological experiments can be used to devise simple fit equations to estimate or validate yield stress measurements.

Lastly, the scaling theory was applied to connect the rheology and microstructure of gelled waxy oils. The structures of gels are highly disordered, but there is much experimental evidence that in certain length scales they are often self-similar and it can be described in terms of fractal geometry. Also, at larger particle fractions, rheological measurements combined to differential scanning calorimetry are suitable to characterize the structure of gels.

The major predictions of the theory were observed for the two model oils investigated in this Thesis. Both **$L_{29}$** and **$B_{53}$** model oils transited from the strong-link to the weak-link regime with the increasing the mass of precipitated wax crystals. The value of the fractal dimension, which describes the combined effects of morphology and spatial distribution patterns of the crystal clusters [126], increased in both cases when the temperature was lowered. It reflects the continuous development of the microstructure of the gelled oils with increasing $\Phi_w$. From the obtained results it is reasonable to assume that the structural failure of waxy gelled materials occurs in the interlink connection of the crystals clusters for temperatures close to 4°C.

# 6 Further Developments

Despite all the efforts towards a complete and unequivocal rheological characterization of waxy oils at different conditions, many challenges remain. The complex and varied crude oils composition, the different thermal and shear histories, the misleading data interpretation due to experimental artifacts represent some of these challenges. The presented suggestions consider that a more fundamental knowledge of microstructural characteristics of gelled waxy oils and its main components is necessary for better understanding its complex rheological changes. In the following, there are some propositions with the potential to complement and expand the results presented in this Thesis:

- Due to high complexity and irregularity structures, the visual interpretation of optical microscopy images is many times hard to achieve, especially when trying to observe the yielding characteristics of a material. A complementary alternative is to use scanning electron microscopy or cryo-scanning electron microscopy. The analysis of cryogenic-scanning electron microscopy images allows, for example, the determination of the length and thickness of the wax cell walls in the gelled material as a function of the wax mass fraction. Tomography image reconstruction may also be a powerful method to assess detailed wax morphological information;

- Advanced techniques based on X-ray scattering, such as SAXS and WAXS, are meaningful tools to assess the gelled material and wax crystals microstructure in more details and gather information of fractal dimension, size distributions, pore sizes, characteristic distances and so forth. The proper training in data acquisition and further analysis is highly demanded.

- Aggregation of microscopic particles diffusing in a fluid medium represents a common process leading to fractal structures. In this regard, the correlations between structure and elastic properties can be analyzed with the fractal dimension perspective. Given its importance, it would be helpful to perform a comparative study on methods of obtaining the fractal dimension, employing rheology, image-based techniques, scattering techniques, and computational simulations.

The interaction between wax crystals is the origin of Newtonian behavior departure when the oil is cooled to a certain temperature. The effect of temperature is extensively investigated, however, the pressure also has influence in the rheology of waxy oils and this data is scarce in the literature. Thus, another point of concern is to obtain the rheological properties of waxy oils under high-pressure and low-temperature conditions. This information has practical relevance to the oil industry since the usual practice in drilling operations is to measure fluid flow characteristics under ambient surface conditions and extrapolate these measurements to downhole conditions.

- Model oils are excellent choices for research purposes due to the complete compositional control. Although, it is of utmost importance to test the conclusions derived from model oils investigation to more complex systems such as crude oils or water-in-crude-oil emulsions. There might be a huge difference in the quantitative evaluation in terms of rheological properties and this difference must be considered and properly evaluated.

# 7 Cited References

[1] A. B. Hansen, E. Larsen, W. B. Pedersen, A. B. Nielsen, and H. P. Rønningsen, “Wax Precipitation from North Sea Crude Oils. 3. Precipitation and Dissolution of Wax Studied by Differential Scanning Calorimetry,” *Energy and Fuels*, vol. 5, no. 6, pp. 914–923, 1991.

[2] K. Paso, M. Senra, Y. Yi, A. M. Sastry, and H. S. Fogler, “Paraffin polydispersity facilitates mechanical gelation,” *Ind. Eng. Chem. Res.*, vol. 44, no. 18, pp. 7242–7254, 2005.

[3] D. Merino-Garcia, M. Margarone, and S. Correra, “Kinetics of waxy gel formation from batch experiments,” *Energy and Fuels*, vol. 21, no. 3, pp. 1287–1295, 2007.

[4] R. Venkatesan, N. R. Nagarajan, K. Paso, Y. Yi, A. M. Sastry, and H. S. Fogler, “The strength of paraffin gels formed under static and flow conditions,” *Chem. Eng. Sci.*, vol. 60, pp. 3587–3598, 2005.

[5] F. H. Marchesini, A. A. Alicke, P. R. De Souza Mendes, and C. M. Ziglio, “Rheological characterization of waxy crude oils: Sample preparation,” *Energy and Fuels*, vol. 26, no. 5, pp. 2566–2577, 2012.

[6] R. F. G. Visintin, R. Lapasin, E. Vignati, P. D’Antona, and T. P. Lockhart, “Rheological behavior and structural interpretation of waxy crude oil gels.,” *Langmuir*, vol. 21, no. 14, pp. 6240–6249, 2005.

[7] M. Dirand, V. Chevallier, E. Provost, M. Bouroukba, and D. Petitjean, “Multicomponent paraffin waxes and petroleum solid deposits structural and thermodynamic state,” *Fuel*, vol. 77, no. 12, pp. 1253–1260, 1998.

[8] M. Kané, M. Djabourov, J.-L. Volle, J.-P. Lechaire, and G. Frebourg, “2003 - Morphology of paraffin crystals in waxy crude oils cooled in quiescent conditions and under flow,” *Fuel*, vol. 82, pp. 127–135, 2003.

[9] D. Tukenov, “Nanochemistry Drives New Method for Removal and Control of Wax,” *J. Pet. Technol.*, vol. 61, no. 2, pp. 77–88, 2015.

[10] R. F. G. Visintin, R. Lapasin, E. Vignati, P. D’Antona, and T. P. Lockhart, “Rheological Behavior and Structural Interpretation of Waxy Crude Oil Gels,” *Langmuir*, vol. 21, no. 14, pp. 6240–6249, 2005.

[11] K. Paso, T. Kompalla, H. Oschmann, and J. Sjoblom, “Rheological degradation of model wax-oil gels,” *J. Dispers. Sci. Technol.*, vol. 30, no. 4, pp. 472–480, 2009.

[12] R. Mendes, G. Vinay, and P. Coussot, “Yield stress and minimum pressure for simulating the flow restart of a waxy crude oil pipeline,” *Energy and Fuels*, vol. 31, no. 1, pp. 395–407, 2017.

[13] P. Singh, H. S. Fogler, and N. Nagarajan, “Prediction of the wax content of the incipient wax-oil gel in a pipeline: An application of the controlled-stress rheometer,” *J. Rheol.*, vol. 43, no. 6, p. 1437, 1999.

[14] H. a Barnes, “The yield stress — a review or ‘ panta roi ’— everything flows ?,” *J. Non-Newtonian Fluid Mech*, vol. 81, pp. 133–178, 1999.

[15] M. Lin, C. Li, F. Yang, and Y. Ma, “Isothermal structure development of Qinghai waxy crude oil after static and dynamic cooling,” *J. Pet. Sci. Eng.*, vol. 77, no. 3–4, pp. 351–358, 2011.

[16] S. Peerapornlerd, S. Edvik, A. P. Leandro, R. Hinckley, M. D. Deo, R. Venkatesan, and J. J. Magda, “Effect of the flow shutdown temperature on the gelation of slurry flows in a waxy oil pipeline,” *Ind. Eng. Chem. Res.*, vol. 54, no. 16, pp. 4455–4459, 2015.

[17] M. R. Davidson, Q. D. Nguyen, C. Chang, and H. P. Rønningsen, “A model for restart of a pipeline with compressible gelled waxy crude oil,” *J. Nonnewton. Fluid Mech.*, vol. 123, no. 2–3, pp. 269–280, 2004.

[18] C. Chang, D. V Boger, and Q. D. Nguyen, “The yielding of waxy crude oils,” *Ind. Eng. Chem. Res.*, vol. 37, no. 4, pp. 1551–1559, 1998.

[19] M. Fossen, T. Oyangen, and O. J. Velle, “Effect of the pipe diameter on the restart pressure of a gelled waxy crude Oil,” *Energy and Fuels*, vol. 27, no. 7, pp. 3685–3691, 2013.

[20] H. M. Princen, “Rheology of Foams and Highly Concentrated Emulsions I. Elastic Properties and Yield Stress of a Cylindrical Model System,” *J. Colloid Interface Sci.*, vol. 91, no. 1, pp. 160–175, 1983.

[21] B. Alejo and A. Barrientos, “International Journal of Mineral Processing Model for yield stress of quartz pulps and copper tailings,” *Int. J. Miner. Process.*, vol. 93, no. 3–4, pp. 213–219, 2009.

[22] H. Teng and J. Zhang, “Modeling the viscoelasto-plastic behavior of waxy crude,”

*Pet. Sci.*, vol. 10, no. 3, pp. 395–401, 2013.

[23] Y. Zhao, L. Kumar, K. Paso, H. Ali, J. Sa, and J. Sjo, “Gelation and Breakage Behavior of Model Wax − Oil Systems: Rheological Properties and Model Development,” *Ind. Eng. Chem. Res.*, vol. 51, p. 8123−8133, 2012.

[24] D. E. V. Andrade, A. C. B. da Cruz, A. T. Franco, and C. O. R. Negrão, “Influence of the initial cooling temperature on the gelation and yield stress of waxy crude oils,” *Rheol. Acta*, vol. 54, no. 2, pp. 149–157, 2014.

[25] G. G. Vargas, E. J. Soares, R. L. Thompson, G. A. B. Sandoval, R. M. Andrade, F. B. Campos, and A. Teixeira, “Emulsion effects on the yield stress of gelled waxy crude oils,” *Fuel*, vol. 222, no. January, pp. 444–456, 2018.

[26] L. F. R. Dalla, E. J. Soares, and R. N. Siqueira, “Start-up of waxy crude oils in pipelines,” *J. Nonnewton. Fluid Mech.*, vol. 263, pp. 61–68, 2019.

[27] P. Gao, J. Zhang, H. Lei, and W. Hai-feng, “Relationship between waxy crude viscosities and wax crystal microstructure,” *J. Cent. South Univ.*, vol. 15, pp. 406–410, 2008.

[28] Y. Miyazaki and A. G. Marangoni, “Structural-mechanical model of wax crystal networks—a mesoscale cellular solid approach,” *Mater. Res. Express*, vol. 1, pp. 1–12, 2014.

[29] C. Bai and J. Zhang, “Effect of carbon number distribution of wax on the yield stress of waxy oil gels,” *Ind. Eng. Chem. Res.*, vol. 52, no. 7, pp. 2732–2739, 2013.

[30] R. C. Sarmento, G. A. S. Ribbe, and L. F. A. Azevedo, “Wax blockage removal by inductive heating of subsea pipelines,” *Heat Transf. Eng.*, vol. 25, no. 7, pp. 2–12, 2004.

[31] A. Aiyejina, D. P. Chakrabarti, A. Pilgrim, and M. K. S. Sastry, “Wax formation in oil pipelines: A critical review,” *Int. J. Multiph. Flow*, vol. 37, no. 7, pp. 671–694, 2011.

[32] H. O. Bidmus and A. K. Mehrotra, “Heat-Transfer Analogy for Wax Deposition from Paraffinic Mixtures,” *Ind. Eng. Chem. Res.*, vol. 43, no. 3, pp. 791–803, 2004.

[33] Z. Ji, C. Li, F. Yang, J. Cai, L. Cheng, and Y. Shi, “An experimental design approach for investigating and modeling wax deposition based on a new cylindrical Couette apparatus,” *Pet. Sci. Technol.*, vol. 34, no. 6, pp. 570–577,

2016.

[34] A. W. Saak, H. M. Jennings, and S. P. Shah, “The influence of wall slip on yield stress and viscoelastic measurements of cement paste,” *Cem. Concr. Res.*, vol. 31, no. 2, pp. 205–212, 2001.

[35] L. T. Wardhaugh and D. V. Boger, “The measurement and description of the yielding behavior of waxy crude oil,” *J. Rheol.*, vol. 35, no. 6, pp. 1121–1156, 1991.

[36] H. Petter Rønningsen, “Rheological behaviour of gelled, waxy North Sea crude oils,” *J. Pet. Sci. Eng.*, vol. 7, no. 3–4, pp. 177–213, 1992.

[37] H. A. Barnes, “The yield stress - a review or ‘panta roi’ - everything flows?,” *J. Nonnewton. Fluid Mech.*, vol. 81, no. 1–2, pp. 133–178, 1999.

[38] R. F. G. Visintin, T. P. Lockhart, R. Lapasin, and P. D’Antona, “Structure of waxy crude oil emulsion gels,” *J. Non-Newtonian Fluid Mech*, vol. 149, no. 1–3, pp. 34–39, 2008.

[39] A. Japper-Jaafar, P. T. Bhaskoro, and Z. S. Mior, “A new perspective on the measurements of wax appearance temperature: Comparison between DSC, thermomicroscopy and rheometry and the cooling rate effects,” *J. Pet. Sci. Eng.*, vol. 147, no. September, pp. 672–681, 2016.

[40] P. Singh, H. S. Fogler, and N. Nagarajan, “Prediction of the wax content of the incipient wax-oil gel in a pipeline: An application of the controlled-stress rheometer,” *J. Rheol.*, vol. 43, no. 6, pp. 1437–1459, 1999.

[41] R. Pal, “Yield stress and viscoelastic properties of high internal phase ratio emulsions,” *Colloid Polym. Sci.*, vol. 277, no. 6, pp. 583–588, 1999.

[42] Z. Huang, H. S. Lee, M. Senra, and H. S. Fogler, “Droplet microfluidics on a planar surface,” *Am. Inst. Chem. Eng.*, vol. 57, pp. 2955–2964, 2011.

[43] C. Van Der Geest, V. C. B. Guersoni, D. Merino-Garcia, and A. C. Bannwart, “A modified elasto-viscoplastic thixotropic model for two commercial gelled waxy crude oils,” *Rheol. Acta*, vol. 54, no. 6, pp. 545–561, 2015.

[44] J. A. Lopes-da-Silva and J. A. P. Coutinho, “Analysis of the isothermal structure development in waxy crude oils under quiescent conditions,” *Energy and Fuels*, vol. 21, no. 6, pp. 3612–3617, 2007.

[45] J. Xu, S. Xing, H. Qian, S. Chen, X. Wei, R. Zhang, L. Li, and X. Guo, “Effect of polar/nonpolar groups in comb-type copolymers on cold flowability and paraffin

crystallization of waxy oils," *Fuel*, vol. 103, pp. 600–605, 2013.

[46] K. Paso, A. Silset, G. Sørland, M. D. a L. Gonc, and J. Sjo, "Characterization of the Formation, Flowability, and Resolution of Brazilian Crude Oil Emulsions Characterization of the Formation, Flowability, and Resolution of Brazilian Crude Oil Emulsions," *Energy & Fuels*, vol. 23, no. 4, pp. 471–480, 2009.

[47] J. P. J. P. Cabanillas, A. T. Leiroz, and L. F. A. Azevedo, "Wax Deposition in the Presence of Suspended Crystals," *Energy and Fuels*, vol. 30, no. 1, pp. 1–11, 2016.

[48] R. Venkatesan, P. Singh, H. S. Fogler, and U. Michigan, "Delineating the Pour Point and Gelation Temperature of Waxy Crude Oils," *SPE J.*, vol. 7, pp. 349–352, 2002.

[49] C. J. Dimitriou, G. H. McKinley, and R. Venkatesan, "Rheo-PIV Analysis of the Yielding and Flow of Model Waxy Crude Oils," *Energy and Fuels*, vol. 25, no. 7, pp. 3040–3052, 2011.

[50] E. Vignati, R. Piazza, R. F. G. Visintin, R. Lapasin, P. D'Antona, and T. P. Lockhart, "Wax crystallization and aggregation in a model crude oil," *J. Phys. Condens. Matter*, vol. 17, no. 45, pp. 651–660, 2005.

[51] R. Mendes, "Rheological behavior and modeling of waxy crude oils in transient flows," Université Paris-Est, 2015.

[52] M. Volk, A. Matzain, J. L. Creek, H.-Q. Zhang, M. S. Apte, and J. P. Brill, "Investigation of Paraffin Deposition During Multiphase Flow in Pipelines and Wellbores—Part 1: Experiments," *J. Energy Resour. Technol.*, vol. 124, no. 3, p. 180, 2002.

[53] C. Barbato, B. Nogueira, M. Khalil, R. Fonseca, M. Gonçalves, J. C. Pinto, and M. Nele, "Contribution to a More Reproductible Method for Measuring Yield Stress of Waxy Crude Oil Emulsions," *Energy & Fuels*, vol. 28, no. 1, p. 1717−1725, 2014.

[54] S. Haj-shafiei, S. Ghosh, and D. Rousseau, "Kinetic stability and rheology of wax-stabilized water-in-oil emulsions at different water cuts," *J. Colloid Interface Sci.*, vol. 410, pp. 11–20, 2013.

[55] S. M. Hodge and D. Rousseau, "Flocculation and coalescence in water-in-oil emulsions stabilized by paraffin wax crystals," *Food Res. Int.*, vol. 36, no. 7, pp. 695–702, 2003.

[56] S. Li, Q. Huang, M. He, and W. Wang, “Effect of Water Fraction on Rheological Properties of Waxy Crude Oil Emulsions,” *J. Dispers. Sci. Technol.*, vol. 35, no. 8, pp. 1114–1125, 2014.

[57] H. Dettman, D. Amin, S. Callahan, X. Guo, J. Tinsley, R. Prud’Homme, S. Shao, R. Kriegel, D. Adamson, and R. Saini, “Effects of Polymers on the Structure and Deposition Behavior of WaxyOils,” *SPE Annu. Tech. Conf. Exhib.*, vol. Internatio, pp. 1–11, 2007.

[58] K. S. Wang, C. H. Wu, J. L. Creek, P. J. Shuler, and Y. Tang, “Evaluation of effects of selected wax inhibitors on paraffin deposition,” *Pet. Sci. Technol.*, vol. 21, no. 3–4, pp. 369–379, 2003.

[59] J. F. Tinsley and R. K. Prud’homme, “Deposition apparatus to study the effects of polymers and asphaltenes upon wax deposition,” *J. Pet. Sci. Eng.*, vol. 72, no. 1–2, pp. 166–174, 2010.

[60] L. F. A. Azevedo and A. M. Teixeira, “A critical review of the modeling of wax deposition mechanisms,” *Pet. Sci. Technol.*, vol. 21, no. 3–4, pp. 393–408, 2003.

[61] D. Tiwary and A. K. Mehrotra, “Phase Transformation and Rheological Behaviour of Highly Paraffinic ‘ Waxy ’ Mixtures,” *Can. J. Chem. Eng.*, vol. 82, no. February, pp. 162–174, 2004.

[62] B. J. Musser and P. K. Kilpatrick, “Molecular characterization of wax isolated from a variety of crude oils,” *Fuel Energy Abstr.*, vol. 40, no. 1, pp. 715–726, 1998.

[63] S. Yi and J. Zhang, “Relationship between waxy crude oil composition and change in the morphology and structure of wax crystals induced by pour-point-depressant beneficiation,” *Energy and Fuels*, vol. 25, no. 4, pp. 1686–1696, 2011.

[64] C. Jiang, K. Zhao, C. Fu, and L. Xiao, “Characterization of Morphology and Structure of Wax Crystals in Waxy Crude Oils by Terahertz Time-Domain Spectroscopy,” *Energy and Fuels*, vol. 31, no. 2, pp. 1416–1421, 2017.

[65] R. Mendes, G. Vinay, G. Ovarlez, and P. Coussot, “Modeling the rheological behavior of waxy crude oils as a function of flow and temperature history,” *J. Rheol.*, vol. 59, no. 3, pp. 703–732, 2015.

[66] R. Mendes, G. Vinay, G. Ovarlez, and P. Coussot, “Modeling the rheological behavior of waxy crude oils as a function of flow and temperature history,” *J. Rheol.*, vol. 59, no. 3, pp. 703–732, 2015.

[67] T. O. Marinho, C. N. Barbato, G. B. Freitas, C. Angela Duncke, D. O. Marcia Khalil, and M. Nele, “Interaction Effects of Predominantly Linear and Branched Waxes on Yield Stress and Elastic Modulus of Waxy Oils,” *Energy & Fuels*, vol. 32, no. 8, pp. 8057–8068, 2018.

[68] K. Almdal, J. Dyre, S. Hvidt, and O. Kramer, “Towards a Phenomenological Definition of the Term ’ Gel ’,” vol. 1, pp. 5–17, 1993.

[69] W. Shih, Y. Shih, S. Kim, J. Liu, and I. A. Aksay, “Scaling behavior of the elastic properties of colloidal gels,” *Phys. Rev. A*, vol. 42, no. 8, pp. 4772–4780, 1990.

[70] Z. Huang, H. S. Lee, M. Senra, and H. S. Fogler, “A Fundamental Model of Wax Deposition in Subsea Oil Pipelines,” *Am. Inst. Chem. Eng.*, vol. 57, no. 504, pp. 2955–2964, 2011.

[71] G. Giacchetta, B. Marchetti, M. Leporini, A. Terenzi, D. Dall, L. Capece, and R. Cocci, “Pipeline wax deposition modeling : A sensitivity study on two commercial software,” *Petroleum*, no. Article in press, 2018.

[72] A. S. Kasumu, S. Arumugam, and A. K. Mehrotra, “Effect of cooling rate on the wax precipitation temperature of ‘waxy’ mixtures,” *Fuel*, vol. 103, pp. 1144–1147, 2013.

[73] S. Han, J. Zhang, and L. Zhu, “Effect of the amount and the composition of precipitated n-alkanes on the yield stress of wax-decane gels,” *J. Pet. Sci. Eng.*, vol. 147, pp. 228–236, 2016.

[74] G. Cazaux, L. Barre, and F. Brucy, “Waxy Crude Cold Start: Assessment Through Gel Structural Properties,” *SPE Annu. Tech. Conf. Exhib.*, pp. 729–739, 1998.

[75] V. Chevallier, “Crystallization of a multiparaffinic wax in normal tetradecane,” *Fuel*, vol. 79, no. 14, pp. 1743–1750, 2000.

[76] M. Dirand, M. Bouroukba, V. Chevallier, D. Petitjean, E. Behar, and V. Ruffier-Meray, “Normal alkanes, multialkane synthetic model mixtures, and real petroleum waxes: Crystallographic structures, thermodynamic properties, and crystallization,” *J. Chem. Eng. Data*, vol. 47, no. 2, pp. 115–143, 2002.

[77] Y. Zhao, L. Kumar, K. Paso, J. Safieva, M. Z. B. Sariman, and J. Sjöblom, “Gelation Behavior of Model Wax−Oil and Crude Oil Systems and Yield Stress Model Development,” *Energy & Fuels*, vol. 26, pp. 6323–6331, 2012.

[78] P. Gao, J. Zhang, and G. Ma, “Direct image-based fractal characterization of

morphologies and structures of wax crystals in waxy crude oils," *J. Phys. Condens. Matter*, vol. 18, no. 50, pp. 11487–11506, 2006.

[79] J. M. Létoffé, P. Claudy, M. V. Kok, M. Garcin, and J. L. Volle, "Crude oils: characterization of waxes precipitated on cooling by d.s.c. and thermomicroscopy," *Fuel*, vol. 74, no. 6, pp. 810–817, 1995.

[80] S. P. Srivastava, R. S. Tandon, Verma P, A. K. Saxena, and G. C. Joshi, "Crystallization behaviour of n-paraffins in Bombay-high middle distillate wax gel," *Fuel*, vol. 71, no. 5, pp. 533–537, 1992.

[81] P. Singh, H. S. Fogler, N. Nagarajan, P. Singh, and H. S. Fogler, "Prediction of the wax content of the incipient wax-oil gel in a pipeline : An application of the controlled-stress rheometer Published by the The Society of Rheology Prediction of the wax content of the incipient wax-oil gel in a pipeline : An application," *J. Rheol.*, vol. 43, pp. 1437–1459, 1999.

[82] M. T. Zaky and N. H. Mohamed, "Comparative study on separation and characterization of high melting point macro- and micro-crystalline waxes," *J. Taiwan Inst. Chem. Eng.*, vol. 41, no. 3, pp. 360–366, 2010.

[83] C. D. Doan, C. M. To, M. De Vrieze, F. Lynen, S. Danthine, A. Brown, K. Dewettinck, and A. R. Patel, "Chemical profiling of the major components in natural waxes to elucidate their role in liquid oil structuring," *Food Chem.*, vol. 214, pp. 717–725, 2017.

[84] J. A. P. Coutinho, J. A. Lopes da Silva, A. Ferreira, M. R. Soares, and J. L. Daridon, "Evidence for the aging of wax deposits in crude oils by Ostwald Ripening," *Pet. Sci. Technol.*, vol. 21, no. 3–4, pp. 381–391, 2003.

[85] A. K. Aboul-Gheit, T. Abd-el-Moghny, and M. M. Al-Eseimi, "Characterization of oils by differential scanning calorimetry," *Thermochim. Acta*, vol. 306, pp. 127–130, 1997.

[86] Y. Zhao, K. Paso, J. Norrman, H. Ali, G. Sørland, and J. Sjöblom, "Utilization of DSC, NIR, and NMR for wax appearance temperature and chemical additive performance characterization," *J. Therm. Anal. Calorim.*, vol. 120, no. 2, pp. 1427–1433, 2015.

[87] Z. Jiang, J. M. Hutchinson, and C. T. Imrie, "Measurement of the wax appearance temperatures of crude oils by temperature modulated differential scanning calorimetry," *Fuel*, vol. 80, no. 3, pp. 367–371, 2001.

[88] J. Chen, J. Zhang, and H. Li, “Determining the wax content of crude oils by using differential scanning calorimetry,” *Thermochim. Acta*, vol. 410, no. 1–2, pp. 23–26, 2004.

[89] P. Claudy, J. M. Létoffé, B. Neff, and B. Damin, “Diesel fuels - determination of onset crystallization temperature, pour point and filter plugging point by differential scanning calorimetry.Correlationwith standard test methods,” *Fuel Energy Abstr.*, vol. 65, pp. 861–864, 1986.

[90] J. M. Létoffé, P. Claudy, M. V. Kok, M. Garcin, and J. L. Volle, “Crude oils: characterization of waxes precipitated on cooling by d.s.c. and thermomicroscopy,” *Fuel*, vol. 74, pp. 810–817, 1995.

[91] J. Chen, J. Zhang, and H. Li, “Determining the wax content of crude oils by using differential scanning calorimetry,” *Thermochim. Acta*, vol. 410, no. 1–2, pp. 23–26, 2004.

[92] J. A. L. da Silva and J. A. Coutinho, “Dynamic rheological analysis of the gelation behaviour of waxy crude oils,” *Rheol. Acta*, vol. 43, no. 5, pp. 433–441, 2004.

[93] D. Johansson, “Weak gels of fat crystals in oils at low temperatures and their fractal nature,” *J. Am. Oil Chem. Soc.*, vol. 72, no. 10, pp. 1235–1237, 1995.

[94] R. P. Chhabra and J. F. Richardson, *Non-Newtonian Flow and Applied Rheology*, Secound. 2008.

[95] T. F. Tadros, *Rheology of Dispersions: Principles and Applications*. Wiley VCH, 2010.

[96] M. Di Febo and P. Paganini, “Centrifugal pump technology in oil & gas refinement,” *World Pumps*, vol. DOI: 10.10, no. 11, pp. 36–40, 2015.

[97] M. Castro, D. W. Giles, C. W. Macosko, and T. Moaddel, “Comparison of methods to measure yield stress of soft solids,” *J. Rheol.*, vol. 54, no. 1, pp. 81–94, 2010.

[98] H. J. Walls, S. B. Caines, A. M. Sanchez, and S. A. Khan, “Yield stress and wall slip phenomena in colloidal silica gels,” *J. Rheol.*, vol. 47, no. 4, pp. 847–868, 2003.

[99] M. Instruments, “Inform White Paper Understanding Yield Stress,” 2012.

[100] C. W. Macosko, *Rheology Principles, Measurements and Applications*. Wiley-VCH, 1994.

[101] H. A. Barnes, *A Handbook of Elementary Rheology*. Wales, 2000.

[102] Q. Q. D. Nguyen, T. Akroyd, D. C. D. C. De Kee, L. L. Zhu, and D. De Kee, “Yield stress measurements in suspensions: an inter-laboratory study,” *Korea-Australia Rheol. J.*, vol. 18, no. 1, pp. 15–24, 2006.

[103] M. Dinkgreve, J. Paredes, M. M. Denn, and D. Bonn, “On different ways of measuring ‘the’ yield stress,” *J. Nonnewton. Fluid Mech.*, vol. 238, pp. 233–241, 2016.

[104] W. Canet, M. D. Alvarez, C. Fernández, and P. Luna, “Comparisons of methods for measuring yield stresses in potato puree: Effect of temperature and freezing,” *J. Food Eng.*, vol. 68, no. 2, pp. 143–153, 2005.

[105] S. Yi and J. Zhang, “Shear-induced change in morphology of wax crystals and flow properties of waxy crudes modified with the pour-point depressant,” *Energy and Fuels*, vol. 25, no. 12, pp. 5660–5671, 2011.

[106] L. H. O. Hellström, M. A. Samaha, K. M. Wang, A. J. Smits, and M. Hultmark, “Errors in parallel-plate and cone-plate rheometer measurements due to sample underfill,” *Meas. Sci. Technol.*, vol. 26, no. 1, pp. 1–4, 2015.

[107] A. Aït-kadi, P. Marchal, L. Choplin, A. Chrissemant, and M. Bousmina, “Quantitative Analysis of Mixer-Type Rheometers using the Couette Analogy,” *Can. J. Chem. Eng.*, vol. 80, no. December, pp. 1166–1174, 2002.

[108] J. Kaur and A. Jaafar, “Yield Stress Measurements of Waxy Crude,” *J. Appl. Sci.*, vol. 14, no. 11, pp. 1114–1122, 2014.

[109] M. Cloitre and R. T. Bonnecaze, “A review on wall slip in high solid dispersions,” *Rheol. Acta*, vol. 56, no. 3, pp. 283–305, 2017.

[110] J. R. Stokes, M. W. Boehm, and S. K. Baier, “Oral processing, texture and mouthfeel: From rheology to tribology and beyond,” *Curr. Opin. Colloid Interface Sci.*, vol. 18, no. 4, pp. 349–359, 2013.

[111] J. H. Kim, S. H. Kwon, S. Kawashima, and H. J. Yim, “Rheology of cement paste under high pressure,” *Cem. Concr. Compos.*, vol. 77, pp. 60–67, 2016.

[112] R. Buscall, J. I. Mcgowan, and A. J. Mortonjones, “The rheology of concentrated dispersions of weakly attracting colloidal particles with and without wall slip,” *J. Rheol. (N. Y. N. Y).*, vol. 37, pp. 621–641, 1993.

[113] S. G. Hatzikiriakos, “Slip mechanisms in complex fluid flows,” *Soft Matter*, vol. 11,

no. 40, pp. 7851–7856, 2015.

[114] H. A. Barnes, “Review of Slip (Wall Depletion) of Polymer Solutions Emusions Pard Particle Suspensions Inviscometers Its Cause Character and Cure,” *J. Non-Newtonian Fluid Mech*, vol. 56, pp. 221–251, 1995.

[115] H. A. Barnes, “A review of slip (wall depletion) of polymer solutions, emusions and particle suspensions in viscometers: its cause, character, and cure,” *J. Nonnewton. Fluid Mech.*, vol. 56, pp. 221–251, 1995.

[116] X. Zhang, E. Lorenceau, P. Basset, T. Bourouina, F. Rouyer, J. Goyon, and P. Coussot, “Wall Slip of Soft-Jammed Systems: A Generic Simple Shear Process,” *Phys. Rev. Lett.*, vol. 119, no. 20, pp. 1–5, 2017.

[117] H. S. Lee, P. Singh, W. H. Thomason, and H. S. Fogler, “Waxy oil gel breaking mechanisms: Adhesive versus cohesive failure,” *Energy and Fuels*, vol. 22, no. 1, pp. 480–487, 2008.

[118] P. Coussout, *Rheometry of pastes, suspensions and granular materials*. Wiley-Interscince, 2005.

[119] W. B. Russel and M. C. Grant, “Distinguishing between dynamic yielding and wall slip in a weakly flocculated colloidal dispersion,” *Colloids Surfaces A Physicochem. Eng. Asp.*, vol. 161, no. 2, pp. 271–282, 2000.

[120] A. Yoshimura, R. K. Prud, A. N. N. Yoshimura, and R. K. P. Homme, “Wall Slip Corrections for Couette and Parallel Disk Viscometers Wall Slip Corrections for Couette and Parallel Disk Viscometers,” *J. Rheol.*, vol. 32, pp. 53–67, 1988.

[121] F. H. Marchesini, M. F. Naccache, A. Abdu, A. A. Alicke, and P. R. de Souza Mendes, “Rheological characterization of yield-stress materials: Flow pattern and apparent wall slip,” *Appl. Rheol.*, vol. 25, no. 5, pp. 1–10, 2015.

[122] H. A. Barnes and Q. D. Nguyen, “Rotating vane rheometry — a review,” *J. Nonnewton. Fluid Mech.*, vol. 98, no. 1, pp. 1–14, 2001.

[123] L. J. Gibson and M. F. Ashby, *Cellular solids: Structure and properties*. Oxford: Pergamon Press, 1988.

[124] P.-G. de Gennes, *Scaling Concepts in Polymer Physics*. Cornell University Press, 1979.

[125] F. Yang, C. Li, and D. Wang, “Studies on the structural characteristics of gelled waxy crude oils based on scaling model,” *Energy and Fuels*, vol. 27, no. 3, pp.

1307–1313, 2013.

[126] D. Tang and A. G. Marangoni, “Modeling the rheological properties and structure of colloidal fat crystal networks,” *Trends Food Sci. Technol.*, vol. 18, no. 9, pp. 474–483, 2007.

[127] H. Wu and M. Morbidelli, “A Model Relating Structure of Colloidal Gels to Their Elastic Properties,” *Langmuir*, vol. 17, no. 4, pp. 1030–1036, 2001.

[128] F. Yang, C. Li, C. Li, and D. Wang, “Scaling of structural characteristics of gelled model waxy oils,” *Energy and Fuels*, vol. 27, no. 7, pp. 3718–3724, 2013.

[129] A. G. Marangoni, “Elasticity of high-volume-fraction fractal aggregate networks:,” *Phys. Rev. B*, vol. 62, no. 21, pp. 951–955, 2000.

[130] A. G. Marangoni and M. A. Rogers, “Structural basis for the yield stress in plastic disperse systems,” *Appl. Phys. Lett.*, vol. 82, no. 19, pp. 3239–3241, 2003.

[131] M. Kané, M. Djabourov, and J. L. Volle, “Rheology and structure of waxy crude oils in quiescent and under shearing conditions,” *Fuel*, vol. 83, no. 11–12, pp. 1591–1605, 2004.

[132] R. W. Connelly and J. Greener, “HighShear Viscometry with a Rotational ParallelDisk Device High-Shear Viscometry with a Rotational Parallel-Disk Device,” *J. Rheol.*, vol. 29, pp. 209–226, 1985.

[133] H. Barnes and K. Walters, “‘The Yield Stress Myth?,’” *Theor. Appl. Rheol.*, vol. 24, pp. 323–326, 1985.

[134] M. I. Zougari and T. Sopkow, “Introduction to crude oil wax crystallization kinetics: Process modeling,” *Ind. Eng. Chem. Res.*, vol. 46, no. 4, pp. 1360–1368, 2007.

[135] B. Jia and J. Zhang, “Yield behavior of waxy crude gel: Effect of isothermal structure development before prior applied stress,” *Ind. Eng. Chem. Res.*, vol. 51, no. 33, pp. 10977–10982, 2012.

[136] A. S. Luyt and I. Krupa, “Thermal behaviour of low and high molecular weight paraffin waxes used for designing phase change materials,” *Thermochim. Acta*, vol. 467, no. 1–2, pp. 117–120, 2007.

[137] D. D. H. Brandolini, Anita J., *NMR Spectra of Polymers and Polymer Additives*. Edison, New Jersey: CRC Press, 2000.

[138] Y. Wei and Z. Li, “Measurement of d-spacing of crystalline samples with SAXS,”

*Meas. J. Int. Meas. Confed.*, vol. 93, pp. 473–479, 2016.

[139] R. Akkal, N. Cohaut, M. Khodja, T. Ahmed-Zaid, and F. Bergaya, “Rheo-SAXS investigation of organoclay water in oil emulsions,” *Colloids Surfaces A Physicochem. Eng. Asp.*, vol. 436, pp. 751–762, 2013.

[140] S. Tadimalla, M. C. Tourell, R. Knott, and K. I. Momot, “Quantifying collagen fibre architecture in articular cartilage using small-angle X-ray scattering,” *Biomed. Spectrosc. Imaging*, vol. 6, no. 1–2, pp. 37–57, 2017.

[141] T. Ogawa, S. Miyashita, H. Miyaji, S. Suehiro, and H. Hayashi, “Fractal properties of polymer crystals,” *J. Chem. Phys.*, vol. 90, no. 3, pp. 2063–2067, 1989.

[142] T. Imai, K. Nakamura, and M. Shibata, “Relationship between the hardness of an oil-wax gel and the surface structure of the wax crystals,” *Colloids Surfaces A Physicochem. Eng. Asp.*, vol. 194, no. 1–3, pp. 233–237, 2001.

[143] R. M. Silverstein, F. X. Webster, and D. J. Kiemle, *Spectrometric Identifications of organic compounds.pdf*, Seventh. John Wiley & Sons, 2005.

[144] W. A. Lopes and M. Fascio, “Flow chart for infrared spectra interpretation of organic compounds,” *Quim. Nova*, vol. 27, no. 4, pp. 670–673, 2004.

[145] A. Messaâdi, N. Dhouibi, H. Hamda, F. Bin, M. Belgacem, Y. H. Adbelkader, N. Ouerfelli, and A. H. Hamzaoui, “A New Equation Relating the Viscosity Arrhenius Temperature and the Activation Energy for Some Newtonian Classical Solvents,” *J. Chem.*, vol. 25, pp. 7–10, 2015.

[146] R. B. Haj-Kacem, N. Ouerfelli, J. V. Herráez, M. Guettari, H. Hamda, and M. Dallel, “Contribution to modeling the viscosity Arrhenius-type equation for some solvents by statistical correlations analysis,” *Fluid Phase Equilib.*, vol. 383, pp. 11–20, 2014.

[147] G. Sun, J. Zhang, and H. Li, “Structural behaviors of waxy crude oil emulsion gels,” *Energy and Fuels*, vol. 28, no. 6, pp. 3718–3729, 2014.

[148] H. A. Barnes, “Measuring the viscosity of large-particle (and flocculated) suspensions - a note on the necessary gap size of rotational viscometers,” *J. Nonnewton. Fluid Mech.*, vol. 94, no. 2–3, pp. 213–217, 2000.

[149] T. O. Marinho, M. N. De Souza, C. N. Barbato, and M. C. K. De Oliveira, “Rheological and Thermal Behavior of Water-Waxy Crude Oil Emulsions,” 2015.

[150] Q. D. Nguyen, T. Akroyd, D. C. De Kee, and L. Zhu, “Yield stress measurements

in suspensions: an inter-laboratory study," *Korea-Australia Rheol. J.*, vol. 18, no. 1, pp. 15–24, 2006.

[151] B. L. Walter, J. P. Pelteret, J. Kaschta, D. W. Schubert, and P. Steinmann, "On the wall slip phenomenon of elastomers in oscillatory shear measurements using parallel-plate rotational rheometry: II. Influence of experimental conditions," *Polym. Test.*, vol. 61, pp. 455–463, 2017.

[152] M. C. Sánchez, C. Valencia, J. M. Franco, and C. Gallegos, "Wall slip phenomena in oil-in-water emulsions: Effect of some structural parameters," *J. Colloid Interface Sci.*, vol. 241, no. 1, pp. 226–232, 2001.

[153] C. Cheng, D. V. Boger, and Q. D. Nguyen, "Influence of Thermal History on the Waxy Structure of Statically Cooled Waxy Crude Oil," *SPE J.*, vol. 5, no. 02, pp. 148–157, 2000.

[154] A. Wachs, G. Vinay, and I. Frigaard, "A 1.5D numerical model for the start up of weakly compressible flow of a viscoplastic and thixotropic fluid in pipelines," *J. Nonnewton. Fluid Mech.*, vol. 159, no. 1–3, pp. 81–94, 2009.

[155] J. F. Tinsley, J. P. Jahnke, H. D. Dettman, and R. K. Prud'home, "Waxy gels with asphaltenes 1: Characterization of precipitation, gelation, Yield stress, and morphology," *Energy and Fuels*, vol. 23, no. 4, pp. 2056–2064, 2009.

[156] R. M. Webber, "Yield properties of wax crystal structures formed in lubricant mineral oils," *Ind. Eng. Chem. Res.*, vol. 40, no. 1, pp. 195–203, 2001.

[157] X. Guo, B. A. Pethica, J. S. Huang, D. H. Adamson, and R. K. Prud'homme, "Effect of cooling rate on crystallization of model waxy oils with microcrystalline poly(ethylene butene)," *Energy and Fuels*, vol. 20, no. 1, pp. 250–256, 2006.

[158] D. E. V. Andrade, M. A. Marcelino Neto, and C. O. R. Negrão, "Non-monotonic response of waxy oil gel strength to cooling rate," *Rheol. Acta*, vol. 57, no. 10, pp. 673–680, 2018.

[159] R. Venkatesan, N. R. Nagarajan, K. Paso, Y. B. Yi, A. M. Sastry, and H. S. Fogler, "The strength of paraffin gels formed under static and flow conditions," *Chem. Eng. Sci.*, vol. 60, no. 13, pp. 3587–3598, 2005.

[160] Q. Q. D. D. Nguyen, T. Akroyd, D. C. D. C. De Kee, L. L. Zhu, and D. De Kee, "Yield stress measurements in suspensions: an inter-laboratory study," *Korea-Australia Rheol. J.*, vol. 18, no. 1, pp. 15–24, 2006.

[161] B. Jia and J. Zhang, “Yield Behavior of Waxy Crude Gel: E ff ect of Isothermal Structure Development before Prior Applied Stress,” *Ind. Eng. Chem. Res.*, vol. 51, p. 10977−10982, 2012.

[162] A. B. Hansen, E. Larsen, W. B. Pedersen, A. B. Nielsen, and H. P. Ronningsen, “Wax Precipitation from North Sea Crude Oils. 3. Precipitation and Dissolution of Wax Studied by Differential Scanning Calorimetry,” *Energy and Fuels*, vol. 5, no. 6, pp. 914–923, 1991.

[163] J. A. P. Coutinho and J. L. Daridon, “The limitations of the cloud point measurement techniques and the influence of the oil composition on its detection,” *Pet. Sci. Technol.*, vol. 23, no. 9–10, pp. 1113–1128, 2005.

[164] R. R. Fernandes, D. E. V. Andrade, A. T. Franco, and C. O. R. Negrão, “Correlation between the gel-liquid transition stress and the storage modulus of an oil-based drilling fluid,” *J. Nonnewton. Fluid Mech.*, vol. 231, pp. 6–10, 2016.

[165] P. Claudy, J.-M. Letoffe, B. Bonardi, D. Vassilakis, and B. Damin, “Interactions between filter plugging point in a diesel fuel . A thermodynamic and cloud depressants study,” *Fuel*, vol. 72, no. 6, pp. 821–827, 1993.

[166] Y. Ji, W. Kang, S. Liu, R. Yang, and H. Fan, “The relationships between rheological rules and cohesive energy of amphiphilic polymers with different hydrophobic groups,” *J. Polym. Res.*, vol. 22, no. 3, pp. 1–7, 2015.

[167] M. Senra, T. Scholand, C. Maxey, and H. S. Fogler, “Role of polydispersity and cocrystallization on the gelation of long-chained n-alkanes in solution,” *Energy and Fuels*, vol. 23, no. 12, pp. 5947–5957, 2009.

[168] Y. H. Jang, M. Blanco, J. Creek, Y. Tang, and W. A. Goddard, “Wax inhibition by comb-like polymers: Support of the incorporation- perturbation mechanism from molecular dynamics simulations,” *J. Phys. Chem. B*, vol. 111, no. 46, pp. 13173–13179, 2007.